Politechnika Wrocławska

FIELD OF SCIENCE: ENGINEERING AND TECHNICAL SCIENCES

DISCIPLINE OF SCIENCE: ENVIRONMENTAL ENGINEERING, MINING AND ENERGY

DOCTORAL DISSERTATION

Influence of volute casing geometry on the energy characteristics of a double-entry centrifugal pump operating in pump and turbine modes

MSc Eng. Anna Chernobrova

Supervisor:
prof. dr hab. Piotr Szulc

Assistant supervisor:
PhD Eng. Artur Machalski

Keywords: centrifugal pump, volute geometry, pump-as-turbine (PAT), specific speed, CFD

WROCŁAW 2026

Acknowledgements

During the preparation of this dissertation, I received invaluable help and support from many people, to whom I would like to express my sincere gratitude.

First and foremost, I would like to thank my supervisor, Professor Piotr Szulc, as well as Dr. Artur Machalski, for their guidance, support, and valuable advice throughout the preparation of this dissertation.

I am also deeply grateful to my colleagues, Dr. Przemysław Szulc, Dr. Dominik Błoński, and Dr. Marek Skowroński, whose knowledge, support, and assistance had a significant influence on the final form of the research and on the completion of this dissertation. I would like to express my sincere gratitude to Professor Marcin Magdziarz for his help with the statistical analysis and to late Professor Dr. Andrzej Błaszczyk for his advice and ideas that contributed to this work.

Special thanks are due to Dr. Marcin Janczak for enabling the collaboration with Hydro-Vacuum S.A. and for providing the pump used in this research.

I would also like to express my sincere gratitude to my husband, Oleksandr Moloshnyi, who stood by my side throughout all the years of preparation of this dissertation.

I am deeply grateful to my family for their support, help, and understanding.

Most of all, I would like to express my deepest gratitude to the Armed Forces of Ukraine, who defended me and my family and made it possible for me to live, work, and complete this dissertation during the full-scale invasion of Ukraine by the russian federation.

The calculations were performed using resources provided by the Wrocław Centre for Networking and Supercomputing (http://wcss.pl)

Streszczenie

Spiralny kanał zbiorczy jest jednym z kluczowych elementów konstrukcji pompy wirowej. Odpowiada za odprowadzenie cieczy z wirnika i skierowanie jej do instalacji hydraulicznej. Jego geometria wpływa na warunki przepływu, położenie optymalnego punktu pracy, sprawność, obciążenia hydrauliczne oraz stabilność pracy zespołu wirującego.

Pompy pracujące jako turbiny są coraz częściej stosowane do odzysku energii z przepływającej cieczy, między innymi w sieciach wodociągowych i instalacjach przemysłowych. Ich zaletą są niższe koszty inwestycyjne i prostsza konstrukcja w porównaniu z klasycznymi turbinami wodnymi. Należy jednak podkreślić, że pompy są projektowane przede wszystkim do pracy w trybie pompowym, dlatego ich elementy przepływowe, w tym spiralny kanał zbiorczy, nie zawsze zapewniają korzystne warunki pracy w trybie turbinowym. Z tego względu istotne jest określenie zasad projektowania spirali, które umożliwią uzyskanie korzystnych parametrów pracy w obu trybach.

Celem rozprawy było określenie wpływu parametrów geometrycznych spiralnego kanału zbiorczego oraz sposobu jego projektowania na charakterystyki energetyczne pompy pracującej w trybie pompowym i turbinowym. Badania przeprowadzono z wykorzystaniem podejścia hybrydowego, obejmującego numeryczne modelowanie przepływu oraz badania eksperymentalne. Model numeryczny został poddany walidacji na stanowisku badawczym umożliwiającym analizę pracy pompy w obu trybach.

W pracy analizowano wpływ wybranych cech geometrycznych spiralnego kanału zbiorczego, takich jak metoda projektowania pól przekrojów poprzecznych, szerokość i średnica wlotowa spiralnego kanału zbiorczego, kształt przekroju poprzecznego oraz kąt rozwarcia ścian. Oceniono ich wpływ na wysokość podnoszenia lub spad, moc mechaniczną, sprawność oraz straty hydrauliczne w spiralnym kanale zbiorczym dla pomp z wyróżnikiem szybkobieżności 23 i 66.

Stopień oraz charakter wpływu parametrów geometrycznych spiralnego kanału zbiorczego określono z wykorzystaniem analizy parametrów pracy, struktury przepływu oraz analizy statystycznej. Uzyskane wyniki potwierdziły, że geometria spiralnego kanału zbiorczego ma większe znaczenie dla pracy pompy w trybie turbinowym niż w trybie pompowym. Oznacza to, że podczas projektowania pomp przewidzianych do pracy odwróconej należy w pierwszej kolejności uwzględniać wymagania wynikające z trybu turbinowego.

Na podstawie analizy wielokryterialnej dwóch pomp wyznaczono geometrię spirali zapewniającą korzystny kompromis pomiędzy pracą pomp w trybie pompowym i turbinowym. Przedstawiono autorskie zalecenia dotyczące doboru parametrów geometrycznych spiralnego kanału zbiorczego. Wyniki pracy mogą stanowić podstawę do projektowania spiral pomp wirowych (z wyróżnikiem szybkobieżności 23 i 66) przewidzianych do pracy zarówno w trybie pompowym, jak i turbinowym.

Abstract

The volute is one of the key structural elements of a centrifugal pump. It is responsible for collecting the liquid from the impeller and directing it to the hydraulic system. Its geometry affects the flow conditions, the position of the best efficiency point, efficiency, hydraulic loads, and the stability of the pump.

Pumps operating as turbines are increasingly used to recover energy from flowing liquid, for example in water supply networks and industrial systems. Their advantages include lower investment costs and a simpler design compared with classical water turbines. However, it should be emphasized that pumps are mainly designed for pump operation. Therefore, their flow components, including the volute, do not always provide favourable operating conditions in turbine mode. For this reason, it is important to define volute design rules that allow favourable operating parameters to be obtained in both modes.

The aim of the dissertation was to determine the influence of the geometrical parameters of the volute and its design method on the energy characteristics of a pump operating in pump and turbine modes. The research was carried out using a hybrid approach that included numerical flow modelling and experimental tests. The numerical model was validated on a test rig that enabled the analysis of pump operation in both modes.

The study analysed the influence of selected geometrical features of the volute, such as the method of designing the cross-sectional areas, the inlet width and inlet diameter of the volute, the cross-sectional shape, and the wall opening angle. Their influence on head, mechanical power, efficiency, and hydraulic losses in the volute for a pumps with a specific speed of 23 and 66 was assessed.

The degree and nature of the influence of the volute geometrical parameters was determined using the analysis of operating parameters, flow structure, and statistical analysis. The obtained results confirmed that the geometry of the volute has a greater influence on pump operation in turbine mode than in pump mode. This means that, when designing pumps intended for reverse operation, the requirements resulting from turbine mode should be considered first.

Based on a multi-criteria analysis, the volute geometry of two pumps that provides a favourable compromise between pump and turbine operation was determined. Original recommendations for selecting the geometrical parameters of the volute were presented. The results of the dissertation may provide a basis for designing volutes of centrifugal pumps (specific speed of 23 and 66) intended to operate both in pump mode and in turbine mode.

Table of Contents

Chapter 1 : Introduction 11
Chapter 2 : Literature review 13
2.1 Centrifugal pump 13
2.2 Pump as turbine 14
2.3 Specific speed 16
2.4 Overview of fundamental literature of volute casing design 17
2.4.1 Design methods 17
2.4.2 Inlet width 18
2.4.3 Inlet diameter 19
2.4.4 Cross-sections shape 19
2.4.5 Wall opening angle 20
2.5 Volute design optimization in pump mode 20
2.5.1 Design methods 20
2.5.2 Cross-sectional area 21
2.5.3 Shape of volute cross section 22
2.5.4 Cutwater 22
2.5.5 Inlet width and diameter 23
2.5.6 Grooved volute casing 24
2.5.7 The effect of the volute casing on pump operation pressure pulsation, wear and losses in volute casing 24
2.6 Volute design optimization in turbine mode 25
2.6.1 Design methods 25
2.6.2 Cross-sectional area 25
2.6.3 Shape of volute cross section 25
2.6.4 Cutwater, pressure pulsation 26
2.6.5 Inlet width and diameter 26
2.6.6 Cavitation and energy losses 26
2.7 Chapter summary 27
Chapter 3 : Subject, purpose, and thesis of the work 29
Chapter 4 : Approach to the problem 30
4.1 Research problem 30

4.2 Subject of the study 30
4.2.1 Description of the DHV.80-270 A pump 31
4.2.2 Description of the Omega 350-430B pump 33
4.3 Investigated geometric parameters of the volute casing 34
4.4 Research approach 36
Chapter 5 : Numerical simulation 39
5.1 Three-dimensional geometry of the pump flow parts 40
5.2 Discrete model of the DHV and Omega pumps 41
5.3 Boundary conditions 43
5.4 Turbulence model selection 45
Chapter 6 : Experimental research 47
6.1 Description of the experimental stand for pump operating in pump mode 47
6.2 Validation of numerical simulation for the DHV pump in pump mode 48
6.3 Experimental stand for DHV pump operating in turbine mode 49
6.4 Validation of numerical simulation for the DHV pump in turbine mode 51
6.5 Validation of numerical simulation for the Omega pump in pump mode 51
6.6 Validation of numerical simulation for the Omega pump in turbine mode 53
6.7 Calculation formulas for pump and turbine energy characteristics 53
6.8 Measurement uncertainty 54
Chapter 7 : Numerical results and statistical analysis for Omega pump 57
7.1 Numerical results 57
7.1.1 Volute wall opening angle influence 57
7.1.2 Design method, D_3, b_3 and cross-section shape influence 58
7.1.3 Selection of the compromise volute casing for pump and turbine operation mode 67
7.1.4 Hydrodynamic analysis 68
7.1.5 Section summary 79
7.2 Statistical analysis 80
7.2.1 Description of the statistical method 80
7.2.2 Pump mode 82
7.2.3 Turbine mode 84
7.2.4 Section summary 89

Chapter 8 : Numerical results and statistical analysis for DHV pump 91
8.1 Numerical results 91
8.1.1 Volute wall opening angle and cross-section shape influence 91
8.1.2 Design method, D_3, b_3 influence 91
8.1.3 Selection of the compromise volute casing for pump and turbine operation mode 98
8.1.4 Hydrodynamic analysis 99
8.1.5 Section summary 106
8.2 Statistical Analysis of the DHV pump 106
8.2.1 Pump mode 107
8.2.2 Turbine mode 108
8.2.3 Regression analysis of best efficient point shift in turbine mode 110
8.2.4 Section summary 111
Chapter 9 : Conclusions 112
9.1 Confirmation of the thesis 112
9.2 Main findings 113
9.3 Design recommendations for pump as turbine design 115
9.4 Industrial implementation 115
9.5 Future work 115
References 116
Appendices 124
Appendix A. Classification of pumps and impellers based on specific speed 124
Appendix B. Detailed overview of fundamental literature of volute casing design 125
Appendix C. Influence of the volute opening angle of the walls on Omega pump and PAT performance. Full graphs 140
Appendix D. Influence of method of volute casing`s design, D_3, b_3, cross-sectional shape on the Omega pump performance. Full graphs 142
Appendix E. Influence of design method, D_3, b_3, cross-sectional shape on Omega PAT performance. Full graphs 144
Appendix F. Comparison of curing curves for Omega PAT at different geometric parameters 146
Appendix G. Change in the velocity triangle components 153

Appendix H. Flow distribution in the Omega PAT with volutes of different geometric parameters 157
Appendix I. Factor effects in the regression model of Omega pump in pump mode 158
Appendix J. Factor effects in the regression model of Omega pump in turbine mode.....160
Appendix K. Factor effects in the regression model of DHV pump in pump mode.....162
Appendix L. Factor effects in the regression model of DHV pump in turbine mode.....165
Appendix M. Confirmation of implementation in production 167

List of most important symbols

Symbols, abbreviations, definitions:

b	–	width, mm
BEP	–	best efficiency point
D	–	diameter, mm
PAT	–	Pump as turbine
c, v	–	absolute velocity, m/s
v_u, c_u	–	circumferential (tangential) component of the absolute velocity, m/s
u, U	–	circumferential velocity, m/s
v_m, c_m	–	meridional component of absolute velocity, m/s
ω	–	angular velocity, rad/s
W	–	relative velocity, m/s
α	–	angle between direction of circumferential and absolute velocity˚
β	–	angle between relative velocity vector and the negative direction of circumferential velocity˚
n_q, n_s	–	specific speed of the pump
n	–	rotating speed, rpm
Q	–	flow rate, m^3/s
H	–	head, m
H_{th}	–	theoretical head of impeller, m
R, r	–	round; distance from the rotation axis, m
P	–	power, kW
K_3, K_2	–	average velocity coefficient in the volute casing
g	–	gravitational acceleration, m/s^2
ρ	–	density, kg/m^3
A, S	–	area, m^2
CV	–	constant velocity method
CAM	–	conservation of angular momentum method
ε	–	wall opening angle,˚
Q–H–curve	–	the headflow curve
VFD	–	Variable Frequency Drive
LTP	–	Losses of total pressure, kPa
Eff	–	Efficiency of turbine, %
R^2	–	Coefficient of Determination of the Full Model
Partial R^2	–	explained Residual Variance
T	–	trapezoidal
F	–	partial Fstatistic for Comparing Nested Models
Δ	–	estimated regression coefficient, difference
A_{max}	–	average deviation from peak efficiency
Flat	–	flatness
di	–	Euclidean distance

Subscripts, superscripts:

0	–	pump inlet
1	–	impeller inlet
2	–	impeller outlet
3	–	volute inlet
CFD	–	numerical simulations
max	–	maximum
mech, m	–	mechanical
min	–	minimum
nom	–	nominal
opt	–	optimal
BEP.P	–	best efficient point for pump
BEP.T	–	best efficient point for turbine
Ref	–	reference
el	–	electrical
h	–	hydraulic
a	–	axial
av	–	average
p	–	pump
t	–	turbine
th	–	theoretical
sp, vol	–	spiral, volute

Chapter 1: Introduction

The development of pump engineering began in antiquity [1] as devices for lifting and transporting water, and contemporary requirements for energy efficiency and reliability make their further improvement relevant today as well. The first centrifugal pump was described in 1689 [2]. Early designs were simple and mainly used in paper mills. A more modern centrifugal pump was introduced in 1818 [3], but the lack of a reliable drive limited its use. The electric motor, developed in the 19th century, became the standard drive for pumps [3], and in 1898, the first standardized centrifugal pump was produced. Since then, pumps have been continuously improved and widely used.

According to the US Energy Information Administration, global energy consumption is projected to increase by almost 50% between 2018 and 2050 [4]. Therefore, continuous technological improvement is essential to reduce energy dependence. Exploring strategies to improve energy efficiency in the industrial sector is crucial for the international community's sustainable development, as it will help address potential energy shortages in the future [5].

Pump systems represent a substantial share of annual energy use, consuming around 21% of the energy in the industrial sector [5] (Figure 1.1). Most of the energy losses occur within pumping systems and pumps (Table 1.1), which exhibit the lowest efficiencies among system components.

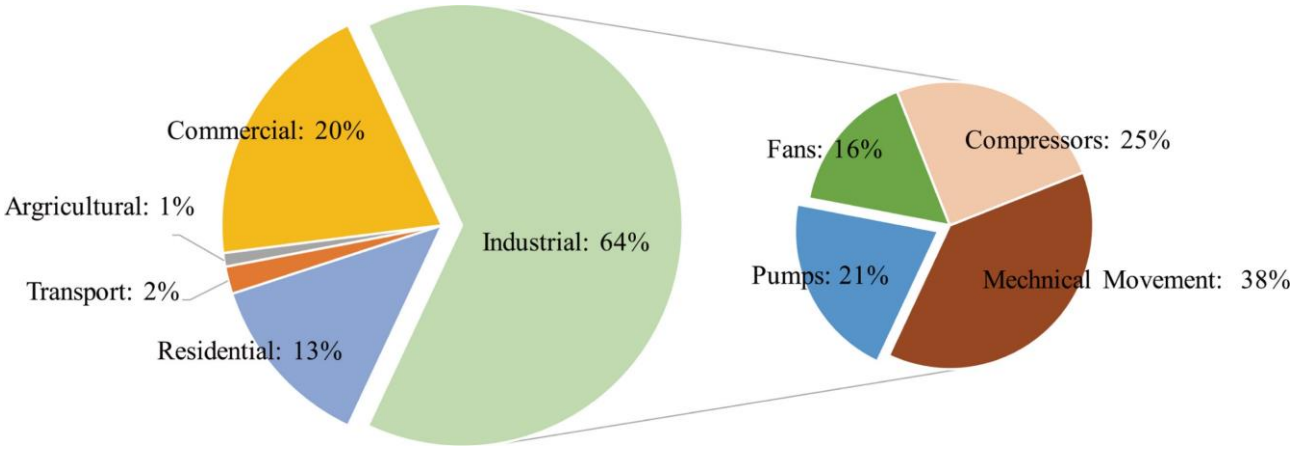

Figure 1.1 - Estimated electricity consumption by electric motors across various sectors [5]

Table 1.1 - Losses and efficiency of each component in a pumping system [5]

Components name	Efficiency (%)
Piping system	50–60
Pumps	85–90
Coupling	~99
Electric Motors	>90
Variable Frequency Drive cables	~98
Variable Frequency Drive	95–98
Transformers	~99

A report by KSB revealed that over 38% of well-designed pumps operate under poor conditions, leading to actual efficiencies falling below 40% [5]. In recent years, the growth of the population, urbanization, and economic development have resulted in a higher demand for energy, water, and food [6]. A substantial body of research and applied science projects in the scientific literature has concentrated on the water-energy-food nexus, clearly emphasizing the crucial role of energy in the efficient use of water resources. There is still untapped potential in using low-capacity hydraulic machines [7]. Instead of dissipating excess head into the environment, turbines can be used. Rotational fluid machines can work in both directions, meaning a pump can also function as a turbine (pump as turbine – PAT). The first description of pumps as turbines was provided by Thoma and Kittredge [8] in 1931. While attempting to assess the full characteristics of pumps, they discovered that pumps could operate highly efficiently in turbine mode [9]. Subsequently, Knapp [10] published the comprehensive pump characteristics for several pump designs, derived from experimental studies.

Pump performance in pump and turbine modes is not the same, even though ideal fluid theory suggests they should be. In turbine mode, the flow rate and head are always higher than in pump mode. The main reason for this difference is the hydraulic losses inside the machine [11].

To improve the operation of the pump, the design of the impeller is most often changed [12]–[27], which has the greatest impact on its operation. However, it is a mistake not to take into account the volute casing design and interaction between the impeller and the volute casing. The liquid from the impeller must flow through the volute casing with the lowest possible losses. The first mention of an improperly selected volute was given in [28]. Bessemer's pump from 1852 achieved only 19% efficiency due to poor flow in the casing, while Appold's pump from the same year reached 68% efficiency. Bowerman and Acosta [29] showed that impeller performance varies with different volute casings, reporting efficiency differences of about 5% for three types of logarithmic volutes. Cumpsty [30] noted that a design mismatch between the impeller and diffuser is a key factor contributing to overall system performance loss. Therefore, researching the volute casing operation is a necessary action that can improve the efficiency of centrifugal pumps.

The influence of volute casing design methodology on its operational performance and overall pump efficiency has not been sufficiently investigated. Existing design methods are primarily focused on determining the cross-sectional area of the volute casing. The literature review (Chapter 2) indicates that there is no clear consensus on which methodology offers the greatest advantages. Moreover, the conditions under which specific design methods should be applied are not clearly defined. There are also no clear guidelines regarding the selection of geometric parameters of the volute casing and their values. As a rule, researchers make their recommendations based on their experimental studies or on the studies of their predecessors.

This work highlights the importance of the volute casing in the operation of both pumps and PATs. It also presents a comparative analysis of volute casing design methods and geometric parameters, supported by experimental and numerical studies aimed at determining their influence on the performance of pumps and turbines with low and high specific speed.

Chapter 2: Literature review

2.1 Centrifugal pump

Pumps are flow machines used for transporting liquids and liquid mixtures. In centrifugal pumps, the mechanical energy of the impeller rotation is converted into the hydraulic energy of the fluid flow. A cross sections of a typical double-entry centrifugal pump are shown in Figure 2.1. In this pump design, the impeller is symmetrical about the mid-plane. The liquid entering the pump casing is divided into two streams, which flow into both inlets of the impeller. The fluid then passes through the impeller and exits the pump via the volute casing. As a result of the impeller's rotation, the pumped liquid gains both pressure (potential) and kinetic energy. The flow of fluid from the impeller is driven by centrifugal force.

The volute casing is a functional element of a pump. It receives the flow leaving the impeller and directs it into the discharge pipeline. The volute performs the following functions [31]–[33]:

collect the liquid leaving the impeller and direct it either to the discharge nozzle or to the impeller of the next stage,

convert kinetic energy into potential energy with minimal losses,

modify the angular momentum along a contour enclosing the impeller.

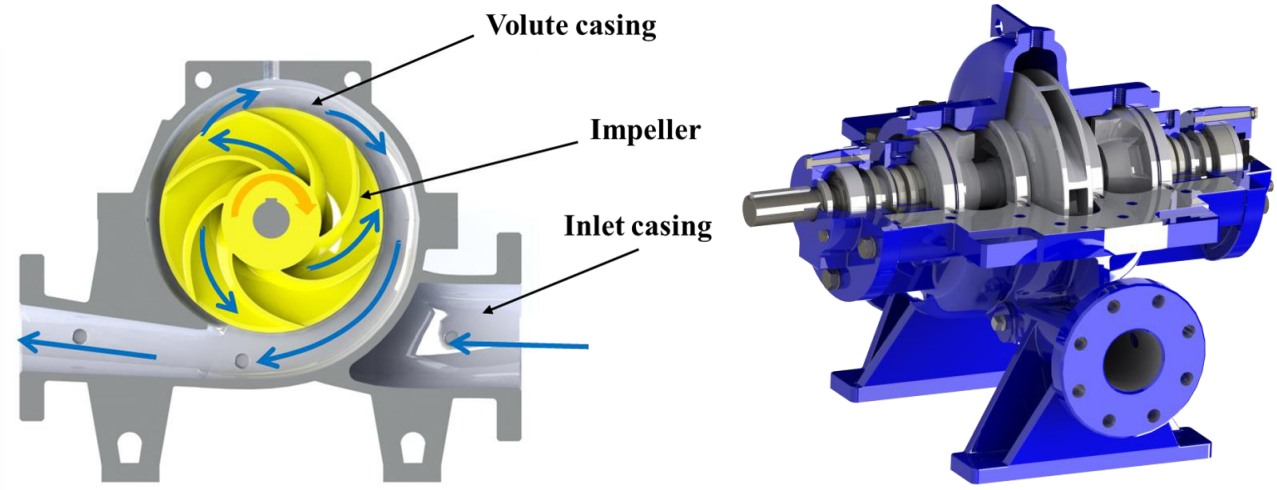

Figure 2.1 – Cross sections of a typical double-entry centrifugal pump

To design a volute casing, in addition to selecting the method, it is necessary to determine the geometric parameters. The most important geometric parameters (Figure 2.2) of the volute casing are: inlet width b_3, volute casing inlet diameter D_3, the opening angle of the walls ε, the shape and area of cross sections (Figure 2.3).

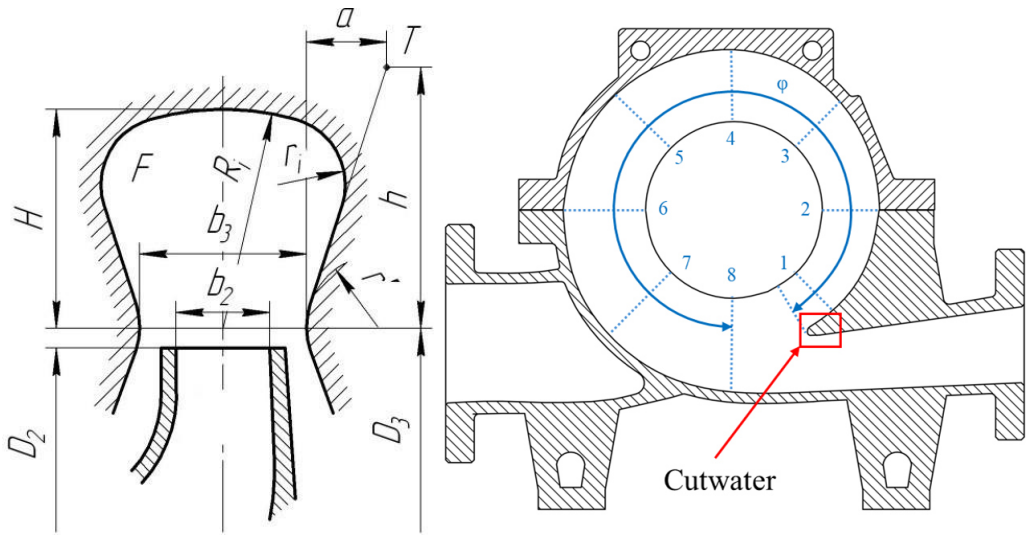

Figure 2.2 – Geometric parameters of the cross section of volute casing: a) cross section [34], b) longitudinal section

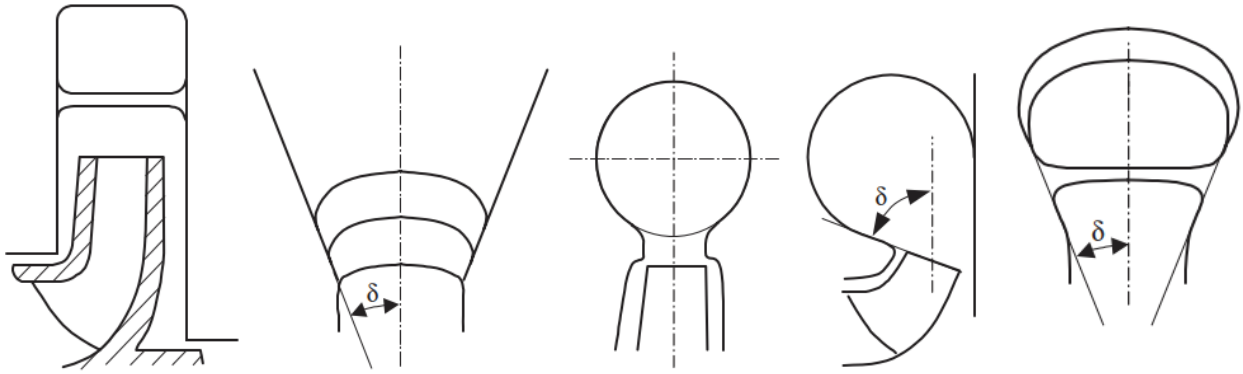

Figure 2.3 – Cross sectional shapes of volute casings: a) Rectangular volute; b) Trapezoidal; c) Round; d) Asymmetric (semi-axial impeller); e) Double volute, where δ – wall opening angle [35]

2.2 Pump as turbine

PAT is a type of hydropower device that can operate in both pumping and turbine modes [36]. It offers several benefits over traditional hydrodynamic turbines, including lower cost, easier production, installation, operation, and maintenance, as well as a shorter lead time for delivery.

The double-entry pumps have demonstrated good performance in both turbine and pump modes [37]. The high efficiency and adaptability of double-entry PAT make it ideal for hybrid energy systems for small and high flow rate.

When a pump operates at its best efficiency point (BEP), the output head in turbine mode is lower than the theoretical ideal due to hydraulic losses, including friction and volumetric losses. When the same machine runs in turbine mode at the same rotational speed *n*, the head required to reach BEP must exceed the ideal value by the amount of hydraulic losses. Under the idealizing assumption that hydraulic losses are equal in both modes at this operating point, the difference between the BEP heads

in pump and turbine modes is therefore roughly twice the hydraulic losses, following the relation[11] given by (1):

$$H_p \approx H_t \cdot \eta_h^2 \quad (1)$$

However, this equation (1) does not always apply. According to the [11] the energy transfer between the fluid and the impeller depends on different parts of the machine in each mode. In pump mode, it depends mostly on the shape and angle of the impeller blades. In turbine mode, it depends more on the shape of the volute casing. Differences in pump design and manufacturing details significantly influence performance. Two pumps with similar impeller designs may exhibit nearly identical characteristics in pumping mode but can perform quite differently when operated as turbines.

Figure 2.4 schematically illustrates the head and efficiency curves for pump and turbine operating modes. The orange and blue lines represent schematic curves that can be obtained by designing volutes with different geometric parameters. Volute design affects the best efficient point (BEP) location and often shifts it towards higher flow rates, sometimes beyond best-practice range. A comparison of pump reliability in pump and turbine modes is provided in Figure 2.5. It can be seen that the area of pump reliability does not overlap for the two operating modes. In turbine mode, it starts to grow and then drops at higher flow rates. However, the peaks of the pump reliability curve are at the same flow rate in both modes.

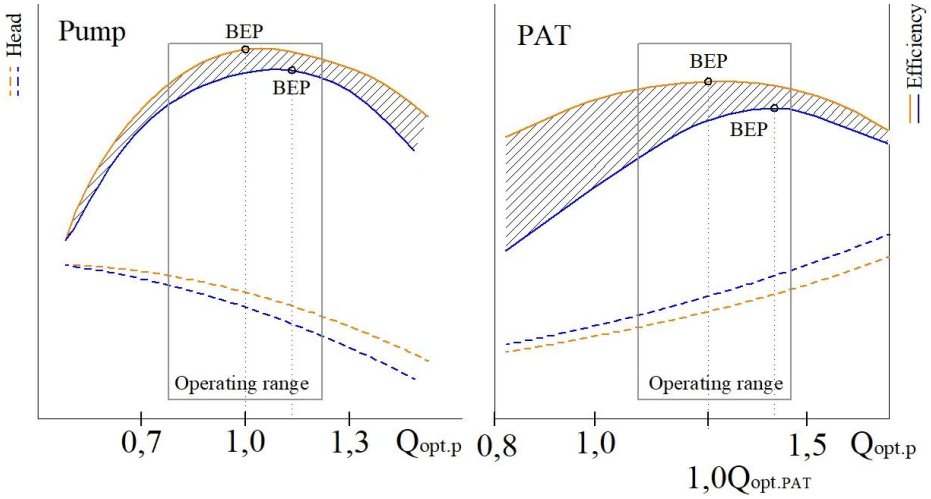

Figure 2.4 - Schematic of the head and efficiency curves in pump and turbine operating modes

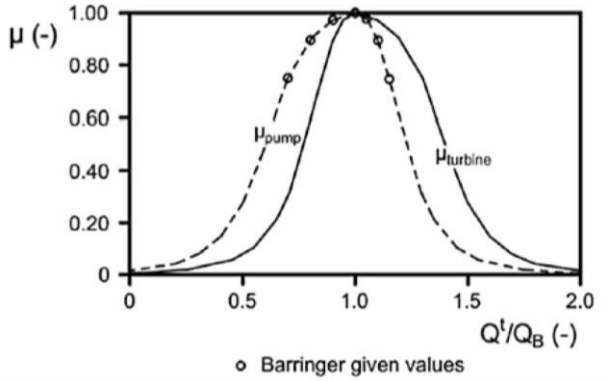

Figure 2.5 - Comparison of pump reliability in pump and turbine mode, where μ - Mean Time to Failure [38]

The problem is that, despite numerous recommendations on selecting geometric parameters, it is not clearly defined which parameters and how the value of these parameters affects the shift of the BEP. Moreover, it remains unclear which geometric parameters should be applied to pumps with different n_q. Geometric parameters influence not only the BEP position but also the maximum efficiency value, the flatness of the efficiency curve, and the curvature of the head curve. From the point of view of operational reliability, excessive increase in optimal flow rate (Q_{opt}) in turbine mode caused by insufficient attention to volute design may lead to excessive growth of mechanical power and forces of hydraulic origin. This increases the load on the shaft, bearings, coupling and other mechanical components, which can lead to their rapid damage. This research gap motivated further studies in the present work.

2.3 Specific speed

Classification by specific speed n_q is the most common and useful approach in the scientific community for comparing operating processes of pumps with different geometrical parameters. n_q makes it possible to define the range of pumps to which the recommendations from the studies conducted in this work can be applied. The specific speed n_q, defined according to the European pump convention, is calculated using Eq.(2), which is based on a comparison with a reference pump, which has Q_{opt} = 1 m^3/s and H_{opt} = 1 m [35, p. 51]. This dissertation also cites literature that uses specific speed n_s (3) the essence of which is a comparison with a reference pump having P_{opt} = 1 hp and H_{opt} = 1 m [35, p. 51]:

$$n_q = \frac{n \cdot \sqrt{Q_{opt}/f_q}}{(H_{tot.opt}/z_{st})^{3/4}} \quad (2) \qquad n_s = \frac{3{,}65 \cdot n \cdot \sqrt{Q_{opt}/f_q}}{(H_{tot.opt}/z_{st})^{3/4}} \quad (3)$$

where:

f_q – number of impeller entries,

$H_{tot.opt}$ – pump head at Q_{opt}, m,

n – rotating speed, rpm,

z_{st} – number of impellers,

Q – flow, m^3/s.

The category of low and high specific speeds may differ in various literary sources. Not many of them provide classification by n_q with clearly specified numerical values. Moreover, various sources assign different pump category names for the same n_q values. Classifications from selected sources are presented in Table A.1 (Appendix A).

It should be noted that some researchers classify pumps based on calculated specific speed. However, the parameters used to determine this value relate to the impeller's operating conditions and describe the flow within the impeller rather than the entire pump. This parameter can also be used to compare operation process in the volute casings for pumps with similar n_q value, but different sizes and even different design features:

n_q – usually determined for the pump, but calculated according to the operation process in a single impeller or one flow of a double-sided impeller;

$n_{q.p}$ – calculated according to the operation process in a single impeller or one flow of a double-sided impeller;

$n_{q.v}$ – calculated according to the operation process in the volute, independent of the number of flow paths through the impeller but referring to one pump stage.

As shown in the Table A.1, the boundaries between low, normal, and high specific speeds are not well-defined. Given this variability in classification schemes, the studied pumps are characterized as having low ($n_{q.p}$ *=23)* and high ($n_{q.p}$ *=66)* specific speeds values in the present work.

2.4 Overview of fundamental literature of volute casing design

Subsection presents a comparison and analyses of recommendations reported by various authors in textbooks, methodological guidelines, and other educational and engineering manuals. These recommendations are based on studies and statistical data of a large number of pumps, rather than on optimisation of a specific pump (reviewed in Chapter 2.5 and 2.6). There is a lack of systematisation of these recommendations and their comparison. This dissertation closes this gap by proposing a systematisation of most common recommendations. This section briefly discusses the recommendations for selecting main 4 geometrical parameters. Detail compare the fundamental literature are provided in Appendix B, where presented a detailed comparison of the following parameters: design method, inlet width (b_3), inlet diameter (D_3), volute throat area, throat height, area of intermediate cross-sections, cross-sections shape, wall opening angle (ε), cutwater angle, diffuser expansion angle.

2.4.1 Design methods

The literature lacks clear guidance on the optimal methods for achieving desired pump and PAT performance. Two main methods exist for designing volute casings:

1) the constant velocity method (CV),

2) the method of conservation of angular momentum of the flow (CAM).

Each method yields different cross-sectional areas perpendicular to the flow direction and indicates tendencies of their variation along the volute casing.

Additionally, there are no clear guidelines on which method to use depending on the pump operating parameters. Only Gülich [35] and Defeld [39] specify their requirements for the application of the methods. Gülich recommends using the following design approach:

1) for $n_q < 25 \ldots 35$ using the constant velocity method, or

2) for $n_q > 25 \ldots 35$ using the method conservation of angular momentum of the flow.

Defeld proposes the following application of volute-casing designs depending on the flow rate and velocity, as presented in Table 2.1.

Table 2.1 - Application of different types of volute casings according to [39]

Flow rate	**Velocity**		**Note**
	v_2>6 m/s	**v_2<6 m/s**	
Low, permanent	I	III	< 20 m^3/h
Low, variable	II or III	III	< 20 m^3/h
Medium, permanent	I or III	III	<1000 m^3/h
Medium, variable	II or III	III	<1000 m^3/h
High, permanent	II or III	IV	>1000 m^3/h
High, variable	II or III	IV	>1000 m^3/h

where:

v_2 – fluid velocity at the impeller outlet,

I. Volutes with guide vanes between the impeller outlet and volute casing inlet D_3,

II. Volutes with diffuser without guide vanes between the impeller outlet and volute casing inlet D_3,

III. Volute casing according to method of conservation of angular momentum of the flow,

IV. Volute casing according to constant velocity method.

The CAM method of the flow assumes that velocity in the volute casing decreases proportionally with increasing distance from the volute cutwater in accordance with (4) [40]:

$$c_u \cdot r = const, \tag{4}$$

where:

c_u – peripheral component of the absolute velocity at a distance r from the rotation axis.

Authors such as Pfleiderer [32], [41], Lomakin [40], Mikhailov [42], Polotskiy [31], Mashin [43], Kolisnichenko [34], Church [44] recommend using CAM design method. Defeld [39], Lazarkiewicz [45], Jędral [46] and Gülich [35] describe CV and CAM methods. The number of literature sources recommending the CV method is lower than that for CAM. CV is recommended only by Aizenstein [47], Stepanoff [33], Lobanoff [48]. When designing a volute casing using the CV method, simplification is assumed in which cross-sectional areas increase proportionally to the angle at which a given cross section is positioned relative to the volute cutwater. According to Stepanoff [33], the average velocity is determined from equation (5):

$$c_3 = K_3 \cdot \sqrt{2gH}, \tag{5}$$

where:

K_3 – average velocity coefficient in the volute casing [33]; its value depends on n_q (Figure B.6).

2.4.2 Inlet width

During the determination of b_3, it is most commonly expressed as impeller outlet width (b_2) or/and impeller outlet diameter (D_2) increased by a coefficient (Table 2.2). The biggest difference in b_3 values is between the recommendations given by Pfleiderer [41] and Stepanoff [33]. According to Pfleiderer b_3 equal b_2 increasing by 1–2 mm, whereas Stepanoff uses the coefficients, which leads to the fact that the b_3 value can reach $2b_2$. Therefore, these recommendations were used as extreme values in the design of the volutes considered in this study.

The formulas are explained in more detail in Appendix B. The data presented in Table 2.2 demonstrate the discrepancy between the recommendations and create ambiguity when choosing them for volute casing design.

Table 2.2 - Empirical formulas for determining b_3

Author	Formulas	Author	Formulas	Author	Formulas
Lobanoff [48]	n_s: 19, $b_3 = 2.0b_2$ n_s: 19-58, $b_3 = 1.75b_2$, n_s: 58, $b_3 = 1.6b_2$	Jędral [46]	$b_3 = 1.4 \dots 1.8(2.0)b_2$	Lomakin	$b_3 = b_2 + 0{,}05 \cdot D_2$ [40]
Kolisnichenko [34]	$b_3 \approx b_2 + 0{,}05D_2$ Double-entry pump: $b_3 \approx 2(b_2 + 0{,}05D_2)$	Gülich [35]	Low n_q b_3 =(2.0…4.0) b_2. Hight n_q b_3=(1.05..1.2) b_2	Polotskiy [31]	$b_3 = b_2 + (0{,}04 \dots 0{,}06) \cdot D_2$
Aizenstein [47]	$b_3 = (0.5 \dots 0.7)b_2$ 0,5 for n_s>130 0,7 for $n_s \leq$130	Pfleiderer [41]	$b_3 = b_2 + 1 \dots 2$	Mashin [43]	$b_3 = m2b_2$, $b_3 = mb_2$, m – coefficient
Stepanoff [33]	Low n_s: $b_3 = 2 \cdot b_2$ Medium n_s: $b_3 = 1.75 \cdot b_2$ n_s>210 $b_3 = 1{,}6 \cdot b_2$	Łazarkiewicz [45]	$b_3 = (1.4 \dots 1.8)\, b_2$	Mikhailov [42]	$b_3 = b_2 + (0{,}02 \dots 0{,}05) \cdot D_2$

2.4.3 Inlet diameter

D_3 is determined based on the D_2 and depends on n_q (Table 2.3). The formulas are explained in more detail in Appendix B. The biggest difference in D_3 values is between the recommendations given by Lomakin [40] and Stepanoff [33], that's why they were chosen for further research as extreme values. The difference arises from the formula recommended for calculating D3. In Stepanoff's approach, the coefficient ρ is selected from a chart and depends on n_q. The low value of D_3 in Lomakin's recommendations results from a small coefficient that is used to multiply D_2. Although there are recommendations for D_3 that link each formula to a specific n_s, it remains unclear which recommendation should be followed and how it will affect the pump characteristic.

Table 2.3 - Empirical formulas for determining D_3

Author	Formulas	Author	Formulas	Author	Formulas
Polotskiy [31]	$D_3 = (1{,}04 \dots 1{,}15)D_2$	Jędral, Lomakin [40], [46]	$D_3 = (1{,}03 \dots 1{,}05) \cdot D_2$	Church [44]	$D_3 = (1{,}1 \dots 1{,}2)D_2$
Mikhailov [42]	$D_3 = (1{,}03 \dots 1{,}05)D_2$ For $n_s \leq$100: $D_3 = (1{,}1 \dots 1{,}15)D_2$ For n_s >100: $D_3 = (1{,}15 \dots 1{,}2)D_2$	Gülich [35]	$\frac{d_z}{d_2} \geq 1.03 + 0.1\frac{n_q}{n_{q\,ref}} + 0.07\frac{\rho}{\rho_{ref}}\frac{H_{st}}{H_{ref}}$	Lobanoff [48]	n_s: 12-19, $D_3 = 1.05D_2$, n_s: 19-29, $D_3 = 1.06D_2$, n_s: 29-48, $D_3 = 1.07D_2$, n_s: 48-78, $D_3 = 1.09D_2$
Aizenstein [47]	$D_3 = D_2 \cdot K_{start}$, K_{start} - coefficient	Kolisnichenko, Mashin [34], [43]	$D_3 = 2R_3 = 2(1{,}03 - 1{,}05)R_2$	Stepanoff Łazarkiewicz [33], [45]	$\rho = \frac{D_3 - D_2}{D_2}$

2.4.4 Cross-sections shape

The literature review shows that, in most cases, authors are not explicit about the choice of the cross-sectional shape. Defeld [39] claims that round shape has less losses, but other shapes such as trapezoidal and rectangular also can be used. In [43] (Mashin) and [34] (Kolisnichenko) the same three shapes are considered, and it is noted that the trapezoidal shape is the most common. Its sharp corners must be rounded with a fillet radius, while maintaining equality of the initial moments of area [41], [40], [42], [43] and [34]. Round and trapezoidal shapes are most popular according to the [32], [47] and [45]. Church recommended use trapezoidal shape [44]. In contrast, Plotskiy [31] states that it does

not significantly influence pump performance and emphasizes that the cross-sectional area at the diffuser entrance has the greatest influence.

The only author who recommends selecting the cross-sectional shape depending on n_q is Lobanoff [48]. The authors suggest that for $n_q < 21$ pumps should use a rectangular volute design, for $n_q < 12$, round volutes are recommended. Gülich [35] argued that flat cross sections (i.e. a cross-section flattened in shape, with its width greater than its height) are expected to produce less secondary flow than round ones, reducing losses. For double volutes, the inner and outer cross sections must be matched to ensure a manufacturable outer wall and a smooth transition to the round discharge nozzle, while also considering casing stresses, deformations, and economical production.

In summary, the authors present quite divergent views on the choice of cross-sectional shape. There is no clear consensus on which shape should be used. Such differences in the recommendations justify the need for systematic research.

2.4.5 Wall opening angle

There is no major disagreement among authors regarding the choice of the wall opening angle. Jędral [46] recommends choosing a range of 30º- 40º, Aizenstein [47] and Lobanoff [48] a range of 35º - 45º, and Mikhailov [42] a range of 20º - 26º. Church [44] claims that maximum total angle between the wall sides is usually about 60˚. He notes that volutes with smaller angles give better results, however, this increases pump dimensions. Authors [34], [43] determine the angle depending on n_s: for n_s = 50 - 60 the wall opening angle is 10º - 16º, and for $n_s > 80$ it is 14º – 22º. For $n_s > 80$, it is recommended to gradually reduce the wall opening angle from the calculated cross section to zero.

There are fewer recommendations on how to select the volute wall opening angle than for other geometric parameters. However, there is still no clear agreement. The key recommendation is to keep the angle below 45˚. This does not apply to recommendation Church [44]. Therefore, it remains unclear which recommendation should be followed.

2.5 Volute design optimization in pump mode

This section presents a literature review on volute casing design optimization. It summarizes key research findings aimed at improving hydraulic efficiency, reducing energy losses, and optimizing volute casing geometry for single pumps.

Different approaches to volute design are examined in this subsection, focusing on how variations in geometry influence energy conversion and flow stability. Attention is given to design strategies, including calculation methods, cross-sectional area optimization, volute cross-section shape, cutwater geometry , and emerging design approaches.

2.5.1 Design methods

Tao Wang et al. [49], [50] presented a volute casing design method that achieves the lowest hydraulic losses compared to other methods. According to the authors volute casings designed using the conservation of angular momentum method exhibit imperfect performance. The authors claim that the actual velocity distribution does not conform to the theory of conservation of angular momentum.

Selecting one method over another results in different cross-sectional area values. In most cases, researchers focus on adjusting the area rather than comparing the methods themselves. An overview of such articles is presented in next subsection.

2.5.2 Cross-sectional area

The cross-sectional area ratio of the volute casing significantly affected the hydraulic efficiency [51]. With an increase in the cross-sectional area, the tangential velocity decreased and the performance of the centrifugal pump increased [52].

The volute casing's effect on the displacement of the BEP was investigated in [29]. The authors demonstrated that the maximum efficiency point could be adjusted to lower flow rates by reducing the volute area, or to higher flow rates by increasing it. In [53], the authors claim that a volute designed according to the constant velocity moment principle leads to the shift of the optimal operating range from the designed value towards the area of smaller flow rate.

Wroster in [28] highlighted how the impeller and volute interact with each other and collectively influence the performance of a centrifugal pump. Experimental measurements have shown that it is the volute rather than the impeller that determines the BEP of pumps of low and moderate specific speed. At low flow rates, the volute causes recirculation in the impeller, while at high flow rates, energy losses in the discharge branch increase. Above specific speeds $N_{s.US}$ of 4000 (n_q = 78), the casing areas have less impact on efficiency, and the impeller inlet conditions become more critical.

Chang Ho Son et al. [54] studied changes in the cross-sectional area of a volute casing designed by using the principle of the Archimedes spiral according to Stepanoff [33]. The authors increased and decreased the cross-sectional area by 10% and 30%. The analysis of the conducted research shows that, as the cross-sectional area increases, the head-flow curve (Q-H-curve) and efficiency curve become flatter, and when the area decreases, the curvature of the characteristics increases. These data are confirmed by the work of Yi Tao et al. [55]. The results demonstrated that increasing the cross-sectional area of the volute leads to a slight decrease in efficiency at the optimal operating point. However, under non-optimal flow rate conditions, efficiency improves. A volute casing with a larger cross-sectional area provides a broader range of high efficiency.

The authors [56] investigated a low-specific-speed centrifugal pump using the constant velocity method. The volute throat area was decreased by 25 and 50% during the research. The decrease in area led to the head–flow curve becoming steeper. Movement of the BEP toward the design point was also observed. Additionally, the article investigated the impact of the volute gap. The authors attribute the improved pump performance (higher head delivered by the impeller) to the improved slip factor across all flow rates. However, the authors compared pumps with volute casings designed by one method and did not set themselves the task of comparing different design methods. In [57], opposite results were obtained. The highest efficiency was 0.909 for a pump with a large volute area because the design condition of the volute at this flow rate is similar to that of the impeller.

In [58] three design variables were chosen based on sensitivity analysis results: the blade outlet angle, the constants used to determine the impeller outlet width, and the volute cross-sectional area. The analysis indicated that parameters such as D_3/D_2 and b_3/b_2 have minimal impact on pump performance. Unsteady flow simulations revealed that reducing the volute area effectively suppressed flow instability in the centrifugal pump.

Stiefel [59] demonstrated that the cross-sectional area of the volute significantly impacts the shape of the performance curve and the stable operating range of the compressor [60]. However, it should be taken into account that the study examined airflow rather than water flow, therefore, the results cannot be directly or fully extrapolated to pumps.

2.5.3 Shape of volute cross section

J. H. Kim et al. in [61] changed the design of the impeller and volute casing. The volute casing with trapezoidal shape designed according to Stepanoff's theory, performed best with the modified impeller. Research by Sunsheng Yang et al. [62] showed that it is preferable to use a round cross sectional shape for the volute casing. The difference in pump efficiency for rectangular and trapezoidal shapes is insignificant. The authors compared only volute casing designed according to the Stepanoff's theory. Worster [28] investigated rectangular and trapezoidal cross section and concluded that the trapezoidal volute has a smoother characteristic in the vicinity of the best efficiency point, but performance was distinctly worse at off-design flow rates. The peak overall efficiency with this volute was similar to that of the wide rectangular section volute, but the hydraulic efficiency was slightly better, as the BEP occurred at a relatively lower flow rate.

The authors of [50] show that the wetted perimeter of volute cross sections greatly influences pump operating parameters. They demonstrated its connection with the losses in the volute casing and proposed their methodology for designing the cross section of the volute casing. A volute casing cross sectional shape was proposed which is a combination of a single round arc and a trapezoid. A different conclusion was reached in [63] during the investigation of a compressor volute casing. It was concluded that the effect of the cross-sectional shape was minimal. The volute casing with a round cross section performed best, exhibiting the lowest loss. The square and rectangular volute casings had higher losses. However, not all studies reached similar conclusions. In [64] a turbocharger compressor with a rectangular-semi-round volute casing and a tangential inlet showed higher efficiency than those with a round volute with a symmetric inlet or a round volute with a tangential inlet. However, it should be noted that the flow of air was studied, not liquid.

2.5.4 Cutwater

Authors [65] claimed that by modifying the cutwater of the volute without changing the entire area it is possible to improve internal flow distribution under off-design flow conditions. To do this, they increased the area near the cutwater region. According to investigations in article [66] the rotor-stator interaction generates the highest pressure pulsation at the volute cutwater when PAT works in pump mode. That is why the authors recommended modification of the volute cutwater. Chunjun Ji et al [67] studied the main factors related to the diffuser and volute affecting the performance of a centrifugal compressor. The authors obtained an increase in polytropic efficiency of 4.5% due to changes in the cross-sectional area and shape, the shape of the cutwater, and the connection between the outlet pipe with the volute. Studying the mixed flow pump, the authors [68] concluded that the main factors for satisfactory design of the volute are the variation pattern of the volute cross sections and the shape of the volute cutwater. However, the cross-sectional shapes of the volute have only a minor effect on volute performance.

Zhenmu Chen et al. [69] investigated the optimum design of the volute cutwater shape and reported an increase in pump efficiency from 72.7% to 75.01% after the modification. A bionic cutwater geometry was applied to three centrifugal pumps in [70], y yielding efficiency gains of 1.5%, 2%, and 2.45%, respectively. In the context of head–flow curve instability, the authors of [71] showed that under overload (high-flow) conditions the dominant losses are concentrated at the volute cutwater and at the volute diffuser.

In articles [72], [73] four parameters were chosen: blade outlet angle, wrapping angle, volute inlet width, and throat area. The most important parameter was the wrapping angle. Selecting optimal geometric parameters (β_2=19˚, φ=220˚, b_3=12mm and St=190 mm^2) allows a reduction in vortex generation and backflow intensity.

2.5.5 Inlet width and diameter

The initial geometric parameters, which are usually determined according to design recommendations and affect all other geometric parameters obtained during the volute calculation process, are the b_3 and D_3 (Figure 2.2).

In the article [74], the authors changed the geometric parameters of the volute with the aim of optimising its geometry to achieve optimal mechanical properties of the pump casing. The geometry has been changed taking into account the condition that the stress should not be beyond material strength given the fragility of cast iron. The optimised design demonstrated high mechanical strength, while only negligible reductions in hydraulic performance and efficiency were observed, resulting from alterations to the volute-shaped flow passage.

Daniel O. Baun et al. [75] investigated the dependence of the centrifugal pump operating process on variations in impeller positioning relative to the geometric center of a round volute. This position was defined by an eccentricity ratio, $\varepsilon = 0.545$, and attitude angle, $\theta = 46.0$˚. At the optimal relative position, the authors reported an increase in efficiency compared to the typical design configuration. In the typical configuration, the geometric center of the impeller coincides with the volute geometric center for both round and spiral volutes.

Studies [76] examining the influence of the volute inlet diameter in low specific sewage pumps showed a minor influence on the velocity distribution within the impeller and a pronounced influence on the volute casing. A further study on the sewage pump [77] considering three models with different D_3 values also indicated that increasing the basic circle diameter contributes to a more uniform flow in the volute, which, in turn, improves pump efficiency and enhances flow stability.

The analysis in [56] of volute gap width effects indicates that a narrower gap shifts the head-flow curve upward, improving hydraulic efficiency at both the design point and overload conditions. However, reducing the gap width can also intensify pressure pulsations, especially in the vicinity of the volute cutwater.

The impact of b_3 was investigated by [78], who adjusted its width while maintaining a constant volute cross-sectional area. Three volute casings were examined, with widths of 5 mm, 4.25 mm, and 3.5 mm. The highest efficiency was achieved with the widest b_3 (5 mm). These results indicate that a larger volute inlet width can effectively reduce flow velocity and pressure losses, ultimately enhancing pump performance.

In [79] the width ratio b_3/b_2 was found to have the most significant effect on the flow rate by minimizing shock and secondary flow losses. The article [49] investigated pumps with three D_3 values, with two different b_3 values chosen for each D_3. It was concluded that the impact of the wetted perimeters of the volute sections on pump performance is more significant than the effect of the volute inlet width. The volute casing with a higher b_3 value had a higher head and efficiency and lower losses compared with the volute having a lower b_3 value.

In article [80] the distance between the impeller and the volute was increased by shroud trimming. A greater reduction in the shroud diameter resulted in a more significant drop in hydraulic

efficiency, with this effect being more evident in pumps with higher specific speed. Similar investigation of impeller volute interaction [81] was conducted on low specific speed centrifugal pump. The impeller with oblique trim at 30˚ on vane trailing edge exhibited a pressure fluctuation coefficient that was lower by 10.3%. When a parallel trim on the volute cutwater was added the pressure fluctuation coefficient increased by 24%.

2.5.6 Grooved volute casing

A modified grooved volute casing can effectively reduce and eliminate flow instability within the impeller channels and the volute [82]. With three grooves [83], the groove structure has a minimal impact on pump performance, ensuring a more stable performance curve. Pressure pulsations are lower at all monitoring points, and as the number of grooves increases, the pulsation amplitude decreases. A three-groove design was shown to significantly improve flow under all conditions. Additionally, by enhancing flow stability, the groove structure influences particle motion, thereby reducing erosion wear on the volute casing's inner wall in solid–liquid flow conditions. In [84], the casing treatment of the an axial pump was studied. Sixty shallow axial grooves were added, positioned only in front of the rotor. The grooves improved the inflow into the rotor channels, leading to enhanced flow deceleration through the blade passage.

2.5.7 The effect of the volute casing on pump operation pressure pulsation, wear and losses in volute casing

The volute casing is frequently investigated in studies on pressure pulsations. In [85], a multichannel pressure sensor was installed to measure pressure on the inner wall of the volute. The authors reported that pulsation intensity decreases as rotational speed increases. In [86], the authors concluded that increasing the volute throat area reduces turbulence intensity in the pump. This reduces pressure pulsations by diminishing rotor-stator interaction. The cutwater design is another important factor affecting pump performance [87]. Pressure fluctuation intensity is strongest near the cutwater. It also shows a non-uniform distribution within the volute casing [88].

Dong R. et al. [89] investigated the gap between the cutwater and the impeller. Increasing the gap up to about 20% of the impeller radius led to a decrease in the level of noise and vibration in the pump, while a further increase led to a negative effect on performance. In [90], to examine the effect of the volute cutwater on pressure pulsations in a low specific speed centrifugal pump, three volute cutwaters were produced by cutting the original cutwater twice. At high flow rates, the cutwater cut had little effect on the pump head, and the heads of the three pumps were nearly identical. At low flow rates, however, cutting the volute cutwater caused a decrease in pump head, with a difference of about 2%.

The choice of volute casing type (double or single) also affects pressure pulsation [91]. At $0.6Q_{opt}$, $1.0Q_{opt}$, and $1.1Q_{opt}$, the main frequency amplitude at the first cutwater of the double volute is reduced by 70%, 38%, and 40%, respectively, compared with the single volute. Additionally, the authors reported that using various volute types has negligible effects on pump efficiency or head, with the variation being less than 2%.

Volute wear is also an important indicator that influences pump performance. Among all pump components, the volute casing is the most susceptible to erosion. The front side experiences more severe erosion than the pressure side [92], [93]. In article [94], the wear of the volute casing of a centrifugal slurry pump was investigated. The areas with the highest erosion intensity are located

around the volute angle near 180˚ and close to the volute cutwater. The study [95] employed the Eulerian–Eulerian method to analyse particle-laden flows in large centrifugal slurry pumps under various operating conditions. The results indicated that at the 0.6Q flow rate, the flow becomes highly unstable, with strong vortices, backflow, and elevated solid velocities near the cutwater, which intensify wear. A slurry pump wear test on a SABC grinding circuit confirmed that the most severe erosion occurs along the volute, particularly near the cutwater region, while additional wear was observed on the front cover wall and the impeller inlet. Increased particle concentration further aggravated flow resistance and wear within the volute passage.

In [96] a methodology for the calculation of the flow and velocity fields in volutes and impellers of centrifugal pumps under off-design operation was proposed. The authors reported that when the flow rate falls below about 4% of Q_{opt}, discharge recirculation, or complete flow reversal, occurs in the channels passing through the first quadrant of the volute, which leads to reduced pump efficiency and increased vibrations and noise.

2.6 Volute design optimization in turbine mode

To ensure the highest operational performance, the operation and design of PAT are constantly being analysed and improved. This subsection highlights how modifications to the volute casing, impeller geometry, hydraulic passages, and operating conditions can elevate overall efficiency, mitigate cavitation, and extend the service life.

Compared with the studies focusing on changes in the geometric parameters of the PAT impeller [97], the volute casing has been less extensively studied. As noted by the authors in [98], volute casing changes affect pump operation in turbine mode more strongly than in pump operation. Even though the efficiency of the pump is higher than that of the turbine [99], researchers consequently continue to investigate and improve PAT designs.

2.6.1 Design methods

The authors in [100] claim that at low flow rates, the method does not significantly influence turbine efficiency. Conversely, at high flow rates, the turbine with a volute casing designed using the constant velocity method achieves the highest efficiency.

2.6.2 Cross-sectional area

In [101], the volute casing was designed according to constant velocity method, with an increased cross-sectional area. As a result, in pump mode, the modified volute casing slightly reduces efficiency at low flow rates but significantly improves head and efficiency at higher flow rates. It also notably decreases radial force, shifting the minimum radial force point to 125% of the BEP flow rate. However, in turbine mode, the enlarged volute casing leads to lower head and power across all flow rates.

2.6.3 Shape of volute cross section

The most common volute casing cross-sectional shapes are rectangular, trapezoidal, and rounded. According to [100] round cross section makes the velocity distribution more uniform. The authors [102] conducted a study for four volute cross-sectional shapes. The difference between the least favourable (rectangular) and the radius-based cross-section exceeded 10%. This was explained by the

fact that changing the cross-sectional geometry altered the turbulence intensity in the cutwater zone and in the flow entering the impeller.

2.6.4 Cutwater, pressure pulsation

The pressure pulsations of PAT were investigated in [103]. The authors concluded that to reduce high-frequency pressure pulsation, the radial gap between the impeller tips and volute cutwater should be increased. During cutwater optimization [100], both the water head reduction and output power decrease as the tilt angle increases. A longer stretch length leads to higher output power and greater water head reduction, but lower efficiency within a limited angle range. Although cutwater optimization does not greatly improve efficiency, it can increase output power while keeping the water head reduction at a reasonable level.

In article [104] the cutwater length and angle were identified as the most influential variables. Optimizing the cutwater design increased hydraulic efficiency from 82.4% to 86.3% without modifying the impeller. In article [105] three cutwater types were investigated. The best cutwater design allows for increased efficiency and output power of up to 8% and 32%.

The vorticity-pressure fluctuation interaction in the volute was investigated in [106]. According to the research, at over-flow-rate conditions, impeller rotation has a greater influence on vortex evolution at the leading edge of the volute cutwater and a lesser influence near the volute walls. The pressure fluctuation intensity was lowest within the volute. In contrast, fluctuations near the volute cutwater were aligned with the blade leading edge.

2.6.5 Inlet width and diameter

The choice of volute casing inlet width affects reverse flow in the sidewall gaps [98]. A study reported in [107] investigated the modification of an existing pump-turbine. Solid rings of various sizes and shapes were added to the side wall gap. This modification reduced friction losses and increased efficiency from 66.7 to 70.2%. This approach can be applied not only at the PAT design stage but also for the optimization of pumps already in operation. Changing the geometric parameters of the impeller, volute casing for PAT and pumps is also described in review articles [36], [108]. However, it should be noted that article [36] is relatively dated, and [108] primarily focuses on the pump flow parameters rather than those of the turbine. Also it does not address modern solutions, and mainly concentrates on impeller modifications. In investigating the influence of D_3, the authors [102] concluded that decreasing the diameter enhances efficiency at discharges below the best efficiency point (BEP), whereas increasing the diameter has a more pronounced effect at higher discharges.

2.6.6 Cavitation and energy losses

The turbine mode is more exposed to cavitation compared with the pump mode. This is explained by the fact a higher head to achieve optimal operating conditions than a pump is required by PAT [109]. According to [110] flow energy dissipation occurs in different components when operating in pump and turbine modes (Figure 2.6). In pump mode, it is observed primarily in the volute, followed by the impeller and the suction chamber. In turbine mode, the highest flow energy dissipation is found in the suction chamber, followed by the impeller, while the internal region of the volute has a relatively small contribution due to smoother flow. The authors recommended modifications to the cross-sectional shape of the volute and the cutwater region.

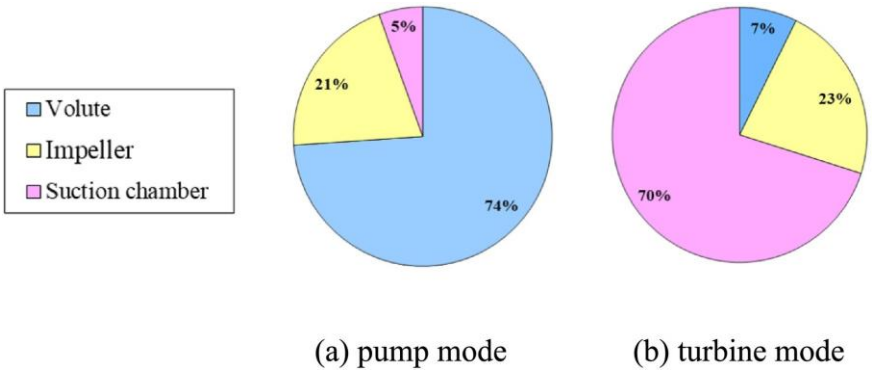

Figure 2.6 – Proportion of flow energy dissipation in different components in pump and turbine mode [110]

Similar studies were conducted for a pump with n_q=24 [111]. The volute plays a major role in hydraulic losses in pump mode, while in PAT mode, energy dissipation is mainly concentrated in the impeller and the suction chamber. Simulation results, which were validated by experiments, indicate that the turbine's best efficiency point occurs at a flow rate and head approximately 1.7 and 2.22 times higher than those of the pump, respectively.

2.7 Chapter summary

The review shows that, although the available design methodologies are based on conceptually similar assumptions, they often lead to different choices of key geometric parameters. However, the literature does not provide a systematic comparison of these recommendations or a clear assessment of how these differences may affect pump performance in both pump and turbine modes. This research gap is addressed in the present dissertation by comparing selected design recommendations and analysing their influence on the geometry and energy characteristics of the investigated pumps. The analysis presented in this section, including Table B.1, Table B.3 - Table B.6, covers the comparison of design choices for the following parameters:

– method of volute casing design (determines the area of volute cross-section),
– inlet width,
– inlet diameter,
– shape of intermediate sections and method of rounding the trapezoidal cross-section,
– wall opening angle,
– cutwater design,
– diffuser expansion angle and geometric parameters.

This lack of consistency results in the absence of definitive recommendations regarding the most appropriate parameter choices for specific pump configurations. Consequently, designers often face ambiguity during the decision-making process, underscoring the necessity for more standardized and clearly defined design guidelines. This ambiguity is further reflected in both fundamental literature (Chapter 2.4) and recent studies (Chapter 2.5 and 2.6). The effects of the geometric parameters remain unclear, including how increasing or decreasing them will change the pump operating parameters.

Two principal methodologies dominate the design of centrifugal pumps:

– constant velocity method,
– conservation of angular momentum of the flow.

These methods differ in the theory on which they are based and the methodology for calculating the flow within the volute casing. The constant velocity method assumes a uniform circumferential velocity distribution, simplifying the design by maintaining a steady flow velocity throughout the volute. In contrast, the angular momentum conservation method accounts for the variation in angular momentum as the fluid moves through the volute casing. Gülich [35] provides practical guidance on selecting between these methods based on the specific speed n_q. Defeld [39] introduces a classification of volute casing designs (Table 2.1) that aligns with different flow rates and velocities, suggesting that the choice of design strategy should be closely tied to the hydraulic characteristics of the pump. These frameworks offer valuable starting points, yet their application in practice often varies, reflecting the complexity and diversity of pump configurations.

Notably, investigations into energy dissipation across components reveal that the volute casing accounts for the highest losses when operating as a pump, whereas the impeller becomes the primary source of losses in turbine mode. These findings underscore the importance of tailoring design strategies to the intended operating regime and suggest that further comparative research is essential to establish reliable guidelines for geometric parameter selection.

The volute configuration most commonly studied is that used in pumps operating in pump mode. However, there are much fewer results for turbine mode. Many recent researchers have studied the influence of one or two main geometric parameters, and specific volute design methods, on pump performance. However, a systematic and comprehensive approach to the simultaneous analysis of multiple factors is still missing, especially for both operating modes of the hydraulic machine in a pump and turbine mode.

Chapter 3: Subject, purpose, and thesis of the work

The conducted literature review indicates that publicly accessible sources provide limited reliable information. In particular, the influence of volute casing geometrical parameters on the energy performance of a pump operating in both pump and turbine modes remains insufficiently described.

The object of this work is a double-entry centrifugal pump operating in pump and turbine modes.

The subject is the energy performance of the pump under as a function of selected geometrical parameters of the volute casing.

The purpose of this work is to determine the relative importance of selected volute casing geometric parameters and to quantify their influence on the energy performance of a centrifugal pump operating in pump and turbine modes. The study evaluates the main operating parameters, including the flow rate at BEP, head, efficiency, mechanical power, and hydraulic losses. It aims to determine both the direction and the magnitude of the influence of individual geometric parameters on pump operation. In addition, the work systematizes literature recommendations for volute casing design and compares the resulting design variants. The final objective is to indicate the preferred directions for selecting volute casing parameters in order to obtain satisfactory performance in both operating modes.

The central thesis of this dissertation: the geometric parameters of the volute casing affect the hydraulic performance of a centrifugal pump in both operating modes, with a stronger influence observed in turbine mode than in pump mode. A combination of these parameters exists that ensures satisfactory performance in both pump and turbine operation.

Chapter 4: Approach to the problem

4.1 Research problem

It is generally accepted that the impeller has a greater influence on pump performance than modifications to the volute. However, the literature review shows that a poorly designed volute can significantly worsen the performance of both the impeller and the pump as a whole.

When a designer begins to design a volute casing, they are faced with many different recommendations concerning the selection of geometric parameters, such as D_3, b_3, the wall opening angle, the cross-sectional shape, and the design method. The literature review made it possible to identify 12 commonly used formulas for calculating b_3 and 9 formulas for calculating D_3. These formulas were taken from books that are the original sources. At the same time, there is a large amount of literature that repeats these formulas, further increasing their number and creating confusion in the selection of geometric parameters.

The author did not find any literature that systematically organises the available recommendations or defines criteria indicating which parameter values should be used for particular pumps. It also remains unclear how pump performance changes when these geometric parameters are increased or decreased, and how such changes affect the flow structure.

The least attention has been given to PAT in this area. It is still unclear how the geometric parameters affect its performance and whether this effect can be beneficial for both pump mode and turbine mode at the same time.

The objectives of this dissertation are the following:

– to systematise and organise the existing recommendations for volute design,

– to assess the influence of pump geometric parameters on performance parameters (head, efficiency, total pressure losses and mechanical power) in both pump mode and turbine mode for two pumps with low and high n_q,

– to investigate the influence of geometric parameters on changes in the velocity triangles,

– to develop recommendations for improving pump performance in both pump mode and turbine mode,

– to identify a trade-off volute variant that performs well in both pump mode and turbine mode.

The conducted research represents a parametric sensitivity study aimed at identifying performance trends caused by changes in selected volute casing geometric parameters. The analysis allowed the relative importance of these parameters to be determined and indicated design directions supporting a favourable trade-off between pump and turbine modes. The obtained results also indicate which parameters should be considered most carefully during the design process.

4.2 Subject of the study

The presented thesis investigates the influence of volute casing design on the operating parameters of two double-entry centrifugal pumps:

- Pump 1: DHV.80-270 A pump produced by the Hydro-Vacuum S.A. company with a radial impeller and low n_q,

- Pump 2: Omega 350-430 B pump produced by the KSB company with a diagonal impeller and high n_q.

The double-entry pump configuration was chosen because it is suitable for higher flow-rate applications and reduces axial thrust compared with single-entry designs. At the same time, this pump type has been studied less extensively than classical single-entry pumps, while the pump manufacturer was interested in addressing the operational issues described above. The two pumps were selected intentionally to represent two substantially different n_q. The DHV pump is characterised by a low n_q and a centrifugal impeller, whereas the Omega pump has a high n_q and a semi-axial impeller. This selection made it possible to assess whether the influence of the volute casing geometric parameters depends on the n_q of the pump and to verify whether a similar design approach can be applied to pumps with different operating parameters.

4.2.1 Description of the DHV.80-270 A pump

The DHV.80-270 A pump is a centrifugal double-entry single-stage with axial split casing (between-bearing pump Figure 4.1). The main parameters of the pump and its characteristics are shown in Table 4.1 and Figure 4.2.

The pump components' geometry, as well as dimensions, were obtained using 3D optical scanning (Figure 4.1). A 3D model of the metal body and fluid domains of the pump (Figure 4.3) was created based on the obtained scan data (a high-density point cloud). The main geometrical parameters are shown in Table 4.2.

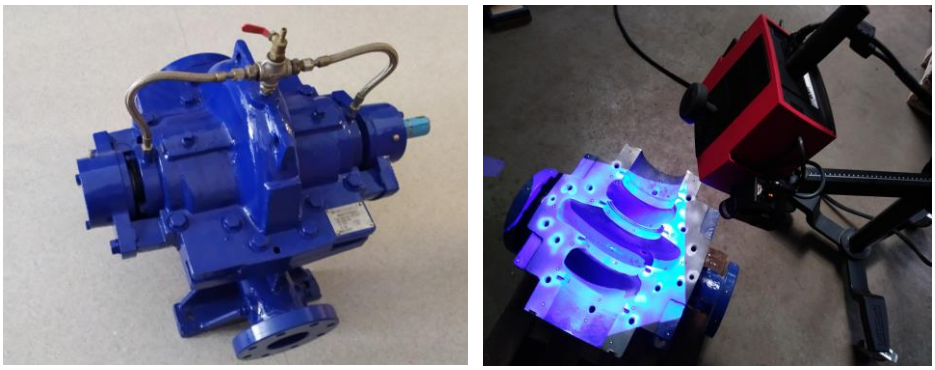

(a) (b)

Figure 4.1 - The DHV.80-270 A pump: a) general view of the pump; b) 3D optical scanning of the bottom casing of the pump

Table 4.1 - Main operating parameters of the pump DHV.80-270 A

Parameter	Symbol	Value	Unit
Flow rate	Q	105	m^3/h
Head	H	25	m
Power	P	11	kW
Rotating speed	n	1460	rpm
Specific speed (volute casing)	$n_{q.v.}$	23	-
Specific speed (impeller)	n_q	16	-
Efficiency	η	79	%

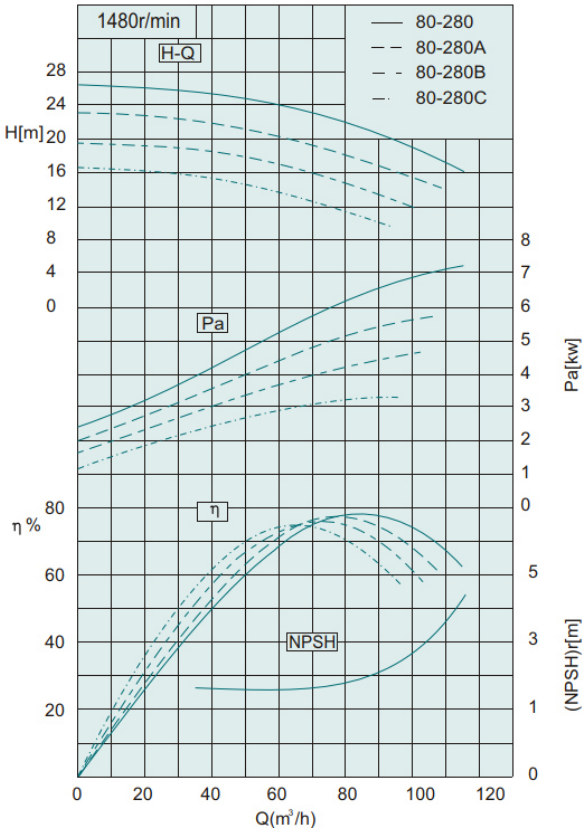

Figure 4.2 – Operation characteristics of the DHV.80-270 A pump [112]

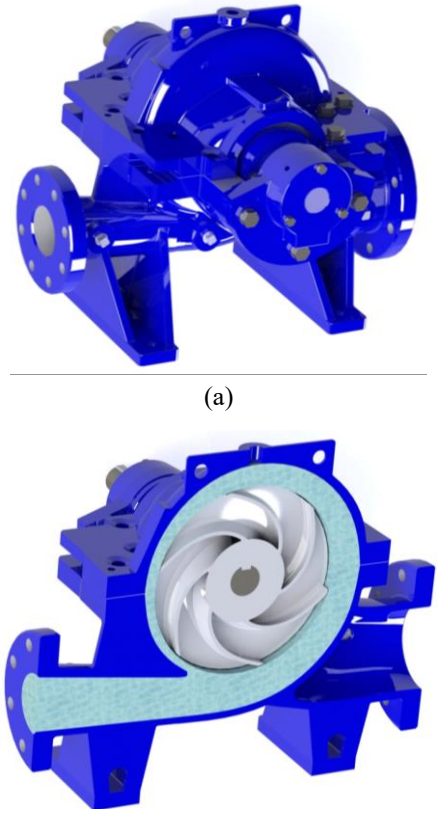

(a)

(b)

Figure 4.3 – The DHV.80-270A pump: a) 3D model; b) cross section

Table 4.2 – Main geometrical parameters of the DHV.80-270 A pump

Parameter	Symbol	Value / Note
Impeller outlet diameter	D_2, mm	270
Impeller outlet width	b_2, mm	26
Volute casing inlet diameter	D_3, mm	276
Volute casing inlet width	b_3, mm	60
Cross-sectional shape	-	Rounded trapezoid with a larger lower base
Wall opening angle	ε	-17
Methods of volute casing design	-	Does not correspond to any method

In Figure 4.2 the characteristic curve is presented with Q in m³/h, which is not an SI unit, but is commonly accepted in the pump industry. For ease of reading, the same scale will be used in all subsequent graphs. A scale expressed as a fraction of Q_{opt} (for example, $0.7Q_{opt}$) is also not used, as it cannot be applied to PAT, since manufacturers do not provide pump performance data for turbine operation.

When changing from pump mode to turbine mode, the flow direction in the flow passage is reversed. However, in this dissertation, the notation of the geometrical diameters D_1, D_2, and D_3 remains unchanged and corresponds to their structural position in the pump, regardless of the operating mode.

4.2.2 Description of the Omega 350-430B pump

The Omega 350-430B pump is a centrifugal double-entry single-stage pump with an axial split casing. It is a between-bearing pump in the research as a reference pump with high n_q. The main parameters of the pump and its characteristics are shown in Table 4.3 and Figure 4.6.

The parameters of the pump's internal flow surfaces were obtained using a 3D scanner (Figure 4.4). A 3D model of the fluid domains of the pump (Figure 4.5) was created based on the obtained scan data (a high-density point cloud). The main geometrical parameters are shown in Table 4.4.

Figure 4.4 – 3D scanning of the pump Omega 350-430B

Figure 4.5 – 3D model of fluid domains of pump Omega 350-430B

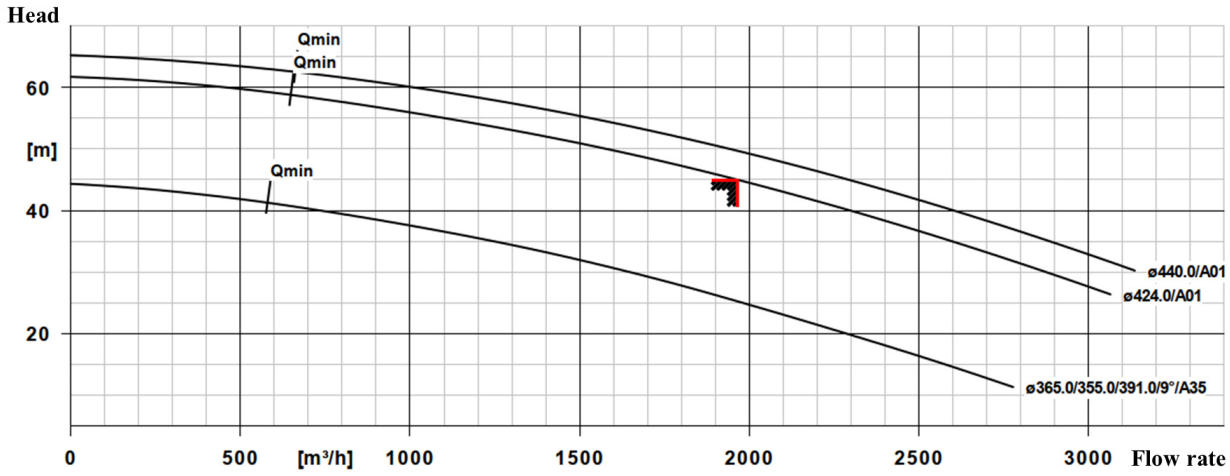

(a)

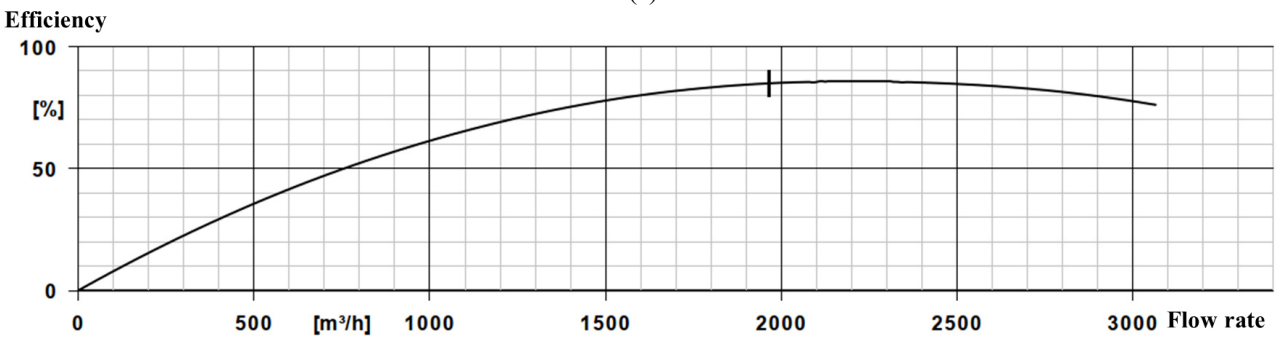

(b)

(c)

Figure 4.6 – Operation parameters of pump Omega 350-430B from the manufacturer's catalog: a) head, b) efficiency, c) Mechanical power [113]

Table 4.3 - Basic operating parameters of the model Omega 350-430B

Parameter	Symbol	Value	Unit
Flow rate	Q	2000	m^3/h
Head	H	43	m
Power	P	283	kW
Rotating speed	n	1488	rpm
Specific speed (volute casing)	n_q	66	-
Specific speed (impeller)	n_q	47	-
Efficiency	η	85	%

Table 4.4 - Geometrical parameters of the pump Omega 350-430B

Parameter	Symbol	Value / Note
Impeller outlet diameter	D_2, mm	428
Impeller outlet width	b_2, mm	104
Volute casing inlet diameter	D_3, mm	485
Volute casing inlet width	b_3, mm	245
Cross-sectional shape	-	Rounded trapezoid with a larger lower base
Wall opening angle	ε	7.5
Methods of volute casing design	-	Does not correspond to any method

4.3 Investigated geometric parameters of the volute casing

The following geometric parameters were changed in the volute casing (Figure 4.7):

– the area of the cross-section, which is determined by the method of design: conservation of angular momentum or constant velocity method,

– volute casing inlet width – b_3,

– volute casing inlet diameter – D_3,

– the shape of cross-sections: trapezoidal and round,

– the wall opening angle – ε.

The separate influence of the volute tongue was outside the scope of this study and should be treated as one of the study's limitations. This element affects the flow structure and pump performance.

However, it represents a separate design issue requiring dedicated analysis. Therefore, the present work focuses on less studied aspects of volute casing geometry.

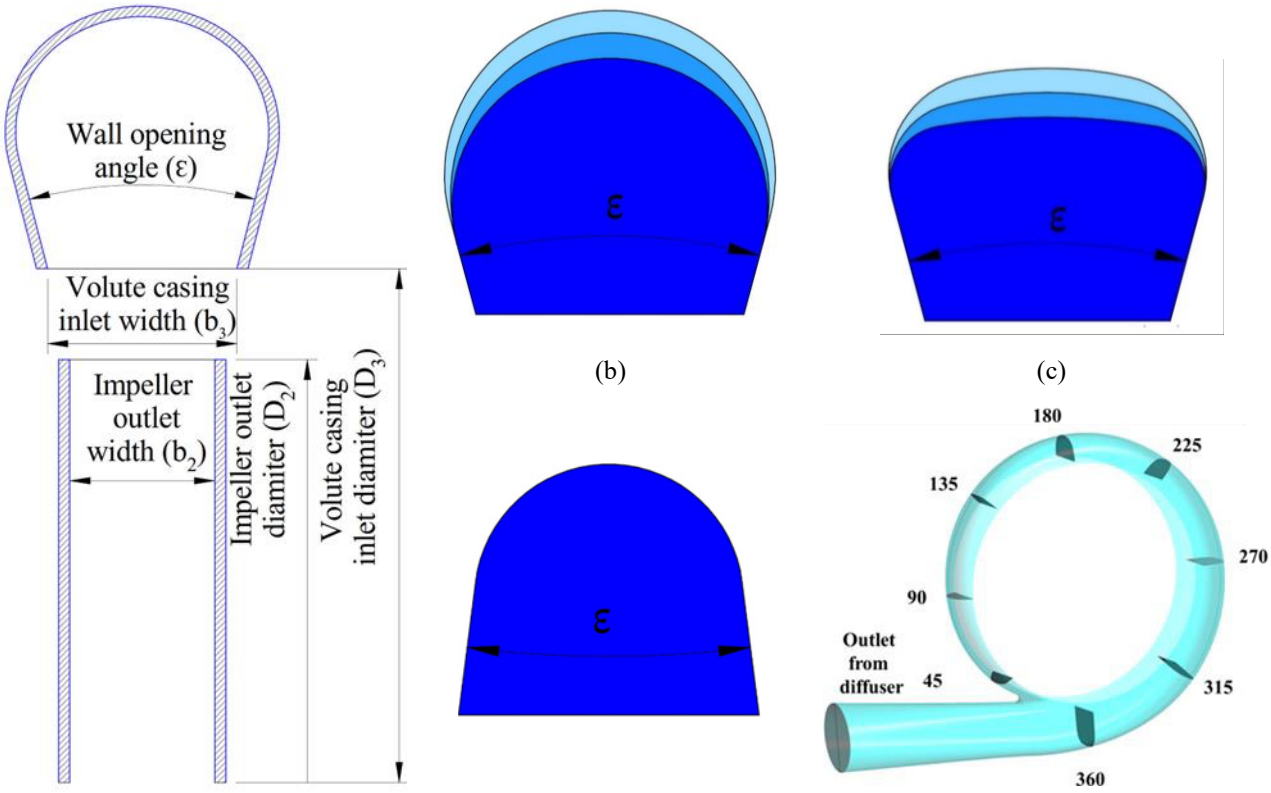

Figure 4.7 – Geometric parameters of the volute a) main dimensions of the impeller and volute casing used in the investigation; Shapes of the volute casing cross-sections: b) round shape; c) trapezoidal shape; d) shape of the reference volute casing e) name and location of the cross-section

When selecting the geometric parameters, we were guided by the objective of verifying the existing, most commonly applied recommendations for their choice. Recommendations presented in the works of Pfleiderer [3], Lomakin [40], and Stepanoff [33] were used, along with the geometric parameters of a reference volute designed by the manufacturer. These particular recommendations were chosen because they differ most significantly from one another.

Table 4.5 presents the formulas proposed by these authors for determining the selected geometric parameters, while Table 4.6 reports the values calculated using these formulas for the pumps under investigation. In addition, the volutes were designed according to the selected design methods. Pfleiderer is an advocate of the conservation of angular momentum method, whereas Stepanoff applies the constant velocity method. These approaches determine the volute cross-sectional area (Figure 4.8) and the procedure for its calculation.

The diffuser opening angle of the volute was kept constant. The diffuser flange did not change its diameter or position and remained as originally designed by the manufacturer. This also makes it possible to keep the inlet and outlet flanges of the pump coaxial.

Table 4.5 - Formula selection matrix for calculating the geometric parameters of a volute for DHV.80-270 A and Omega 350-430B

Parameter	Variable		
Method of volute casing design	1.Conservation of angular momentum [32], [40]; 2. Constant velocity method [33]; 3. Designed by manufacturer. Does not correspond to any method		
b_3	$b_3 = b_2 + 0{,}05 \cdot D_2$ [40];	$b_3 = 2 \cdot b_2$ DHV [33]; $b_3 = 1.75 \cdot b_2$ Omega [33];	$b_3 = 1..2 + b_2$ [32]
D_3	$D_3 = (1{,}03 \ldots 1{,}05) \cdot D_2$ [40];	$D_3 = (\rho + 1) \cdot D_2$[33];	Manuf. design Omega; $D_3/D_2 = 1.22$ DHV

Table 4.6 - Values of the volute's parameters for DHV.80-270 A, Omega 350-430B

Parameter	Variable
b_3, mm for DHV	40; 52; 27
b_3, mm for Omega	126; 183; 105
D_3, mm for DHV	281; 297; 329
D_3, mm for Omega	448; 522; 485
Cross-sectional shape for Omega and DHV	Trapezoidal; Round
Wall opening angle for Omega and DHV	10˚, 20˚, 30˚, 40˚, 50˚, 60˚, 70˚, 75˚, 90˚

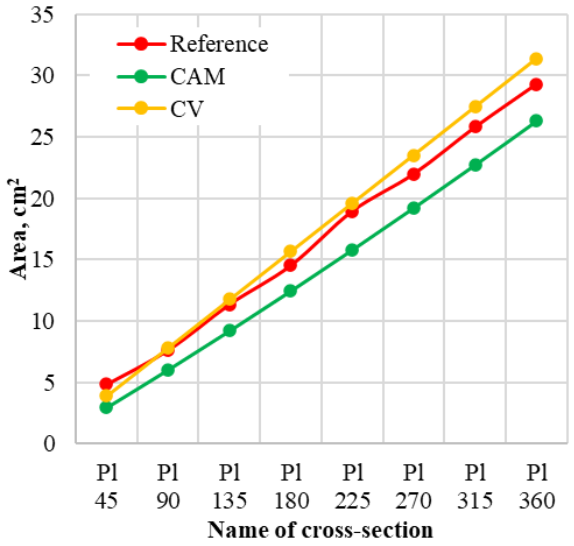

(a) DHV pump

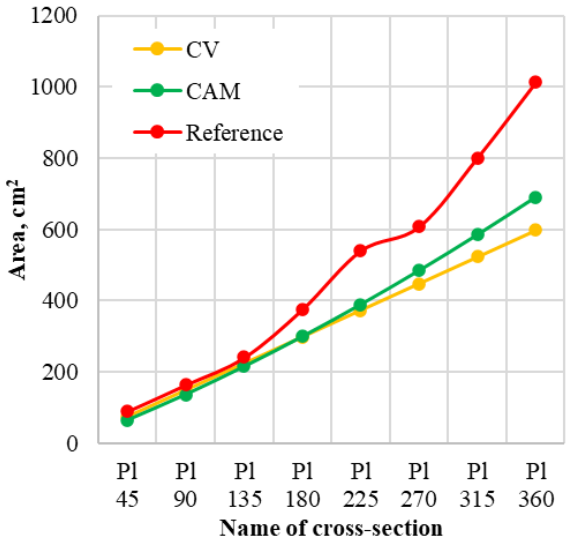

(b) Omega pump

Figure 4.8 – Area of volute casing cross-sections

4.4 Research approach

To investigate the issues described above, the following qualitative and quantitative analyses were performed:

1. A literature review was carried out. In addition, 14 key publications were selected, as they provided recommendations for the choice of volute geometric parameters. The systematisation covered not only the geometric parameters that are the main focus of this study (Appendix B), but also other

parameters, such as shape of intermediate sections and method of rounding the trapezoidal cross-section, cutwater design, diffuser expansion angle and geometric parameters.

2. Numerical simulations were used to analyse different volute geometries. For the Omega pump, 36 combinations of geometric parameters were created. The geometry was selected so that only one parameter was changed at a time, while the remaining parameters were kept constant. In this way, comparable pairs were created.

These volutes were analysed for both pump and PAT operation over a flow rate range from 1400 to 2600 m³/h. For the PAT, calculations were carried out for shaft rotational speeds of 1520 rpm and 1020 rpm. These values were selected because they correspond to asynchronous electric generator operating speeds at 50 Hz grid taking into account negative slip. Since the effect of rotational speed can be taken into account using conversion formulas, the results for 1020 rpm are not presented in this dissertation.

The results for the Omega pump are considered the main results of this study. Therefore, not all volute models were simulated for the DHV pump. The influence of the cross-sectional shape on the Omega pump operating parameters was analysed and found to be relatively small. Therefore, only a limited number of verification simulations were performed for the DHV pump. These simulations confirmed similar trends. To reduce the number of calculations, the trapezoidal cross-sectional shape was used in all further simulations, as it showed higher efficiency values. For the DHV pump, calculations were carried out in both pump mode and turbine mode over a flow rate range from 62 to 170 m³/h.

Detailed information on the mesh parameters is provided in Chapter 5, while the calculation results are presented in Chapter 7.

3. The numerical results for DHV pump with the volute design specified by the manufacturer were validated on a test stand specially built for this doctoral study. Experimental tests were not carried out for other volute designs. For the validation of the PAT model, the test stand was further extended. The validation showed that, at the BEP of both the pump and the PAT, the difference between the numerical and experimental results was below 4%.

For the Omega pump, validation was carried out by comparing the numerical results with the manufacturer's catalogue data, since the electrical power limitations of the laboratory did not allow experimental testing of this pump. The manufacturer does not provide experimental data for operation in turbine mode. Therefore, it was decided to apply the pump-to-turbine performance prediction model to verify Omega PAT model. Additionally, since the mesh for the DHV pump was prepared in the same way as for the Omega pump, it was assumed that the positive validation of the DHV model confirms the correctness of the adopted methodology also for the Omega pump. A more detailed description of the experiment is given in Chapter 6.

4. An analysis of the characteristic curves of the Omega pump and PAT obtained from the numerical simulations was carried out. The optimal range of the volute opening angle was determined. Changes in the characteristic curves resulting from variations in the geometric parameters were analysed. The best volute for turbine mode, pump mode and a trade-off volute geometry that performs best in both pump and turbine modes were identified using the Pareto front. In addition, the volute that provides the flattest efficiency curve while maintaining a high efficiency level was determined. A similar analysis was carried out for the DHV pump.

5. The flow structure in the volute and impeller at the Omega and DHV pump in pump and turbine was analysed. Velocity triangles at the impeller inlet in turbine mode were also considered, together with their changes resulting from variations in the geometric parameters.

6. A statistical analysis was performed using multiple linear regression estimated by the ordinary least squares method. This method was used to determine which geometric parameters are more important and how the pump and PAT performance parameters change when the value of each geometric parameter is varied at different flow rates.

7. Based on the results obtained using different methods, the influence of each geometric parameter of the volute casing was determined. Subsequently, design recommendations were developed for the selection of geometric parameters for pump and PAT operation at low and high n_q.

Chapter 5: Numerical simulation

As the main tool for evaluating pump performance, numerical flow modelling was selected. One of the modelling approaches is the use of Computational Fluid Dynamics (CFD). CFD modelling is often the only non-invasive method for assessing the correctness of the designs of the machines under investigation. The investigated volute is formed by two bodies of the double-entry pump, and it is not possible to examine all volute casings by physically modifying the real pump. CFD significantly reduces time and costs of research.

CFD software employs the finite volume method to iteratively solve the conservation equations of mass, momentum, and energy, enabling the simulation of flows in a wide range of applications. It then predicts the behaviour of the flow and other physical parameters. This allows repeated studies to be conducted by modifying both the geometric parameters of the device and the boundary conditions, making it possible to design a structure that is optimal with respect to the phenomena occurring within it.

Numerical modelling is carried out according to a standard sequence of steps:

– Preparation of the three-dimensional geometry of the pump flow parts (SolidWorks);

– Creation of the computational mesh based on the 3D flow parts geometry (Ansys Meshing);

– Specification of the boundary conditions for the simulation (CFX-Pre);

– Configuration of the parameters and execution of the steady-state calculation (CFX-Solver Manager);

– Processing of the obtained simulation results (CFX-Post).

Turbulence models used in RANS simulations provide a simplified description of the Reynolds stress distribution in the computational domain. Most turbulence models describe the flow by means of turbulent viscosity. In numerical simulations, two-equation models are among the most commonly used approaches, as they solve two transport equations to determine the main turbulence parameters. Below are some of the most common turbulence models [114].

The k-ε model is one of the most widely used turbulence models. It introduces the turbulence kinetic energy k and its dissipation rate ε. However, its standard version has limited accuracy in flows with separation, strong curvature of flow paths, and large pressure gradients. Nevertheless, in the present study, the k–ε model was applied as a RANS-type model for a comparative analysis of the influence of volute geometry on flow parameters and the hydraulic characteristics of the pump. This choice was made because the main aim of the study was to determine the effect of changes in volute geometry on the mean flow pattern, pressure distribution, flow losses, and overall performance parameters of the machine, rather than to reproduce in detail all local and unsteady turbulent phenomena in the region of interaction between the impeller and the volute tongue. In this context, the k-ε model represents a justified compromise between computational cost, numerical stability, and the possibility of reliable comparison between the analysed design variants.

The k-ω model gives a better representation of near-wall flow and of flows with strong pressure gradients, provided that a sufficiently fine computational mesh is used.

The k–ω SST *model* combines the advantages of the k-ε and k-ω models. It uses the k-ω model in the near-wall region and the k-ε model in the core flow region.

A physical experiment was conducted to validate the results obtained by the numerical method through comparison of the calculated and actual operating parameters of the pump. The use of this approach is considered sufficiently accurate for solving similar problems [35], [115], [116].

5.1 Three-dimensional geometry of the pump flow parts

The foundation of developing a numerical model of any hydraulic machine is the creation of a three-dimensional model that reflects the geometry of the machine's flow domain.

The solid model of the DHV pump's computational fluid domain includes the inlet pipe, inlet casing, volute casing, sidewall gaps, impeller, and outlet pipe (Figure 5.1 a). The Omega pump model (Figure 5.1 b) consisted of the same elements. Sidewall gaps were also modelled and are included as part of the volute casing, therefore, they are not indicated separately in the Figure 5.1b.

For the PAT investigation, the same mesh as for the pump was used. To perform the simulations, the rotational speed of the impeller was reversed and adjusted to the corresponding synchronous speed of the generator. For the asynchronous machine operating in generator mode, a rotational speed of 1520 rpm was adopted, which is slightly higher than the synchronous speed of 1500 rpm for a 4-pole machine at 50 Hz, in order to account for the slip required for generator operation. The direction of fluid flow through the pump was also reversed to the opposite direction, by the inversion of the input-output positions.

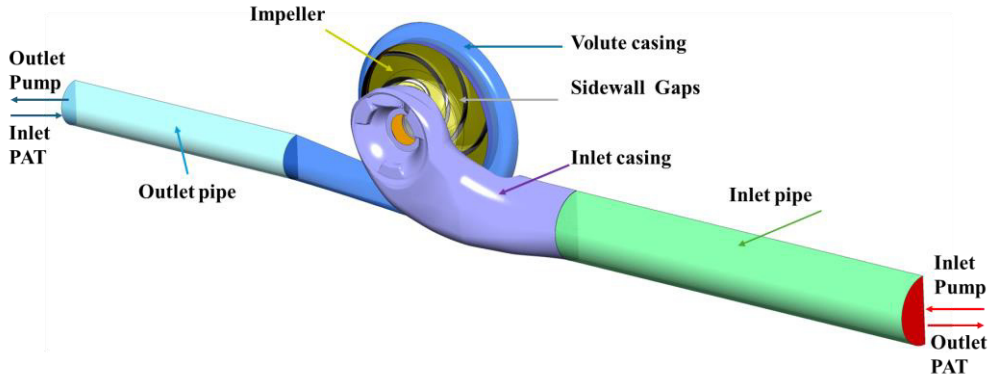

(a) DHV pump

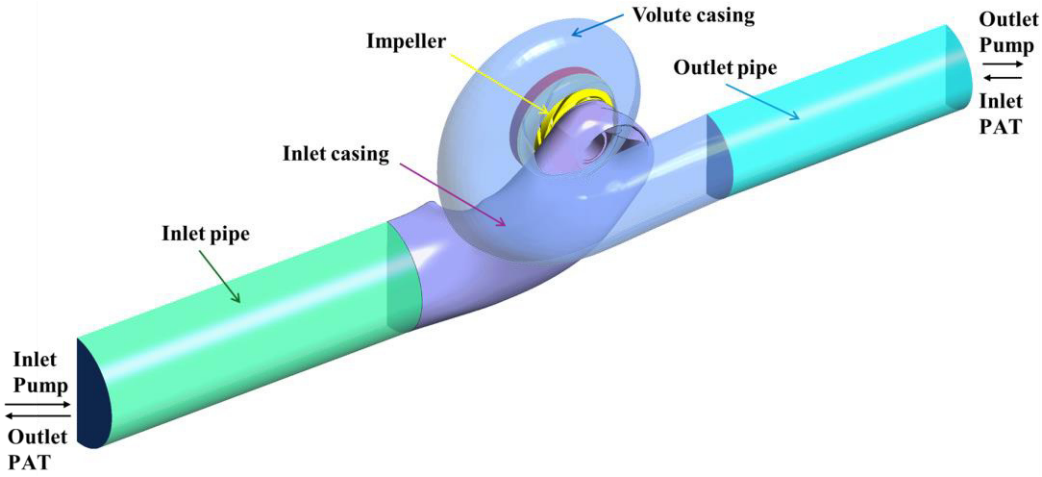

(b) Omega pump

Figure 5.1 - Division of the fluid model into domains

The inlet and outlet of the fluid domain were located at a distance equal to 5 pipe diameters from the pump inlet and outlet flanges. For turbine mode, the outlet distance downstream of the turbine was equal to 16 pipe diameters.

To reduce the number of elements of the computational grid, the analysed computational area consisted of half of the flow part of the double-entry pump [117]. Half-pump simulations were compared with full-pump simulation results. The difference in head was less than 0.4% for pump at flow rate 105 m^3/h (optimal point for pump), and 0.45% for PAT at flow rate 126 m^3/h.

5.2 Discrete model of the DHV and Omega pumps

The discretization process involves dividing the fluid domain of the analysed pump model into smaller control volumes, forming the computational mesh. The unstructured mesh was generated in Ansys Meshing. Tetrahedral elements were used in the core of the flow domain, and layers of prisms were used near the walls. To accurately reproduce the flow characteristics, mesh refinement was applied in regions where large gradients of the computed variables were expected.

An example view of the mesh is shown in Figure 5.2. The number of mesh elements was determined based on the mesh-independence test (Figure 5.3), in which the stability of the model parameters was examined as the number of elements increased. The exact number of grid elements is described in the

Table 5.1 and Table 5.2. The element sizes ensure Y+ values within the recommended range of 30–300 [114].

Mesh quality was evaluated against the specified standard and found to be compliant. In particular, the values were in the range [114]:

- Average element quality was within the satisfactory range (0.25-1.0 - good),
- Aspect ratio met the recommended criterion (0-80 - good),
- Skewness remained within range (0-0.89 - acceptable),
- Orthogonal quality satisfied the required range (0.2-1 - good).

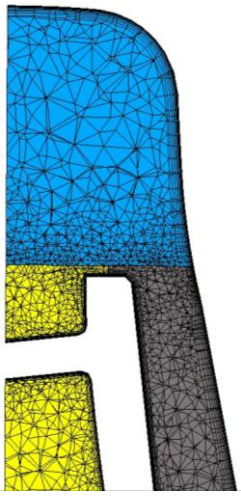

(a) DHV pump

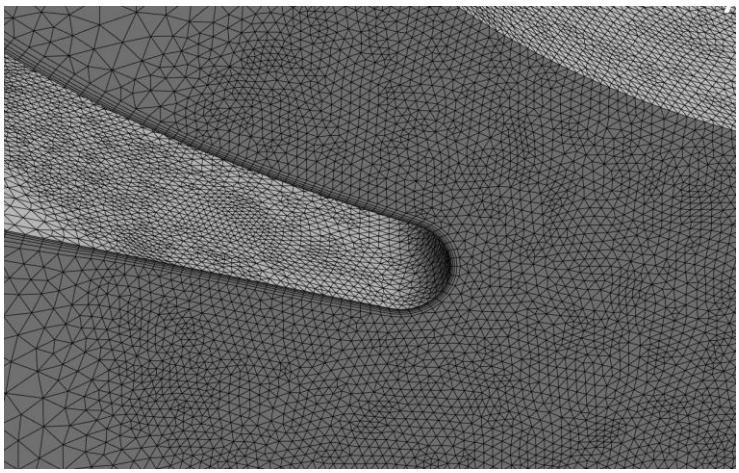

(b) DHV pump

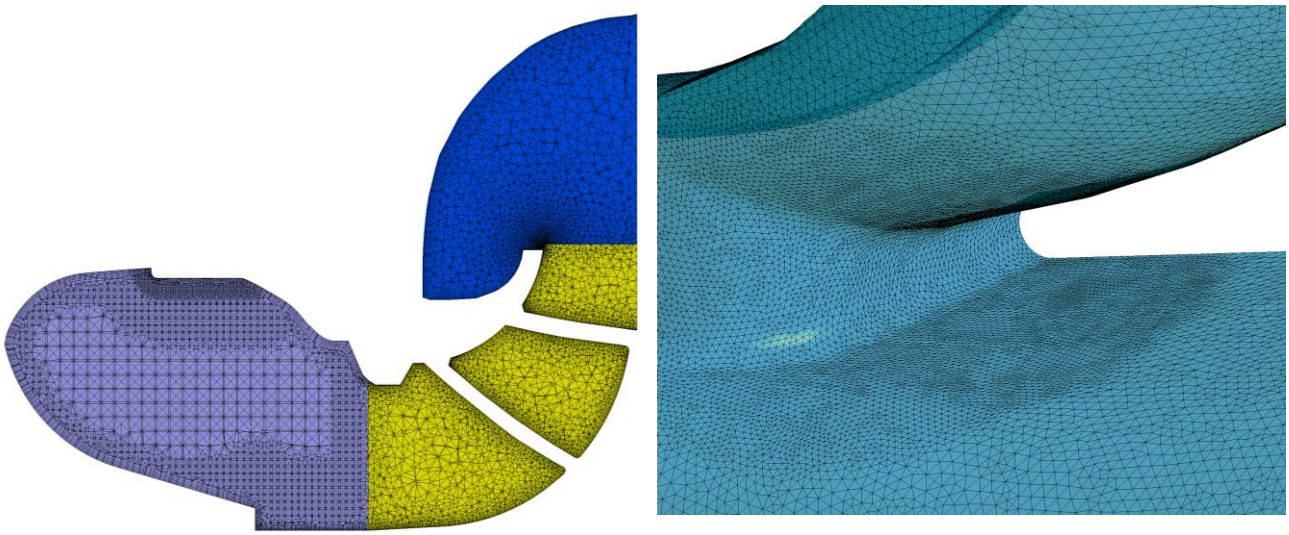

(c) Omega pump (d) Omega pump

Figure 5.2 - Example of the computational mesh: a), c) cross-sections of the volute, impeller, and side wall gap; b), d) volute tongue

The minimum number of mesh elements was determined based on the independence test, which consisted of examining the stability of the numerical model parameters with an increasing number of mesh elements [118]. The test results are presented in Figure 5.3 a,b.

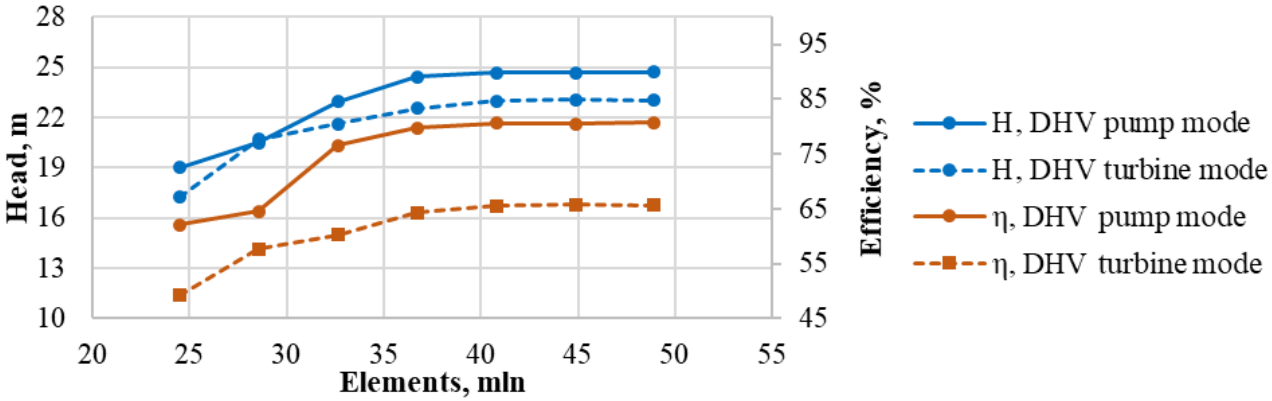

(a) DHV pump

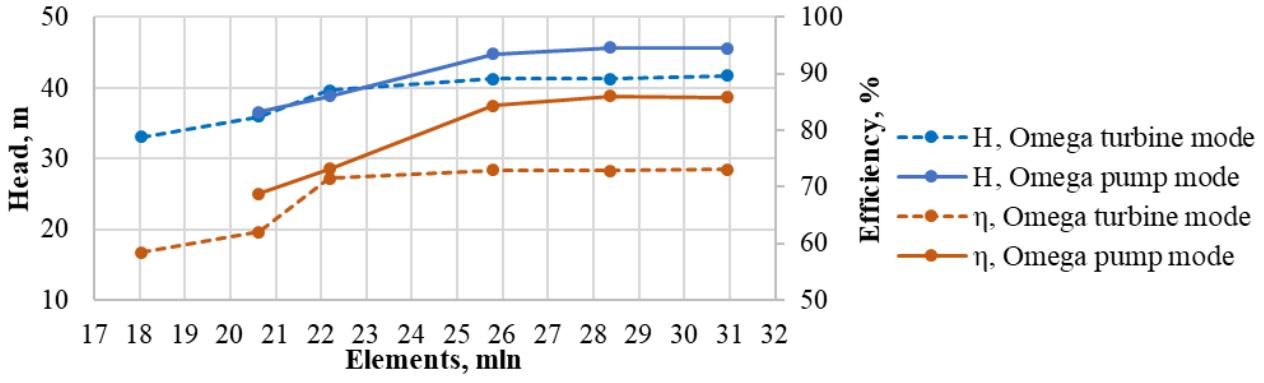

(b) Omega pump

Figure 5.3 – Mesh independence test for DHV and Omega pumps in pump and turbine modes

Table 5.1 - Mesh information for DHV reference pump

Domain	Nodes	Elements	Tetrahedra	Wedge	Pyramid	Hexahedra
Sidewall gaps	953312	2475820	1077187	1395958	2675	0
Inlet pipe	770694	2795493	2015567	779926	0	0
Outlet pipe	115801	391536	266950	124586	0	0
Seal	2655095	8827301	7773017	0	31948	1022336
Inlet casing	2206390	12158320	12158320	0	0	0
Volute casing	394372	1286250	862834	423416	0	0
Impeller	3847884	12454042	7843237	4607292	3513	0
All Domains	10943548	40388762	31997112	7331178	38136	1022336

Table 5.2 - Mesh information for Omega reference pump

Domain	Nodes	Elements	Tetrahedra	Wedge	Pyramid	Hexahedra
Inlet pipe	753300	730696	0	0	0	730696
Inlet casing	1808138	7177087	5632874	1543488	725	0
Impeller	1944450	6030389	3671959	2358430	0	0
Volute casing	2135094	11532980	11532980	0	0	0
Outlet pipe	331320	318171	0	0	0	318171
All Domains	6972302	25789323	20837813	3901918	725	1048867

5.3 Boundary conditions

The pump operation was simulated using the Ansys CFX program. Each of the studied computational models (Figure 5.4) was divided into two types of domains: a rotating domain that performs rotary motion (the impeller) and a stationary domain that is fixed in space (volute casings, inlet casing, pipelines, sidewall gaps).

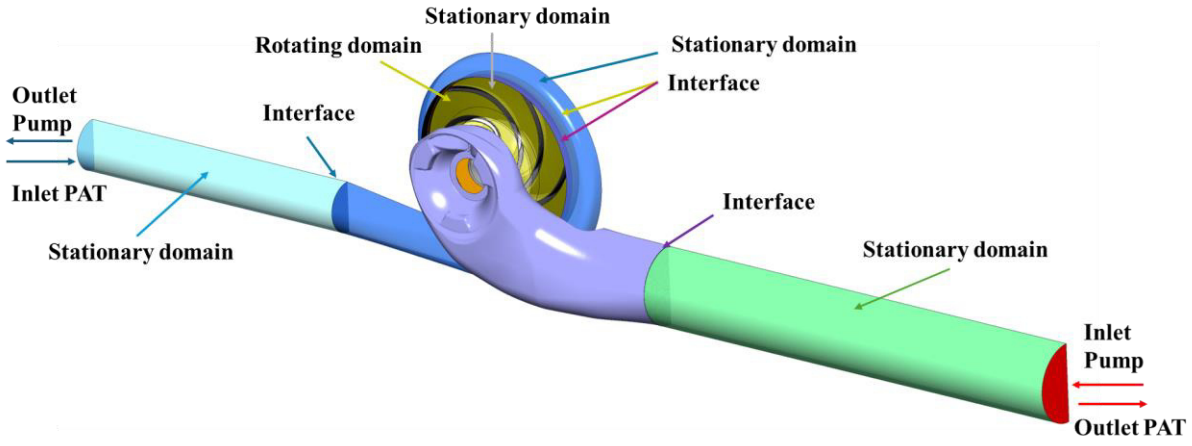

(a) DHV pump

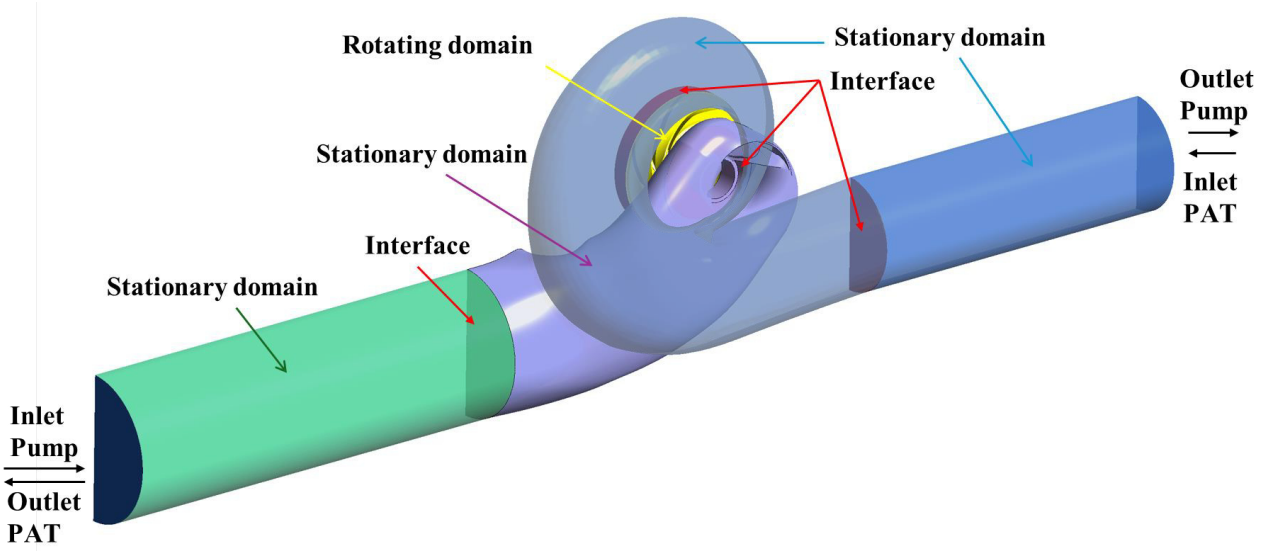

(b) Omega pump

Figure 5.4 - Boundary conditions of the computational model

The Rhie-Chow algorithm was used to implement the scheme for pressure-velocity coupling in CFX. The simulations were performed as steady-state analyses. The steady-state approach with a mixing plane interface provides circumferentially averaged flow quantities at the rotor-stator interface. As a result, unsteady rotor-stator interaction, including periodic pressure and velocity fluctuations, is not resolved.

During the calculations, mass flow rate and total pressure at the inlet and outlet of the model were monitored. The calculations were terminated after the parameters stabilized for at least 3500 iterations and when the convergence level of the equations reached below 0.0001. The interfaces between the rotary and stationary components were set as stage rotor interfaces. The analysed models take into account the influence of wall roughness on the obtained results, which was measured as an arithmetical mean roughness (R_a) and converted to sand grain roughness height (k_s= 5.863R_a) [119]. The basic solver settings and boundary conditions are presented in Table 5.3.

Table 5.3 - Boundary conditions and main simulation settings for both pumps

Parameter	**Setting**
Turbulence model	Standard k-ε
Analysis type	Steady-state
Method	Reynolds-Averaged Navier-Stokes (RANS)
Wall function	Scalable
Inlet	Flow rate with turbulence intensity 5%
Outlet	Opening - Static pressure
Rotating domain	Rotation speed
Liquid	Water: density $\rho(H_2O)$ = 998.29 kg/m^3, dynamic viscosity $\mu(H_2O)$ = 0.0010005 Pas.
Fixed walls	No–slip Wall, rotation speed = 0 m/s, roughness on the walls
Movable walls	No-slip, rotation speed, roughness on the walls

5.4 Turbulence model selection

Numerical simulations of the DHV pump in both pump and turbine mode were performed with three turbulence models: k-ε, k-ω, and k-ω SST - in order to assess their suitability for the present application. All three models yielded comparable head and efficiency values, with the k-ε model producing the closest agreement with the experimental data (Figure 5.5a, Figure 5.6a). Hydraulic and mechanical losses of 4% and 1%, respectively [46] , were added as a post-correction to the CFD results to account for leakage and disk-friction effects not resolved by the present model.

The dominance of the k-ε model in this comparison is consistent with the operating regime studied. At the BEP, the flow is relatively well guided by the blades and no large separation zones are observed. The main integral parameters, such as head and shaft torque, are mainly governed by the momentum exchange in the impeller and volute, rather than by detailed near-wall flow effects.

Under these conditions, the k-ε model can provide reliable results, as it is well suited for fully turbulent flows. In contrast, the main advantage of the k-ω SST model, namely the accurate resolution of the near-wall region, can only be fully used when a low-Reynolds-number mesh with y+ ≈ 1 is applied over the wetted surfaces. Moreover, the SST model may overpredict turbulent kinetic energy in stagnation regions, such as near the volute cutwater, which can lead to an underprediction of head.

Since the main aim of this study is a comparative analysis of different geometrical variants, the use of the same turbulence model for all cases is more important than achieving the highest local accuracy in selected flow regions.

Taking into account the substantially longer computational time and the finer near-wall mesh required by k-ω and k-ω SST, the k-ε model was selected for all subsequent simulations. At Q_{nom} in pump mode the differences between numerical and experimental values were 2.2% for head and 1.1% for efficiency; in turbine mode at 126 m³/h the corresponding differences were 0.5% for head and 1.8% for efficiency. These deviations are within the range typically reported for well-validated RANS simulations of centrifugal turbomachinery at the design point.

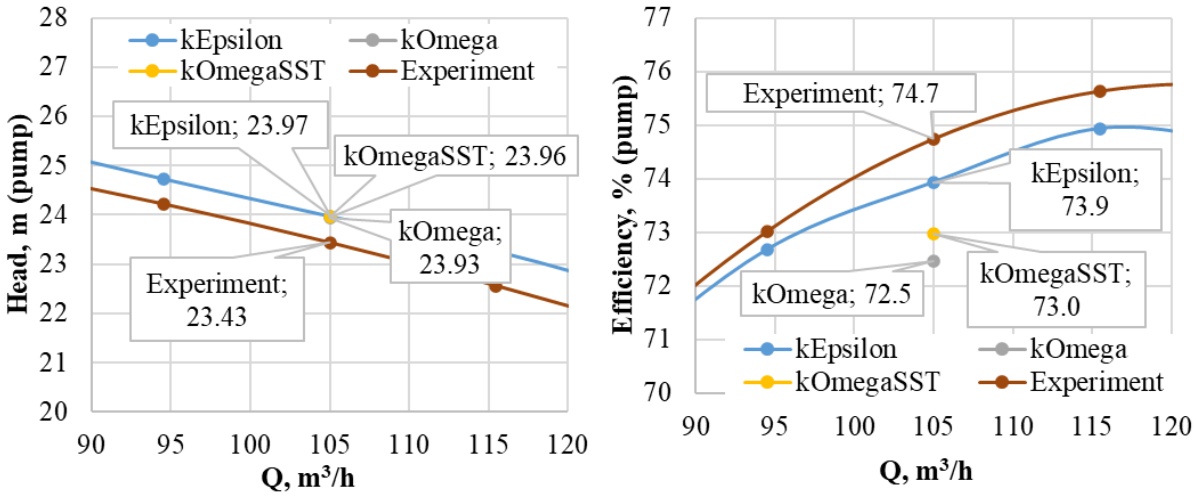

Figure 5.5 - Comparison of turbulence models for the DHV pump in pump mode: a) head, b) efficiency

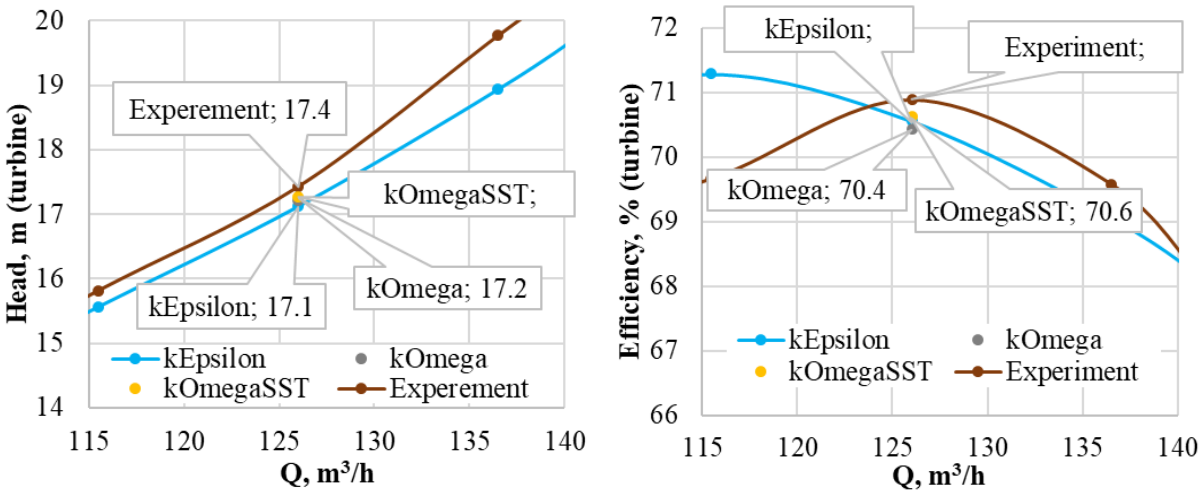

(a) (b)

Figure 5.6 - Comparison of turbulence models for the DHV pump in turbine mode: a) head, b) efficiency

Chapter 6: Experimental research

This section describes two variants of the experimental stand for the DHV pump in pump and turbine modes and presents the research methodology and the validation results of the numerical studies for both pumps.

6.1 Description of the experimental stand for pump operating in pump mode

In order to carry out the series of tests necessary to achieve the objectives of the work, a specialised experimental stand was designed and built.

The experimental stand is shown in Figure 6.1 and was constructed as a closed circuit in accordance with the recommendations of ISO 9906, with the accuracy corresponding to Grade 1B. [120]. The main characteristics of the laboratory measurement equipment are presented in Table 6.1.

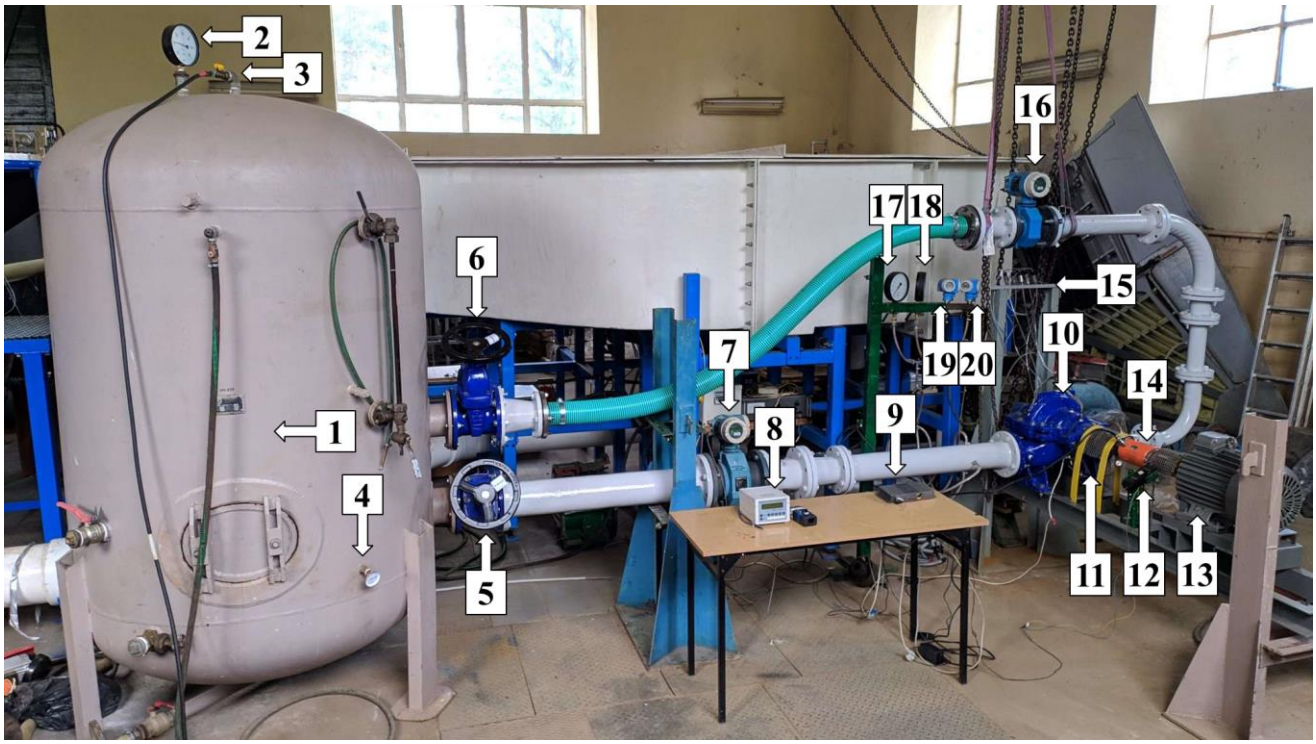

Figure 6.1 - The pump experimental stand: 1 – tank 3.25 m^3, 2 – pressure gauge, 3 – vent valve, 4 – thermometer, 5, 6 – gate valves, 7, 16 – flow meter, 8 – shaft torque recorder, 9 – specially created recording module, 10 – DHV.80–270A pump, 11 – jaw coupling, 12 – photo/contact tachometer, 13 – electric motor, 14 – torque meter, 15 – static pressure sensors, 17, 18, 19, 20 – suction and discharge pressure measurement set: pressure gauges and electronic pressure transmitters with display

The main element of the stand was the pump assembly, which consisted of an 11 kW electric motor and the tested double-entry pump. A Variable Frequency Drive (VFD) was used to regulate the pump performance by adjusting its rotational speed.

The working medium was clean water at a temperature of 20˚C. Data acquisition started after at least 15 min of pump operation, which was necessary to stabilize the operating parameters of the pump and electric motor after start-up, including the thermal conditions of the bearing units. During the experiment, the liquid temperature and rotational speed were monitored.

Table 6.1. Main characteristics of the laboratory measurement equipment

Sensor Type	Measured Quantity	Range	Accuracy
Electromagnetic flowmeter	Flow rate	8.5–283	±0.5%
Electromagnetic flowmeter	Flow rate	19–636	±0.5%
Electronic pressure transmitters with display	Pressure	0–1 MPa	±0.05%
Electronic pressure transmitters with display	Pressure	0–0.2 MPa	±0.05%
Thermometer	Temperature	0–60˚C	±1%
Torque meter	Torque on the pump shaft	0–100 Nm	±0.5%
Photo/contact tachometer	Speed rotation	5–100000 rpm	±0.05%
VFD for DHV pump with wattmeter INVT GD20-015G-4-EU	Electrical power	15 kW	±3.0%
VFD for 2-nd pump in turbine mode with wattmeter GD20-022G-4-EU	Electrical power	22 kW	±3.0%

The experimental stand enables measurement and automatic reading of operating parameters such as static pressure at the inlet and outlet of the pump, flow rate, torque on the shaft, shaft rotational speed and electrical power. The measurement data were collected using a specially created recording module. The module converted the analogue signal of the sensors into a digital signal. This signal was sent to the laptop. The obtained data were converted using a specially developed program into comma-separated values (CSV).

6.2 Validation of numerical simulation for the DHV pump in pump mode

During the experiment, parameters were measured at 11 flow rate points with a 10% increment between adjacent points. Data from the measuring devices were recorded every second. For each flow rate point, the measurement time was 30 s. Then, the data obtained for 30 s were averaged.

The simulations were carried out for varying flow rates. Since complete valve closure is not a normal operating condition of the pump, simulations for flow rates close to 0 m³/h were intentionally omitted. In addition, the more throttled the flow is, the more frequently unsteady phenomena occur, which leads to difficulties in steady-state numerical simulations.

The pump model with the reference volute was validated on an experimental stand at a rotational speed of 1460 rpm. The deviation of the numerical simulation results from the experiment for the head was 2.2 %, and for efficiency, it was 1.1% at $1.0Q_{opt}$, which is an acceptable level of discrepancy for numerical simulation (Figure 6.2). In the CFD model, hydraulic losses were assumed to be 4%, according to [46], while mechanical losses were assumed to be 1% [46].

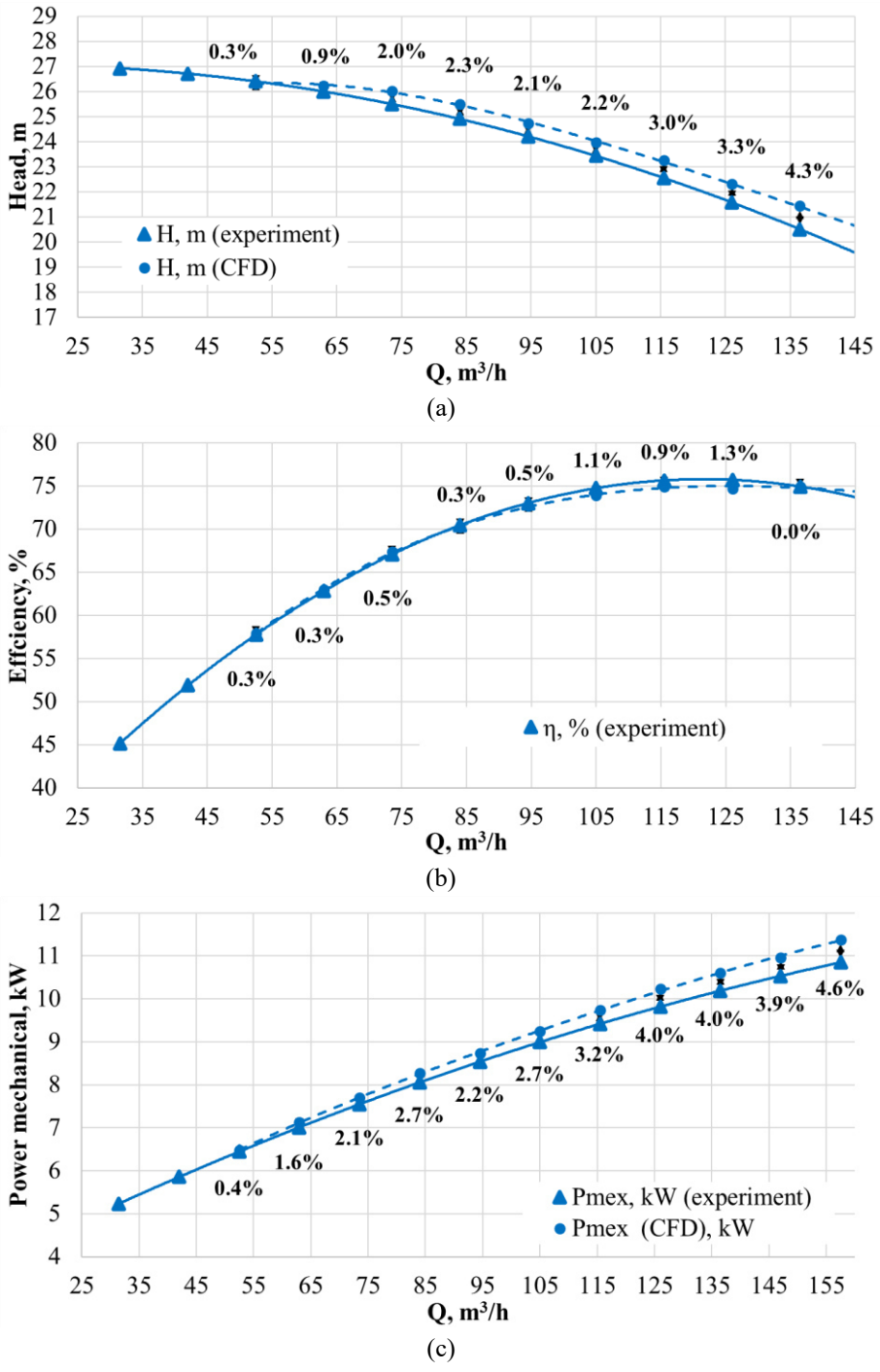

Figure 6.2 - Comparative characteristics of experiment and CFD results for DHV pump in pump mode: a) head, b) efficiency, c) mechanical power curves

6.3 Experimental stand for DHV pump operating in turbine mode

For the investigation of the pump operating in turbine mode, it was necessary to modify the experimental stand by adding a pump to circulate water in the experimental stand. In this setup, the DHV pump (pos. 10 in Figure 6.3; Figure 6.4) was operated as a turbine. The main pipeline system, fittings, and measuring instruments remained unchanged. The main characteristics of laboratory measuring equipment have already been described in Table 6.1.

The experimental stand was modified (Figure 6.3) by adding the Fr pump (21), which supplied water to the existing DHV PAT (pos. 10). A new VFD (23) was also installed (Figure 6.4) to operate the electric motor (13) as a generator and to receive the electrical energy generated by the PAT. Both frequency converters (23) and (24) were interconnected.

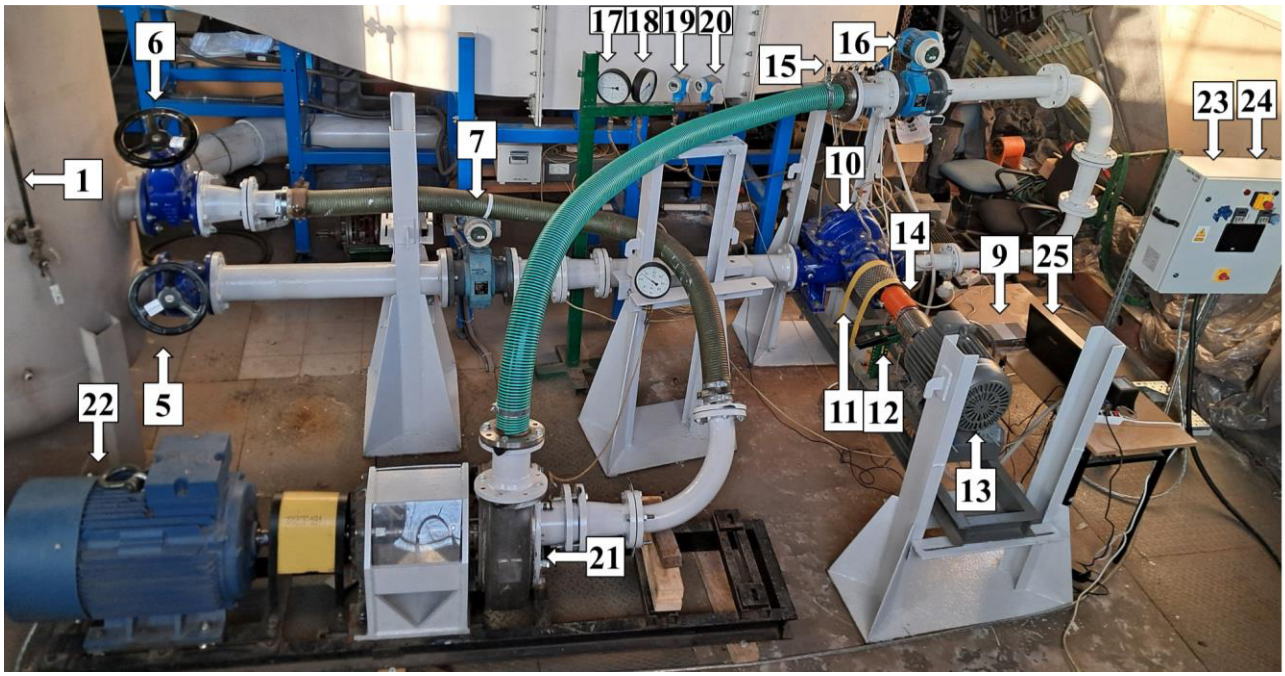

Figure 6.3 – The experimental stand after rebuilding for PAT and PAP modes:
1 – tank, 5, 6 – valves, 7, 16 – flow meter, 9 – data recorder for electronic measuring instruments, 10 – PAT DHV.80-270A, 11 – couplings, 12 – photo/contact tachometer, 13 – electric motor as generator, 14 – torque meter, 15 – static pressure sensors, 17, 18, 19, 20 – pressure measurement set on pump suction and discharge: pressure gauges and electronic pressure transducers with display, 21 – Fr pump, 22 – electric motor, 23, 24 – VFD, 25 – computer

The experimental stand operates as follows: VFD (24) supplies power to the electric motor (22) of the Fr. pump (21), which pumps water from the tank (1) to the pump-turbine (10) and back to tank (1), forming a closed water loop. VFD (23) excites the rotor of the electric motor (13). The PAT (10) is mechanically coupled to motor (13), which, operating in generator mode, produces electricity. The generated current is directed to the rectifier of VFD (23) and then to the shared DC bus of VFD (23) and (24). The electric motor (22) of the Fr pump (21) is powered by VFD (24), drawing electricity from both the shared DC bus (generated energy) and the mains grid.

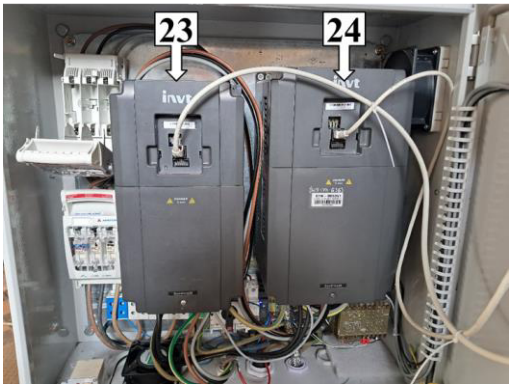

Figure 6.4 - VFD for the DHV pump-turbine (23) and the Fr pump (24)

6.4 Validation of numerical simulation for the DHV pump in turbine mode

The pump in turbine operation mode with a reference volute was validated on an experimental stand (Figure 6.3). The deviation of the numerical simulation results from the experiment for the head was 2.2%, for efficiency 0.4% at flow rate 126 m^3/h (corresponds to the PAT BEP), which is an acceptable level of discrepancy for numerical simulation (Figure 6.5).

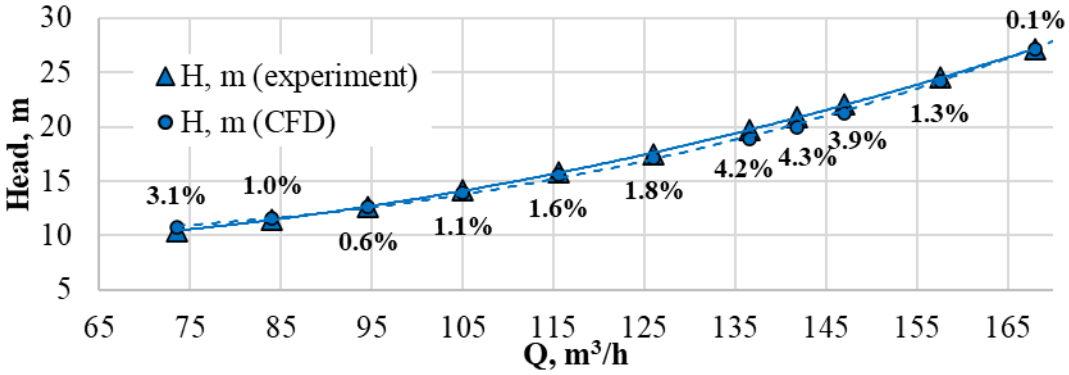

(a)

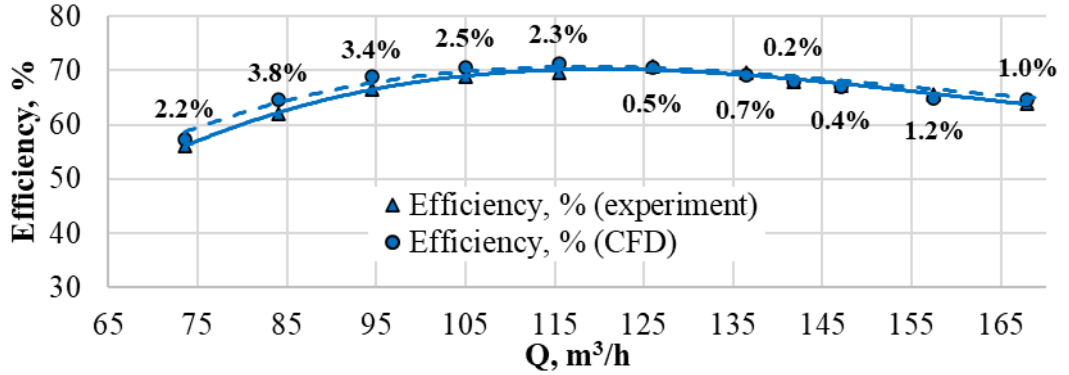

(b)

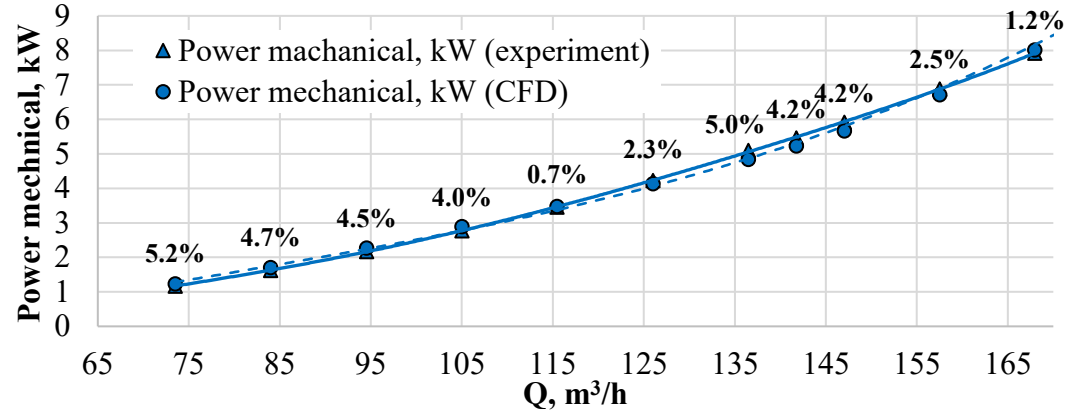

(c)

Figure 6.5 - Comparative characteristics of the experiment and CFD results for the DHV pump in turbine mode: a) head, b) efficiency and c) mechanical power curves

6.5 Validation of numerical simulation for the Omega pump in pump mode

Due to the high power required for the Omega pump to operate, it was not possible to conduct experimental investigations in laboratory conditions. Therefore, the results of numerical studies of the

pump in pump mode were compared with the data provided in the manufacturer's catalogue (Figure 4.6).

The deviation of the numerical simulation results from the manufacturer's catalogue for the head was 1%, and for efficiency, it was 1% at 1.0 Q_{opt}, which is an acceptable level of discrepancy for numerical simulation (Figure 6.6).

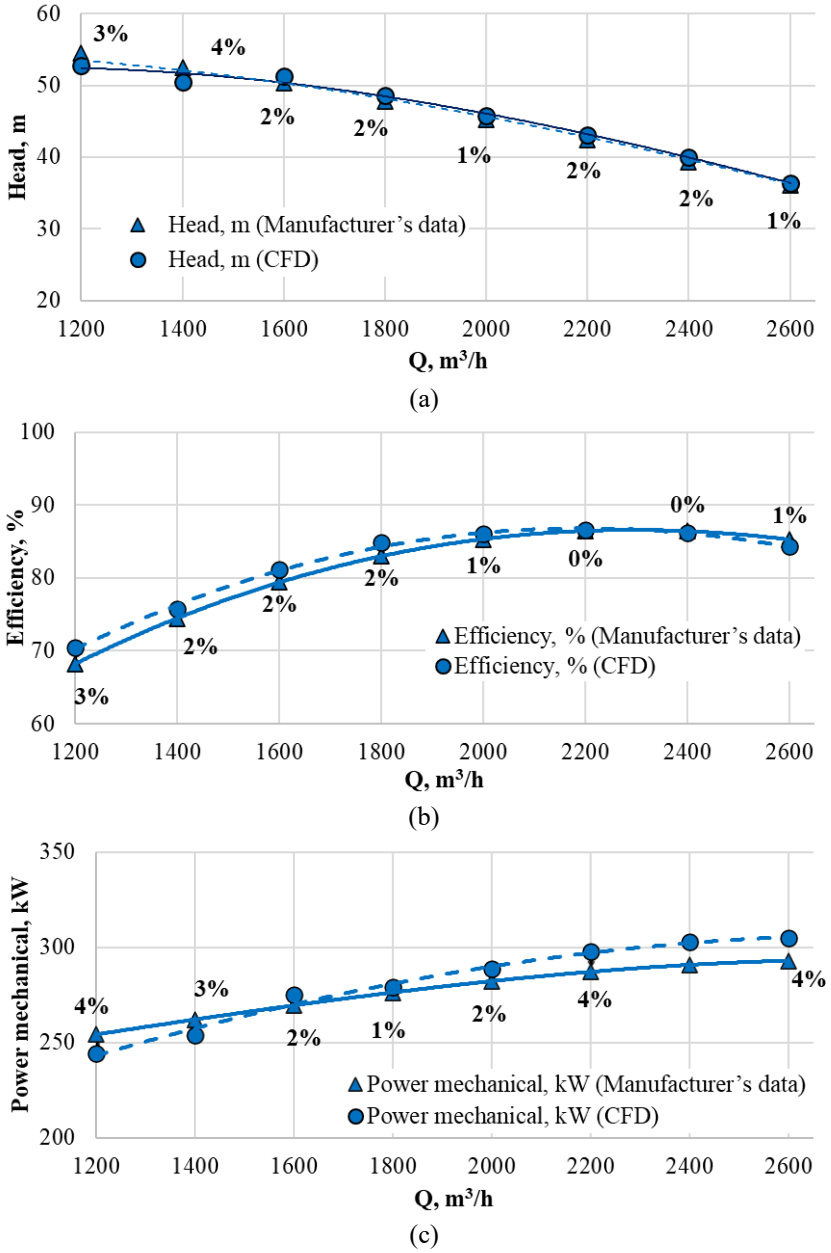

Figure 6.6 - Comparative characteristics of the data in the manufacturer's catalogue and CFD results for the Omega pump in pump mode: a) head, b) efficiency and c) mechanical power curves

The accuracy of CFD is often lower for low n_q pumps because their flow contains stronger adverse pressure gradients, local separation, recirculation, leakage, and secondary flows, which are harder to represent with conventional steady RANS models [35]. Thus, the larger discrepancy observed for the DHV pump agrees with the literature, while the results obtained for the higher n_q Omega pump can be treated with greater confidence.

6.6 Validation of numerical simulation for the Omega pump in turbine mode

The Omega pump has not been tested in turbine mode by the manufacturer, so the numerical results for turbine mode cannot be validated against catalogue data. Therefore, it was decided to convert the performance curves using a performance prediction model, according to the recommendations presented in the paper

[121]. This model was not developed for a double-entry pump therefore it provided reasonably approximate results (Figure 6.7). At a flow rate of 2300 m^3/h, the results agree well. When the flow rate changes by 100 m^3/h, the difference increases to 3%, while at higher flow rates it reaches up to 8%. At the BEP, the numerical results are consistent with the values obtained using the prediction model.

Since the Omega pump in turbine mode was modelled using the same CFD procedure like DHV pump, including the model setup, boundary conditions, and calculation assumptions, this agreement supports the reliability of the numerical results within the analyzed operating range.

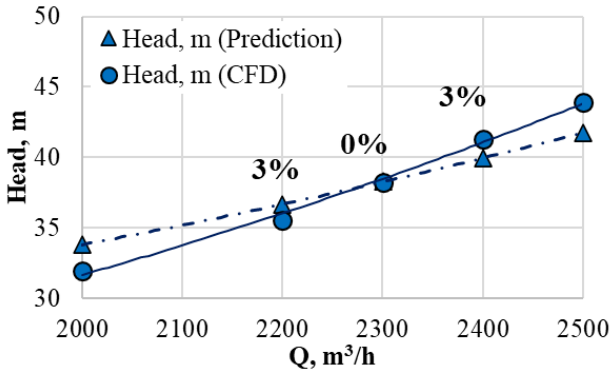

Figure 6.7 - Comparison of CFD results and PAT performance prediction results

6.7 Calculation formulas for pump and turbine energy characteristics

The energy characteristics of the pump in pump and turbine mode were determined based on the *H*, *Q*, and *P* parameters obtained at individual measurement points. The following relationships were used to calculate the values of these parameters according to [120].

The head (*H*) was determined using formula:

$$H = \Delta z_m + \frac{p_{m2} - p_{m1}}{\rho \cdot g} + \frac{U_2^2 - U_1^2}{2g} \quad (6)$$

$$U = \frac{Q}{A} \quad (7)$$

where:

A – area, m^2,

U - mean velocity, m/s,

Δz_m- difference in the elevation of the pressure gauges,

p_{m1}/ p_{m2} - gauge pressure in inlet and outlet,

Q - (volume) rate of flow, m^3/s.

Water density ρ, depending on the temperature t, according to [122] was determined using equation:

$$\rho \quad = 999.974950 \cdot [1 - \frac{(t - 3.983035)^2 \ \cdot (\mathrm{t} + 301.797)}{522528.9(\mathrm{t} + 69.34881)}] \tag{8}$$

The hydraulic power *Ph* of the pump was determined using equation:

$$P_h = Q \cdot H \cdot g \cdot \rho \tag{9}$$

The mechanical power P_m of the pump and PAT was determined using equation:

$$P_m = \omega \cdot M_m \tag{10}$$

$$\omega = \frac{2 \cdot \pi \cdot n}{60} = \frac{\pi \cdot n}{30}$$

The total efficiency η of the pump and PAT was determined as the ratio of the hydraulic power P_h to the mechanical power P_m , according to equations:

$$\eta_\mathrm{p} = \frac{\mathrm{P}_h}{\mathrm{P}_\mathrm{m}} \tag{11}$$

$$\eta_\mathrm{p} = \frac{\mathrm{Q} \ \cdot \mathrm{H} \ \cdot \mathrm{g} \cdot \rho}{\frac{\pi \cdot n}{30} \cdot \mathrm{M}_m}. \tag{12}$$

6.8 Measurement uncertainty

In the analysis of measurement errors, it was assumed that all random errors (of the nature of independent events) follow a normal distribution. In the analysis of measurement uncertainty, the following notation was adopted: a capital letter symbol represents total uncertainty, a lowercase letter represents partial uncertainty. The error analysis procedure was performed as follows [120]:

1. Relative measurement uncertainties:

- partial

$$\delta_Q = \frac{class_{flow\ meter} \cdot range_{flow\ meter}}{indication_{flow\ meter}} \tag{13}$$

total

$$\delta Q = \pm\sqrt{\delta_Q^2 + \delta n^2} \tag{14}$$

where: uncertainty measurement error of the pump shaft rotational speed δn = 0,1.

a) Uncertainty of head measurement *H*:

partial uncertainty of suction and discharge pressure measurement:

$$\delta_{p.s} = \frac{class_{pressure\ gauge} \cdot range_{pressure\ gauge}}{indication_{pressure\ gauge}}$$

$$\delta_{p.d} = \frac{class_{pressure\ gauge} \cdot range_{pressure\ gauge}}{indication_{pressure\ gauge}} \tag{15}$$

total uncertainty of head measurement:

$$\delta H = \pm\sqrt{\delta_{p.s}^2 + \delta_{p.d}^2 + 4\delta n^2} \tag{16}$$

b) Uncertainty of hydraulic power P_h:

- total uncertainty of hydraulic power measurement:

$$\delta P_h = \pm\sqrt{\delta Q^2 + \delta H^2 + \delta\rho^2} \tag{17}$$

where: uncertainty of water density determination $\delta\rho$ = 0,1.

c) Uncertainty of torque M consumed by the pump:

- partial uncertainty of torque measurement:

$$\delta_{torq} = \frac{class_{torq} \cdot range_{torq}}{indication_{torqq}} \tag{18}$$

d) Uncertainty of mechanical power P_m:

- total uncertainty of mechanical power measurement:

$$\delta P_m = \pm\sqrt{\delta_{torq}^2 + 4\delta n^2} \tag{19}$$

e) Uncertainty of efficiency measurement

- total uncertainty of pump or PAT efficiency measurement η:

$$\delta\eta = \pm\sqrt{\delta P_h^2 + \delta P_m^2} \tag{20}$$

2. Absolute measurement uncertainties:

The absolute uncertainty of each measurement was determined from equation

$$\Delta X = \frac{\delta X \cdot X}{100\%} \tag{21}$$

where:

δX - relative measurement uncertainty value of „X”,

X - value of the measured quantity.

Since the obtained uncertainty values are small, uncertainty bars were omitted in the graphs. The uncertainty calculation for the reference volute is presented in Table 6.2 and Table 6.3. Due to similar values for the other tested volutes, their presentation was omitted.

Table 6.2. Measurement uncertainties for the pump in pump mode

Relative uncertainty, %					Absolute uncertainty				
Designation	**84 m³/h**	**105 m³/h**	**126 m³/h**	**157 m³/h**	**Designation**	**84 m³/h**	**105 m³/h**	**126 m³/h**	**157 m³/h**
δ_Q	0.017	0.013	0.011	0.009	ΔQ, m³/h	0.085	0.106	0.127	0.158
δQ	0.101	0.101	0.101	0.100	ΔH, m	0.050	0.047	0.043	0.036
δn	0.100	0.100	0.100	0.100	ΔP_m, W	0.016	0.018	0.020	0.022
$\delta_{p.s}$	0.002	0.002	0.002	0.003	ΔP_h, W	0.014	0.017	0.018	0.019
$\delta_{p.d}$	0.002	0.002	0.002	0.003	$\Delta\eta$, %	0.225	0.238	0.238	0.226
δH	0.200	0.200	0.200	0.200					
$\delta\rho$	0.100	0.100	0.100	0.100					
δP_h	0.246	0.245	0.245	0.245					
δ_{torq}	0.014	0.013	0.012	0.011					
δP_m	0.200	0.200	0.200	0.200					
$\delta\eta$	0.317	0.317	0.317	0.317					

Table 6.3 - Measurement uncertainties for the pump in turbine mode

Relative uncertainty, %					Absolute uncertainty				
Designation	**84 m³/h**	**105 m³/h**	**126 m³/h**	**142 m³/h**	**Designation**	**84 m³/h**	**105 m³/h**	**126 m³/h**	**142 m³/h**
δ_Q	0.017	0.013	0.011	0.010	ΔQ, m³/h	0.085	0.106	0.127	0.143
δQ	0.101	0.101	0.101	0.100	ΔH, m	0.024	0.030	0.038	0.052
δn	0.100	0.100	0.100	0.100	ΔP_m, W	0.003	0.003	0.009	0.015
$\delta_{p.s}$	0.001	0.001	0.001	0.000	ΔP_h, W	0.007	0.011	0.016	0.027
$\delta_{p.d}$	0.010	0.011	0.012	0.014	$\Delta\eta$, %	0.197	0.217	0.221	0.208
δH	0.200	0.200	0.200	0.200					
$\delta\rho$	0.100	0.100	0.100	0.100					
δP_h	0.246	0.246	0.245	0.246					
δ_{torq}	0.027	0.016	0.012	0.009					
δP_m	0.202	0.201	0.200	0.200					
$\delta\eta$	0.318	0.317	0.317	0.317					

Chapter 7: Numerical results and statistical analysis for Omega pump

This section describes the results obtained through numerical investigations. The influence of the opening angle of the walls, design methods, cross-sectional shape, volute casing inlet width, and volute casing inlet diameter on the pump operating parameters in turbine mode and in pump mode, is analysed. This section also includes a description of the statistical methods used and the results of the statistical analysis of the numerical data.

7.1 Numerical results

7.1.1 Volute wall opening angle influence

7.1.1.1 Pump mode

At the beginning of the study, the influence of volute wall opening angle on the pump operation in pump mode was analysed. The investigation was carried out for angles ranging from 10˚ to 90˚. Various methods and cross-sectional shapes were taken into consideration. The difference between the selected pump characteristics is shown in Figure 7.1.

According to the obtained results, the volutes with the largest opening angles of 75˚ and 90˚ have the lowest head and efficiency. The difference between the pump with the most suitable volute design and the least favourable amounted to 1.8% and 1.5% for head and efficiency. In contrast, the difference between pumps with volute opening angles of 10˚ to 50˚ is small, 0.6% for head and efficiency.

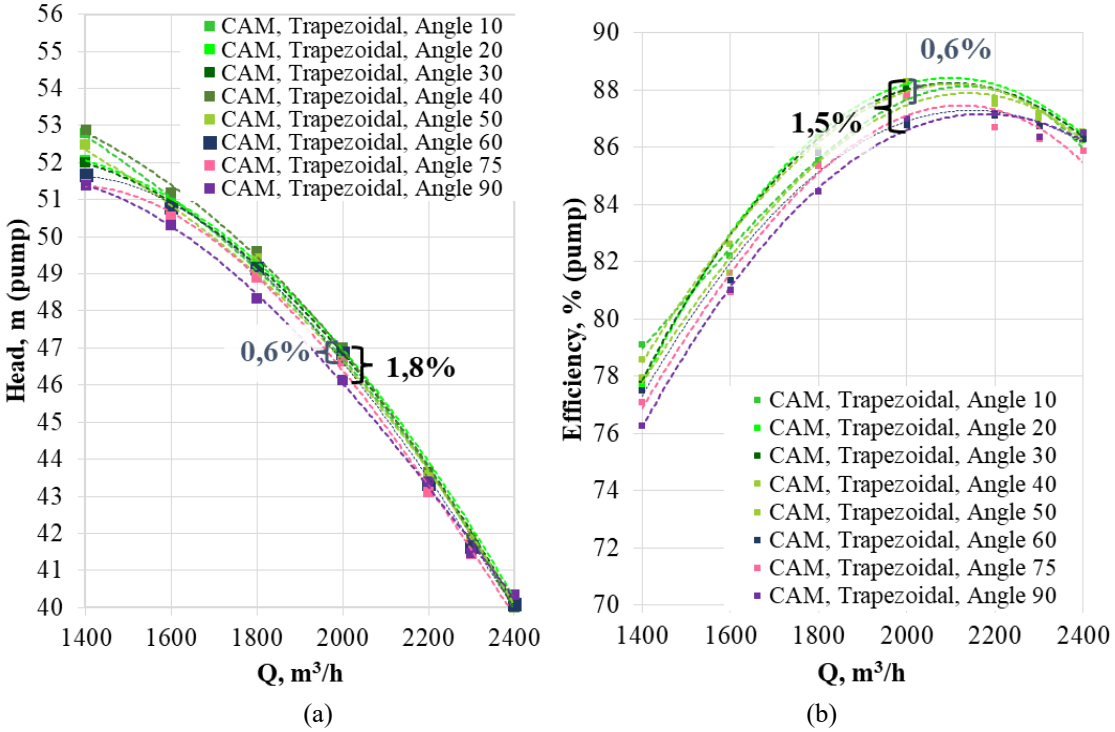

Figure 7.1 – Influence of the volute walls opening angle the on the pump characteristics in pump mode (graph does not display all the investigated volutes for better readability, see complete graph in Appendix C Figure C.10): a) head curves and b) efficiency curves

7.1.1.2 Turbine mode

The investigation was carried out for the same volute variants as in 7.1.1.1 when pump works as turbine. The difference between the selected PAT characteristics is shown in Figure 7.2.

According to the obtained results for PAT the same as for the pump mode, the volutes with the largest opening angles of 75˚ and 90˚ have the lowest head and efficiency. The difference between the pump with the best volute design and the least favourable amounted to 7.6% for head and 1.1% for efficiency. The difference between pumps with volute opening angles of 10˚ to 50˚ is small, 4.3% for head and 0.9% for efficiency.

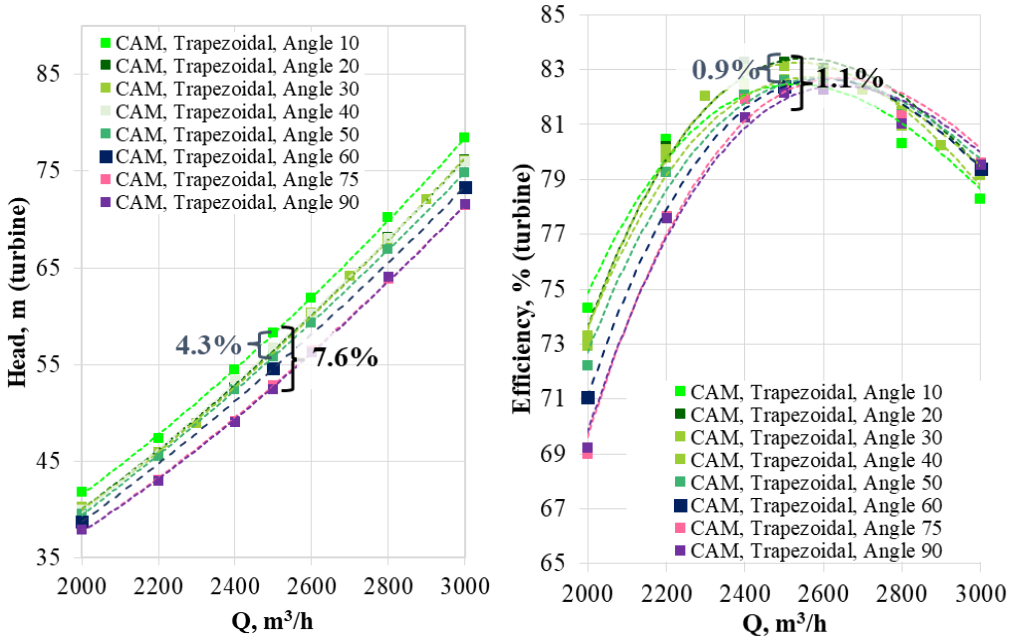

Figure 7.2 – Influence of the volute opening angle of the walls on the PAT characteristics in turbine mode (shortened graph This figure does not display all the investigated volutes for better readability, the complete Figure C.20 is provided in the Appendix C): a) head curves and b) efficiency curves

7.1.1.3 Optimal range for both operating modes

The analysis showed that the optimal range of the volute wall opening angle for pump and turbine mode is 10˚–50˚. Within optimal range, the angle of 30˚ most often provided the highest efficiency, while 40˚ provided comparable performance. Because the differences in pump and turbine performance between the models were small, the volute wall opening angle was identified as an insignificant geometrical parameter. Therefore, to reduce the number of analysed volutes, all subsequent volutes were studied with a volute wall opening angle of 30˚, with 40˚ considered as an alternative design option.

7.1.2 Design method, D_3, b_3 and cross-section shape influence

The analysis was conducted on 36 volute casing designs that differed in their design method, D_3, b_3, and cross-sectional shape. The parameters were selected according table Table 4.6, such that each volute casing had a “pair” with three identical geometric parameters and one differing parameter.

When the geometric parameters were changed within a single design method, the cross-sectional area always remained constant.

The names of the volute casings and the geometric parameters used for their construction are presented in Table 7.1. The cell colours indicate recommendations taken from the same scientific source: Lomakin [40] (green cell), Stepanoff [33] (yellow cell), Pfleiderer [32] (blue cell) and manufacture design (red cell).

All variants were simulated at the nominal rotational speed of pump 1488 rpm in pump mode and 1520 rpm in turbine mode, corresponding to the operating conditions of the DHV pump on the test

Table 7.1 - Geometric parameters and design variations of the analysed volute casings of Omega pump

No.	Volute name	Method	D_3	b_3	ε	Cross-sectional shape
1	CAM_D448_b105_R30	CAM	448	105	30	Round
2	CAM_D448_b105_T30	CAM	448	105	30	Trapezoidal
3	CAM_D448_b126_R30	CAM	448	126	30	Round
4	CAM_D448_b126_T30	CAM	448	126	30	Trapezoidal
5	CAM_D448_b183_R30	CAM	448	183	30	Round
6	CAM_D448_b183_T30	CAM	448	183	30	Trapezoidal
7	CAM_D485_b105_R30	CAM	485	105	30	Round
8	CAM_D485_b105_T30	CAM	485	105	30	Trapezoidal
9	CAM_D485_b126_R30	CAM	485	126	30	Round
10	CAM_D485_b126_T30	CAM	485	126	30	Trapezoidal
11	CAM_D485_b183_R30	CAM	485	183	30	Round
12	CAM_D485_b183_T30	CAM	485	183	30	Trapezoidal
13	CAM_D522_b105_R30	CAM	522	105	30	Round
14	CAM_D522_b105_T30	CAM	522	105	30	Trapezoidal
15	CAM_D522_b126_R30	CAM	522	126	30	Round
16	CAM_D522_b126_T30	CAM	522	126	30	Trapezoidal
17	CAM_D522_b183_R30	CAM	522	183	30	Round
18	CAM_D522_b183_T30	CAM	522	183	30	Trapezoidal
19	CV_D448_b105_R30	CV	448	105	30	Round
20	CV_D448_b105_T30	CV	448	105	30	Trapezoidal
21	CV_D448_b126_R30	CV	448	126	30	Round
22	CV_D448_b126_T30	CV	448	126	30	Trapezoidal
23	CV_D448_b183_R30	CV	448	183	30	Round
24	CV_D448_b183_T30	CV	448	183	30	Trapezoidal
25	CV_D485_b105_R30	CV	485	105	30	Round
26	CV_D485_b105_T30	CV	485	105	30	Trapezoidal
27	CV_D485_b126_R30	CV	485	126	30	Round
28	CV_D485_b126_T30	CV	485	126	30	Trapezoidal
29	CV_D485_b183_R30	CV	485	183	30	Round
30	CV_D485_b183_T30	CV	485	183	30	Trapezoidal
31	CV_D522_b105_R30	CV	522	105	30	Round
32	CV_D522_b105_T30	CV	522	105	30	Trapezoidal
33	CV_D522_b126_R30	CV	522	126	30	Round
34	CV_D522_b126_T30	CV	522	126	30	Trapezoidal
35	CV_D522_b183_R30	CV	522	183	30	Round
36	CV_D522_b183_T30	CV	522	183	30	Trapezoidal
37	Reference	Reference	485	245	17	Manuf. design

7.1.2.1 Pump mode

The investigation showed that, in pump mode, the geometric parameters of the volute have only a limited influence on the pump performance curves. The difference in operation parameters between models with various volutes is shown in Figure 7.4. This figure does not display all the investigated volutes for better readability (see full picture Figure D.11 in Appendix D).

According to the Figure 7.4 the biggest difference in pump performance between models with reference volute and volute designed by author (parameters: CV, D_3 =522 mm, b_3=126 mm, Round shape) at $Q_{nom.p}$ is 3% in head and efficiency, in power mechanical 1,3% and 57% in losses.

Head

The largest effects on head have b_3 and the cross-sectional shape. The maximum difference in head is 1.8% at $Q_{nom.p}$ due to varying b_3, while keeping the remaining geometric parameters constant (Figure 7.3). For the cross-sectional shape, the corresponding difference is 1.5% (Figure 7.3b). The design of a round volute cross-section shape and a high b_3 value increases head.

Efficiency

The analysis shows that b_3 has the strongest influence on the efficiency curve. Increasing b_3, leads to higher efficiency, accompanied by and increase in head, both attributable to a reduction of hydraulic losses in the volute. The maximum difference was 1.7% between the models with volutes characterised by constant D_3 and varying b_3 (Figure 7.3c)

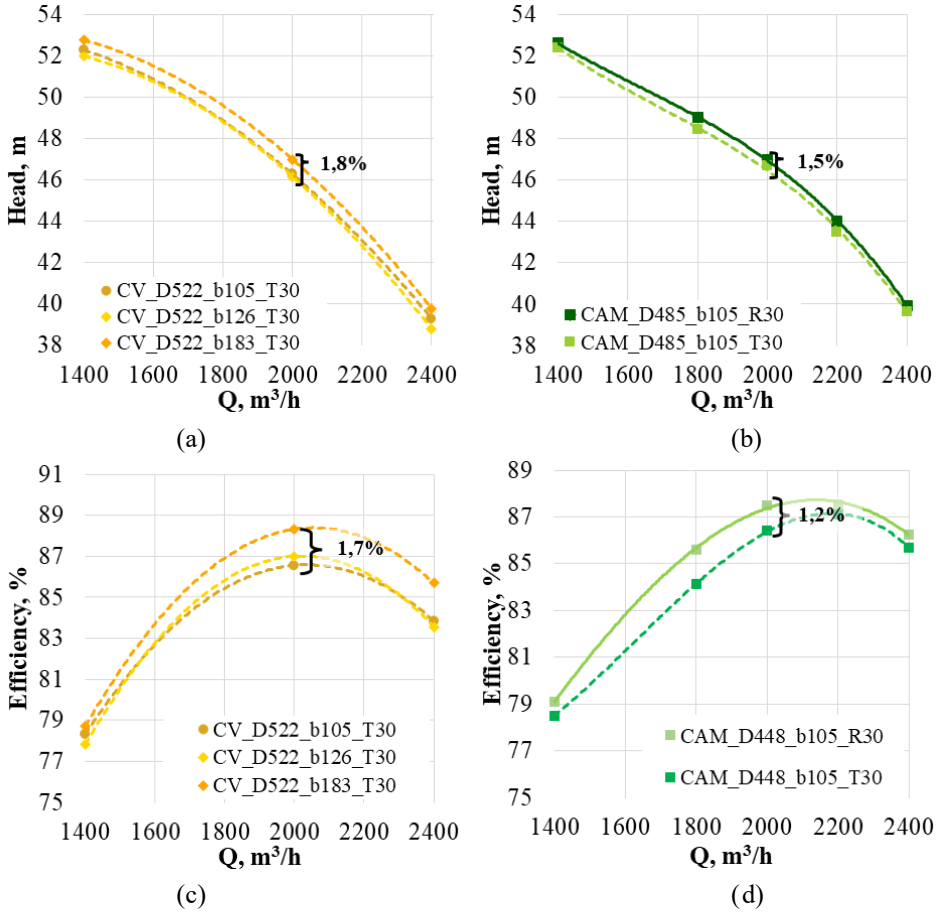

Figure 7.3 – The effect of volute geometrical parameter on head a) b_3, b) shape, on efficiency c) b_3, d) shape

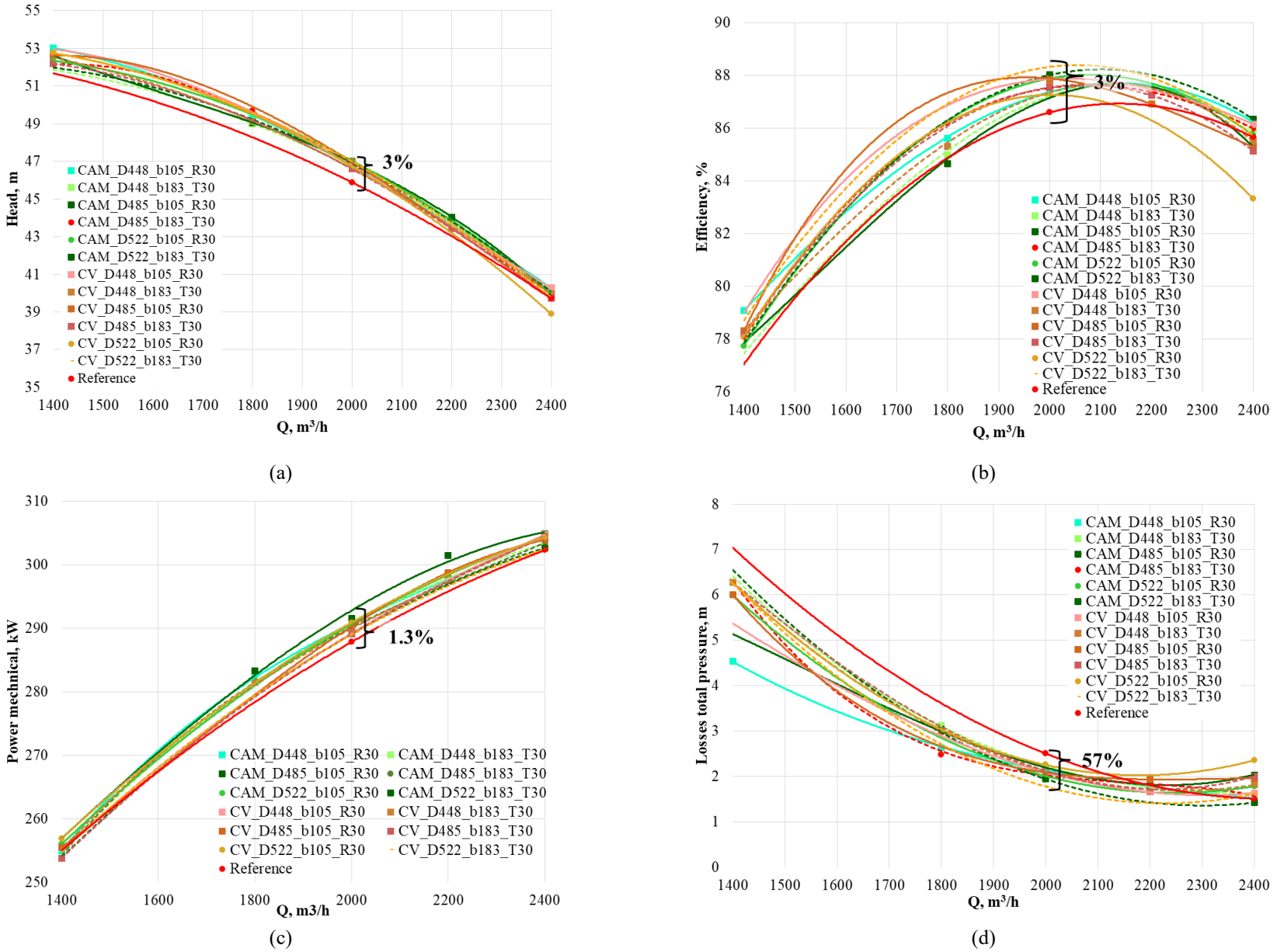

Figure 7.4 – Pump characteristics for different volute geometries (graph does not display all the investigated volutes for better readability, see complete graph Figure D.11): a) Head curves, b) Efficiency curves, c) Mechanical power curves, d) Total pressure losses curves

The volute cross-sectional shape is also important for efficiency. The maximum difference in efficiency between the models with round and trapezoidal volute shapes was 1.2% (Figure 7.3d). To increase efficiency, a larger b_3 value and a round volute cross-section should be selected. No systematic changes in the shape of the efficiency curve were observed with variations in D_3 or with the design method.

The optimal volute design for pump mode was selected using the Pareto front and the Utopia point distance method [123], based on two criteria: the highest efficiency and the smallest Q_{BEP} (Figure 7.5a). The Pareto-front data were normalised to the range 0-1, where 0 indicates the worst result and 1 the best result, using equations (22) and (23).

$$Q_{BEP} = \frac{Q_{BEP.max} - A}{Q_{BEP.max} - Q_{BEP.min}} \quad (22) \qquad Eff_{norm} = \frac{Eff - Eff_{min}}{Eff_{max} - Eff_{min}} \quad (23)$$

The Utopia point (Figure 7.5) represents the ideal solution with the maximum efficiency and the minimum Q_{BEP} of the efficiency curve. It has coordinates (1, 1). The minimum Euclidean distance from Eq. (24) identifies the volute with the best efficiency and Q_{BEP} performance.

$$d_i = \sqrt{(Eff_{norm,i} - 1)^2 + (Q_{BEP.norm,i} - 1)^2} \quad (24)$$

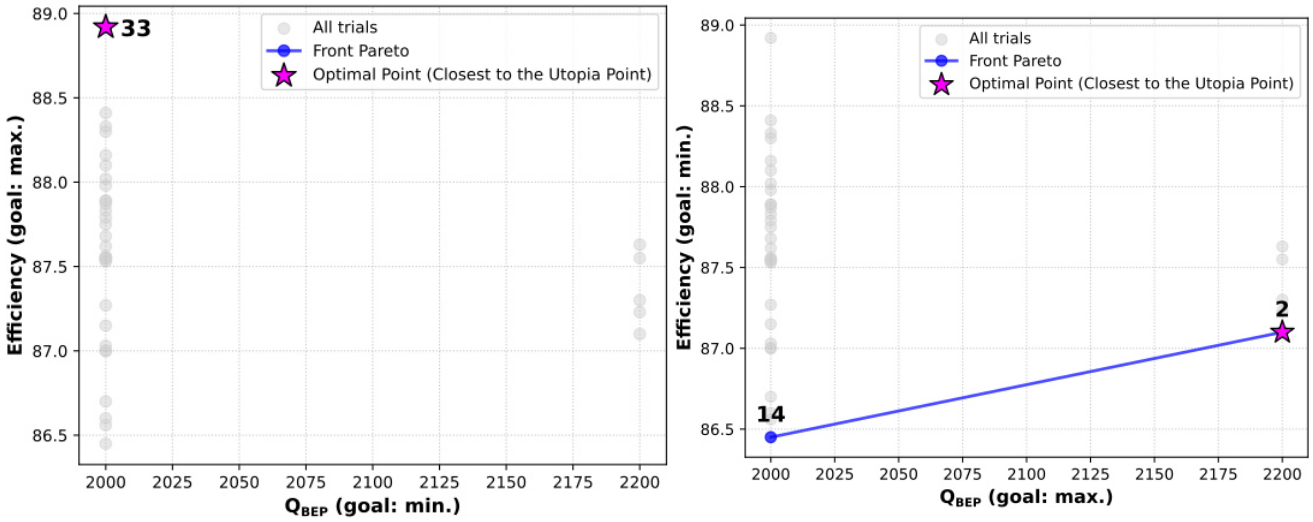

(a) Most favourable for pump

No.	Method	D_3	b_3	Shape	$Q_{BEP.T}$	$Eff.$	Utopia distance
33★	**CV★**	**522★**	**126★**	**R**	**2000★**	**88.9★**	**0.2★**

(b) Least favourable for pump

No.	Method	D_3	b_3	Shape	$Q_{BEP.T}$	$Eff.$	Utopia distance
2★	**CAM★**	**448★**	**105★**	**T★**	**2200★**	**87.1★**	**0.26★**

Figure 7.5 – Selection of the volute: a) most favourable for pump, least favourable for pump

According to the Figure 7.5, volute No. 33 was identified as the most favourable for pump mode, while volute No. 2 was identified as the least favourable.

Losses of Total Pressure

The round cross-section of the volute has an advantage over the trapezoidal one due to lower hydraulic losses, with the maximum difference between them reaching 0.6 m (30%) at. Lower losses are also obtained for volutes with a larger b_3, where the maximum difference between b_3 variants reached 0.7 m (28%) at $Q_{opt.p}$. Variations of D_3 and of the design method (CAM vs. CV) did not systematically affect head loss.

7.1.2.2 Turbine mode

The difference in operation parameters between models with various volutes is shown in Figure 7.7 and in Figure E.12. The analysis indicates that the design methods have a substantial effect on head. At a flow rate of 2400 m^3/h, the maximum difference between PATs with various volute designs is 29% for head, 5% for efficiency. For mechanical power it is 32%, while for hydraulic losses in volute is 63%. The reference volute shows the lowest performance.

Head, mechanical power, losses

The results show that increasing D_3 leads to higher head, mechanical power, and hydraulic losses, whereas increasing b_3 reduces these parameters. The CAM design method contributes to a reduction in head, mechanical power, but increases hydraulic losses. The cross-sectional shape has a smaller effect on the pump performance parameters. The trapezoidal shape increases hydraulic losses, as well as head and mechanical power.

Efficiency

A low D_3 value (448 mm) shifts the BEP towards higher flow rates (Q = 2500…2700 m^3/h). In contrast, a larger D_3 value (522 mm) shifts the BEP further to the lower flow rates by about 5% (Q = 2300 m^3/h), compared with the volute where D_3 is 448 mm. For the trapezoidal shape, the BEP shift is 2% compared to round shape. At the lowest flow rates, the highest efficiency was obtained for the volute designed using the CV method, which was on average 4% higher than that of the CAM method.

Parameter b_3 exhibits the opposite effect on the BEP displacement. Lower b_3 values (105 mm) place the BEP at the optimal flow rate, whereas higher b_3 values (183 mm) shift the BEP towards higher flow rates on 4%.

Among the analysed volutes, the most favourable and least favourable volute for PAT was selected using Pareto front (Figure 7.1).

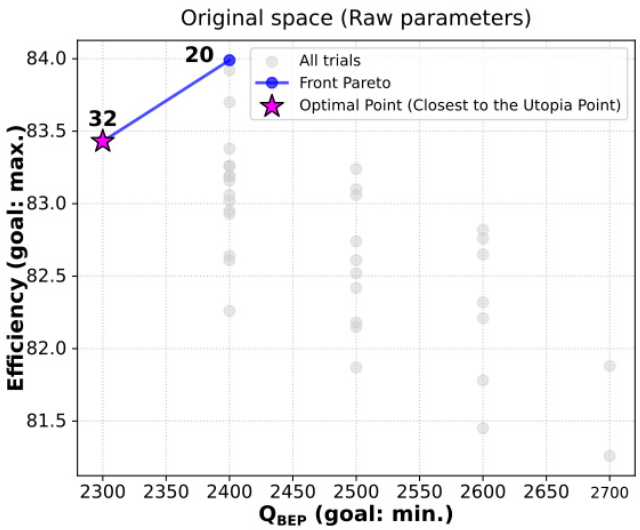

(a) Most favourable for PAT

No.	Method	D_3	b_3	Shape	$Q_{BEP.T}$	*Eff* .	Utopia distance
32★	**CV★**	**522★**	**105★**	**T★**	**2300★**	**83.4★**	**0.2★**

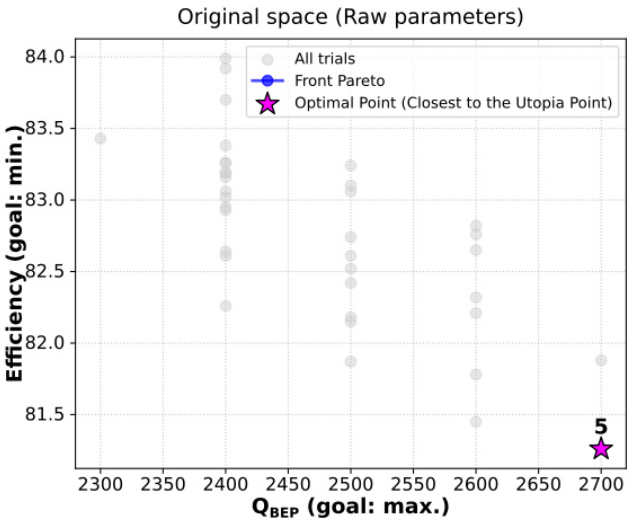

(b) Least favourable for PAT

No.	Method	D_3	b_3	Shape	$Q_{BEP.T}$	*Eff* .	Utopia distance
5★	**CAM★**	**448★**	**183★**	**R★**	**2700★**	**81.3★**	**0★**

Figure 7.6 – Selection of the volute: a) most favourable for PAT, least favourable for PAT

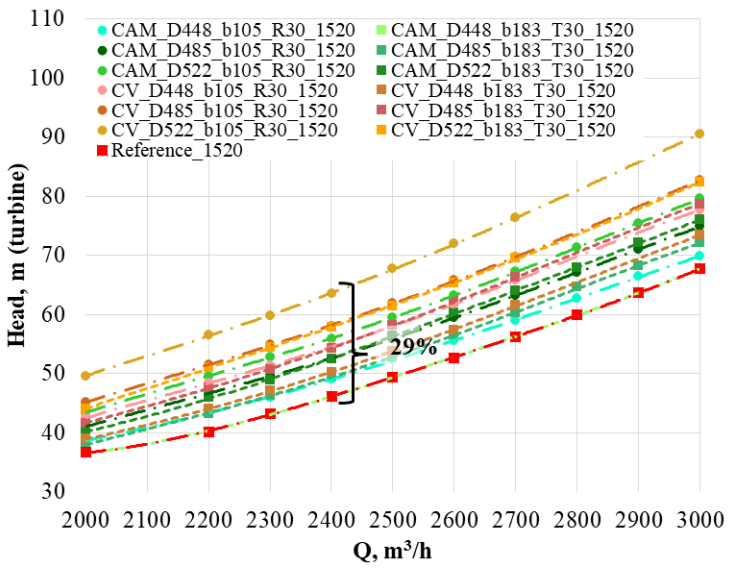

(a)

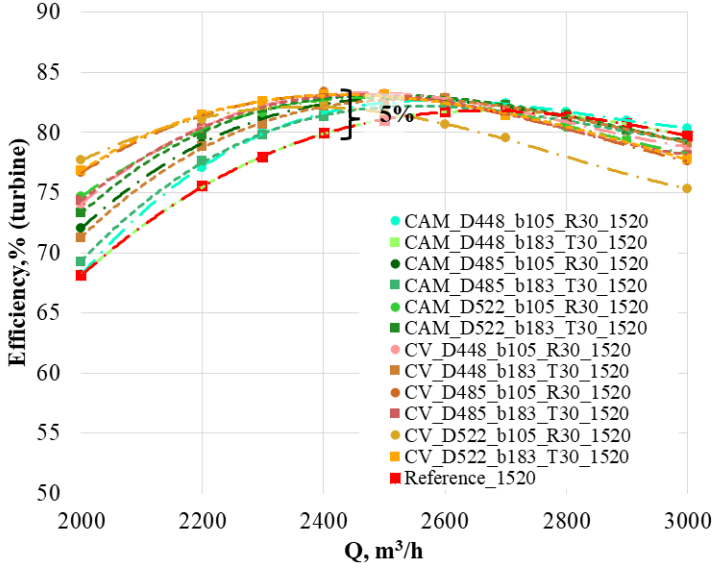

(b)

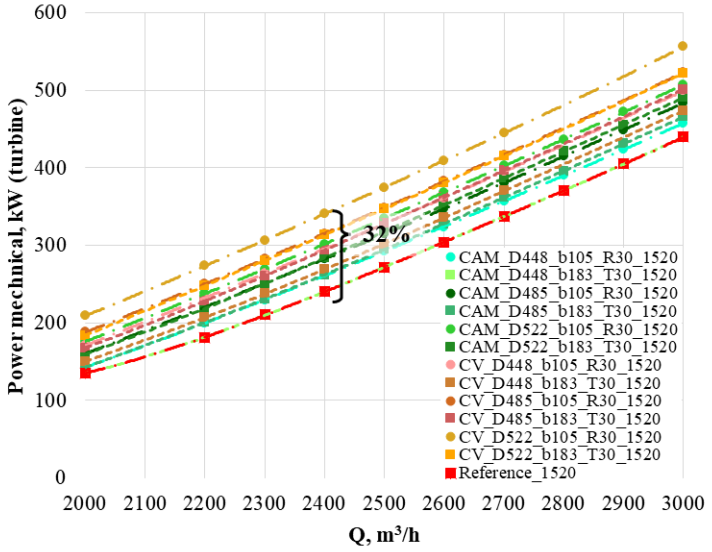

(c)

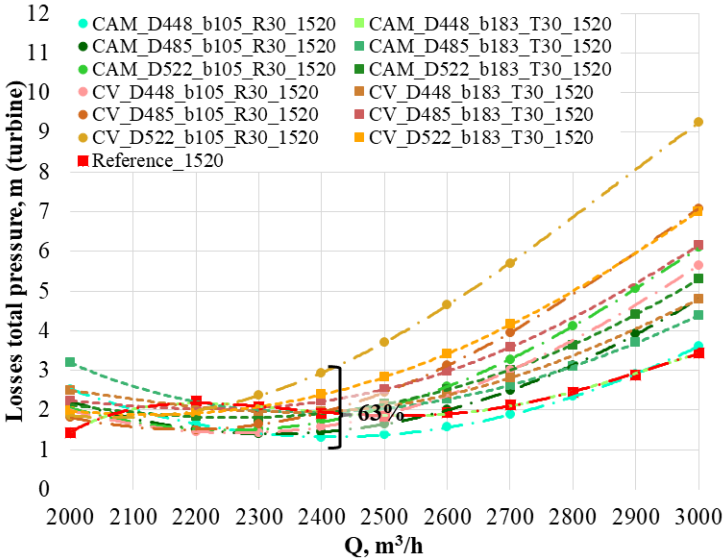

(d)

Figure 7.7 – PAT characteristics for different volute geometries (graph does not display all the investigated volutes for better readability, see complete graph Figure E.12): a) Head curves, b) Efficiency curves, c) Power mechanical curves, d) Total pressure losses curves

A more detailed comparison of the influence of geometric parameters on PAT efficiency is presented in Figure F.13 - Figure F.16 in Appendix F.

The flatness of the efficiency curve

To compare the "flatness" of efficiency curves the average deviation of the efficiency from its maximum value over the entire flow-rate range was evaluated. This was done by computing the area between the horizontal line at $\eta_{\max}$ and the measured curve *η(Q)* using the trapezoidal rule. The area was normalised by the width of the Q-range. As a result, the deviation from peak efficiency A was obtained using (25), where lower A values indicate flatter curves.

$$A = \frac{1}{Q_n - Q_1} \sum_{i=1}^{n-1} \frac{(\eta_{\max} - \eta_i) + (\eta_{\max} - \eta_{i+1})}{2} (Q_{i+1} - Q_i) \tag{25}$$

The quantity A represents the average decrease in efficiency relative to its maximum value over the entire investigated flow-rate range. It is a measure of the flatness of the efficiency curve.

Calculated results for all volutes are presented in Table 7.2. According to these data, the flattest efficiency curve is generally associated with the CAM design method and a round cross-sectional shape, although this trend is not observed in all cases. Overall, the CAM method and the round shape tend to flatten the curve, but they also shift the BEP towards higher flow rates. Table 7.9 shows a statistical analysis of the results reported in the table. Based on this analysis, the design method is identified as the most influential parameter.

Table 7.2 – Average deviation from peak efficiency A (Flatness)

Nr	max	Method	D_3	b_3	Shape	Nr	A_{max}	Method	D_3	b_3	Shape	Nr	A_{max}	Method	D_3	b_3	Shape
37	0.46	CAM	522	183	Round	24	0.69	CAM	448	105	Round	11	1.54	CV	485	105	Trapezoidal
2	0.53	CAM	522	126	Round	28	0.70	CAM	448	126	Trapezoidal	13	1.58	CV	522	126	Round
4	0.57	CAM	448	126	Round	26	0.71	CAM	485	126	Round	15	1.64	CV	522	183	Trapezoidal
6	0.58	CV	485	183	Round	30	0.71	CAM	448	105	Trapezoidal	17	1.69	CV	448	126	Trapezoidal
8	0.59	CV	448	126	Round	32	0.74	CAM	448	183	Trapezoidal	19	1.71	CV	485	126	Trapezoidal
10	0.60	CAM	522	183	Trapezoidal	34	0.77	CV	448	183	Round	21	1.75	CAM	522	126	Trapezoidal
12	0.62	CAM	448	183	Round	36	0.86	CV	448	183	Trapezoidal	23	1.83	CV	485	105	Round
14	0.62	CAM	485	183	Trapezoidal	1	1.30	CV	522	105	Trapezoidal	25	1.89	CV	485	126	Round
16	0.63	CAM	485	105	Round	3	1.43	CV	522	126	Trapezoidal	27	1.91	CAM	485	105	Trapezoidal
18	0.64	CV	448	105	Round	5	1.45	CV	522	105	Round	29	2.01	CV	448	105	Trapezoidal
20	0.65	CAM	485	183	Round	7	1.51	CV	522	183	Round	31	2.08	CAM	522	105	Round
22	0.69	CAM	485	126	Trapezoidal	9	1.54	CAM	522	105	Trapezoidal	33	2.12	CV	485	183	Trapezoidal
												35	3.11	Reference	485	245	Reference

The analysis of the optimal volute design, based on the criteria of the highest efficiency and the flattest efficiency curve, was carried out using the Pareto front (Figure 7.8) and the Utopia point distance method [123]. The Pareto-front data were normalised to the range 0-1, where 0 indicates the worst result and 1 the best result, using equations (26) and (1).

$$Flat_{norm} = \frac{A_{max} - A}{A_{max} - A_{min}} \tag{26}$$

$$Eff_{norm} = \frac{Eff - Eff_{min}}{Eff_{max} - Eff_{min}} \tag{27}$$

The minimum Euclidean distance (28) identifies the point corresponding to the pump volute with the best combined performance in terms of efficiency and flatness.

$$d_i = \sqrt{(Eff_{norm,i} - 1)^2 + (Flat_{norm,i} - 1)^2} \tag{28}$$

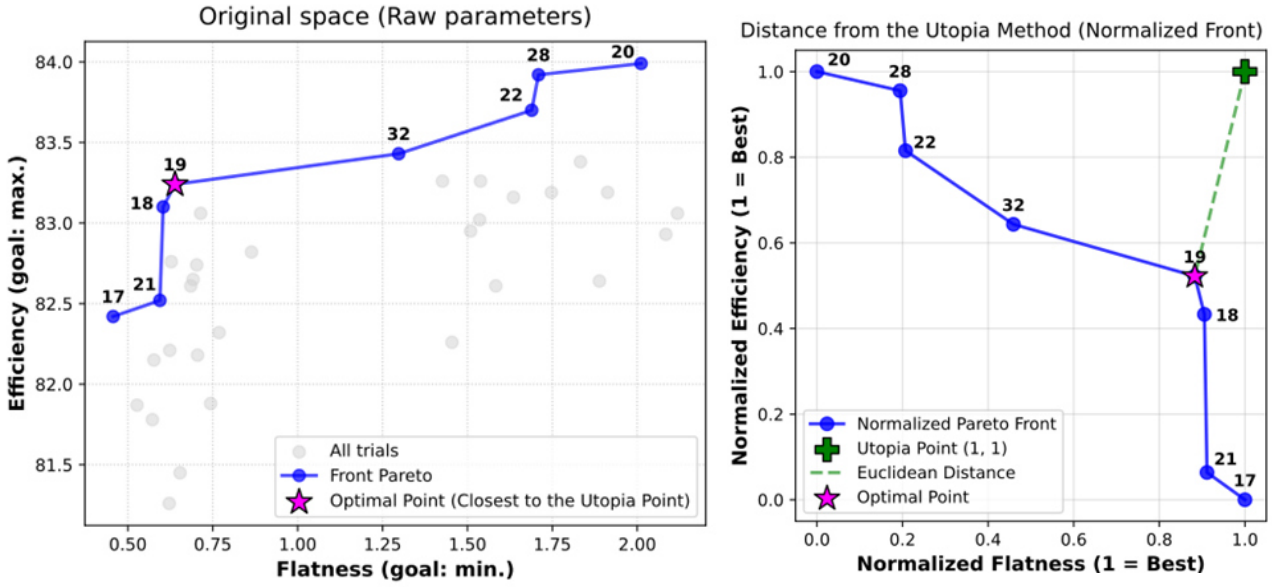

(a) (b)

No.	Method	D_3	b_3	Shape	Flatness	Efficiency	Utopia Distance
19	**CV★**	**448★**	**105★**	**Round★**	0.64	83.2	**0.49 ★**
18	CAM	522	183	Trapezoidal	0.60	83.1	0.57
32	CV	522	105	Trapezoidal	1.3	83.4	0.65

Figure 7.8 – Selection of the flattest curve with high efficiency: a) Pareto front, b) Utopia point distance

According to the presented data, the pump with the volute that has the flattest efficiency curve, and at the same time the highest efficiency under the given conditions, is volute No. 19 (Utopia Distance = 0.49). A larger Euclidean distance is obtained for the pump with the volute No. 18 (Utopia Distance = 0.57) and for the pump with the volute No. 32 (Utopia Distance = 0.76).

Overall, the CAM method combined with a round cross-section gives the flattest efficiency curves. However, when the maximum efficiency and the flatness of the efficiency curve are considered together, the CV method with a smaller base-circle diameter and a narrow inlet gives a better compromise. The cross-sectional shape has a secondary influence, because several trapezoidal variants reach efficiency values similar to those obtained for round variants. This result confirms that a compromise volute geometry can combine high maximum efficiency with stable operation over a wide flow-rate range.

Overall, the CAM method combined with a round cross-section produces the flattest efficiency curves; however, when peak efficiency is considered jointly with flatness, the CV method with a small base-circle diameter and a narrow inlet emerges as the better compromise. The choice of cross-sectional shape plays a secondary role, with several trapezoidal variants reaching efficiency levels comparable to the round ones. This finding supports the existence of a compromise volute geometry combining high peak efficiency with operational flexibility across a wide flow-rate range.

7.1.3 Selection of the compromise volute casing for pump and turbine operation mode

Using the Pareto front, the volute design providing the compromise between operation in turbine and pump mode was identified (Figure 7.9). The optimal point was selected based on a four-criteria Pareto analysis. The following criteria were considered: maximization of efficiency in pump mode, maximization of efficiency in turbine mode, minimization of the flow rate at the BEP in pump mode ($Q_{BEP.P}$), and minimization of the flow rate at the BEP in turbine mode ($Q_{BEP.T}$).

Volute CV_D522_b105_T30 (No. 32) was found to be the most favourable solution, with a Utopia distance of 1.08. Slightly less favourable, but still close to the best solution, were volute CV_D485_b105_R30, (No. 25) and volute CV_D448_b126_T30 (No. 22), with a Utopia Distance of 1.18. The obtained results indicate a clear tendency that the CV design method is the best approach for finding a compromise in efficiency between pump mode and turbine mode. The least favourable solution is CAM_448_183_R30 (No. 5) with a Utopia distance of 1.85.

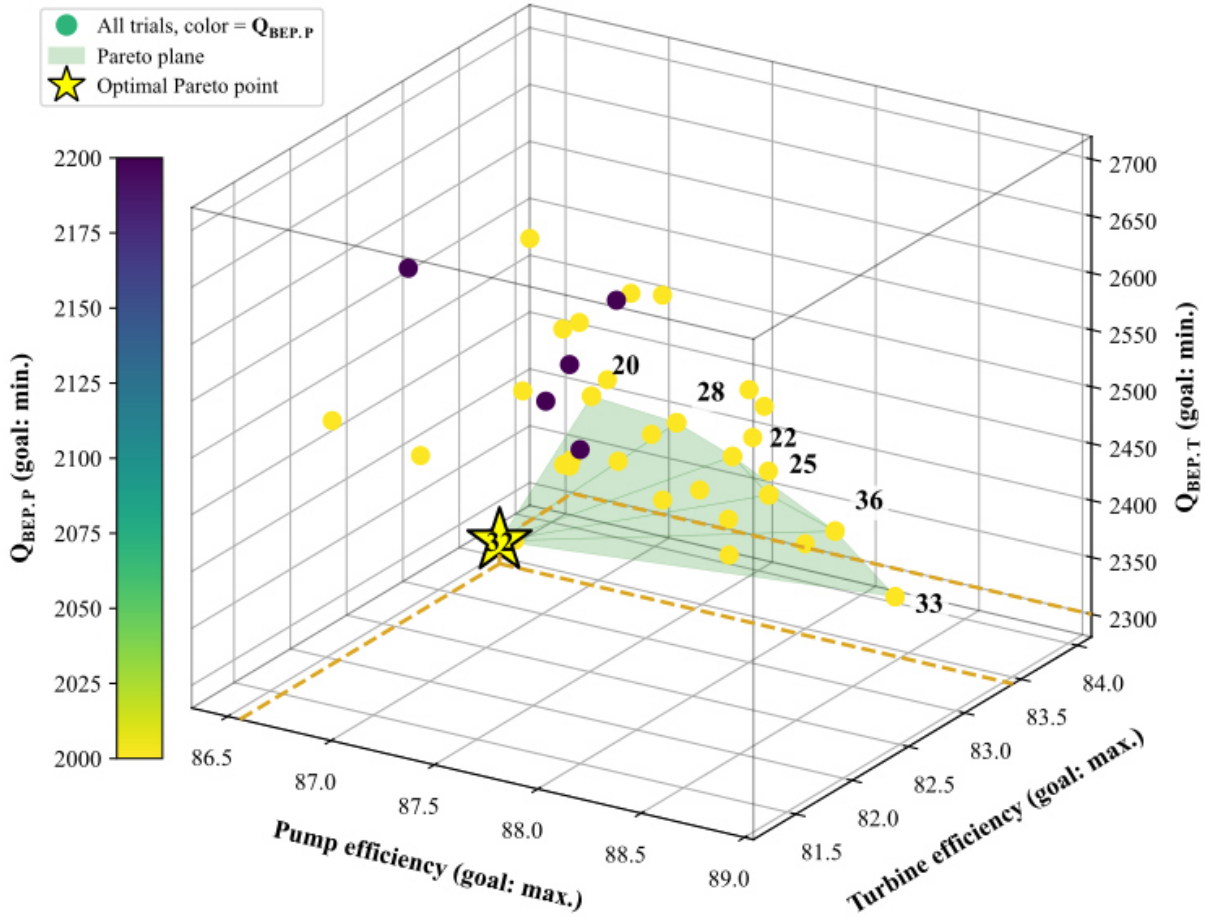

No.	Method	D_3	b_3	Shape	Pump Eff.	Turbine Eff.	$Q_{BEP.P}$	$Q_{BEP.T}$	Utopia Distance
32 ★	**CV** ★	**522** ★	**105** ★	**T** ★	**86.6** ★	**83.4** ★	**2000** ★	**2300** ★	**1.08** ★
25	CV	485	105	R	87.9	83.4	2000	2400	1.18

Figure 7.9 – Selection of the favourable volute design for pump and turbine modes (Pareto front)

7.1.4 Hydrodynamic analysis

7.1.4.1 Analysis of the selected volutes

Based on the analysis presented in Sections 7.1.1.2 and 7.1.3 the volutes listed in Table 7.3 were selected for further analysis.

Table 7.3 – Representative volute variants selected for further analysis

No.	Volute design category	Method	D_3	b_3	Shape	Selection criteria
32	Most favourable performance in turbine mode	CV	522	105	Trapezoidal	Max. efficiency with smallest Q_{BEP}
19	Flattest efficiency curve in turbine mode	CV	448	105	Round	Max. efficiency and the max. flatness of the efficiency curve
32	Compromise solution for both pump and turbine operation	CV	522	105	Trapezoidal	Max. efficiency with smallest Q_{BEP} for pump and PAT
25		CV	485	105	Round	
5	Least favourable performance in turbine mode	CAM	448	183	Round	Min. efficiency with higher Q_{BEP}

According to the Pareto Front the best compromise solution is volute No. 32 (Utopia distance 1.08). At the same time this volute is the most favourable for turbine operation. In order to extend the analysis it was decided to additionally analyse volute No. 25. This volute is not the optimal point in the Pareto plot, but ranks second (Utopia distance 1.18). In the following sections, volute No. 25 is called the compromise variant.

The pump with the above-mentioned volutes is compared with the corresponding pumps operating in pump mode in Figure 7.10.

The comparison of the volutes in the Figure 7.10 shows that, in pump mode, the differences in efficiency and head are smaller than in turbine mode. In PAT mode, the maximum shift of the BEP towards higher flow rates for the selected volutes reaches 15%, whereas in pump mode this value is 9%. Similarly, the difference in head reaches 31% in PAT mode and 1.5% in pump mode

In pump mode efficiency curve of most favourable volute decreases sharply at high flow rates compared with the other volutes. The least favourable volute for PAT has a flatter efficiency curve than the most favourable volute for PAT.

The influence of the volute geometry on PAT performance can be interpreted through the Euler equation for turbomachines, which relates the theoretical specific work to the change of angular momentum across the impeller. For a centrifugal machine operating in turbine mode, the theoretical head is given by $H_{th} = u_1 \cdot c_{u1} - u_2 \cdot c_{u2}/g$, where indices 1 and 2 refer to the impeller inlet and outlet, respectively. Since the volute geometry directly determines the velocity field at the impeller inlet, c_{u1} is the primary link through which volute design influences the head and, consequently, the efficiency of the PAT.

A graphical illustration of the velocity triangles for other PATs is presented in Figure G.20, Figure G.23 (Appendix G). The greatest influence on c_u is observed for D_3, b_3, and the design method. Increasing D_3 and selecting the CV method increase c_u, whereas increasing b_3 decreases it. The statistical analysis of the influence of volute geometry on changes in c_u is presented in 7.2.3.

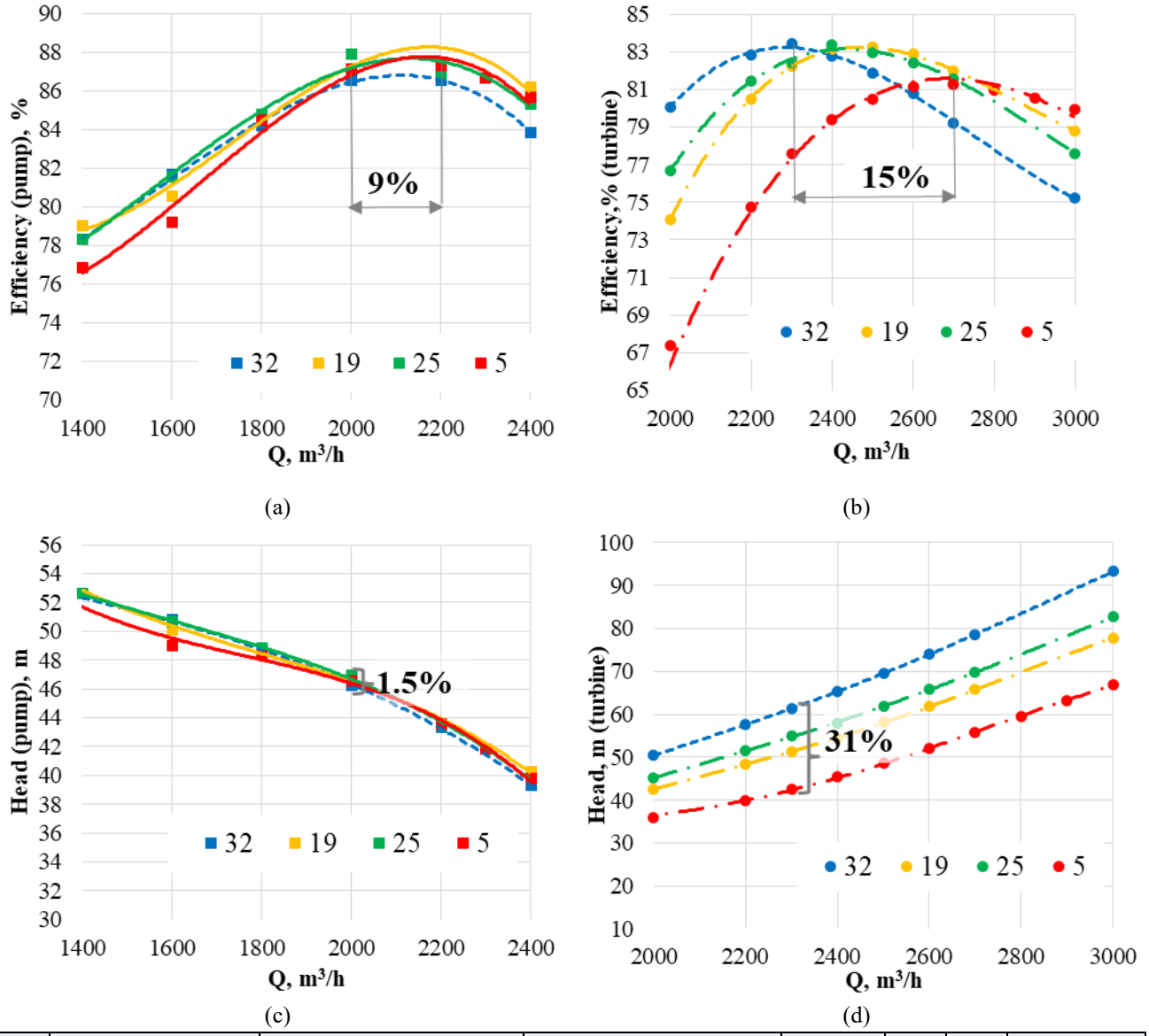

No.	Volute design category	Turbine mode		Pump mode		Method	D_3	b_3	Shape
		$Q_{BEP.T}$, m³/h	Efficiency at $Q_{BEP.T}$, %	$Q_{BEP.P}$, m³/h	Efficiency at $Q_{BEP.P}$,%				
32	Most favourable	2300	83.4	2000	86.6	CV	522	105	Trapezoidal
19	Flattest	2500	83.2	2000	87.9	CV	448	105	Round
25	Compromise solution	2400	83.4	2000	87.9	CV	485	105	Round
5	Least favourable	2700	81.3	2200	87.3	CAM	448	183	Round

Figure 7.10 - Performance curves for selected volutes: a) pump efficiency, b) PAT efficiency, c) pump head, b) turbine head

The distribution of the absolute velocity components at the impeller inlet (D_2) in the PAT for the volutes selected in the previous sections is shown in Figure 7.11. A higher value of c_u contributes to an increase in efficiency and head. For the PAT with the most favourable volute (blue curves), the highest value of c_u is observed. In contrast, the lowest value is found for the least favourable volute (red curves). The values of c_u for the PAT with the compromise volute (green curves) and the flattest volute (orange curves) are quite similar.

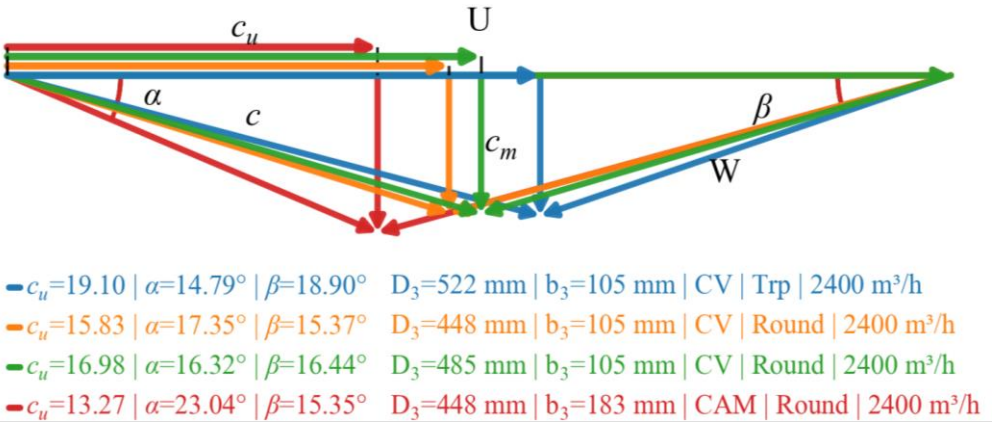

Figure 7.11 - Distribution of the absolute velocity components for PAT with selected volutes at 2400 m^3/h

A graphical illustration of the velocity triangles for other PATs is presented in Appendix G.

Changes in c_u are not the only factor affecting the shape of the characteristic curve, although their systematic influence can be clearly observed. For a complete assessment, the influence of the tongue and changes in the side wall gap geometry should also be included in the analysis. However, these issues are beyond the scope of this dissertation and may be addressed in future research.

7.1.4.2 Flow field visualization and analysis

This section analyses of the flow distribution in pump and PAT presented only for selected volutes, which represent the most significant changes in the flow structure and are of the greatest interest from the point of view of their operating parameters:

- the most favourable volute for PAT No. 32 (CV_D522_b105_T30),
- least favourable volute for PAT No. 5 (CAM_D448_b183_R30),
- compromise volute No. 25 (CV_D485_b105 _R30).

An analysis of the flow inside the volute in the PAT, shows that absolute velocity gradually from volute inlet to outlet with corresponds to the increase in flow rate. It can be observed that at the same flow rate, the absolute velocity (Figure 7.12) near the impeller inlet (D_2) is higher for PAT with the most favourable volute than for the PAT with the least favourable volute. This difference is mainly connected with increasing of c_u. The pressure distribution remains relatively in both volutes (Figure 7.13). Moreover, a distinct trace of the fluid motion, characterised by lower velocity and total pressure values and originating from the volute tongue, can be observed.

The same analysis was carried out for the pump operating in pump mode with the same volute geometries (Figure 7.13). For both volutes No. 32 and No. 5, the velocity and pressure distributions are markedly less uniform in pump mode than in turbine mode (Figure 7.13 and Figure 7.15), with the asymmetry being most pronounced for variant No. 32.

At the lowest analysed flow rate (Q = 1400 m^3/h, Figure 7.13), the absolute velocity near the impeller outlet is higher than at higher flow rates for the same variants. This is a typical off-design effect. At low flow rate, the flow is not sufficient to fill the expanding volute cross-section uniformly. As a result, the main stream is concentrated near the inner part of the passage, where the fluid keeps the highest tangential momentum from the impeller. The outer part of the passage becomes a zone of weak or recirculating flow.

The static pressure distribution confirms this behaviour. The pressure is lower near the impeller in the 45˚ –225˚ sector and increases at larger radii, where the velocity is lower (Figure 7.15).

It should be noted that the local increase in c_u in the inner part of the passage at low Q does not improve pump performance. The recirculation in the outer part of the passage causes additional friction and mixing losses. These losses are greater than the local benefit of higher c_u, which is reflected in the lower pump-mode efficiency obtained for these variants.

A non-uniform distribution of velocity and pressure can be observed in the region near the volute inlet, together with flow separation from the volute tongue. This phenomenon is present in both volutes and may occur either in the diffuser region or within the 0˚ – 90˚ sector of the volute. Worse performance in pumping mode may be explained by the fact that these volutes are oversized relative to the pump and were designed for higher flow rates.

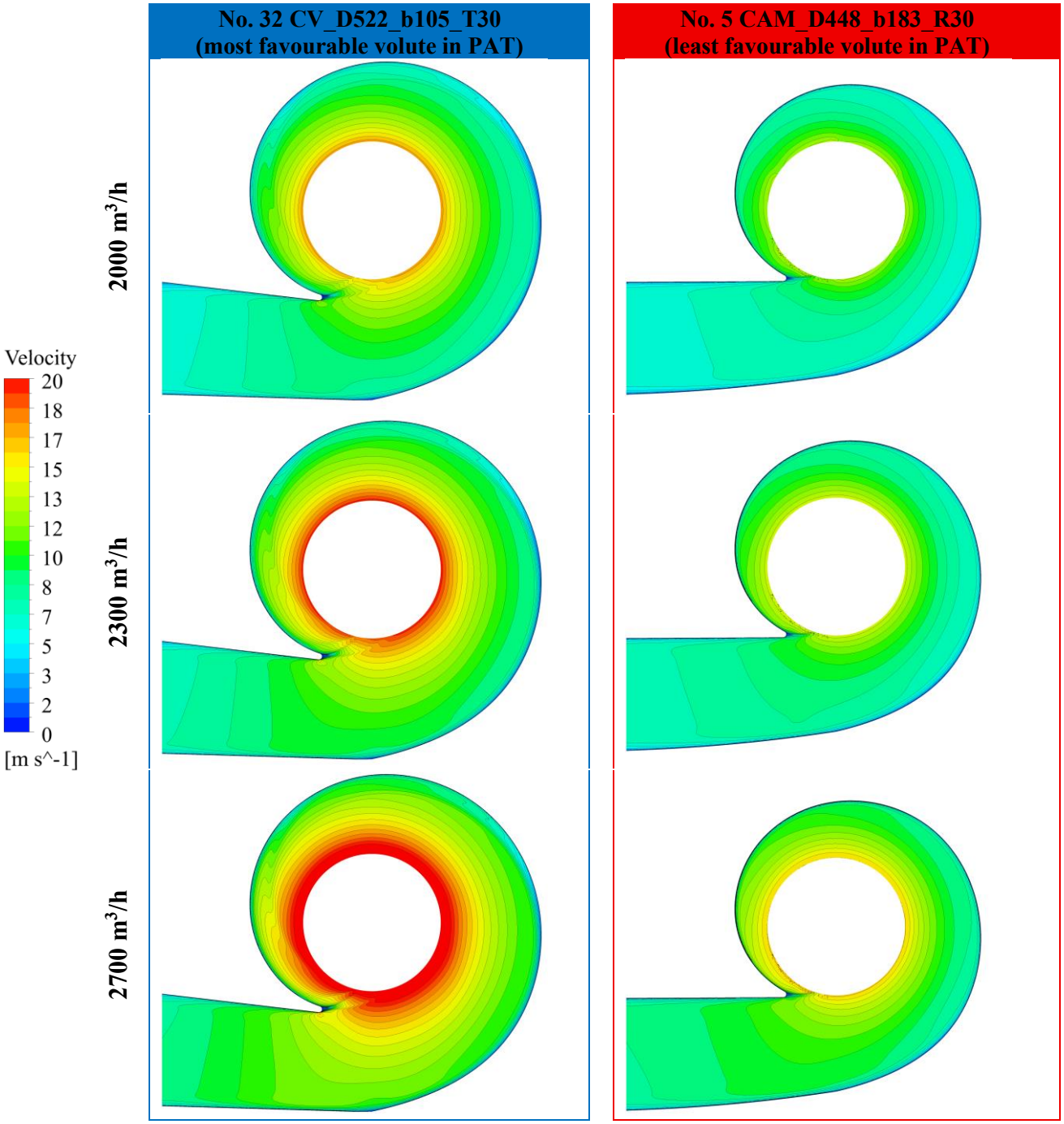

Figure 7.12 – Distribution of absolute velocity at the longitudinal cross-sectional plane in the PAT under different Q

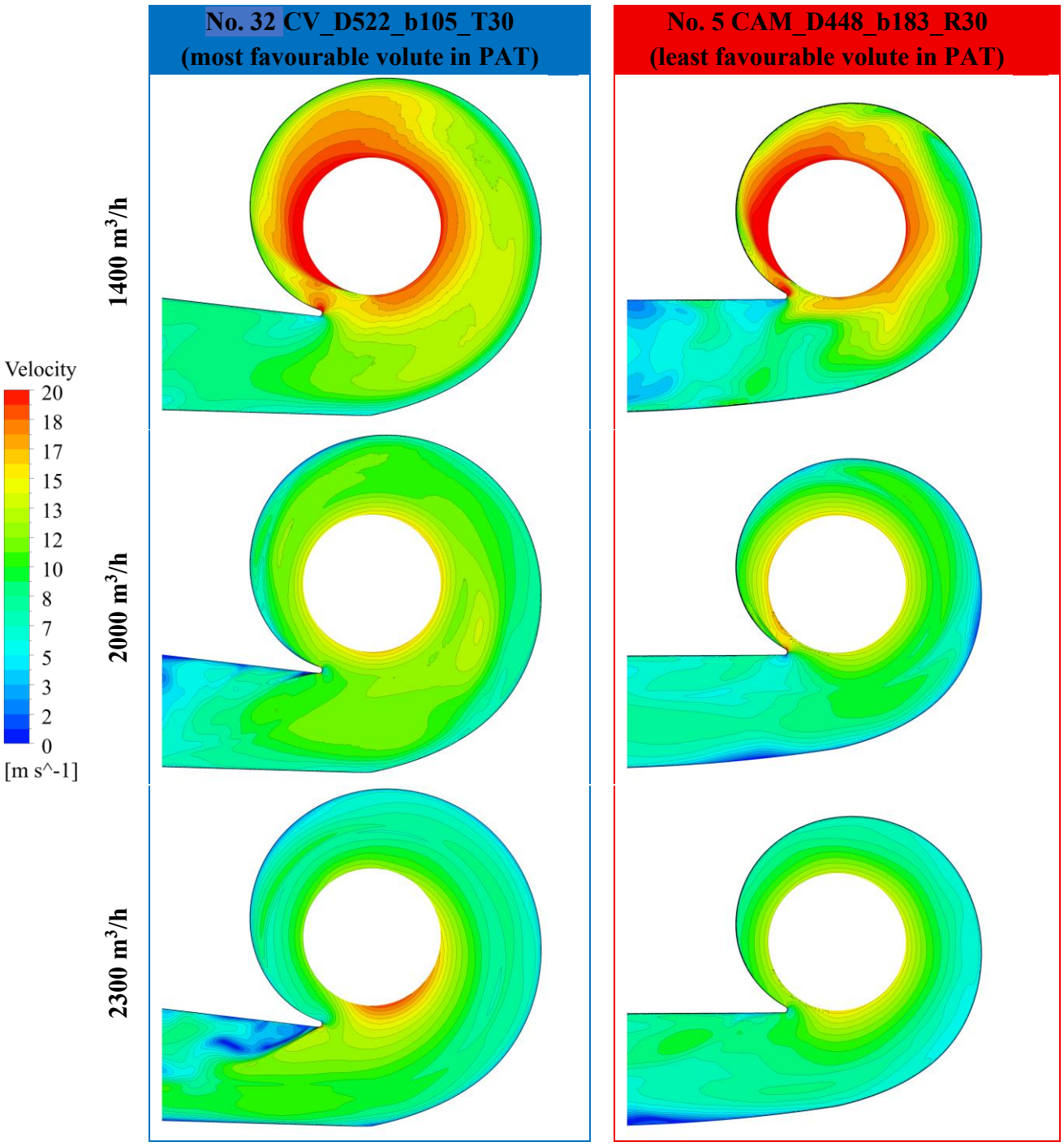

Figure 7.13 – Distribution of absolute velocity at the longitudinal cross-sectional plane in the pump under different flow rates

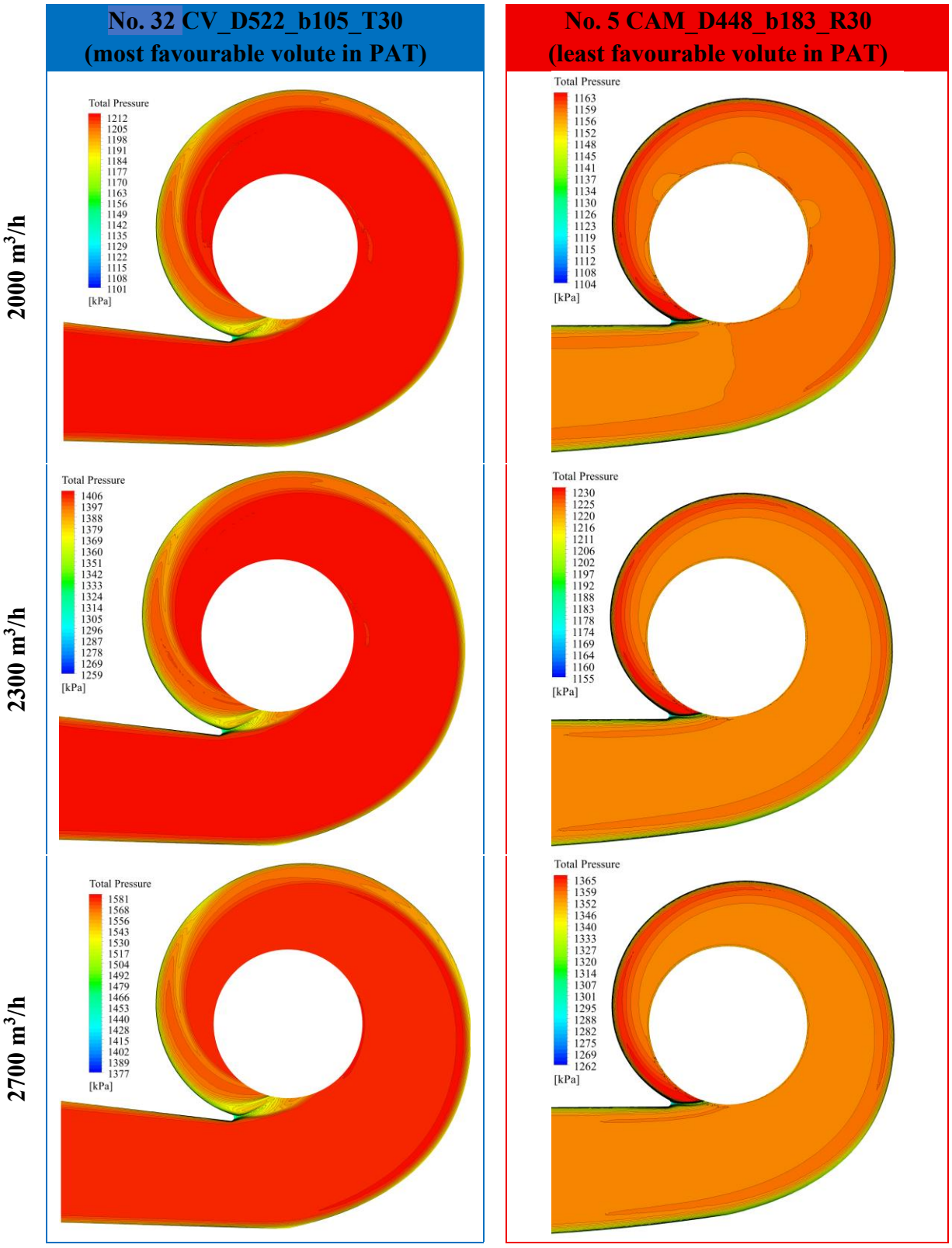

Figure 7.14 – Distribution of total pressure at the longitudinal cross-sectional plane in the PAT under different flow rates

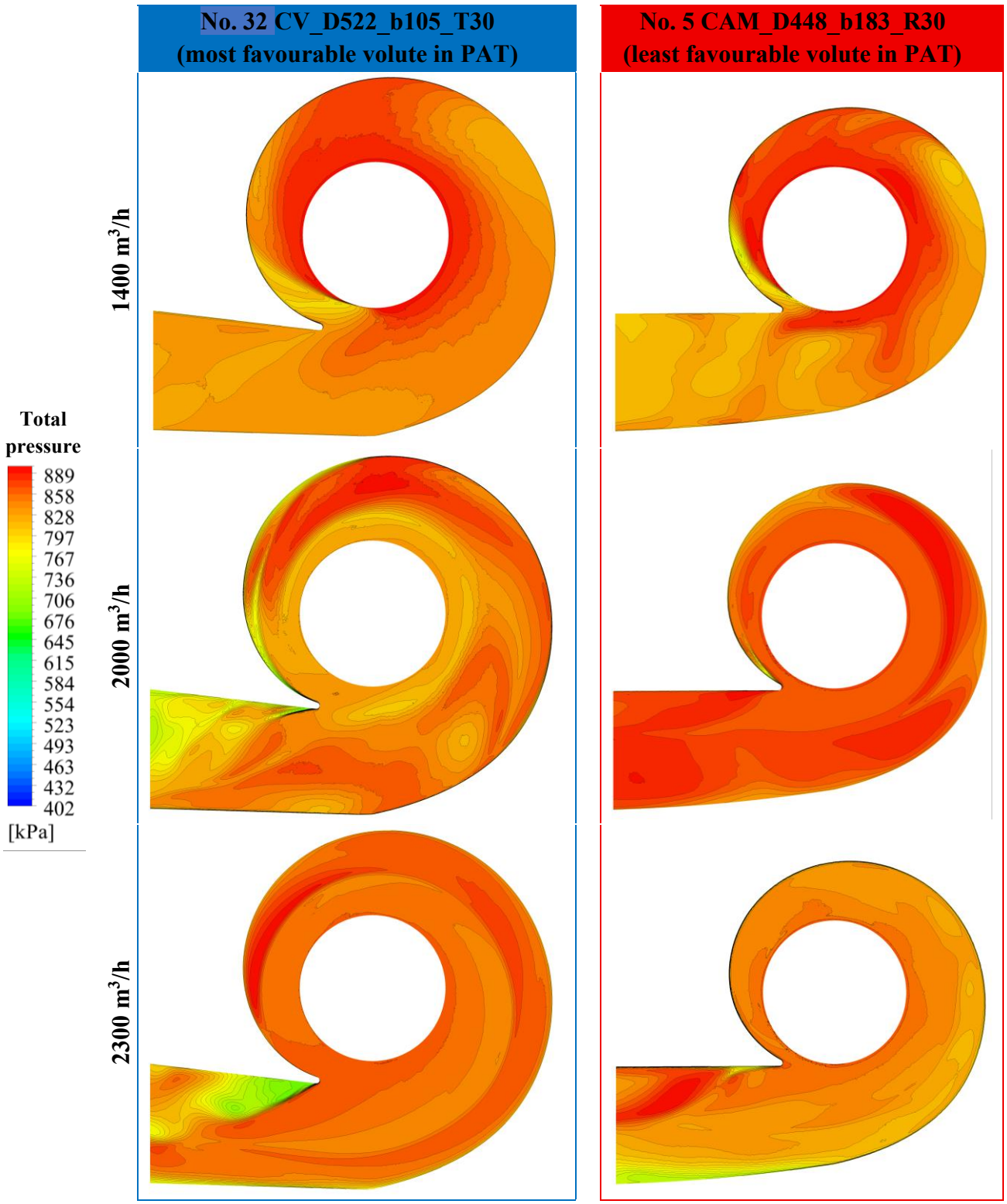

Figure 7.15 – Distribution of total pressure at the longitudinal cross-sectional plane in the pump under different flow rates

In PAT operation, the volute guides the flow into the impeller. Therefore, it affects the formation of secondary flow structures and vortices inside the blade channels. Figure 7.16 shows the flow structure in the impeller at the BEP of each mode: Q = 2000 m^3/h in pump mode and Q = 2300 m^3/h in PAT operation. The results are shown for volute No. 32, identified as the most favourable for PAT operation, and volute No. 5, identified as the least favourable for PAT operation.

For the impeller with volute No. 32, no significant vortical structures are observed in the blade channels in PAT operation. In contrast, the impeller with volute No. 5 shows strong vortices in the blade channels at the same flow rate. These vortices become weaker as the flow rate increases. Additional streamline visualisations for other variants and operating points are provided in Appendix H.

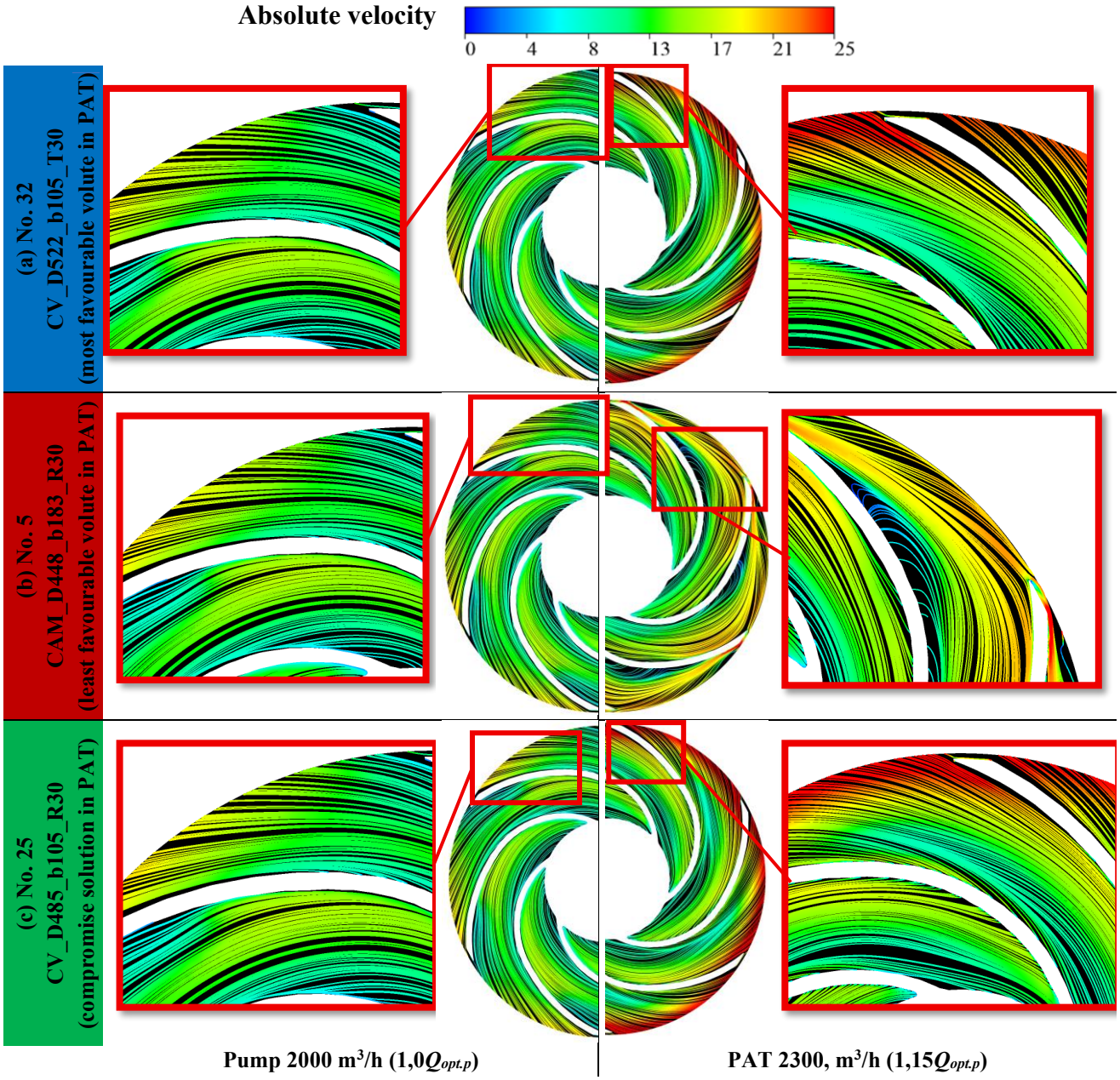

Figure 7.16 – Flow streamlines inside the pump impeller at Q = 2000 m^3/h, PAT impeller at Q = 2300, m^3/h

In pump mode, the flow pattern in the impeller is uniform for all analysed volutes and remains almost unchanged between variants. This difference confirms observations: the impeller flow field is much more sensitive to volute geometry in turbine mode than in pump mode.

The total pressure distribution in the impeller, in both pump and PAT operation, is presented in Figure 7.17. The total pressure increases with the flow rate and, in PAT mode, with the developed head. For variant No. 32 at Q = 2300 m3/h, the total pressure in the impeller inlet region at D_2 is higher than for variant No. 5 at the same flow rate. This is consistent with the higher pressure recovery in the volute of variant No. 32.

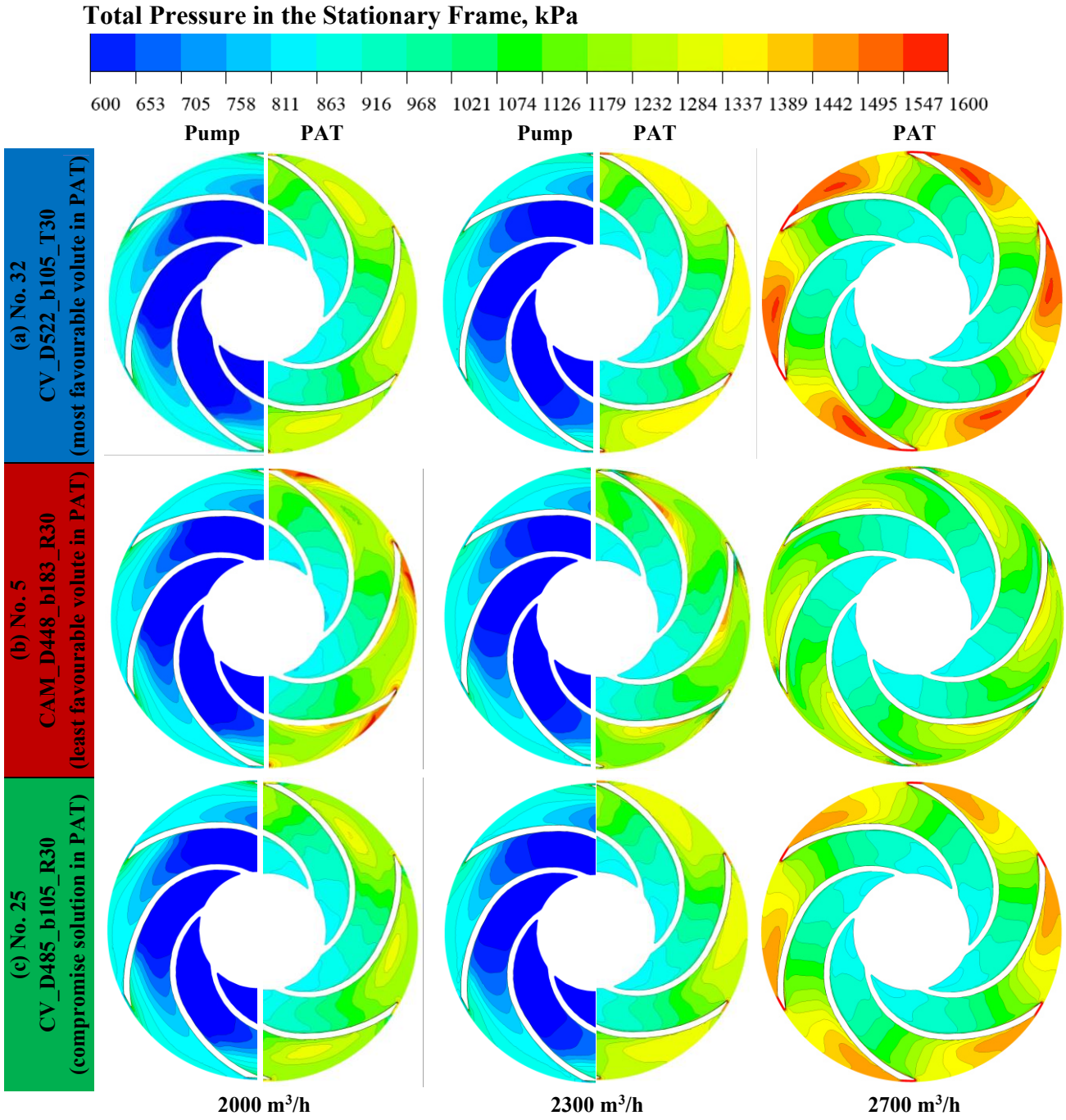

Figure 7.17 – Distribution of total pressure at the impeller in the pump and PAT under different flow rates

Local regions of increased pressure are also visible on the blade pressure side. These regions are related to a non-zero incidence angle of the incoming flow relative to the blade leading edge. The compromise variant No. 25 gives a pressure distribution close to that observed for the most favourable variant No. 32. In pump mode, the pressure distribution in the impeller is almost insensitive to volute geometry. This confirms, at the level of internal flow fields, the asymmetry already observed in the integral performance curves.

One of the key parameters affecting PAT efficiency is the flow angle α, at which the liquid enters the impeller blades at D_2. However, the mean value of α alone is not sufficient to fully describe the inlet flow conditions. The uniformity of α across the impeller inlet passage is also important, as well as the homogeneity of the flow over the whole passage width, between the front and back shrouds. Another important factor is the alignment of the incoming flow with the blade leading edges, which determines how close the flow is to shock-free entry conditions.

Figure 7.18 presents the flow structure in the PAT volute at cross-section Pl 180.

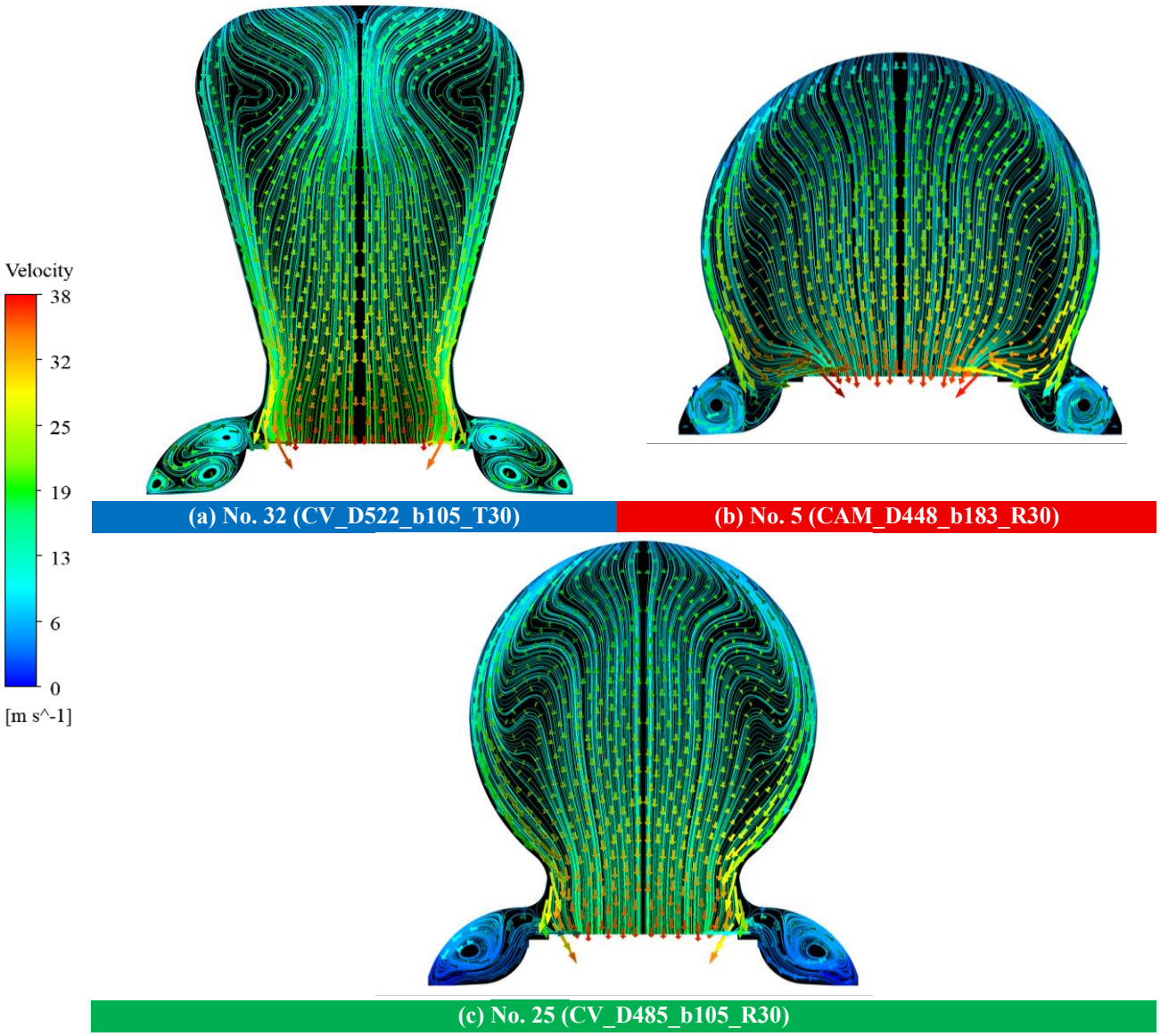

Figure 7.18 – Flow structure in the PAT volute cross-section Pl 180 at Q = 2300 m³/h: a) No. 32, b) No. 5, c) No. 25

Figure 7.18a shows that the variant with a narrow inlet b_3 (105 mm) and a trapezoidal cross-section guides the flow more uniformly towards the impeller, despite the presence of two symmetrical vortices in the upper part of the volute. In contrast, the wide variant (b_3 = 183 mm) gives a more uniform flow structure in the central and upper parts of the volute cross-section (Figure 7.18b). However, the flow slows down near the side walls of the volute because recirculation zones are formed there. As a result, the flow changes direction before entering the impeller, which worsens the inflow conditions at the impeller inlet passage.

The compromise variant (Figure 7.18c, b_3 = 105 mm, D_3 = 485 mm) shows a more disturbed flow structure near the side regions of the volute than variant No. 32 (b_3 = 105 mm, D_3 = 522 mm). This is related to its smaller diameter and shorter circumferential development length. However, this variant supplies the flow to the impeller passage with similar directional uniformity. This explains its good PAT performance, even though the flow field in the volute itself is less developed.

The flow distribution in the same volute geometries operating in pump mode is presented in Figure 7.19.

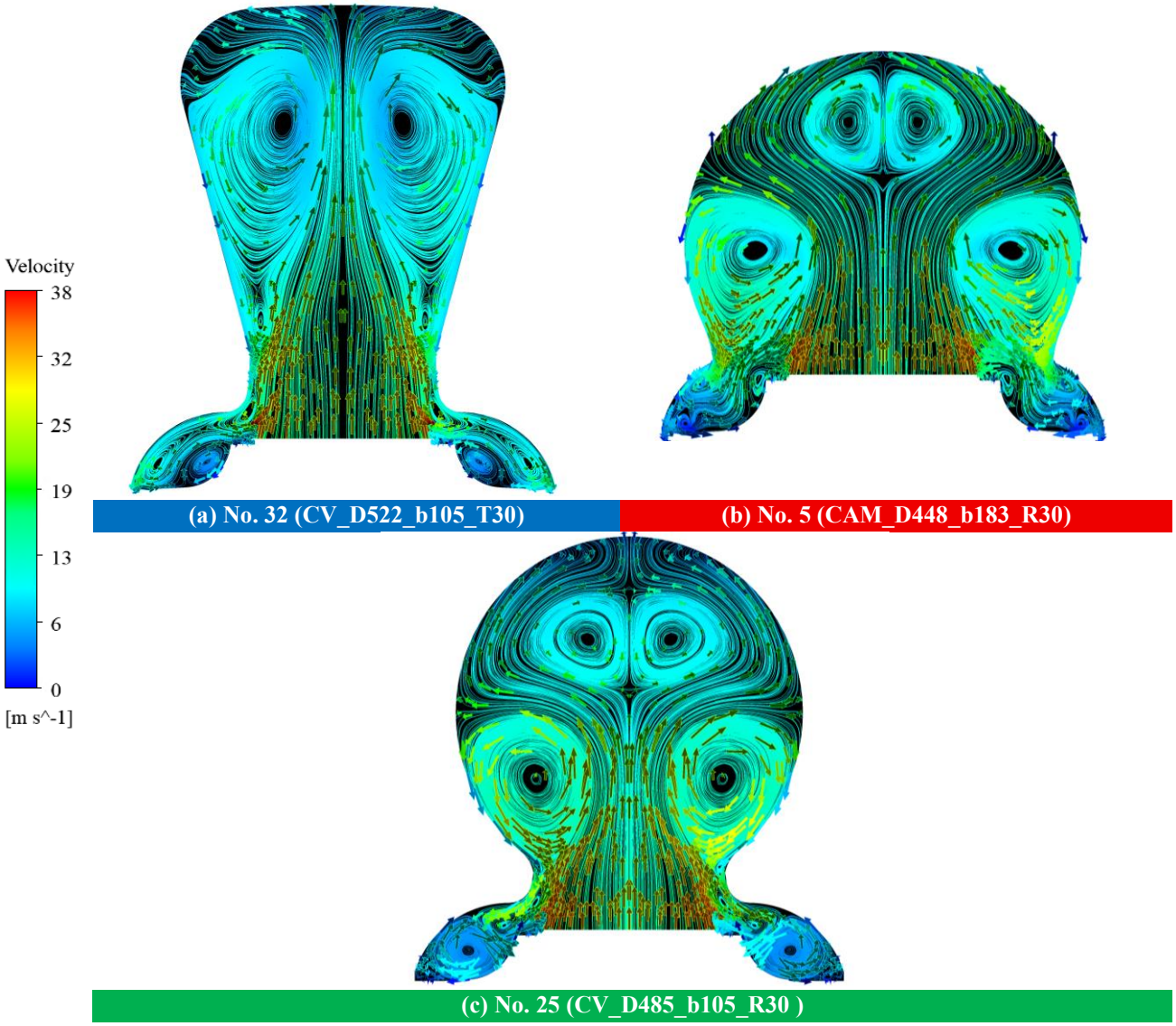

Figure 7.19 – Flow structure in the pump volute cross-section Pl 180 at Q=2000 m³/h: a) No. 32, b) No. 5, c) No. 25

In PAT operation, the flow enters the impeller in a relatively organised way. In pump mode, however, the volute cross-section shows strong non-uniformity, with large recirculation zones in the upper and side regions of the passage. The main flow leaves the impeller in the radial direction and moves towards the outer wall of the volute. After reaching this wall, it splits into two symmetrical side vortices. These vortices indicate flow separation from the side walls of the volute cross-section and locally lower velocity values, especially in the outer regions of the passage.

The flow pattern shows that the volute identified as the most favourable volute for turbine operation No. 32 (Figure 7.18a) shows poorer performance in pump mode (Figure 7.19a) and flow structure at cross-section Pl 180. The pump has a maximum efficiency only of 86.5% at Q_{opt}, and it decreases quickly (83.6%) as Q increases to 2400 m^3/h (Figure 7.10a). The flow is strongly elongated in the vertical direction. Two large symmetric vortices occupy the upper part of the section, while additional low-velocity recirculation zones are formed near the lower side regions. The main flow is concentrated in the central part of the cross-section, which suggests a relatively non-uniform velocity distribution.

In contrast, the variant identified as the least favourable for turbine operation, variant No. 5 (Figure 7.18b) demonstrates better performance in pump mode. Its efficiency is 87,3% at Q_{opt} and 85,6% at $1{,}2Q_{opt}$. The flow field is dominated by several distinct recirculation structures distributed over the upper and lateral parts of the section.

The compromise volute variant No. 25 performs well in both pump and turbine modes (Figure 7.16c, Figure 7.18c). It exhibits the most favourable flow structure. Symmetrical vortices are still present in the upper and side regions of the cross-section, but the central flow passage is more organised and better aligned with the impeller inlet. This more ordered flow field is consistent with the balanced pump- and turbine-mode performance of the compromise variant.

7.1.5 Section summary

The recommended range of the volute wall opening angle is 10˚–50˚. The range of 30˚–40˚ can be considered the most favourable for both pump and turbine modes.

Comparing the effects of geometric parameters on pump performance in pump mode and in turbine mode shows that their impact is greater in turbine than in pump operation mode. In pump mode, the maximum difference between the analysed variants is 3% for both head and efficiency, 1.3% for mechanical power, and 57% for total pressure losses. In turbine mode, the corresponding values are 29%, 5%, 32%, and 63%, respectively. The high relative difference in pressure losses in both modes results from the fact that pressure losses are a relatively small residual value. Therefore, a large relative difference gives only a small absolute effect on head and efficiency. These results confirm the main conclusion of this study: volute geometry has a much stronger influence on PAT performance than on pump performance. Therefore, when designing a centrifugal pump that may operate as a PAT, the volute geometry should mainly be selected for turbine-mode operation.

Changes in the volute geometry affect the position of the Q_{BEP}. The difference in Q_{BEP} between the volutes is 9% in pump mode and 15% in turbine mode.

The geometrical parameters of the volute affect the velocity triangle at the impeller inlet. The circumferential velocity component c_u is the most sensitive parameter. The strongest influence on c_u is observed for the design method, D_3, and b_3.

A four-criteria Pareto-front analysis was carried out using the following criteria: maximum efficiency in both modes and minimum Q_{BEP} in both modes. This analysis identified volute No. 32 (CV_D522_b105_T30) as the closest variant to the Utopia point (1.08). Therefore, this volute was selected as the recommended compromise solution for dual-mode operation. Although this variant shows a steeper decrease in pump-mode efficiency at off-design flow rates than some other variants, it gives the best overall balance according to the assumed criteria.

Volute No. 25 (CV_D485_b105_R30), which ranked second on the pump-turbine Pareto front with Utopia Distance = 1.18, was analysed as a turbine-oriented compromise variant. It has the same CV design method and narrow inlet width b_3 = 105 mm as volute No. 32. Volute No. 19 (CV_D448_b105_R30) was identified in a separate two-criteria Pareto analysis, based on efficiency and efficiency-curve flatness, as the variant with the best combination of high maximum efficiency and a flat efficiency curve in pump mode. Therefore, volute No. 19 represents a different optimisation approach and was included for completeness.

The hydrodynamic analysis showed that the main differences between the compromise variants, No. 25 and No. 32, and the least favourable variant, No. 5 (CAM_D448_b183_R30), are related to the intensity of the recirculation zones near the side walls of the volute and to the flow swirl at the impeller inlet in turbine mode. The strongest swirl is observed for variant No. 5. The compromise variants guide the flow into the impeller passage with better directional uniformity. In pump mode, no significant differences in impeller flow swirl are observed between the variants. This confirms, at the flow-field level, that the sensitivity to volute geometry is much stronger in turbine mode than in pump mode.

7.2 Statistical analysis

7.2.1 Description of the statistical method

The analysis uses multiple linear regression [124] estimated by ordinary least squares (OLS) to quantify the effect of a set of factors on a dependent variable Y. The general form of the model is:

$$Y_i = \beta_0 + \beta_1 X_{1i} + \beta_2 X_{2i} + \cdots + \beta_k X_{ki} + \varepsilon_i \tag{29}$$

where:
Y_i is the value of the dependent variable for the i-th observation,
β_0 is the intercept,
$\beta_1, \beta_2, \ldots, \beta_k$ are the regression coefficients for the independent variables $X_1, X_2, \ldots, X_k$,
ε_i is the random error term.

First, a full regression model including all factors as categorical predictors is fitted, and overall model fit is summarized using coefficient of determination (R^2). Then, the contribution of each factor is assessed via nested-model comparison (drop-one) for each factor, a reduced model excluding that factor is fitted and compared with the full model. Based on this comparison, the change in R^2 after removing the factor ($\Delta R^2 = R^2_{\text{full}} - R^2_{\text{reduced}}$) is computed as a measure of the factor's unique contribution to the explained variance. The partial coefficient of determination (partial R^2) is calculated to reflect the proportion of reduction in the residual sum of squares attributable to adding that factor to

the model. Statistical significance of each factor is evaluated using a partial F-test for nested model. The null hypothesis states that the factor has no effect after controlling for the other factors, and the p-value is obtained from the F-distribution with the corresponding degrees of freedom. The model treats observations as independent.

To characterize differences between individual factor levels, the same multiple linear regression model estimated by OLS is used to estimate linear contrasts. In this model, one level of each factor is treated as the reference. The fitted coefficients then represent how much the mean value of Y changes when a given level replaces the reference level, while the other factors are kept the same. Pairwise comparisons between two non-reference levels are computed by subtracting their effects relative to the same reference level (for example (B-A) – (C-A)=B-C). Inference on these differences is based on t-tests for the corresponding contrasts and is reported with 95% confidence intervals.

The following metrics were used in the analysis:

– R^2 *(Coefficient of Determination of the Full Model).* The proportion of the total variability in the dependent variable (Y) explained by the full model including all predictors (factors). In this research Y: Head, Mechanical power, Losses of total pressure, Efficiency,

– ΔR^2 *(drop-one) (Change in* ΔR^2 *under Drop-One Factor Removal*). The unique contribution of a factor to the explained variance, quantified as the difference between the R^2 of the full model and the R^2 of the model fitted without that factor,

– Partial R^2 *(Explained Residual Variance)*. The proportion of the remaining (unexplained) variability that is additionally explained by a given factor after controlling for the other factors,

– *F (Partial F-statistic for Comparing Nested Models).* Tests whether a factor, treated as a block of parameters, yields a statistically significant improvement in model fit relative to the reduced model without that factor,

– *Numerator df (Numerator Degrees of Freedom)* the number of parameters (constraints) tested jointly for the given factor,

– *Denominator df (Denominator Degrees of Freedom).* The residual degrees of freedom of the full model used to estimate the error variance after fitting all parameters,

– *p-value of the Partial F-test for the Factor*. The probability of obtaining the observed (or more extreme) *F* value under the null hypothesis that the factor has no effect after controlling for the other factors. A factor is typically considered statistically significant when $p < 0.05$ (5% significance level), if $p \geq 0.05$, the evidence is insufficient to reject the null hypothesis,

Δ *the estimated regression coefficient* that quantifies how much the expected value of Y changes when moving to a given factor level relative to the base level, after accounting for the other factors included in the model,

– 95% CI (*confidence interval*) is the interval that provides a range of plausible values for the true coefficient Δ,

– *VIF (Variance Inflation Factor)* was used to assess multicollinearity between the predictors. A VIF value close to 1 indicates the absence of multicollinearity, values below 5 are generally considered acceptable, whereas values above 10 indicate strong multicollinearity and possible instability of the regression coefficients.

– *Durbin–Watson statistic (DW)* was used to assess the independence of residuals. A value close to 2 indicates no autocorrelation, while values in the approximate range of 1.5–2.5 are usually considered acceptable,

– *RMSE (Root Mean Square Error)* was used to quantify the average prediction error of the model.

7.2.2 Pump mode

A summary of the key statistical parameters describing the influence of geometrical parameters on pump performance at Q_{nom} 2000 m^3/h is presented in Table 7.4. The results for flow rates of 1400 m^3/h and 2400 m^3/h are presented in Appendix I (Table I.1, Table I.).

The Factor column shows the names of the factors in order of decreasing impact. The Partial R^2 metric shows the magnitude of the impact as a numerical value. Parameters marked in grey in the p-value column are statistically insignificant (p-value > 0.05).

Analysis of the presented statistical results showed that b_3 is the statistically significant and the most dominant factor for head, mechanical power and efficiency at the lower flow rate (1400 m^3/h). It is showed by the highest partial R^2 and p-values <0.05. Shape affects only on mechanical power. D_3 shows a statistically significant effect only for total pressure losses.

For the optimal flow rate (2000 m^3/h) shape become more influential. It is dominant factor for head and efficiency. At the same time b_3 is still the most important factor for mechanical power and total pressure losses.

At flow rates higher than the optimal (2400 m^3/h) D_3 becomes the dominant factor for head. The influence of methods also increased. It becomes the second most important factor for head, total pressure losses and the dominant factor for efficiency. The b_3 is still the most important factor for mechanical power, total pressure losses. The influence of shape is smaller than at the lowest flow rate.

Table 7.4 - Factor effects in the regression model at flow rate 2000 m^3/h

Head								Power mechanical							
Factor	R^2	ΔR^2 (drop-one)	Partial R^2	F	Numerator df	Denominator df	p-value	Factor	R^2	ΔR^2 (drop-one)	Partial R^2	F	Numerator df	Denominator df	p-value
Shape	0.346	0.175	0.211	7.75	1	29	9.36×10^{-3}	b_3	0.833	0.784	0.824	68.04	2	29	1.12×10^{-11}
b_3	0.346	0.152	0.189	3.38	2	29	4.78×10^{-2}	D_3	0.833	0.028	0.143	2.42	2	29	1.07×10^{-1}
Method	0.346	0.018	0.026	0.79	1	29	3.83×10^{-1}	Method	0.833	0.021	0.113	3.70	1	29	6.42×10^{-2}
D_3	0.346	0.001	0.002	0.03	2	29	9.67×10^{-1}	Shape	0.833	0.000	0.002	0.05	1	29	8.23×10^{-1}
Efficiency								Losses total pressure							
Factor	R^2	ΔR^2 (drop-one)	Partial R^2	F	Numerator df	Denominator df	p-value	Factor	R^2	ΔR^2 (drop-one)	Partial R^2	F	Numerator df	Denominator df	p-value
Shape	0.380	0.177	0.222	8.27	1	29	7.49×10^{-3}	b_3	0.360	0.196	0.234	4.43	2	29	2.10×10^{-2}
b_3	0.380	0.156	0.201	3.65	2	29	3.87×10^{-2}	Shape	0.360	0.089	0.122	4.05	1	29	5.36×10^{-2}
Method	0.380	0.045	0.068	2.12	1	29	1.56×10^{-1}	D_3	0.360	0.043	0.063	0.98	2	29	3.88×10^{-1}
D_3	0.380	0.003	0.004	0.06	2	29	9.41×10^{-1}	Method	0.360	0.032	0.047	1.45	1	29	2.39×10^{-1}

Analise show that the effect of the geometric parameters changes with flow rate. A graphical representation of variations of Partial R^2 with a change in flow rate is shown in the Figure 7.20.

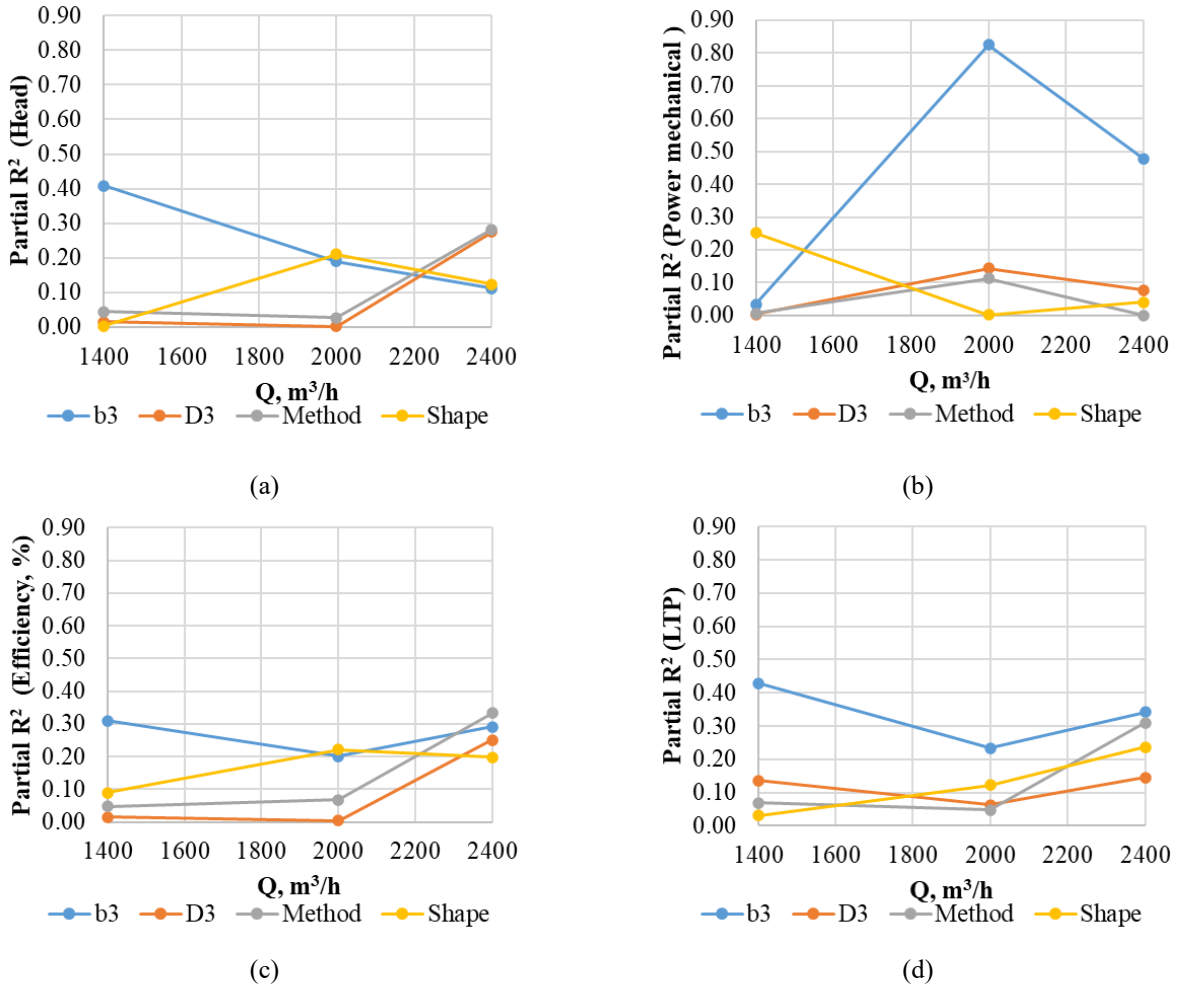

Figure 7.20 - Comparison of factors by partial R^2: a) Head, b) Mechanical power, c) Efficiency, d) Losses of total pressure

Estimated effects of factor levels relative to the base level, obtained using the least squares method in a linear regression model for Q_{nom} are presented in Table 7.5. The results for flow rates of 1400 m³/h and 2400 m³/h are presented in Appendix I (Table I.2, Table I.4).

The base level was defined as the first sorted category for each factor: Method - CAM, 448 and 485 mm for D_3, 105 and 126 mm for b_3, and Round for Shape.

For most observations at a flow rate of 1400 and 2000 m³/h, factors are not statistically significant (p-value > 0.05). This implies that, given the available data, we cannot confidently conclude that this factor (or its levels) exerts a real effect, because the observed difference may be attributable to random variation. The statistically significant effect showed that maximum change in head is 0.7 m, for power mechanical – 1.45 kW, efficiency - 0.97 pp., total pressure losses – 0.9 m.

Based on the obtained results, it can be stated that the most favourable parameter set for the pump operating in pump mode is the CV method, the smallest D_3 value (448 mm), and the highest b_3 value (183 mm) for 2000 and 2400 m³/h, for 1400 m³/h, a smaller b_3 value (105 mm) performs better. Similarly, a volute with a trapezoidal cross-section performs best at the lower flow rate, whereas a round cross-section is preferable at the optimal and higher flow rates (2000 and 2400 m³/h).

In summary, the most important parameters to select are b_3 (highest value), shape (Round), and Method (CV), whereas D_3 is of secondary importance (in terms of maximum overall dimensions, it is preferable to smallest value 448mm).

Table 7.5 - OLS estimates of factor-level effects vs base level at flow rate 2000 m^3/h

Head								Power mechanical							
Factor	**Parametr**			**Δ, m**	**p-value**	**95% CI, lower**	**95% CI, upper**	**Parametr**			**Δ, kW**	**p-value**	**95% CI, lower**	**95% CI, upper**
Method	CAM	lower than	CV	-0.09	0.38	-0.29	0.11	CAM	higher than	CV	0.30	0.06	-0.02	0.63
D_3	448	lower than	485	-0.01	0.96	-0.25	0.24	448	higher than	485	0.03	0.86	-0.36	0.43
D_3	448	higher than	522	0.02	0.85	-0.22	0.27	448	higher than	522	0.38	0.06	-0.01	0.78
D_3	485	higher than	522	0.03	0.81	-0.22	0.27	485	higher than	522	0.35	0.08	-0.04	0.74
b_3	105	higher than	126	0.20	0.10	-0.04	0.45	105	higher than	126	2.248	1.88E-12	1.85	2.64
b_3	105	lower than	183	-0.11	0.38	-0.35	0.14	105	higher than	183	1.24	4.81E-07	0.85	1.64
b_3	126	lower than	183	-0.31	0.02	-0.55	-0.06	126	lower than	183	-1.005	1.44E-05	-1.40	-0.61
Shape	Round	higher than	Trapezoidal	0.27	0.01	0.07	0.47	Round	higher than	Trapezoidal	0.04	0.82	-0.29	0.36
Efficiency								**Losses total pressure**						
Factor	**Parametr**			**Δ, pp**	**p-value**	**95% CI, lower**	**95% CI, upper**	**Parametr**			**Δ, m**	**p-value**	**95% CI, lower**	**95% CI, upper**
Method	CAM	lower than	CV	-0.25	0.16	-0.61	0.10	CAM	higher than	CV	0.10	0.24	-0.07	0.28
D_3	448	lower than	485	-0.02	0.93	-0.45	0.41	448	higher than	485	0.07	0.50	-0.14	0.29
D_3	448	lower than	522	-0.07	0.74	-0.51	0.36	448	higher than	522	0.15	0.17	-0.07	0.36
D_3	485	lower than	522	-0.05	0.81	-0.49	0.38	485	higher than	522	0.08	0.48	-0.14	0.29
b_3	105	lower than	126	-0.30	0.170	-0.73	0.14	105	higher than	126	0.296	0.01	0.08	0.51
b_3	105	lower than	183	-0.57	0.01	-1.01	-0.14	105	higher than	183	0.24	0.03	0.02	0.45
b_3	126	lower than	183	-0.27	0.206	-0.71	0.16	126	lower than	183	-0.060	0.57	-0.28	0.15
Shape	Round	higher than	Trapezoidal	0.50	0.007	0.14	0.85	Round	lower than	Trapezoidal	-0.17	0.05	-0.35	0.003

7.2.3 Turbine mode

A similar analysis was carried out for the PAT. A summary of the key statistical parameters describing the influence of geometrical parameters on PAT performance at 2400 m^3/h is presented in Table 7.6. The results of 2000 m^3/h and 2700 m^3/h is presented in Table J.1, Table J.3 (Appendix J).

Table 7.6 - Factor effects in the regression model at flow rate 2400 m^3/h on the PAT

Head								Power mechanical							
Factor	**R^2**	**ΔR^2 (drop-one)**	**Partial R^2**	**F**	**Numerator df**	**Denominator df**	**p-value**	**Factor**	**R^2**	**ΔR^2 (drop-one)**	**Partial R^2**	**F**	**Numerator df**	**Denominator df**	**p-value**
D_3	0.95	0.39	0.90	123.76	2	29	6.33×10^{-15}	**D_3**	0.96	0.36	0.890	117.15	2	29	1.29×10^{-14}
Method	0.95	0.31	0.87	198.80	1	29	1.64×10^{-14}	**Method**	0.96	0.32	0.878	208.15	1	29	8.99×10^{-15}
b_3	0.95	0.22	0.83	70.38	2	29	7.45×10^{-12}	**b_3**	0.96	0.23	0.837	74.51	2	29	3.74×10^{-12}
Shape	0.95	0.04	0.48	26.27	1	29	1.79×10^{-5}	**Shape**	0.96	0.06	0.556	36.28	1	29	1.50×10^{-6}
Efficiency								**Losses total pressure**							
Factor	**R^2**	**ΔR^2 (drop-one)**	**Partial R^2**	**F**	**Numerator df**	**Denominator df**	**p-value**	**Factor**	**R^2**	**ΔR^2 (drop-one)**	**Partial R^2**	**F**	**Numerator df**	**Denominator df**	**p-value**
Method	0.67	0.23	0.41	20.00	1	29	1.10×10^{-4}	**D_3**	0.77	0.34	0.600	21.73	2	29	1.71×10^{-6}
b_3	0.67	0.20	0.37	8.61	2	29	1.16×10^{-3}	**Method**	0.77	0.25	0.526	32.21	1	29	3.89×10^{-6}
Shape	0.67	0.17	0.34	14.66	1	29	6.35×10^{-4}	**Shape**	0.77	0.10	0.311	13.07	1	29	1.12×10^{-3}
D_3	0.67	0.08	0.20	3.72	2	29	3.64×10^{-2}	**b_3**	0.77	0.08	0.258	5.05	2	29	1.31×10^{-2}

The analysis of the presented statistical results in Table 7.6 and Table J.2, Table J.4 (Appendix J) shows that almost all parameters exhibit a statistically significant effect for all dependent variables (p-value < 0.05). The coefficient of determination R^2 varies with flow rate. In most cases, its value is greater than 0.9. The lowest degree of variation is observed for efficiency and total pressure losses, for which the coefficient of determination, R^2, may range from 0.6 to 0.7.

Effects of factor levels relative to the base level estimated by the method of least squares in a linear regression model, are presented in Table 7.7, Table J.2 and Table J.4. The base level for each factor: method - CAM, D_3 - 448 and 485 mm, b_3 - 105 and 126 mm, shape - Round.

Table 7.7 - OLS estimates of factor-level effects vs base level at flow rate 2400 m^3/h

Head									Power mechanical							
Factor	**Parametr**			**Δ, m**	**Δ, %**	**p-value**	**95% CI, lower**	**95% CI, upper**	**Parametr**			**Δ, kW**	**Δ, %**	**p-value**	**95% CI, lower**	**95% CI, upper**
Method	CAM	lower than	CV	-5.79	-10.45	1.64×10^{-14}	-6.62	-4.95	CAM	lower than	CV	-34.59	-11.60	9.13×10^{-15}	-39.49	-29.69
D_3	448	lower than	485	-3.35	-6.33	2.58×10^{-7}	-4.38	-2.32	448	lower than	485	-19.23	-6.80	3.58×10^{-7}	-25.23	-13.22
D_3	448	lower than	522	-7.88	-13.71	1.07×10^{-15}	-8.91	-6.85	448	lower than	522	-44.80	-14.52	2.17×10^{-15}	-50.80	-38.79
D_3	485	lower than	522	-4.53	-7.88	6.75×10^{-10}	-5.55	-3.50	485	lower than	522	-25.57	-8.29	1.38×10^{-9}	-31.57	-19.56
b_3	105	higher than	126	0.705	1.44	1.71×10^{-1}	-0.32	1.73	105	higher than	126	5.167	1.999	8.90×10^{-2}	-0.84	11.17
b_3	105	higher than	183	5.48	12.43	8.94×10^{-12}	4.45	6.51	105	higher than	183	33.30	14.45	3.52×10^{-12}	27.30	39.31
b_3	126	higher than	183	4.775	10.83	2.08×10^{-10}	3.75	5.80	126	higher than	183	28.134	12.212	1.72×10^{-10}	22.13	34.14
Shape	Round	lower than	Trapez.	-2.10	-4.07	1.79×10^{-5}	-2.94	-1.26	Round	lower than	Trapez.	-14.44	-5.19	1.50×10^{-6}	-19.34	-9.54
Efficiency									**Losses total pressure**							
Factor	**Parametr**			**Δ, p.p**	**Δ, %**	**p-value**	**95% CI, lower**	**95% CI, upper**	**Parametr**			**Δ, m**	**Δ, %**	**p-value**	**95% CI, lower**	**95% CI, upper**
Method	CAM	lower than	CV	-1.04	-1.25	1.10×10^{-4}	-1.51	-0.56	CAM	lower than	CV	-0.50	-26.72	3.89×10^{-6}	-0.68	-0.32
D_3	448	lower than	485	-0.38	-0.46	1.96×10^{-1}	-0.95	0.20	448	lower than	485	-0.34	-19.95	3.59×10^{-3}	-0.57	-0.12
D_3	448	lower than	522	-0.77	-0.94	1.07×10^{-2}	-1.35	-0.19	448	lower than	522	-0.71	-34.14	3.20×10^{-7}	-0.94	-0.49
D_3	485	lower than	522	-0.40	-0.48	1.71×10^{-1}	-0.98	0.18	485	lower than	522	-0.37	-17.73	1.87×10^{-3}	-0.59	-0.15
b_3	105	higher than	126	0.42	0.52	1.49×10^{-1}	-0.16	1.00	105	higher than	126	0.340	32.726	3.92×10^{-3}	0.12	0.56
b_3	105	higher than	183	1.16	1.44	3.06×10^{-4}	0.58	1.74	105	higher than	183	0.12	9.52	2.78×10^{-1}	-0.10	0.34
b_3	126	higher than	183	0.74	0.92	1.39×10^{-2}	0.16	1.32	126	lower than	183	-0.220	-17.488	5.16×10^{-2}	-0.44	0.00
Shape	Round	lower than	Trapez.	-0.89	-1.07	6.35×10^{-4}	-1.36	-0.41	Round	lower than	Trapez.	-0.32	-18.85	1.12×10^{-3}	-0.50	-0.14

The analysis of the Table 7.7, Table J.2 and Table J.4 indicates that, for the PAT, most results are statistically significant. The maximum absolute between-level differences are 9 m for head, 48 kW for mechanical power, 5 pp. for efficiency, and 1,38 m for total pressure losses.

The overall ranking of the effects of geometrical factors, together with the direction of change required to increase or decrease PAT performance, is summarized in Table 7.8.

Table 7.8 - Geometric factor effects and recommended adjustment directions

Performance parameter	Ranking of factor influence	To increase performance parameter	To decrease performance parameter
Head	D_3 > Method > b_3> Shape	D_3: increase, Method: CV, b_3: reduce, Shape: trapezoidal	D_3: decrease, Method: CAM, b_3: increase, Shape: round
Mechanical power	D_3 > Method > b_3 > Shape	D_3: increase , Method: CV, b_3: reduce, Shape: trapezoidal	D_3: decrease, Method: CAM, b_3: increase, Shape: round
Efficiency	D_3 > Method > b_3 > Shape	D_3: increase, Method: CV, b_3: reduce, Shape: trapezoidal	D_3: decrease, Method: CAM, b_3: increase, Shape: round
Loses of total pressure	D_3> Method > Shape > b_3	D_3: increase, Method: CV, b_3: reduce, Shape: trapezoidal	D_3: decrease, Method: CAM, b_3: increase, Shape: round

The influence of the geometrical parameters changes with the flow rate (Figure 7.21).

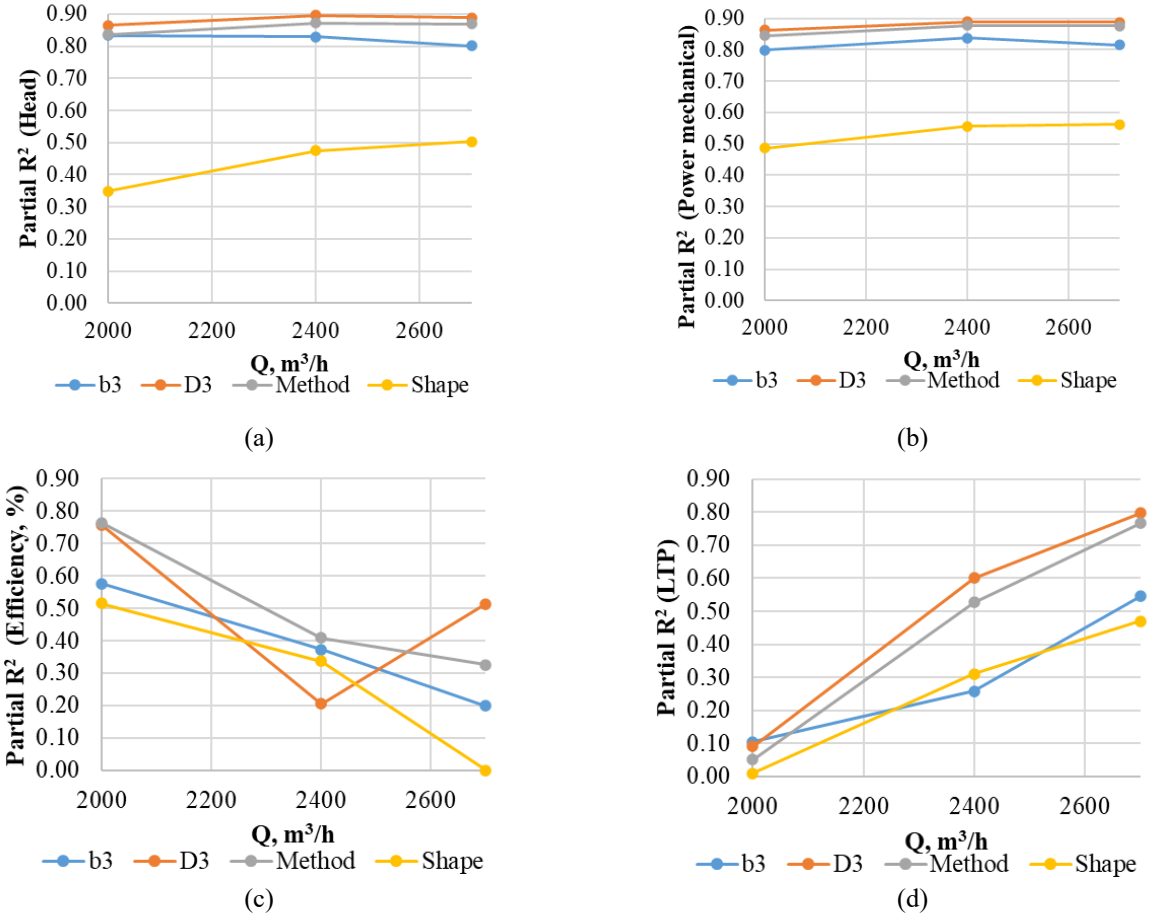

Figure 7.21 - Comparison of factors by partial R^2: a) Head, b) Power mechanical, c) Efficiency, d) Losses of total pressure

The influence of the geometric parameters increases with increasing flow rate for head and losses of total pressure. For mechanical power, the effects remain relatively stable, whereas for efficiency the overall influence of the parameters decreases as flow rate increase, while the influence of D_3 increases. For the PAT, the most influential parameters are D_3, b_3, method. However, shape has the smallest effect, even though in pump mode shape and b_3 were the most important parameters.

The statistical results show the influence of geometrical parameters on the flatness of the efficiency curve, as presented in Table 7.9. According to the partial R^2 value, the most influential parameter is method. The D_3 and shape have a smaller influence. The results for b_3 are not statistically significant.

Table 7.9 - Summary of the influence of geometric parameters on PAT efficiency-curve flatness

Efficiency-curve flatness							
Factor	**R^2**	**ΔR^2 (drop-one)**	**Partial R^2**	**F**	**Numerator df**	**Denominator df**	**p-value**
Method	0.50	0.20	0.29	11.71	1	29	0.002
D_3	0.50	0.12	0.19	3.43	2	29	0.046
b_3	0.50	0.10	0.17	2.94	2	29	0.069
Shape	0.50	0.08	0.14	4.89	1	29	0.035

The quantitative effect on the flatness indicator A is shown in Table 7.10. A is the average drop in efficiency relative to its maximum value over the entire flow-rate range. It should be noted that, in the flatness analysis, lower values of the flat parameter correspond to a flatter efficiency curve. Therefore, the recommended configuration for achieving a flat efficiency curve includes the CAM method, the smallest D_3 value (448 mm), the largest b_3 value (183 mm), and a round volute cross-section shape.

Table 7.10 - OLS estimates of flatness factor-level effects vs base level

Flatness (A_{max})							
Factor	**Parametr**			**Δ, p.p**	**p-value**	**95% CI, lower**	**95% CI, upper**
Method	CAM	lower than	CV	-0.50	1.87×10^{-3}	-0.79	-0.20
D_3	448	lower than	485	-0.35	5.50×10^{-2}	-0.72	0.01
D_3	448	lower than	522	-0.44	1.99×10^{-2}	-0.80	-0.07
D_3	485	lower than	522	-0.08	6.46×10^{-1}	-0.45	0.28
b_3	105	higher than	126	0.209	2.48×10^{-1}	-0.15	0.57
b_3	105	higher than	183	0.43	2.18×10^{-2}	0.07	0.79
b_3	126	higher than	183	0.221	2.23×10^{-1}	-0.14	0.58
Shape	Round	lower than	Trapezoidal	-0.32	3.50×10^{-2}	-0.62	-0.02

The geometric parameters considered in this dissertation do not explain all factors affecting the flatness of the efficiency curve. The role of the volute tongue in PAT performance has an assumed that it may also affect.

7.2.3.1 Regression analysis of best efficiency point shift

To assess the shift of the best efficiency point Q_{BEP} depending on the geometric parameters of the volute, multiple linear regression with logarithmically transformed variables was used. The dependent variable was $\ln(Q_{BEP})$. The numerical geometric parameters D_3 and b_3 were also transformed into logarithmic form. This transformation allows the regression coefficients to be interpreted as the relative change in Q_{BEP} caused by a relative change in a geometric parameter.

The volute design method was introduced into the model as a categorical factor. In the model, CAM was used as the reference level.

The model was written as:

$$ln(Q_{BEP}) = \beta_0 + \beta_1 ln(b_3) + \beta_2 ln(D_3) + \beta_3 Method(CV) + \varepsilon$$

where β are the regression coefficients, and ε is the random error of the model.

According to the obtained data, the geometric parameters have the greatest effect on changes in circumferential component of the absolute velocity c_u and the BEP position (Figure 8.9). The strongest effect is observed for changes in D_3. When D_3 is increased from its minimum to its maximum value, the Q_{BEP} shifts by 5.2% to the lower flow rate, while c_u decreases by 9.02%. A shift of Q_{BEP} toward lower flow rates can also be caused by selecting a smaller b_3 (ΔQ_{BEP} =4,2%), the CV method (ΔQ_{BEP} =3,73%), and a trapezoidal shape (ΔQ_{BEP} =1,98%).

Table 7.11 - The relationship between geometrical parameters, c_u and the Q_{BEP} shift

Change parameter	Δc_u	ΔQ_{BEP}
D_3:448 (1.04D_2) → 522 (1.22 D_2)	←9.0%	←5.2%
b_3: 105 (1.05b_2) → 183 (1.74b_2)	→7.7%	→4.2%
Method: CAM → CV	←6.7%	←3.7%
Shape: Round → Trapezoidal	←1.5%	←1.9%

The model has good quality. It is statistically significant (F=34.89, p-value<0.001) and explains about 82% of the variation in c_u and Q_{BEP} (R^2 = 0.818, Adjusted R^2 = 0.795). The RMSE value is low (0.017), indicating a small prediction error. No multicollinearity was observed (VIF=1.0), and the Durbin–Watson test (DW=2.091) indicates no autocorrelation of residuals. Therefore, the model can be considered reliable.

The percentages shown in the table may differ from those reported in the numerical analysis section. This is because the statistical analysis presents averaged effects estimated using linear regression, whereas the numerical analysis reports the maximum observed deviation rather than the average effect.

7.2.3.2 Dimensionless regression model of the BEP position in PAT

A multiple linear regression model was developed to describe the effect of volute geometry on the $Q_{BEP.T}$ for the Omega PAT. The regression analysis gave the following equation:

$$Q_{BEP} = 3244.515 - 1.802D_3 + 1.32b_3 - 94.444CV - 50T \quad (30)$$

According to the analysis of variance, the model was statistically significant (F=36.56, p-value <0.001). Developed model explains 82.5% of the variation (R^2) in the Q_{BEP} position, and the adjusted coefficient of determination also remains high (Adjusted R^2 = 0.803). All four predictors were found to be statistically significant. The collinearity diagnostics showed that all predictors had VIF=1.0. The Durbin–Watson statistic was DW=2.049. This value is close to 2, which indicates the absence of substantial autocorrelation in the residuals. For this type of data, this result can be considered acceptable.

The obtained equation is an empirical regression relationship and can be used only within the studied ranges of the parameters D_3 (448–522 mm) and b_3 (105–183 mm). The model is limited to the CAM and CV design methods and to the Round and Trapezoidal cross-sectional shapes

An equation (30) written directly for $Q_{BEP.T}$ in m^3/h is related to the specific scale of the analysed pump. Therefore, it cannot be directly applied to geometrically similar pumps of a different size. To generalize the results of the study on the influence of volute casing geometry on the BEP position in turbine mode, a dimensionless regression model was developed.

The flow coefficient at the best efficiency point in turbine mode was used as the dependent variable:

$$\varphi_{BEP.T} = \frac{Q_{BEP.T}}{n \cdot D_2^3} \quad (31)$$

The model coefficients were calculated using the least squares method in JASP. As a result, the following equation was obtained:

$$\varphi_{BEP.T} = 0.454 - 0.108\frac{D_3}{D_2} + 0.019\frac{b_3}{b_2} - 0.013 \cdot \text{Method} - 0.007 \cdot \text{Shape} \quad (32)$$

where:

$\frac{D_3}{D_2}$ – describes the size of the volute casing relative to the impeller outer diameter,

$\frac{b_3}{b_2}$ – describes the ratio of the volute inlet width to the impeller outlet width,

Method – variable, where Method = 1 for CV, Method = 0 for CAM,

Shape – variable, where Shape = 1 for trapezoidal cross-section, Shape = 0 for round cross-section.

The obtained model showed a good approximation quality. The coefficient of determination was $R^2 = 0.825$, adjusted $R^2 = 0.825$. The root mean square error was RMSE = 0.006 which corresponds to 1.7% of $\varphi_{BEP.T}$. The model as a whole was statistically significant F = 36.55, p-value < 0.001. All factors included in the model were also statistically significant. No multicollinearity was observed between the model variables (VIF = 1.0). Therefore, the effect of each factor can be interpreted independently of the others.

Two-factor interactions between the relative geometric parameters and the categorical factors of design method and cross-sectional shape were also tested. Adding these interactions did not significantly reduce RMSE, and none of the interaction terms was statistically significant at (p-value < 0.05). In addition, the model with interactions showed high multicollinearity. Therefore, the simpler main-effects model was selected for further analysis.

The absolute value of the flow rate at BEP can be calculated using the similarity equation:

$$Q_{BEP.T} = \varphi_{BEP.T} \cdot \text{n} \cdot D_2^3 \quad (33)$$

For practical use, the equation can be written in a form where $Q_{BEP.T}$ is obtained in m³/h, n is given in rpm, and D_2 is in mm.

$$Q_{BEP.T} = 6 \cdot 10^{-8} \cdot \text{n[rpm]} \cdot D_2^3\text{[mm]} \cdot (0.454 - 0.108\frac{D_3}{D_2} + 0.019\frac{b_3}{b_2} - 0.013 \cdot \text{Method} - 0.007 \cdot \text{Shape}) \quad (34)$$

The equation (34), the ratios D_3/D_2 and b_3/b_2 are dimensionless. Therefore, the corresponding dimensions can be substituted using the same units.

7.2.4 Section summary

In this section, a statistical analysis using the OLS method was carried out. The effects of geometric parameters on the performance of the Omega pump were examined in pump mode and turbine mode.

The results show that, in pump mode, the effects of geometric parameters are not statistically significant in most cases. The largest effects are associated with b_3 and shape. However, these effects are small. For head, the maximum mean difference (Δ) is 0.7 m. For mechanical power, it is 1.45 kW. For efficiency, it is 0.97 pp. For total pressure losses, it is 0.9 m.

To improve the Omega pump performance in pump mode, it is necessary to select the largest b_3, round shape, the CV method, and the smallest D_3.

In contrast, the same geometric parameters have a much stronger effect in turbine mode. Almost all parameters show a statistically significant effect. The maximum absolute between-level differences are much larger than in pump mode. They are 9 m for head, 48 kW for mechanical power, 5 pp. for efficiency, and 1.38 m for total pressure losses.

In turbine mode, the most important parameters are D_3, method, and b_3, while shape has the smallest weight. The direction of these effects is opposite to that in pump mode.

To improve turbine-mode performance, a larger value of D_3 should be selected. In the present study, D_3 was selected according to recommendations [33] and was equal to 522 mm. At a flow rate of 2400 m³/h, change of D_3 from minimum to maximum value raises efficiency by 0.94%. The CV method leads to an increase of 1.25%, while the trapezoidal shape gives an 0.89% improvement compared with the round shape. In addition, reducing b_3 to its minimum value of 105 mm results in a 1.44% increase in efficiency.

The magnitude of the effect of the parameters on pump performance in both operating modes varies with flow rate (Figure 7.20, Figure 7.21).

This section also analysed the effects of geometric parameters of PAT on the flatness of the efficiency curve. The most influential parameters are the volute design method (Partial $R^2 = 0{,}29$), D_3 (Partial $R^2 = 0{,}19$), and shape (Partial $R^2 = 0{,}14$). The results for b_3 are not statistically significant. The CAM method produces a flatter efficiency curve than the other methods. Higher flatness is associated with a CAM method ($\Delta A = 0{,}5$ pp.), smaller D_3 (448 mm, $\Delta A = 0{,}44$ pp.), a larger b_3 (183 mm, $\Delta A = 0{,}2$ pp.) and a round cross-sectional shape.

Given the limited effect of geometric parameters on pump-mode performance, the author notes that the volute geometric parameters can be selected according to the recommendations for turbine-mode operation.

An equation (34) was developed to estimate the $Q_{BEP.T}$ for geometrically similar pumps. The model has good statistical quality and does not show multicollinearity.

Chapter 8: Numerical results and statistical analysis for DHV pump

For the Omega pump, the main comprehensive study was carried out, and its results formed the basis for the conclusions. For the DHV pump, a smaller verification study was performed to check whether the observed relationships could also be found in this case. Accordingly, a full repetition of all calculation and research variants was not conducted.

8.1 Numerical results

8.1.1 Volute wall opening angle and cross-section shape influence

8.1.1.1 Pump mode

Previous research showed that the reasonable range of wall opening angles is 10–50˚, so, for the DHV pump, the study focused on angles within this range. Changing the wall opening angle affects the all pump performance parameters by less than 0.5% at flow rates other than $Q_{nom.p}$, while at $Q_{nom.p}$, no noticeable changes are observed. The effect of the cross-sectional shape is about 0.5%. As the changes in the performance parameters were very small, the plots were not presented.

8.1.1.2 Turbine mode

In turbine mode, the difference between PATs with different volute wall opening angles is slightly higher than in pump mode. At 126 m³/h, the average difference is about 4% for head, 1% for efficiency, and 4% for mechanical power. At the higher flow rate of 147 m^3/h, the difference increases to 5% for head, 5% for mechanical power, and 1% for efficiency.

The average difference between pumps with different volute`s cross-sectional shapes at a flow rate of 126 m³/h, is 2% for head, 2.5% for mechanical power, and 0.5% for efficiency. At 147 m³/h, the difference increases to 2.8% for head, 2.8% for mechanical power, and 0.4% for efficiency. The results do not show a clear advantage of one cross-sectional shape, but the trend suggests that the trapezoidal shape has the most positive effect on the performance parameters.

To limit the number of calculations, the further study was carried out for volutes with a wall opening angle of 40˚ and a trapezoidal cross-section. These values were kept constant because the influence of these parameters on performance proved to be relatively small. The angle of 40˚ was as a representative mid-range value within the analysed band, while the trapezoidal shape was retained as the marginally better-performing option.

8.1.2 Design method, D_3, b_3 influence

The analysis of DHV pump was conducted on 16 volute casing designs that differed in their design method, D_3 and b_3. When the geometric parameters were changed within a single design method, the cross-sectional area always remained constant. The names of the volute casings and the geometric parameters used for their construction are presented in Table 8.1. The cell colours indicate recommendations taken from the same scientific source: Lomakin [40] (green cell), Stepanoff [33] (yellow cell), Pfleiderer [32] (blue cell) and the ratio $D_3/D_2 = 1.22$ (pink cell).

All variants were simulated at the nominal rotational speed of pump 1460 rpm in pump mode and 1520 rpm in turbine mode, corresponding to the operating conditions of the DHV pump on the test

Table 8.1 - Geometric parameters and design variations of the analysed volute casings of DHV pump

No.	Volute name	Method	D_3	b_3	Cross-sectional shape
1	CAM_D281_b27	CAM	281	27	Trapezoidal
2	CAM_D281_b40	CAM	281	40	Trapezoidal
3	CAM_D281_b52	CAM	281	52	Trapezoidal
4	CAM_D297_b27	CAM	297	27	Trapezoidal
5	CAM_D297_b40	CAM	297	40	Trapezoidal
6	CAM_D297_b52	CAM	297	52	Trapezoidal
7	CAM_D329_b27	CAM	329	27	Trapezoidal
8	CAM_D329_b52	CAM	329	52	Trapezoidal
9	CV_D281_b27	CV	281	27	Trapezoidal
10	CV_D281_b40	CV	281	40	Trapezoidal
11	CV_D281_b52	CV	281	52	Trapezoidal
12	CV_D297_b27	CV	297	27	Trapezoidal
13	CV_D297_b40	CV	297	40	Trapezoidal
14	CV_D297_b52	CV	297	52	Trapezoidal
15	CV_D329_b27	CV	329	27	Trapezoidal
16	CV_D329_b52	CV	329	52	Trapezoidal
	Reference	Reference	276	60	Manufacture design

8.1.2.1 Pump mode

Head

The results of the influence of the volute casing design method on the head are shown in Figure 8.1. The maximum difference in the head value between the pumps with the various volute casings is 8% at 115 m^3/h (Q_{BEP} for reference pump).

Efficiency

The maximum change in efficiency for pumps with different volute geometries at BEP for reference pump (115 m^3/h) reaches 8%. Using the Pareto front, the most favorable (No. 3) and the least favorable (No. 7) volutes were selected (Figure 8.6). The highest efficiency (80.5%) at the lowest $Q_{OPT.P}$ = 115 m^3/h was obtained for the volute No. 3 with CAM method, smallest D_3 = 281 mm and b_3 = 52 mm.

The lowest efficiency at $Q_{OPT.P}$ = 126 m^3/h was found for the volute (No. 7) with the CAM method, largest diameter, D_3 = 329 mm, and b_3 = 27 mm, where the efficiency was 74.9%. Low efficiency (77.8%) at $Q_{OPT.P}$ = 147 m^3/h, also was obtained for pump (No. 11) with D_3 = 281 mm and b_3 = 27 mm.

Losses of Total Pressure

The maximum difference in losses between pumps with different volute casings at 115 m^3/h is 40%. The smaller cross-sectional area of the CAM volute casing results in the coincidence of the point of lowest losses with the Q_{nom}. In contrast CV method, hight D_3, smaller b_3 shift the point of least losses to the hight flow rate.

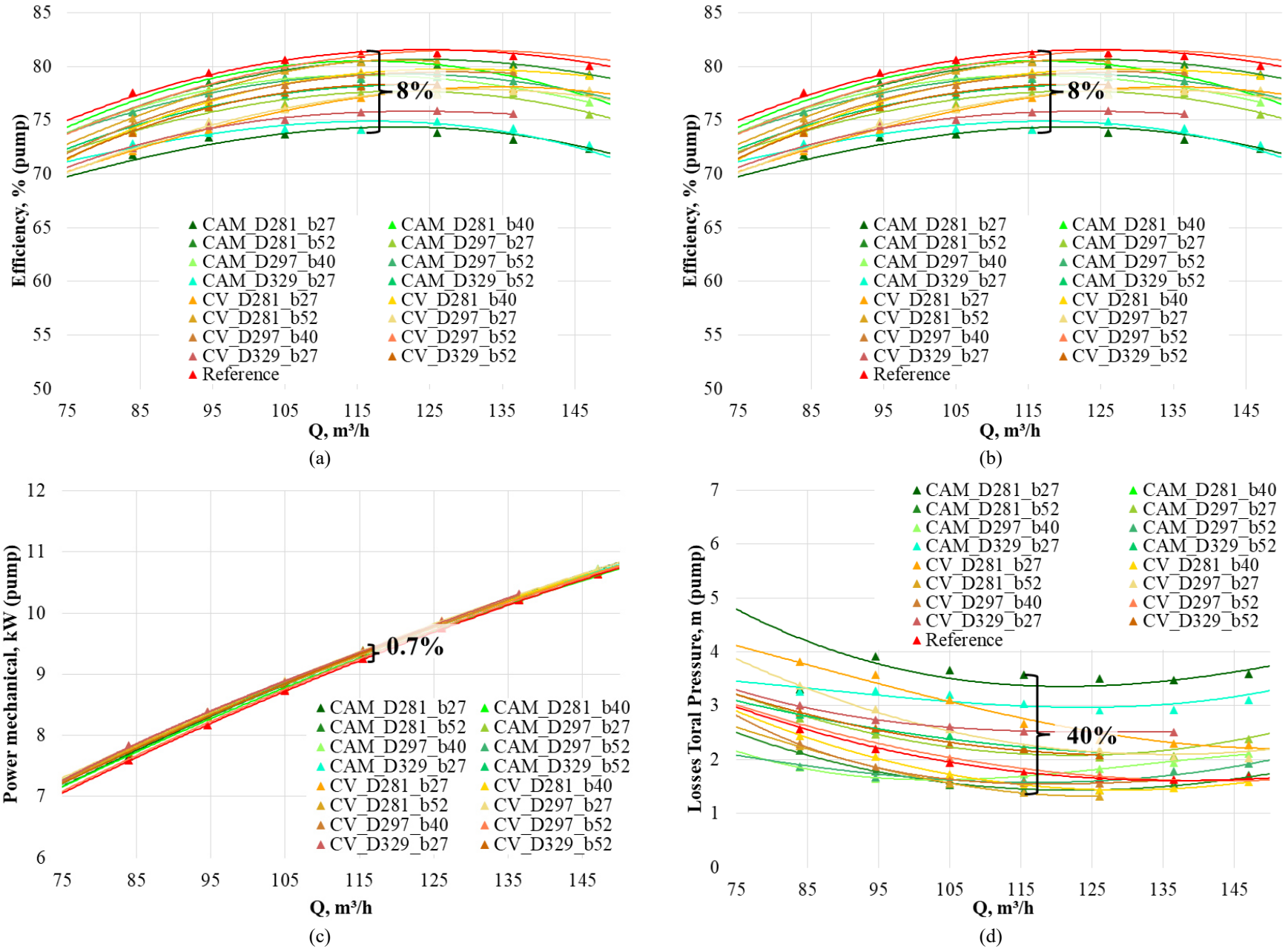

Figure 8.1 – Pump characteristics for different volute geometries: a) Head curves, b) Efficiency curves, c) Power mechanical curves, d) Total pressure losses curves

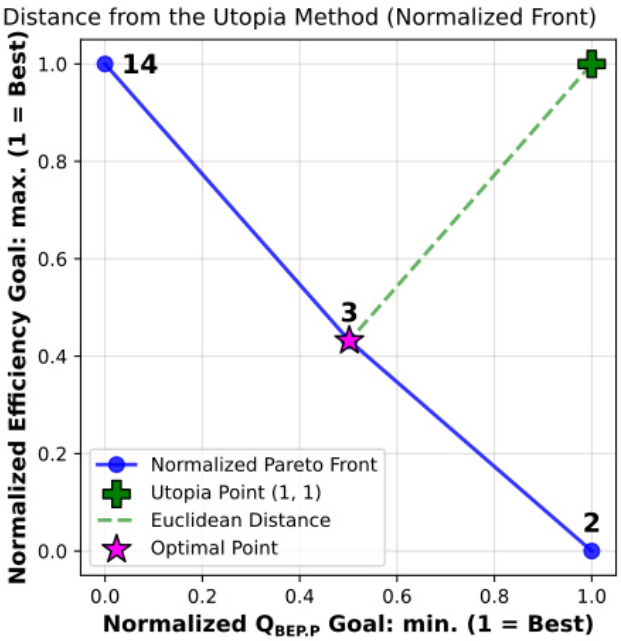

(a) Most favourable for pump

No.	Method	D_3	b_3	$Q_{BEP,T}$	*Eff*.	Utopia Distance
3★	**CAM★**	**281★**	**52★**	**115★**	**80.5★**	**0.75★**

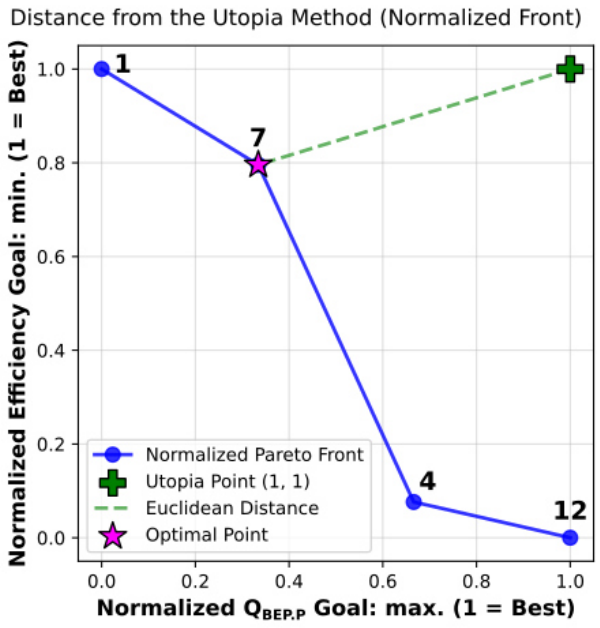

(b) Least favourable for pump

No.	Method	D_3	b_3	$Q_{BEP,T}$	*Eff*.	Utopia Distance
7★	**CAM★**	**329★**	**27★**	**126★**	**74.9★**	**0.70★**

Figure 8.2 – Selection of the volute: a) most favourable for pump, least favourable for pump

8.1.2.2 Turbine mode

The difference in operation parameters between models with various volutes is shown in Figure 8.4. At a flow rate at 147 m^3/h, the maximum difference between PATs with various volute designs is 25% for head, 7,8% for efficiency. For mechanical power it is 22%, while for hydraulic losses in the volute is 76%.

Head, mechanical power, losses

The results show that using CAM method and increasing D_3 leads to higher head (by 17% and 20% respectively), mechanical power, and hydraulic losses, whereas increasing b_3 reduces (Figure 8.3).

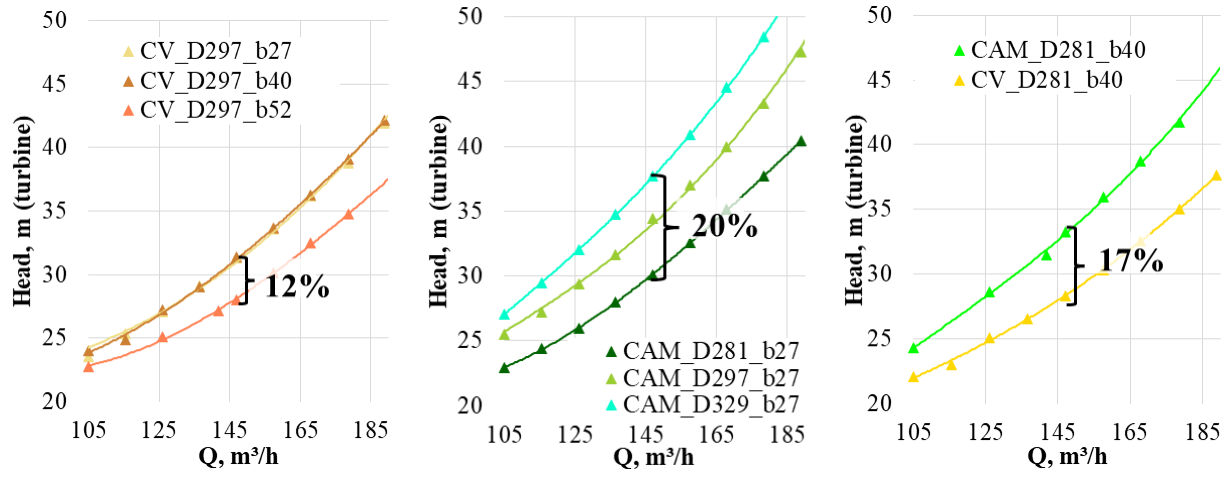

(a) (b) (c)

Figure 8.3 - Effects of geometric parameters on head with changes in: a) D_3, b) b_3, c) design method

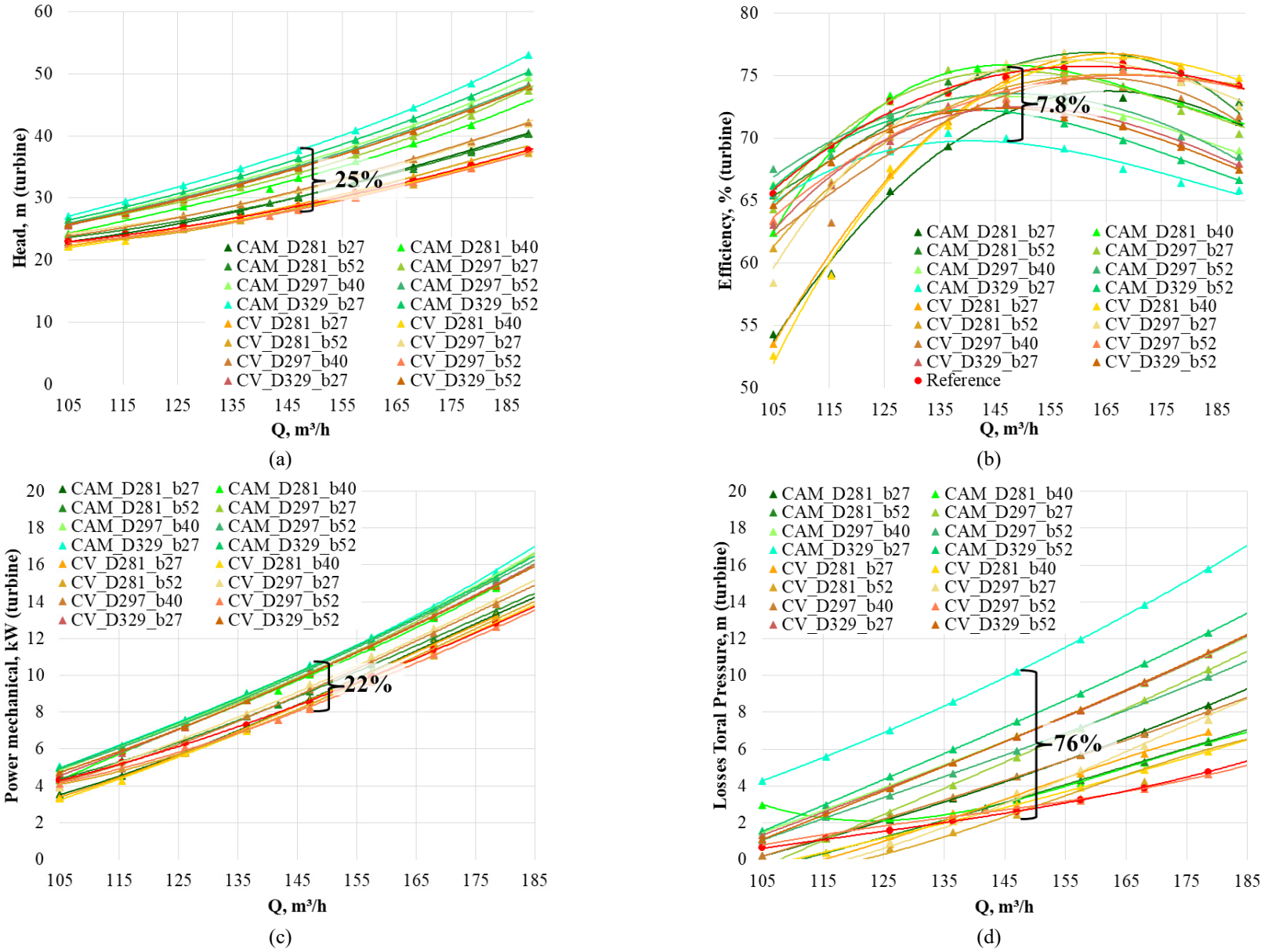

Figure 8.4 – PAT characteristics for different volute geometries: a) Head curves, b) Efficiency curves, c) Power mechanical curves, d) Total pressure losses curve

Efficiency

In turbine mode, unlike in pump mode, the influence of the parameters is observed more clearly. In particular, a smaller cross-sectional area shifts the BEP towards lower flow rates (Figure 8.5). This shift is 8%. It should be noted that, for the pump with low n_q, the smaller cross-sectional area was obtained using the CAM method than for the CV method, whereas the opposite trend was observed for the pump with a high specific speed. An increase of D_3 also shifts the BEP towards lower flow rates, on average by 12% (4,2% for Omega PAT). The effect of changes in b_3 on efficiency is difficult to define, as it is not observed in all combinations of geometric parameters.

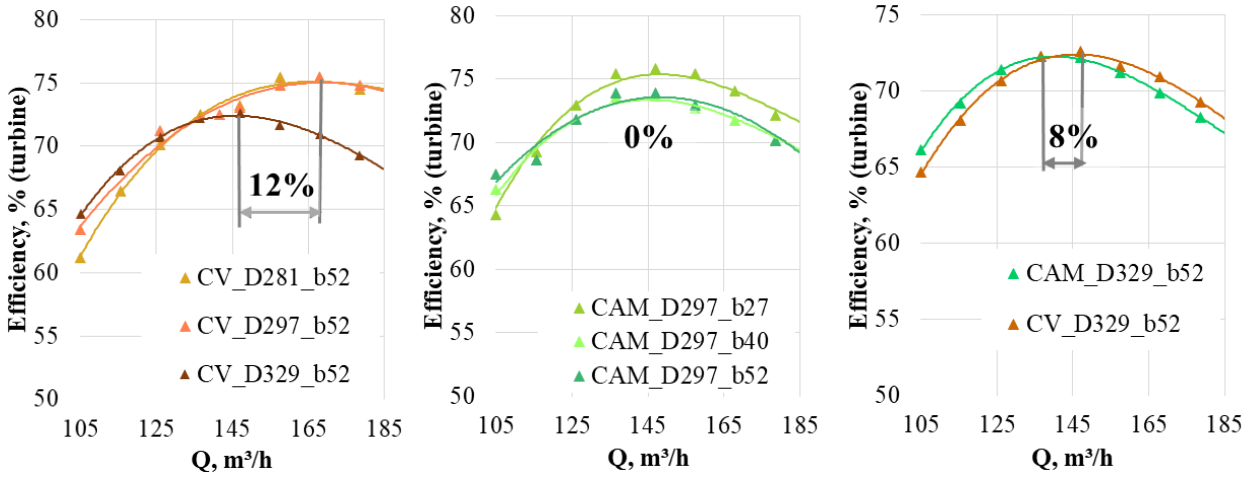

(a) (b) (c)

Figure 8.5 - Effects of geometric parameters on efficiency with changes in: a) D_3, b) b_3, c) design method

Among the analysed volutes, the most favourable volute for turbine mode was selected using Pareto front (Figure 8.6). The selection criteria were the highest efficiency at the lowest flow rate. These criteria were met by the volute No. 4 designed using the CAM method, with D_3 = 297 mm and b_3 = 27 mm. Similarly, the least favourable volute was identified. This volute No. was designed using CAM method, with D_3 = 281 mm, b_3 = 27 mm.

To check whether all recommendations are equally useful for pumps with high and low n_q, an additional volute was calculated for the DHV pump. Its parameters D_3 and b_3 were selected according to the most favourable result obtained for the Omega pump. Thus, b_3 was calculated using the same equation as for the Omega pump: $b_3 = b_2 + 1 \dots 2$ [41] (b_3 = 21 mm for DHV pump, b_3 = 105 mm Omega pump). The value of D_3 was calculated using the ratio corresponding to the Omega pump: D_3/D_2 = 1.22 (D_3 = 329 mm for DHV pump, D_3 = 522 mm Omega pump).This recommendation does not give the most favourable result for DHV. For DHV pump this volute (No. 8) has the lowest efficiency among all analysed volutes (70% at Q_{opt}, see Figure 8.9), but at the same time it has lowest Q_{opt} = 136 m^3/h. An excessively large value of D_3 caused the maximum shift of Q_{BEP} towards lower flow rates and made the efficiency curve flatter. However, it also reduced the efficiency. Similar results were obtained by authors in article [125].

This means that changes in geometrical parameters have a limited beneficial range for pumps. This range differs depending on the specific speed n_q. Beyond this range, further changes do not lead to the expected improvement in performance. Therefore, not all recommendations for selecting geometrical parameters are equally suitable for pumps with different values of n_q.

The verification of the Omega-derived recommendation on DHV demonstrates that the optimum geometric ratios depend on n_q, and that recommendations developed for one specific speed cannot be transferred uncritically to machines of substantially different specific speed. This finding is consistent with the conclusions of [125].

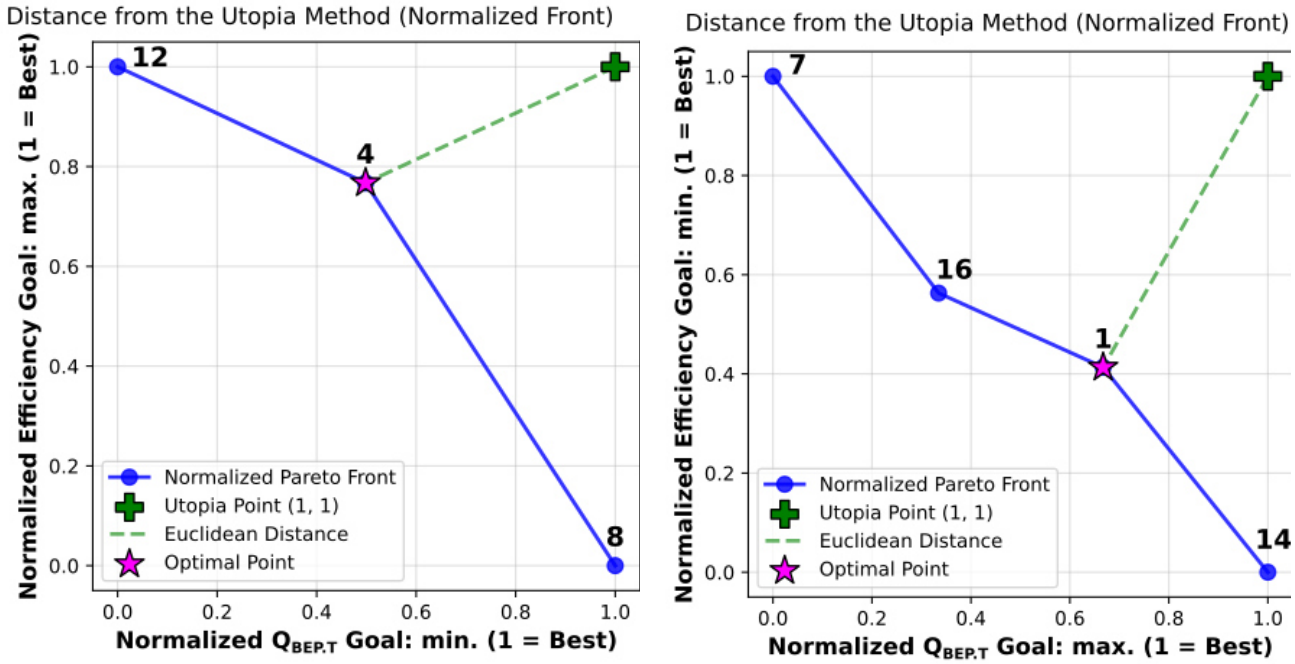

(a) Most favourable for PAT

No.	Method	D_3	b_3	$Q_{BEP.T}$	*Eff*.	Utopia Distance
4 ★	**CAM** ★	**297** ★	**27** ★	**147** ★	**75.8** ★	**0.55** ★

(b) Least favourable for PAT

No.	Method	D_3	b_3	$Q_{BEP.T}$	*Eff*.	Utopia Distance
1 ★	**CAM** ★	**281** ★	**27** ★	**157** ★	**73.4** ★	**0.67** ★

Figure 8.6 – Selection of the volute: a) most favourable for PAT, least favourable for PAT

The flatness of the efficiency curve

The selection of the volute with the flattest efficiency curve and the highest efficiency was carried out using the same method as described in 0. Table 8.2 presents the calculated results for all volutes. According to these data, the flattest efficiency curve has volute designed by the CV method, D_3 = 297 mm and hight b_3 = 52 mm. The result is similar to that obtained for the Omega pump.

Table 8.2 – Average deviation from peak efficiency A (Flatness)

N_r	A_{max}	Method	D_3	b_3	N_r	A_{max}	Method	D_3	b_3
14	0.32	CV	297	52	11	1.17	CV	281	52
10	0.65	CV	281	40	2	1.18	CAM	281	40
3	1.04	CAM	281	52	9	1.20	CV	281	27
13	1.06	CV	297	40	1	1.28	CAM	281	27
16	1.12	CV	329	52	4	1.32	CAM	297	27
5	1.13	CAM	297	40	15	1.36	CV	329	27
8	1.14	CAM	329	52	7	1.41	CAM	329	27
6	1.15	CAM	297	52	12	1.59	CV	297	27

The analysis of the optimal volute design, based on the criteria of the highest efficiency and the flattest efficiency curve, was carried out using the Pareto front (Figure 8.7) and the Utopia point distance method. According to the presented data, the pump with the volute that has the flattest efficiency curve, and at the same time the highest efficiency under the given conditions, is volute designed by CV method, has smallest D_3 value (281 mm) and middle b_3 (40 mm).

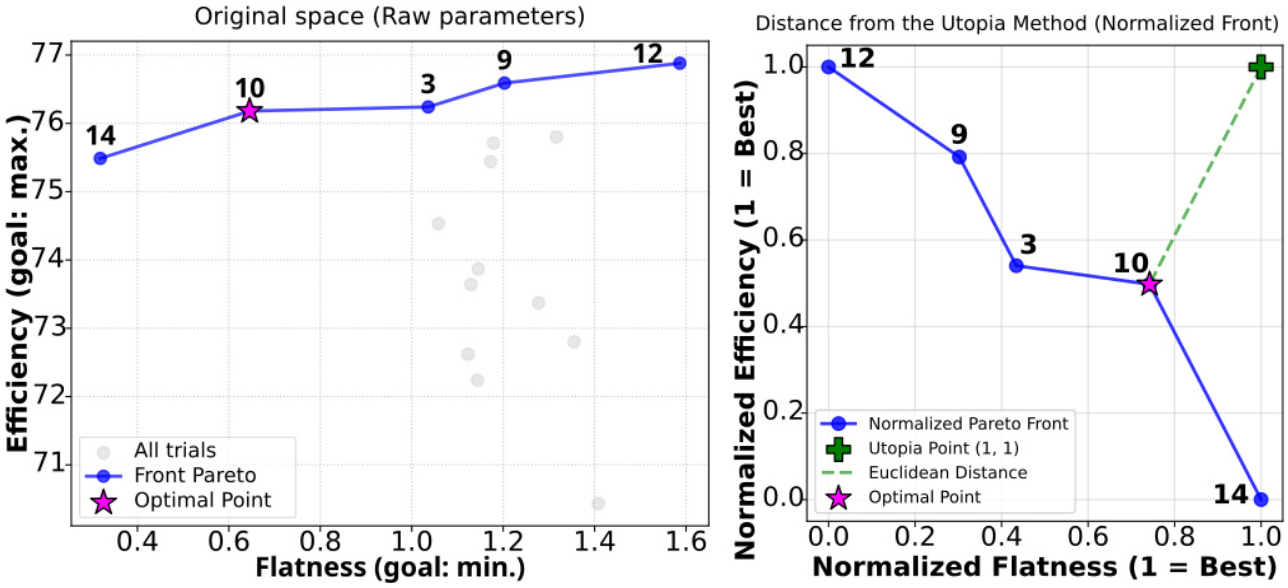

(a) (b)

No.	Method	D_3	b_3	Flatness	Efficiency	Utopia Distance
10 ★	**CV** ★	**281** ★	**40** ★	**0.65** ★	**76.18** ★	**0.56** ★
3	CAM	281	52	1.04	76.24	0.73

Figure 8.7 – Selection of the flattest curve with hight efficiency: a) Pareto front, b) Utopia point distance

8.1.3 Selection of the compromise volute casing for pump and turbine operation mode

Using the Pareto front, the volute design providing the compromise between operation in turbine and pump mode was identified (Figure 8.8).

The volute was selected using based on a four-criteria Pareto analysis: maximization of efficiency in pump and turbine mode, minimization of $Q_{BEP.P}$, and $Q_{BEP.T}$. According to this criterion, the compromise design was the CAM volute (No. 3) with the smallest value of D_3, equal to 281 mm, and the largest value of b_3, equal to 52 mm. At the same time, this volute has one of the flattest efficiency curves (Figure 8.7).

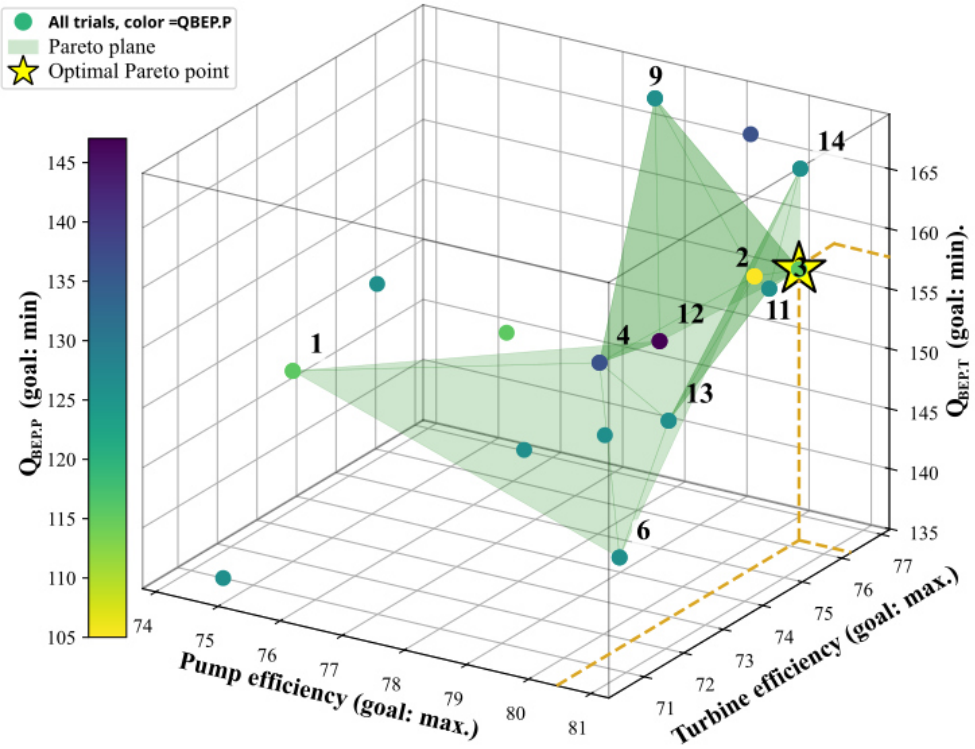

No.	Method	D_3	b_3	Pump Eff.	Turbine Eff.	$Q_{BEP.P}$	$Q_{BEP.T}$	Utopia Distance
3	**CAM** ★	**281** ★	**52** ★	**80.45** ★	**76.24** ★	**115** ★	**157** ★	**0.74** ★

Figure 8.8 – Selection of the favourable volute design for pump and turbine modes (Pareto front)

8.1.4 Hydrodynamic analysis

8.1.4.1 Analysis of the selected volutes

Based on the analysis presented in Section 0, the volutes listed in Table 8.3 were selected for further analysis.

Table 8.3 – Representative volute variants selected for further analysis

No.	Volute design category	Method	D_3	b_3	Selection criteria
4	Most favourable performance in turbine mode	CAM	297	27	Max. efficiency with smallest Q_{BEP}
10	Flattest efficiency curve in turbine mode	CV	281	40	Max. efficiency and the max. flatness of the efficiency curve
3	Compromise solution for both pump and turbine operation	CAM	281	52	Max. efficiency with smallest Q_{BEP} for pump and PAT
1	Least favourable performance in turbine mode	CAM	281	27	Min. efficiency with higher Q_{BEP}
8	Suboptimal for turbine	CAM	329	27	Adopted from Omega best-performing volute ratio (D_3/D_2 = 1.22)

The pump with the above-mentioned volutes is compared with the corresponding pumps operating in pump mode in Figure 8.9. The comparison indicates that, in pump mode, the differences in efficiency and head are not as significant as in turbine mode. In PAT mode, the maximum shift of the BEP towards higher flow rates for the selected volutes reaches 19% whereas in pump mode this value is 15%. Similarly, the difference in head reaches 25% in PAT mode and 7% in pump mode.

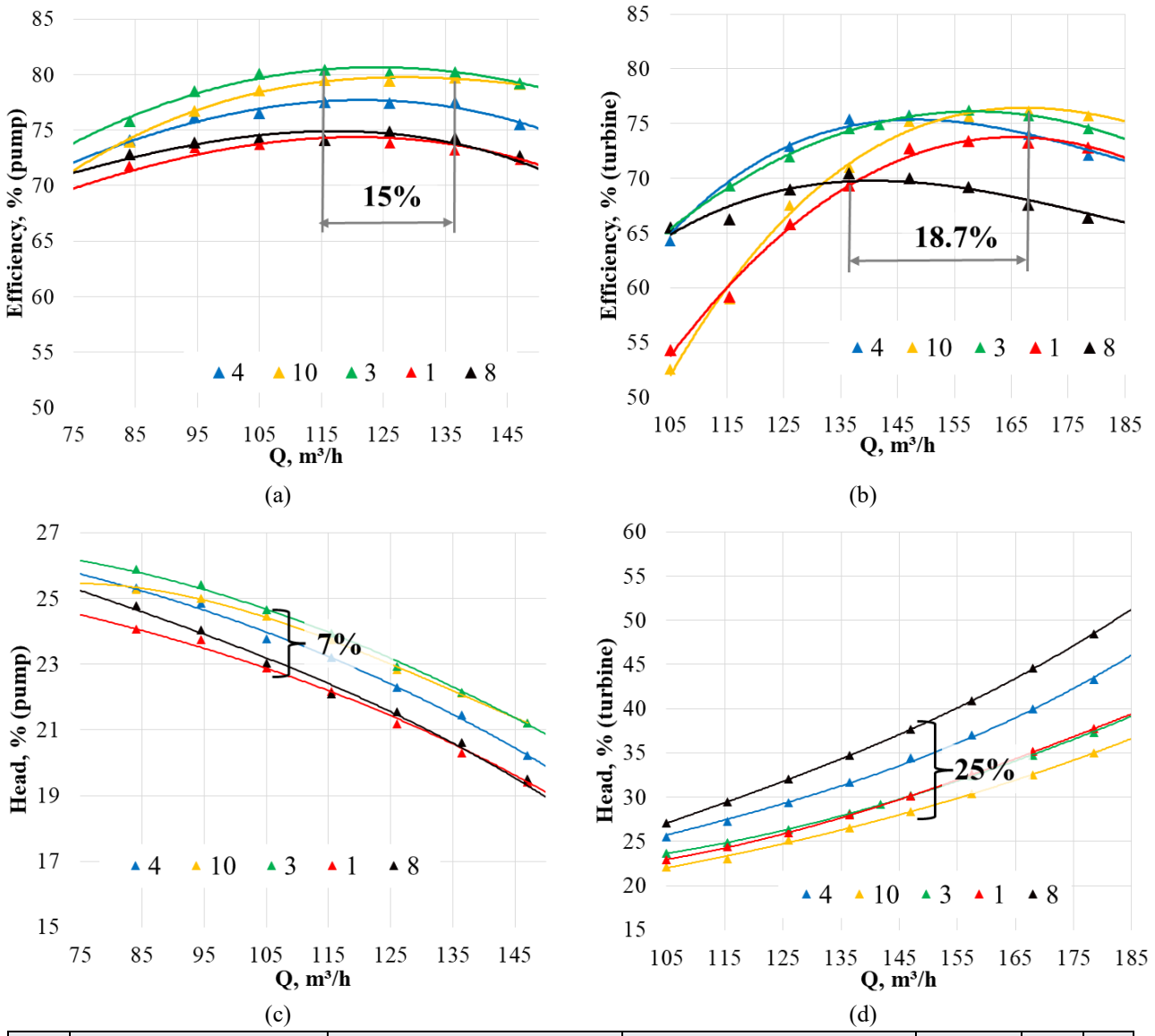

No.	Volute design category	Turbine		Pump		Method	D_3	b_3
		$Q_{BEP.T}$, m³/h	Efficiency at $Q_{BEP.T}$, %	$Q_{BEP.P}$, m³/h	Efficiency at $Q_{BEP.P}$, %			
4	Most favourable	147	75.8	136	77.5	CAM	297	27
10	Flattest	168	76.2	136	79.7	CV	281	40
3	Compromise solution	157	76.2	115	80.5	CAM	281	52
1	Less favourable	157	73.4	115	74.1	CAM	281	27
8	Suboptimal for turbine	136	70.4	126	74.9	CAM	329	27

Figure 8.9 - Performance curves for selected volutes: a) pump efficiency, b) PAT efficiency, c) pump head, b) turbine head

Comparing these data with the results for the high-n_q Omega pump, it can be stated that the Q_{BEP} shift is greater for the low-n_q pump than for the high-n_q pump.

The distribution of the absolute velocity components at the impeller inlet (D_2) in the PAT for the volutes selected in the previous section is shown in Figure 8.10. Similarly to the results presented in Section 7.1.4.2 the pump with the most favourable volute (blue curve) has a high value of c_u, which is responsible for shifting Q_{BEP} towards lower flow rates. The highest value of c_u was observed for the

volute selected as suboptimal for turbine mode (has lowest efficiency). It can be attributed to exceptionally high hydraulic losses occurring within the volute casing itself (Figure 8.4d), which explains why the highest circumferential velocity component does not lead to the best turbine performance.

This observation refines the relationship between c_u and performance established for the Omega pump. A high value of c_u is necessary for high PAT performance, but it is not sufficient. It must be achieved without excessive losses in the volute itself.

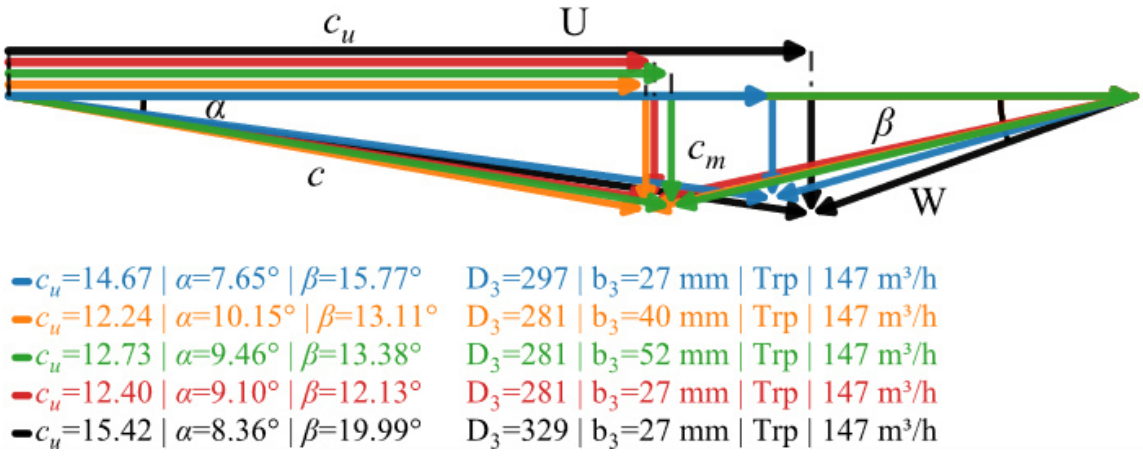

Figure 8.10 - Distribution of the absolute velocity components for PAT with selected volutes at $Q_{BEP.T}$ (147 m³/h)

8.1.4.2 Flow field visualization and analysis

Next analyses of the flow distribution in pump and PAT presented only for selected volutes, which represent the most significant changes in the flow structure and are of the greatest interest from the point of view of their operating parameters:

- the most favourable volute for PAT No. 4 (CAM D297 b27),
- least favourable volute for PAT No. 1 (CAM D281 b27),
- compromise volute No. 3 (CAM D281 b52).

The volute absolute velocity distribution at the longitudinal cross-sectional plane of pump operating in turbine mode is shown in Figure 8.11.Figure 8.11. It can be observed that, at the same flow rate, the absolute velocity near the impeller inlet (D_2) is higher and more uniform in volute No. 4 than in volute No. 1. In the least favourable volute, a large flow separation zone occurs in the region between 180˚ and 270˚, in contrast, in the most favourable volute, this zone is barely noticeable.

An analogous cross-section is presented for the same volutes operating in pump mode (Figure 8.12). Volute No. 4 shows a less uniform velocity distribution in pump mode than in turbine mode. This non-uniformity is observed in the diffuser and results from the flow behaviour within the 0˚ sector of the volute. The volute identified as the least favourable in turbine mode also shows stronger vortices in diffuser.

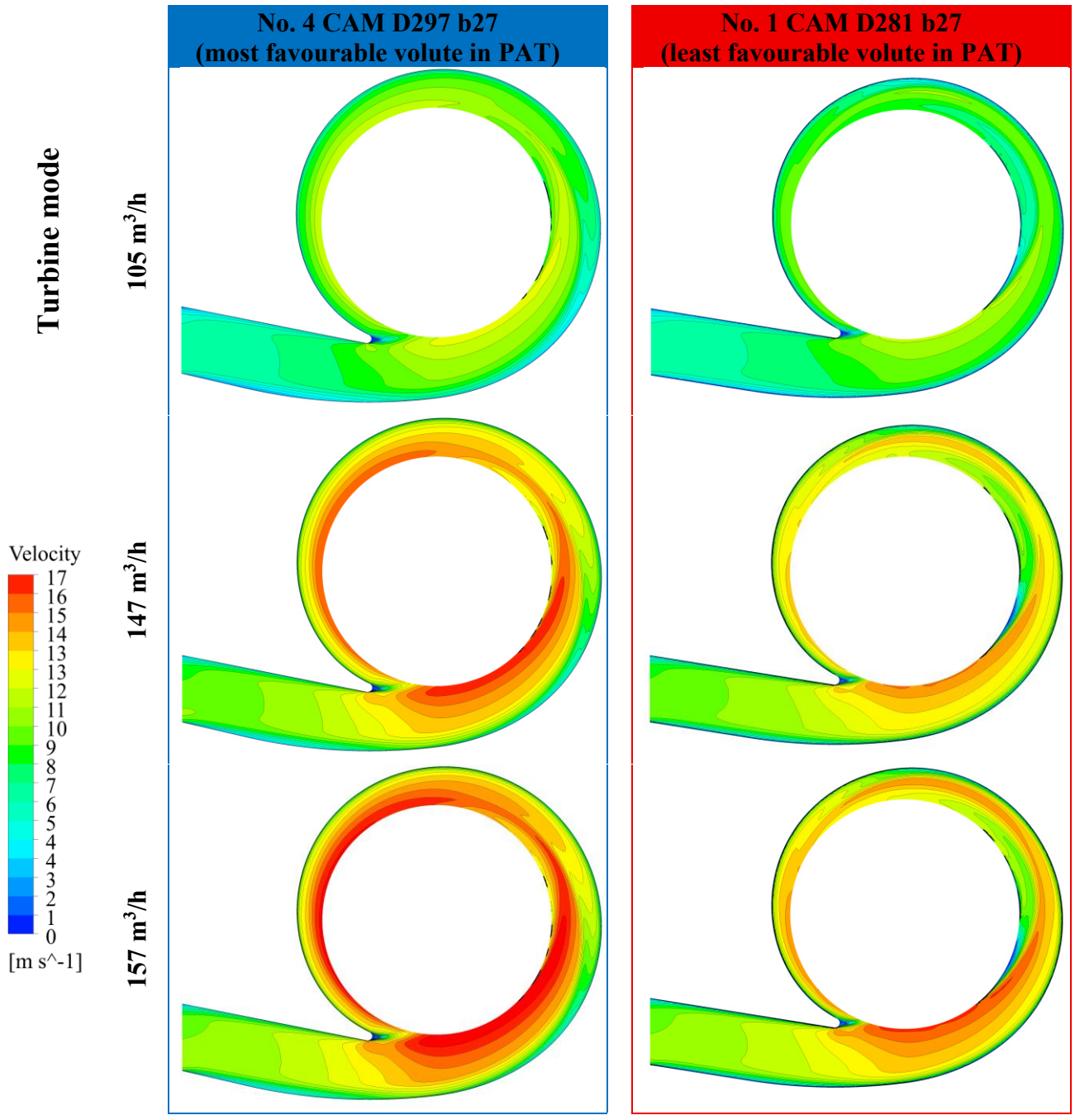

Figure 8.11 – Distribution of absolute velocity at the longitudinal cross-sectional plane in the **PAT** under different flow rates

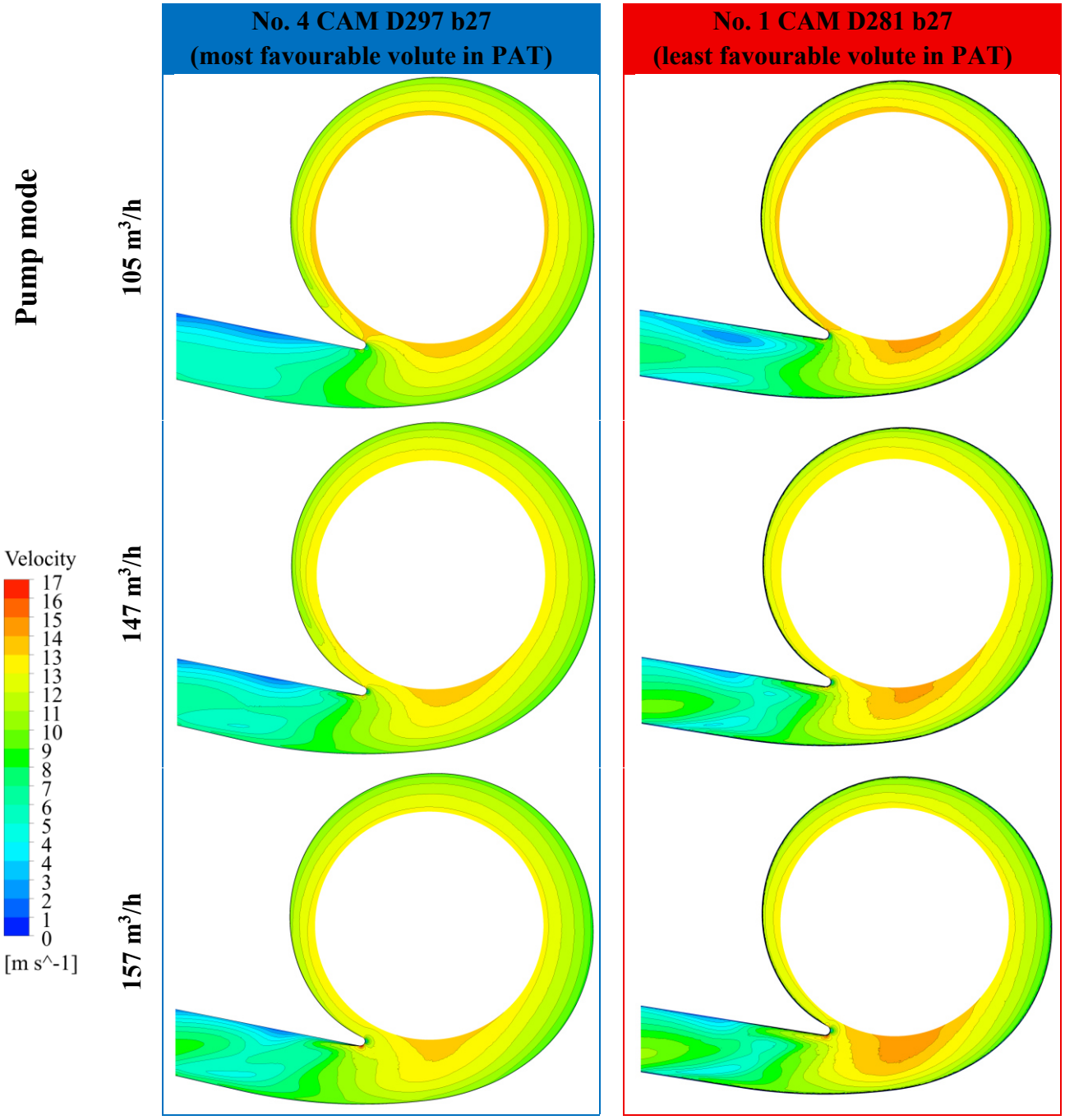

Figure 8.12 – Distribution of absolute velocity at the longitudinal cross-sectional plane in the **pump** under different flow rates

In PAT mode, the volute guides the flow towards the impeller and affects vortex formation inside the impeller passages. Figure 8.13, Figure 8.14 present the flow structure in the impeller at flow rates of 115 and 147 m³/h for both pump and PAT operation, corresponding to the BEP conditions.

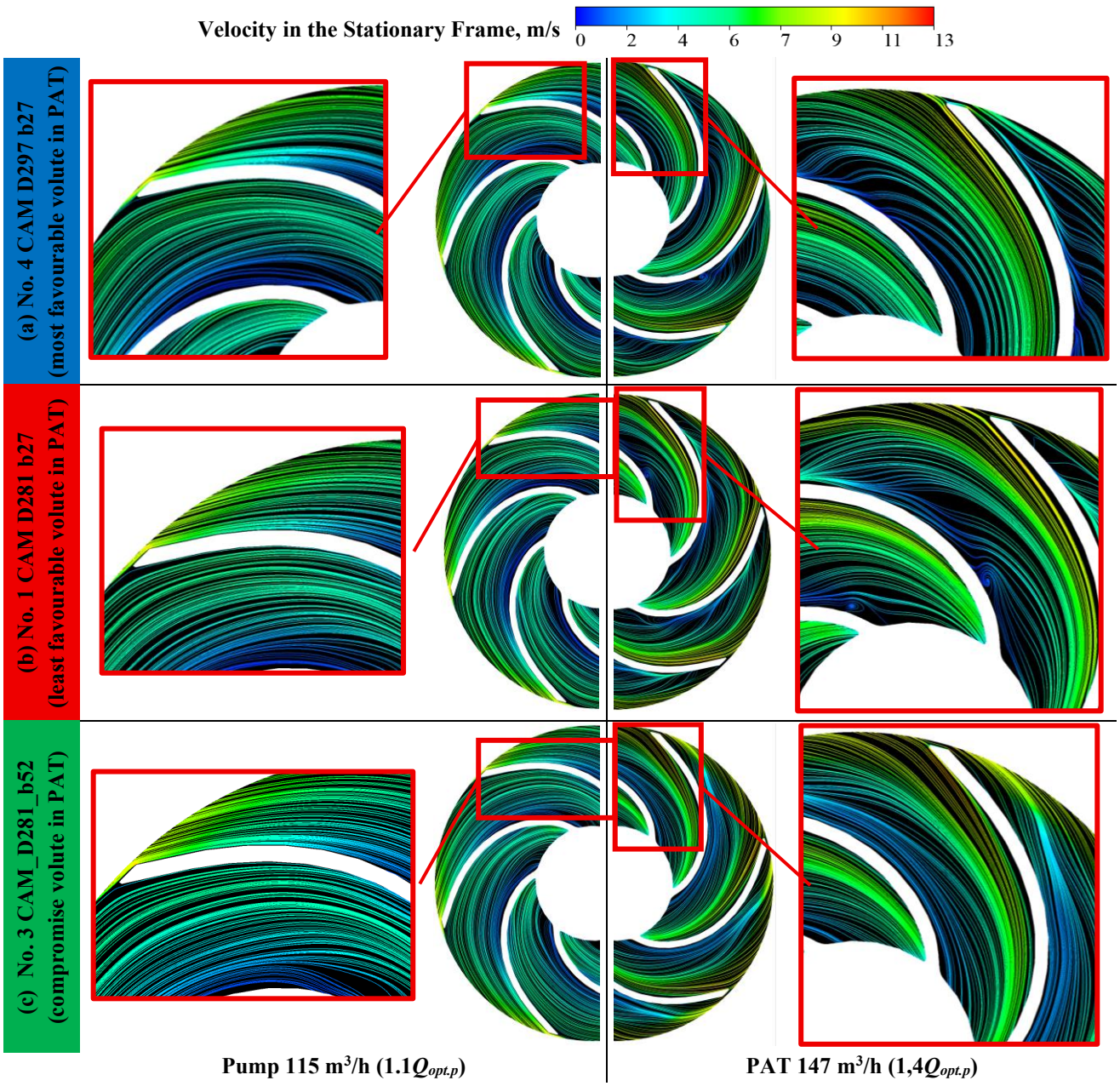

Figure 8.13 – Flow streamlines inside the pump impeller at Q = 115 m³/h, PAT impeller at Q = 147 m³/h

For the most favourable volute in PAT mode No. 4, the not uniformly guided into the blade passage, and local deviations of the streamlines from the blade direction can be observed near the leading edge. This indicates possible incidence losses and local flow separation, which may negatively affect the hydraulic performance of the impeller. The observed streamline pattern in the impeller suggests unfavourable inlet flow conditions. In turbine mode, these conditions correspond to the outlet flow conditions from the volute. For the volute identified as the least favourable, the flow structure in the impeller is even less stable, and a vortex zone can be observed near the blade pressure side,

according to the pump-mode blade orientation. As the flow rate increases, this vortex zone becomes weaker. Among the three analysed variants, the impeller with the compromise volute casing shows the most favourable flow distribution, although it is not fully uniform.

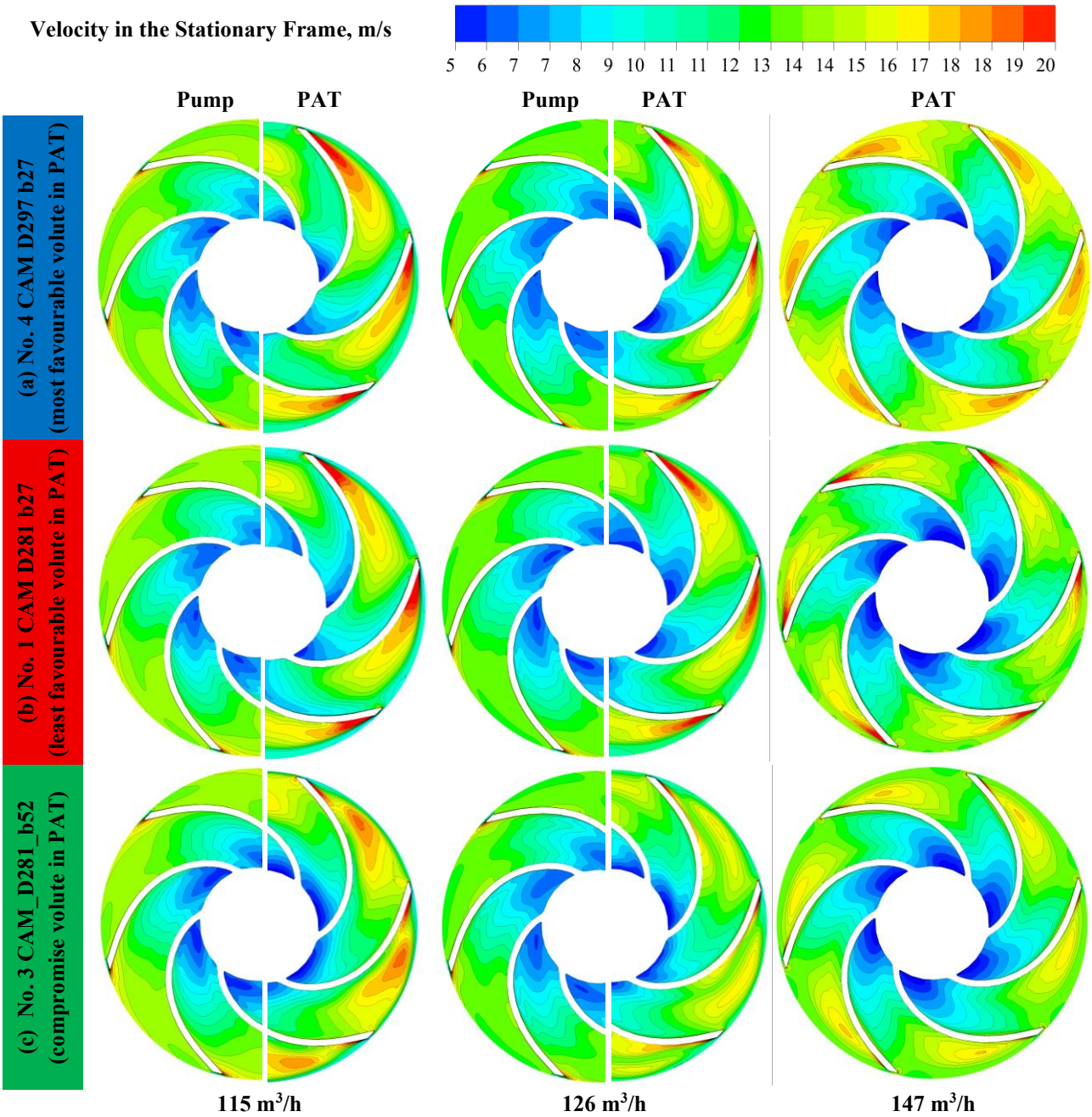

Figure 8.14 – Distribution of absolute velocity at the impeller in the pump and PAT under different flow rates

For all three analysed pump operating in pump mode, the flow pattern in the impeller is uniform. At the same time, a gradual increase in fluid velocity from the inlet to the outlet of the impeller blade passages can be observed for all flow rate (Figure 8.14). In turbine mode, the opposite trend is observed. The highest velocity occurs near the outlet edge on the blade pressure side. Then, the velocity decreases along the impeller blade passage and towards the impeller inlet from the volute.

8.1.5 Section summary

The aim of DHV pump study was to verify the results obtained for the Omega pump. Therefore, it was carried out using a smaller number of analysed volutes. The DHV study confirmed that changes in geometric parameters have a similar effect on pumps with both high and low n_q.

It was found that the change in cross-sectional shape did not show a clear advantage of either the round or trapezoidal shape. However, the observed trend indicated a slight advantage of the trapezoidal shape, as in the case of the Omega pump. Therefore, to reduce the number of calculations, the DHV study was limited to volutes with a trapezoidal cross-section and a volute wall opening angle of 40˚.

The influence of the volute geometric parameters for the DHV pump at Q_{BEP} = 115 m^3/h in pump mode is 8% for head, 0.7% for mechanical power, 8% for efficiency, and 40% for pressure losses in the volute. In turbine mode, these values are 25% for head, 22% for mechanical power, 7.8% for efficiency, and 76% for pressure losses in the volute. The maximum shift of Q_{BEP} was 18,7% in turbine mode and 15% in pump mode.

Among the analysed volutes, the trapezoidal volute (No. 1) designed using the CAM method, with D_3 = 281 mm and b_3 = 27 mm, was selected as the least for turbine mode, because it met the criterion of the smallest efficiency at the higher flow rate. The most favourable volute for PAT (No. 4) was designed by CAM method with D_3 = 297 mm and b_3 = 27 mm.

A volute, which designed with the same D_3/D_2 ratio and use the same equation for b_3, as the most favourable Omega volute, was the least favourable among all volutes designed for the DHV pump, both in pump and turbine modes. This confirms that not all recommendations for geometric parameters are equally suitable for pumps with different values of n_q and the selection of the volute casing geometric parameters is subject to certain limitations.

The pump that has the flattest efficiency curve, and at the same time the highest efficiency under the given conditions, has volute designed by CV method with smallest D_3 value (281 mm) and middle b_3 (40 mm).

The compromise volute design, which provides the highest efficiency in both pump and turbine modes and the lowest flow rate at Q_{BEP}, is the volute designed be CAM method with the smallest value of D_3 (281 mm), and the largest value of b_3 (52 mm).

The analysis of the flow structure in the volute casing and the impeller indicated the reasons for the reduction in operating parameters. These were mainly related to the non-uniform inflow to the impeller in turbine mode, which deteriorated the flow structure in the inter-blade passages of the impeller and, in some cases, caused vortex regions. This also led to a local increase in velocity at the impeller inlet.

In pump mode, a uniform increase in velocity is observed within the inter-blade passages of the impeller. However, at the volute inlet, the velocity increases significantly in the region upstream of the volute tongue, which subsequently results in a non-uniform flow distribution in the volute diffuser.

8.2 Statistical Analysis of the DHV pump

A statistical analysis was carried out using the same approach as described in Section 7.2 using multiple linear regression estimated by ordinary least squares.

8.2.1 Pump mode

The degree of influence of the geometric parameters on the pump performance in pump mode at Q_{BEP} (115 m^3/h) is presented in Table 8.4. The results for the 1.0$Q_{nom.p}$, 0.7$Q_{nom.p}$ and 1.2 $Q_{nom.p}$ are presented in Appendix K. The Partial R² metric expresses this influence as a numerical value.

Table 8.4 - Factor effects in the regression model at $Q_{BEP.P}$

Head								Power mechanical							
Factor	R^2	ΔR^2 (drop-one)	Partial R^2	F	Numerator df	Denominator df	p-value	Factor	R^2	ΔR^2 (drop-one)	Partial R^2	F	Numerator df	Denominator df	p-value
b_3	0.833	0.580	0.777	17.40	2	10	5.54×10^{-4}	b_3	0.430	0.361	0.387	3.16	2	10	8.63×10^{-2}
D_3	0.833	0.122	0.423	3.66	2	10	6.42×10^{-2}	Method	0.430	0.031	0.052	0.55	1	10	4.75×10^{-1}
Method	0.833	0.044	0.209	2.63	1	10	1.36×10^{-1}	D_3	0.430	0.021	0.035	0.18	2	10	8.38×10^{-1}
Efficiency								**Losses total pressure**							
Factor	R^2	ΔR^2 (drop-one)	Partial R^2	F	Numerator df	Denominator df	p-value	Factor	R^2	ΔR^2 (drop-one)	Partial R^2	F	Numerator df	Denominator df	p-value
b_3	0.844	0.611	0.796	19.53	2	10	3.52×10^{-4}	b_3	0.756	0.572	0.700	11.69	2	10	2.41×10^{-3}
D_3	0.844	0.119	0.433	3.81	2	10	5.88×10^{-2}	D_3	0.756	0.076	0.237	1.55	2	10	2.59×10^{-1}
Method	0.844	0.028	0.153	1.81	1	10	2.08×10^{-1}	Method	0.756	0.026	0.096	1.06	1	10	3.26×10^{-1}

The statistical analysis showed (Table 8.4) that the only statistically significant factor affecting the pump performance parameters is b_3. It affects head and efficiency, and its influence increases with increasing flow rate (Figure 8.15). The influence of the parameters on mechanical power and losses is statistically insignificant at all flow rates (p-values >0.05). Therefore, it is not shown in Figure 8.15.

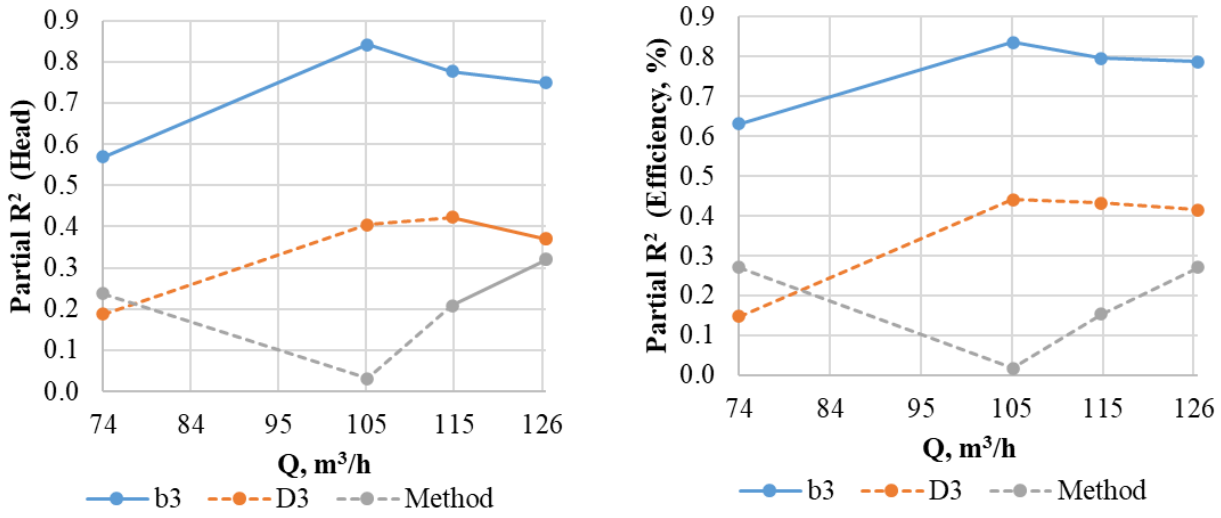

(a) (b)

Figure 8.15 - Comparison of factors by partial R^2: a) Head, b) Efficiency, where solid lines indicate statistically significant results (p-values <0.05), while dashed lines indicate statistically insignificant results (p-values >0.05)

Estimated effects of factor levels relative to the base level by the method of least squares in a linear regression model at Q_{BEP}, are presented in Table 8.5, where the base level is the first sorted category for each factor: Method - CAM, D_3 281 and 297 mm, b_3 27 and 40 mm.

Table 8.5 - OLS estimates of factor-level effects vs base level at $Q_{BEP.P}$

Head								Power mechanical							
Factor	Parametr			Δ, m	p-value	95% CI, lower	95% CI, upper	Parametr			Δ, kW	p-value	95% CI, lower	95% CI, upper
Method	CAM	lower than	CV	-0.24	0.14	-0.57	0.09	CAM	lower than	CV	-0.01	0.48	-0.05	0.02
D_3	281	lower than	297	-0.04	0.81	-0.42	0.34	281	lower than	297	0.00	0.98	-0.04	0.04
D_3	281	higher than	329	0.46	0.04	0.02	0.91	281	lower than	329	-0.01	0.59	-0.06	0.04
D_3	297	higher than	329	0.51	0.03	0.06	0.95	297	lower than	329	-0.01	0.60	-0.06	0.04
b_3	27	lower than	40	-0.82	0.00	-1.26	-0.38	27	higher than	40	0.03	0.16	-0.02	0.08
b_3	27	lower than	52	-0.95	0.00	-1.32	-0.57	27	higher than	52	0.04	0.03	0.00	0.08
b_3	40	lower than	52	-0.12	0.54	-0.57	0.32	40	higher than	52	0.01	0.56	-0.03	0.06
Efficiency								**Losses total pressure**						
Factor	Parametr			Δ, p.p	p-value	95% CI, lower	95% CI, upper	Parametr			Δ, m	p-value	95% CI, lower	95% CI, upper
Method	CAM	lower than	CV	-0.70	0.21	-1.86	0.46	CAM	higher than	CV	0.19	0.33	-0.22	0.61
D_3	281	lower than	297	-0.12	0.85	-1.46	1.22	281	higher than	297	0.18	0.43	-0.30	0.66
D_3	281	higher than	329	1.69	0.04	0.13	3.26	281	lower than	329	-0.27	0.32	-0.83	0.30
D_3	297	higher than	329	1.81	0.03	0.24	3.38	297	lower than	329	-0.45	0.11	-1.01	0.12
b_3	27	lower than	40	-3.02	0.00	-4.59	-1.45	27	higher than	40	0.961	0.00	0.39	1.53
b_3	27	lower than	52	-3.57	0.00	-4.90	-2.23	27	higher than	52	0.94	0.00	0.46	1.42
b_3	40	lower than	52	-0.55	0.46	-2.11	1.02	40	lower than	52	-0.019	0.94	-0.59	0.55

For most observations at Q_{BEP}, $1.0Q_{nom.p}$, $0.7Q_{nom.p}$ and $1.2\ Q_{nom.p}$ factors are not statistically significant (p-value > 0.05), similarly to the results presented in Table 8.4. Based on the statistically significant results, it can be concluded that a volute with a smaller D_3 and a larger b_3 should be used to increase head and efficiency.

8.2.2 Turbine mode

A similar analysis was carried out for the PAT mode

The degree of influence of the geometric parameters on the PAT performance at $Q_{BEP.T}$ (147 m^3/h) is presented in Table 8.6,. The same analysis at flow rate 126 m^3/h and 157 m^3/h see Appendix L.

Table 8.6 - Factor effects in the regression model at $Q_{BEP.T}$

Head								Power mechanical							
Factor	R^2	ΔR^2 (drop-one)	Partial R^2	F	Numerator df	Denominator df	p-value	Factor	R^2	ΔR^2 (drop-one)	Partial R^2	F	Numerator df	Denominator df	p-value
D_3	0.904	0.606	0.863	31.52	2	10	4.81×10^{-5}	D_3	0.817	0.490	0.728	13.40	2	10	1.48×10^{-3}
Method	0.904	0.285	0.748	29.66	1	10	2.82×10^{-4}	Method	0.817	0.313	0.631	17.13	1	10	2.02×10^{-3}
b_3	0.904	0.040	0.293	2.07	2	10	1.77×10^{-1}	b_3	0.817	0.054	0.228	1.47	2	10	2.75×10^{-1}
Efficiency								**Losses total pressure**							
Factor	R^2	ΔR^2 (drop-one)	Partial R^2	F	Numerator df	Denominator df	p-value	Factor	R^2	ΔR^2 (drop-one)	Partial R^2	F	Numerator df	Denominator df	p-value
D_3	0.501	0.408	0.450	4.09	2	10	5.04×10^{-2}	D_3	0.896	0.659	0.863	31.57	2	10	4.78×10^{-5}
b_3	0.501	0.007	0.014	0.07	2	10	9.32×10^{-1}	Method	0.896	0.168	0.617	16.14	1	10	2.45×10^{-3}
Method	0.501	0.005	0.010	0.10	1	10	7.58×10^{-1}	b_3	0.896	0.041	0.283	1.97	2	10	1.90×10^{-1}

The statistical analysis showed that the statistically significant factors affecting the PAT head, losses of total pressure and mechanical power is D_3 and method. All results for efficiency are

statistically unsignificant (p-value >0,05). The effects of this parameters are relatively stable with changing of flow rate (Figure 8.16). The main influence geometrical parameters are D_3 and method.

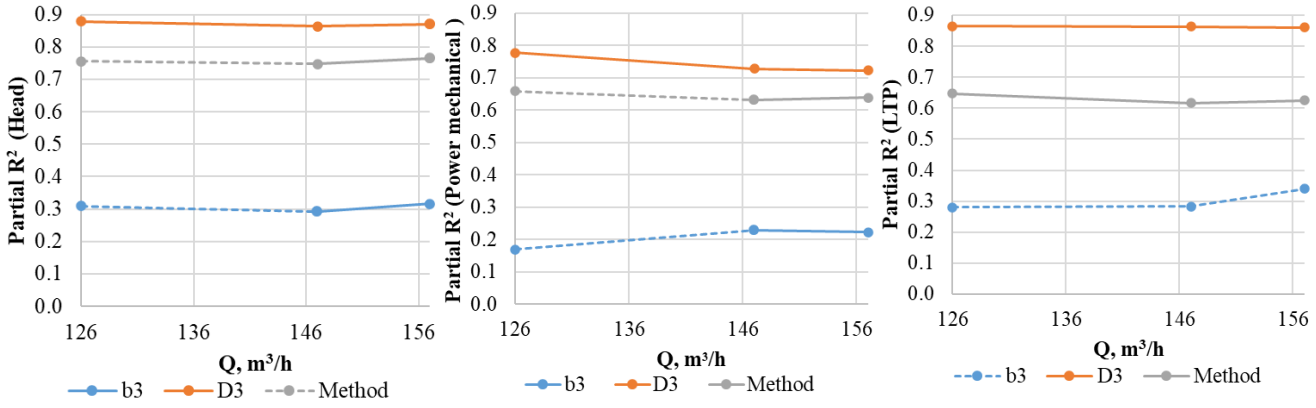

Figure 8.16 - Comparison of factors by partial R^2: a) Head, b) Mechanical power, c) Losses of total pressure, where solid lines indicate statistically significant results (p-values <0.05), while dashed lines indicate statistically insignificant results (p-values >0.05)

Estimated effects of factor levels relative to the base level by the method of least squares in a linear regression model are presented in Table 8.7.

Table 8.7 - OLS estimates of factor-level effects vs base level at $Q_{BEP.T}$

Head								Power mechanical							
Factor	Parametr			Δ, m	p-value	95% CI, lower	95% CI, upper	Parametr			Δ, kW	p-value	95% CI, lower	95% CI, upper
Method	CAM	higher than	CV	3.34	0.00	1.97	4.70	CAM	higher than	CV	0.95	0.00	0.44	1.46
D_3	281	lower than	297	-2.81	0.00	-4.39	-1.23	281	lower than	297	-0.81	0.01	-1.40	-0.22
D_3	281	lower than	329	-6.57	0.00	-8.42	-4.72	281	lower than	329	-1.57	0.00	-2.26	-0.88
D_3	297	lower than	329	-3.76	0.00	-5.61	-1.91	297	lower than	329	-0.76	0.03	-1.45	-0.07
b_3	27	lower than	40	-0.95	0.28	-2.80	0.90	27	lower than	40	-0.29	0.37	-0.98	0.40
b_3	27	higher than	52	0.73	0.32	-0.84	2.31	27	higher than	52	0.24	0.39	-0.35	0.82
b_3	40	higher than	52	1.68	0.07	-0.17	3.53	40	higher than	52	0.53	0.12	-0.16	1.22
Efficiency								**Losses total pressure**							
Factor	Parametr			Δ, p.p	p-value	95% CI, lower	95% CI, upper	Parametr			Δ, m	p-value	95% CI, lower	95% CI, upper
Method	CAM	lower than	CV	-0.22	0.76	-1.80	1.35	CAM	higher than	CV	1.70	0.00	0.76	2.64
D_3	281	higher than	297	0.18	0.83	-1.65	2.00	281	lower than	297	-1.50	0.01	-2.59	-0.41
D_3	281	higher than	329	2.56	0.02	0.42	4.70	281	lower than	329	-4.55	0.00	-5.83	-3.27
D_3	297	higher than	329	2.38	0.03	0.25	4.52	297	lower than	329	-3.05	0.00	-4.33	-1.77
b_3	27	lower than	40	-0.13	0.891	-2.27	2.00	27	higher than	40	0.051	0.93	-1.23	1.33
b_3	27	higher than	52	0.21	0.80	-1.61	2.03	27	higher than	52	0.90	0.10	-0.19	1.98
b_3	40	higher than	52	0.34	0.73	-1.79	2.48	40	higher than	52	0.844	0.17	-0.43	2.12

For most observations at a flow rate of 126 and 157 m³/h (Appendix L) b_3 are not statistically significant (p-value > 0.05). Based on the statistically significant results in Table 8.7, a higher value of D_3 and CAM method increase the head (Figure 8.3). In contrast, to increase efficiency, it is better to use a smaller D_3. This statistical analysis shows the best parameters for a single flow-rate point and does not account for the shift in Q_{BEP}. Indeed, Figure 8.5 show that in some volute comparisons at

147 m³/h, higher efficiency is obtained when the CV method and a smaller D_3 are used. However, this is also associated with a steeper efficiency curve and a shift of Q_{BEP} towards higher flow rates, and it reflects results for a single flow rate point rather than the overall behaviour.

The results for the DHV pump are mostly statistically insignificant, in contrast to the Omega pump. This is mainly because the effect of the sidewall gap and volute tongue. Figure 8.17 shows an example of the 180˚ cross-section for the reference Omega and DHV pumps. The yellow square marks the area corresponding to the sidewall gap. In the Omega pump, this area represents only a small part in comparison to the volute channel. In contrast, in the DHV pump, the sidewall gap area is larger than the area of the volute cross-section at 180˚.

A test calculation was performed for the volute with and without the sidewall gap in pump and turbine mode for DHV pump. The difference in efficiency at $Q_{nom.p}$ was 3% and at $Q_{BEP.T}$ 13% in accordance. Therefore, it can be concluded that the sidewall gap has a significant influence on pump and even more for PAT performance. The analysis of the sidewall gap is outside the scope of this dissertation, although it is a promising topic for future research.

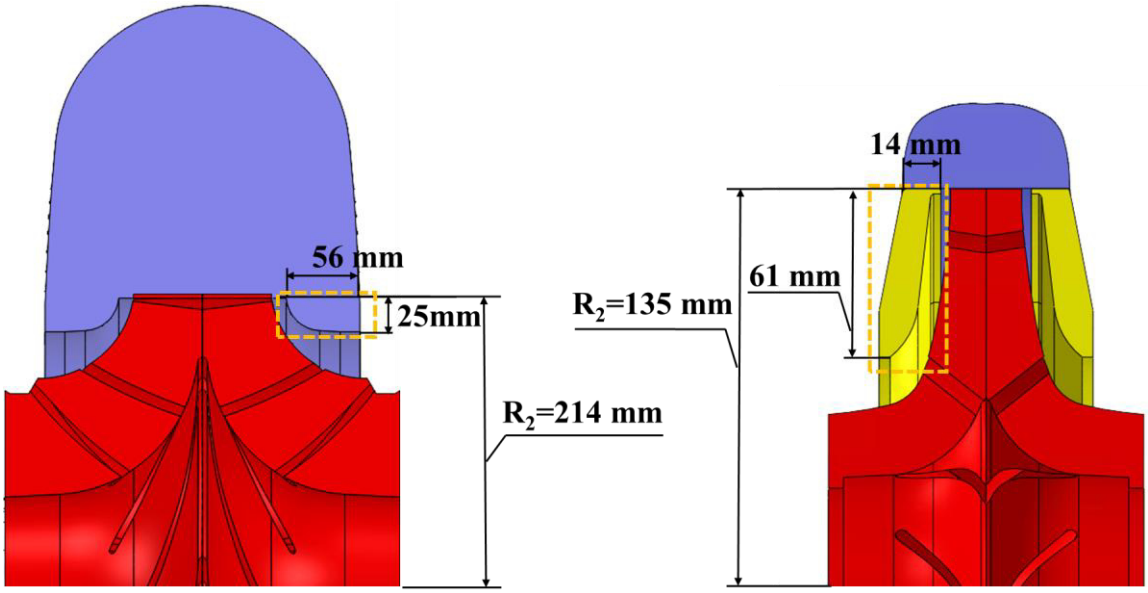

Figure 8.17 - Comparison of the sidewall gap region at the 180˚ cross-section: a) Omega pump, b) DHV pump

8.2.3 Regression analysis of best efficient point shift in turbine mode

The statistical analysis of the BEP shift was carried out using the same approach as described in Section 7.2.3.1.

According to the results presented in Table 8.8, the shift of $Q_{BEP.T}$ is mainly determined by the diameter D_3 and the volute design method. An increase in D_3, while the other parameters remain constant, shifts $Q_{BEP.T}$ towards lower flow rates by 11%. The use of the CV method, compared with CAM, shifts $Q_{BEP.T}$ towards higher flow rates by 8%. The effect of b_3 on the position of $Q_{BEP.T}$ was not statistically confirmed in this model.

Table 8.8 - The relationship between geometrical parameters and $\Delta Q_{BEP.T}$ shift

Change parameter	$\Delta Q_{BEP.T}$
D_3, mm: 281 (1.04D_2) → 329 (1.22 D_2)	← 11%
b_3, mm: 27 (1.04b_2) → 52 (2b_2)	→ 0.13%
Method: CAM → CV	→ 8%

The model quality assessment showed that the applied logarithmic regression model describes the shift of $Q_{BEP.T}$ well. The model was statistically significant F=24.25, p-value <0.001. The coefficient of determination (R^2=0.858) and the adjusted coefficient (Adjusted R^2=0.823) indicate that the model explains 85.8% and 82.3% of the variation in the dependent variable, respectively. The low value of (RMSE=0.028) indicates a small mean prediction error on the logarithmic scale, which corresponds to an approximate typical relative error of 2.8% for $Q_{BEP.T}$. The values (VIF = 1.001) and (Tolerance = 0.999) indicate no multicollinearity problem between the predictors.

The percentages shown in the table may differ from those reported in the numerical analysis section. This is because the statistical analysis presents averaged effects estimated using linear regression, whereas the numerical analysis reports the maximum observed deviation rather than the average effect.

8.2.4 Section summary

The statistical analysis was carried out in the same way as for the Omega pump. The main difference is that, for the DHV pump, most results are statistically insignificant. In pump mode, b_3 is the only statistically significant factor over the analysed range. At flow rates higher than Q_{BEP}, the design method and D_3 also become statistically significant. Based on the significant results, a smaller D_3 and a larger b_3 increase head and efficiency in pump mode.

In turbine mode, the statistically significant factors are D_3 and the design method, which mainly affect head, total pressure losses, and mechanical power. Their influence remains relatively stable over the analysed flow-rate range. The effects on efficiency are not statistically significant. The DHV pump results are mostly statistically insignificant because of the stronger influence of the sidewall gap and the volute tongue.

The regression analysis of the $Q_{BEP.T}$ shift showed that its position is mainly controlled by D_3 and the volute design method. A larger D_3 shifts $Q_{BEP.T}$ towards lower flow rates (11%), while the CV method shifts it towards higher flow rates compared with CAM (8%). The effect of b_3 was not statistically confirmed.

Chapter 9: Conclusions

This dissertation systematizes the influence of volute casing geometry on the energy characteristics of a double-entry centrifugal pump operating in pump and turbine modes. The analysis was carried out for two pumps with different specific speeds using CFD simulations, experimental validation, and statistical methods.

The literature review showed that many recommendations for selecting geometric parameters exist and confirmed the need for a systematic comparison of volute casing design recommendations and for a more detailed analysis of their influence on pump performance. This is especially important for pumps operating as turbines, where the available design guidelines are still limited and not sufficiently standardized. Such a systematization was carried out in this dissertation.

The influence of volute geometric parameters was investigated numerically for a high-specific-speed pump n_q = 66 (Omega). The CFD model was verified in pump mode by comparison with the manufacturer's catalogue data. The validation in turbine mode was performed using PAT performance prediction. The analysis was extended to a low-specific-speed pump n_q = 23 (DHV) and validated experimentally in both operating modes.

9.1 Confirmation of the thesis

The thesis formulated in Chapter 3 has been confirmed for two double-entry centrifugal pumps. The results showed that turbine-mode performance is more strongly influenced by changes in geometrical parameters than pump-mode performance.

For the Omega pump (n_q =66):

–in pump mode $\Delta Q_{BEP.P}$ = 9%, maximum difference for head and efficiency = 3%,

–in turbine mode $\Delta Q_{BEP.T}$ = 15%, maximum difference for head = 29% for efficiency = 5%,

For the DHV pump (n_q = 23):

– in pump mode $\Delta Q_{BEP.P}$ = 15%, maximum difference for head = 8%, for efficiency = 8%,

– in turbine mode $\Delta Q_{BEP.T}$ = 19%, maximum difference for head = 25%, for efficiency = 8%.

By appropriately selecting the geometrical parameters of the volute casing, it is possible to achieve a trade-off between pump and turbine performance with an acceptable decrease in pump-mode efficiency. The compromise volute for pump and turbine modes was identified using the following criteria: maximum efficiency and minimum Q_{BEP} in both modes. For Omega pump (high n_q) volute designed with smallest cross-section area (CV), with higher D_3 (522 mm), lowest b_3 (105 mm) and with trapezoidal shape was found to be the most favourable solution for both operation modes according to Pareto- Front analysis.

For the DHV pump, the following volute was selected as a compromise solution: smallest D_3 (281 mm), higher b_3 (52 mm), a trapezoidal cross-section, designed with smallest cross-section area (CAM method).

9.2 Main findings

Based on the experimental measurements, numerical simulations, and statistical analyses, the following conclusions can be drawn:

1. The influence of geometric parameters on the shift of the best efficiency point $Q_{BEP.T}$ was statistically determined.

For the Omega PAT:

- D_3, mm: 448 (1.04 D_2) → 522 (1.22 D_2) ← 5.2% $Q_{BEP.T}$
- b_3, mm: 105 (1.05 b_2) → 183 (1.74 b_2) → 4.2% $Q_{BEP.T}$
- Method: CAM → CV ← 3.73% $Q_{BEP.T}$
- Shape: Round → Trapezoidal ← 1.98% $Q_{BEP.T}$

For the DHV PAT:

- D_3, mm: 281 (1.04 D_2) → 329 (1.22 D_2) ← 11% $Q_{BEP.T}$
- b_3, mm: 27 (1.04 b_2) → 52 (2 b_2) → 0.13% $Q_{BEP.T}$
- Method: CAM → CV → 8% $Q_{BEP.T}$

2. An equation was proposed to describe the relationship between the volume flow rate at the $Q_{BEP.T}$ for the high n_q PAT and the geometrical parameters of the volute.

3. According to multiple linear regression estimated by ordinary least squares for the pump with high n_q, the most influential parameters in pump mode are b_3 and the cross-sectional shape. The other parameters are statistically insignificant. In turbine mode, the most influential parameters are D_3, b_3, and the design method.

For the pump with low n_q, only b_3 is statistically significant in pump mode, while the other parameters are not significant. In turbine mode, D_3 and the design method are the most important parameters, while b_3 has a smaller influence.

For the flatness of the efficiency curve, the most influential parameter is the design method, D_3 and the cross-sectional shape have a smaller influence. The effect of b_3 is not statistically significant.

4. The influence of geometric parameters on pump performance in both operating modes changes depending on the flow rate. In turbine mode, for the pump with n_q = 66, the influence of the geometrical parameters on total pressure losses in the volute increases with increasing flow rate. In contrast, their influence on efficiency decreases, while their influence on head and mechanical power remains relatively stable. For the pump with n_q = 23, most of the analysed geometrical parameters were statistically insignificant, and their influence did not change noticeably with the flow rate.

5. The study of the DHV pump showed that not all relative geometric parameter values are equally favourable for both specific speed values. This finding indicates an important limitation of the present design framework: relative geometric parameters should not be directly transferred between pumps of different specific speeds without recalibration.

6. However, although geometrical parameters have a limited beneficial range, the general direction of their influence remains consistent for both analyzed pumps. The graphical interpretation of the influence of geometric parameters on PAT performance curves for low and high specific speed pumps is presented in Table 9.1. The influence of geometrical parameters in pump mode generally shows trends opposite to those presented in Table 9.1.

Table 9.1 - Summary of the influence of geometric parameters on PAT performance curves for both values of n_q = 23 and 66

Design param.	Method (CV, CAM)	Shape (Trapezoidal, Round)	D_3 change	b_3 change
Modification	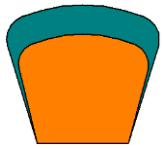	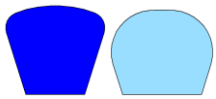	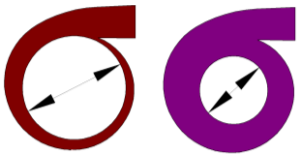	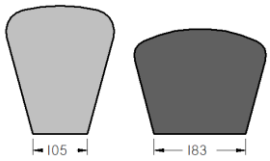
c_u	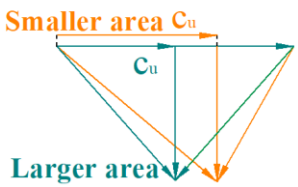	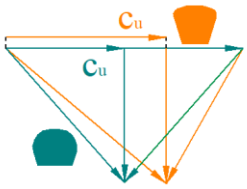	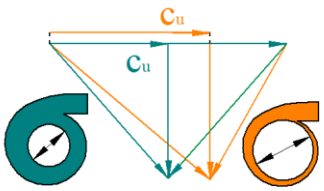	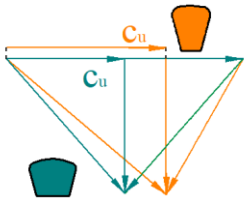
H-Q curve	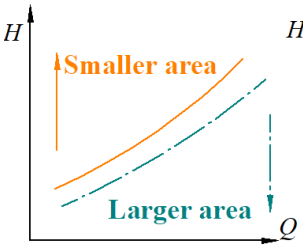	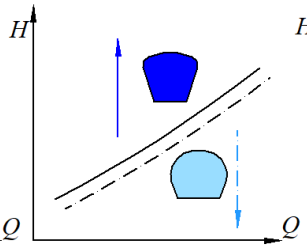	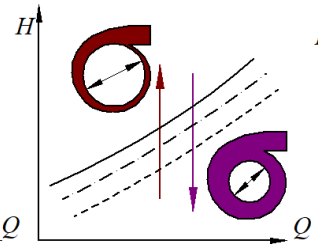	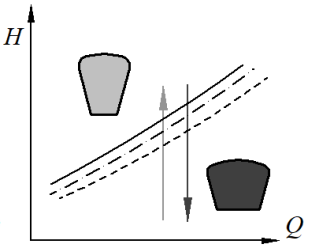
Pm-Q curve	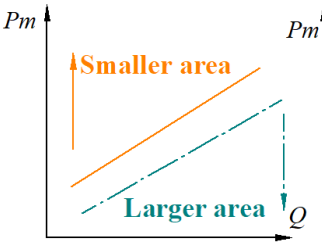	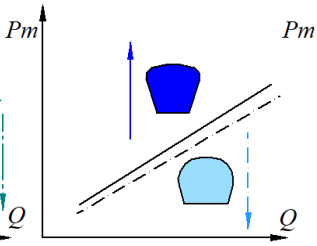	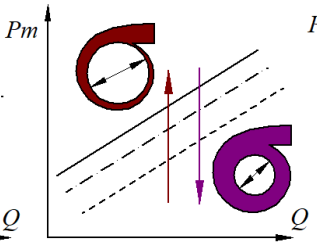	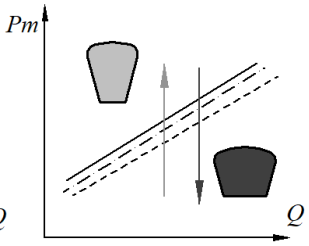
LTP-Q curve	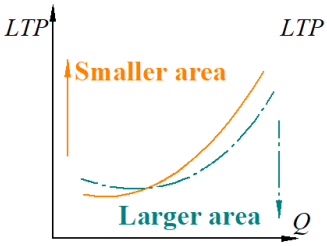	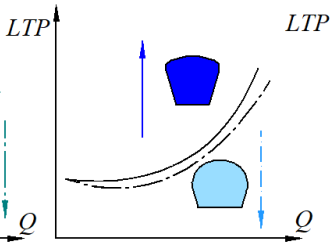	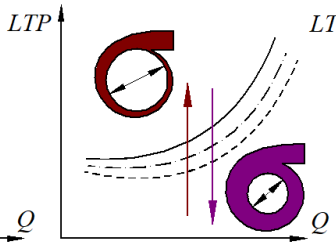	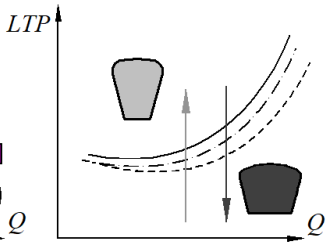
Eff-Q curve	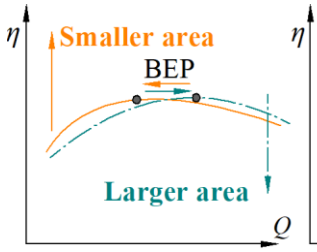	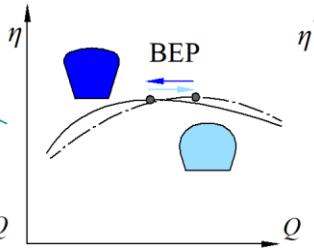	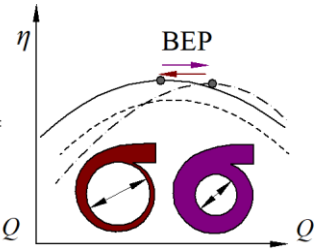	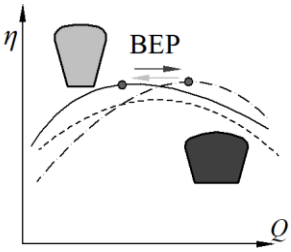

*a smaller cross-sectional area is obtained for low specific speed when using the CAM method, and for high specific speed when using the CV method

7. The analysis of the velocity triangles at the high n_q PAT impeller inlet made it possible to assess the direction and degree of the influence of volute geometry on the BEP and on the head increase. It was shown that increasing D_3 from 448 mm to 522 mm increases c_u by 9%. A smaller cross-sectional area (CV) also increases c_u by 6.7% compared with the larger cross-sectional area obtained using the CAM method. A trapezoidal cross-sectional shape increases c_u by 1.5%. In contrast, increasing the inlet width b_3 from 105 mm to 183 mm leads to a decrease in c_u by 7.7%.

9.3 Design recommendations for pump as turbine design

1. If there is a potential for using the pump in turbine mode, it is recommended to follow the design recommendations for turbine operation when designing the volute. This recommendation results from the fact that changes in volute geometry have a much stronger influence on the turbine-mode characteristics than on the pump-mode characteristics.
2. b_3 - recommended to use the Pfleiderer equation: $b_3 = b_2 + 1 \dots 2$ [41].
3. D_3 - recommended to use the Stepanoff recommendation [33].
4. The recommended range of the volute wall opening angle is 10-50˚, optimal 30-40˚.
5. For turbine-mode operation, a trapezoidal volute cross-section is recommended.
6. The use of a smaller cross-sectional area is recommended. A smaller cross-sectional area is obtained using the CAM method for low-specific-speed pumps and the CV method for high-specific-speed pumps.
7. For geometrically similar pumps, the equation (34) for predicting the shift of Q_{BEP} can be applied.

9.4 Industrial implementation

The design recommendations developed during the preparation of this doctoral dissertation were adopted by the manufacturer, Hydro-Vacuum Grudziądz, and used in the production of the centrifugal pump NHVf.80-200. This pump has been included in the manufacturer's commercial product line. This implementation confirms the practical usefulness of the proposed design recommendations (Appendix M).

9.5 Future work

The results indicate that the modification of volute channel parameters is not the only factor affecting the operation of a pump and a pump operating as a turbine (PAT). The sidewall gap, whose dimensions depend on both the impeller and the volute casing geometry, may also significantly influence the flow structure and energy performance. Numerical simulations of the DHV pump conducted with and without the sidewall gap showed that this region changed the efficiency by approximately 3% at $Q_{nom.p}$ in pump mode and by approximately 13% at $Q_{BEP.T}$ in turbine mode. This influence was mainly related to the formation of a recirculation zone in the space between the impeller and the volute casing. Therefore, future research should include a more detailed analysis of the sidewall gap and its interaction with the volute casing geometry, especially in turbine-mode operation.

References

[1] O. Moloshniy, “Influence of the inlet device construction of the sealless close coupled pump with a hollow shaft on its working process and characteristics,” Thesis, Sumy State University, 2019.

[2] D. Papini, “Rotatilis suctor et preffor hasfiacus,” *Acta Erud.*, pp. 317–322, 1689.

[3] R. Neumaier, *Hermetic pumps: the latest innovations and industrial applications of sealless pumps*. Houston, Tex: Gulf Pub. Co, 1997.

[4] U. S. Briefing, “International energy outlook 2013,” *US Energy Inf. Adm.*, vol. 506, p. 507, 2013.

[5] X. Gan, J. Pei, G. Pavesi, S. Yuan, and W. Wang, “Application of intelligent methods in energy efficiency enhancement of pump system: A review,” *Energy Rep.*, vol. 8, pp. 11592–11606, Nov. 2022.

[6] “A New Low-Cost Technology Based on Pump as Turbines for Energy Recovery in Peripheral Water Networks Branches.” [Online]. Available: https://www.mdpi.com/2073-4441/14/10/1526. [Accessed: 02-Apr-2025].

[7] M. Kramer, K. Terheiden, and S. Wieprecht, “Pumps as turbines for efficient energy recovery in water supply networks,” *Renew. Energy*, vol. 122, pp. 17–25, Jul. 2018.

[8] D. Thoma and C. Kittredge, “Centrifugal pumps operated under abnormal conditions,” *Power*, vol. 73, pp. 881–884, 1931.

[9] S. V. Jain and R. N. Patel, “Investigations on pump running in turbine mode: A review of the state-of-the-art,” *Renew. Sustain. Energy Rev.*, vol. 30, pp. 841–868, Feb. 2014.

[10] R. T. Knapp, “Centrifugal-Pump Performance as Affected by Design Features,” *Trans. Am. Soc. Mech. Eng.*, vol. 63, no. 3, pp. 251–260, Dec. 2022.

[11] J.-M. Chapallaz, G. Fischer, and P. Eichenberger, *Manual on Pumps Used as Turbines*. Informatica International, Incorporated, 1992.

[12] T. Lin, J. Zhang, B. Wei, Z. Zhu, and X. Li, “The role of bionic tubercle leading-edge in a centrifugal pump as turbines(PATs),” *Renew. Energy*, vol. 222, p. 119869, Feb. 2024.

[13] N. K. Bhukya and A. K. Rai, “Effect of wrap angle on performance of Pump As Turbine (PAT) in both pump and turbine modes,” *IOP Conf. Ser. Earth Environ. Sci.*, vol. 1411, no. 1, p. 012029, Nov. 2024.

[14] Y. Ji, Z. Yang, J. Ran, and H. Li, “Multi-objective parameter optimization of turbine impeller based on RBF neural network and NSGA-II genetic algorithm,” *Energy Rep.*, vol. 7, pp. 584–593, Nov. 2021.

[15] A. Nasir, E. Dribssa, M. Girma, and T. Demeke, “A Comparative Study of Impeller Modification Techniques on the Performance of the Pump as a Turbine,” *Int. J. Rotating Mach.*, vol. 2022, no. 1, p. 1944753, 2022.

[16] M. Polák, “Innovation of Pump as Turbine According to Calculation Model for Francis Turbine Design,” *Energies*, vol. 14, p. 2698, May 2021.

[17] M. H. Shojaeefard and S. Saremian, “Analyzing the impact of blade geometrical parameters on energy recovery and efficiency of centrifugal pump as turbine installed in the pressure-reducing station,” *Energy*, vol. 289, p. 130004, Feb. 2024.

References

[18] L. Wang, S. N. Asomani, J. Yuan, and D. Appiah, “Geometrical Optimization of Pump-As-Turbine (PAT) Impellers for Enhancing Energy Efficiency with 1-D Theory,” *Energies*, vol. 13, no. 16, p. 4120, Jan. 2020.

[19] Z. Zhu, Q. Gu, H. Chen, Z. Ma, and B. Cao, “Investigation and optimization into flow dynamics for an axial flow pump as turbine (PAT) with ultra-low water head,” *Energy Convers. Manag.*, vol. 314, p. 118684, Aug. 2024.

[20] M. H. Shojaeefard and S. Saremian, “Effects of impeller geometry modification on performance of pump as turbine in the urban water distribution network,” *Energy*, vol. 255, p. 124550, Sep. 2022.

[21] M. H. Shojaeefard and S. Saremian, “Studying the impact of impeller geometrical parameters on the high-efficiency working range of pump as turbine (PAT) installed in the water distribution network,” *Renew. Energy*, vol. 216, p. 119060, Nov. 2023.

[22] M. Bade, R. Gaji, A. Doshi, and P. Singh, “Influence of impeller blade rounding and surface roughness on the internal hydraulics and performance of pump as turbine,” *Arch. Mech. Eng.*, vol. 70, pp. 219–245, Jul. 2023.

[23] A. M. Tchada, N. Tchoumboué, A. L. A. Mesquita, and P. Hendrick, “Enhancing Pump as Turbine (PAT) performances: A numerical investigation into the impact of impeller leading edge rounding,” *Heliyon*, vol. 10, no. 15, p. e34663, Aug. 2024.

[24] T. Wang, L. Lei, Y. Liu, Q. Guo, and T. Huang, “Effect of blade profile on the hydraulic performance of a double-suction centrifugal pump as turbine based on enstrophy dissipation theory,” *Phys. Fluids*, vol. 36, Aug. 2024.

[25] M. Sen-chun, Z. Hong-biao, W. Ting-ting, W. Xiao-hui, and S. Feng-xia, “Optimal design of blade in pump as turbine based on multidisciplinary feasible method,” *Sci. Prog.*, vol. 103, no. 4, p. 0036850420982105, Oct. 2020.

[26] K. Wang, S. Wang, P. Meng, C. Wang, Y. Li, W. Zheng, J. Liu, and J. Kou, “Strategies employed in the design and optimization of pump as turbine runner,” *Renew. Energy*, vol. 216, p. 119080, Nov. 2023.

[27] L. Xin, Q. Li, and Y. Liu, “Dynamic analysis of the impeller under optimized blade design for a pump-turbine,” *J. Energy Storage*, vol. 107, p. 114900, Jan. 2025.

[28] R. C. Worster, “The Flow in Volutes and Its Effect on Centrifugal Pump Performance,” *Proc. Inst. Mech. Eng.*, vol. 177, no. 1, pp. 843–875, Jun. 1963.

[29] R. D. Bowerman and A. J. Acosta, “Effect of the Volute on Performance of a Centrifugal-Pump Impeller,” *Trans. Am. Soc. Mech. Eng.*, vol. 79, no. 5, pp. 1057–1069, Feb. 2022.

[30] N. A. Cumpsty, *Compressor aerodynamics*. Malabar, Fla. : Krieger Pub., 2004.

[31] I. Polotskiy, F. Bognitskaya, and R. Agulnik, *Raschet otvodyashchikh ustroystv tsentrobezhnogo nasosa*. Moscow, USSR: PMB CINTIhimneftemash, 1967.

[32] C. Pfleiderer and H. Petermann, *Strömungsmaschinen*, 7th edition. Springer, 2005.

[33] A. J. Stepanoff, *Centrifugal and Axial Flow Pumps: Theory, Design, and Application*. Wiley, 1957.

[34] V. Kolisnichenko, S. O. Luhova, V. O. Panchenko., *Metodychni vkazivky do vykonannya kursovoho proektu zi spetsial'nosti na temu «Rozrakhunok i proektuvannya vidvidnykh prystroyiv»*. Sumy: Sums′kyy derzhavnyy universytet, 2013.

References

[35] J. F. Gulich, *Centrifugal Pumps*. Berlin, Heidelberg: Springer, 2014.

[36] S. N. Asomani, J. Yuan, L. Wang, D. Appiah, and F. Zhang, "Geometrical effects on performance and inner flow characteristics of a pump-as-turbine: A review," *Adv. Mech. Eng.*, vol. 12, no. 4, p. 1687814020912149, Apr. 2020.

[37] B. Jalilpour, S. Jafarmadar, M. Khalilian, and S. M. Taleby, "Performance analysis of double suction pumps as turbines (DS-PaT) for clean energy generation and storage in hybrid systems: Experimental and numerical insights," *J. Energy Storage*, vol. 102, p. 114094, Nov. 2024.

[38] A. Carravetta, S. Derakhshan Houreh, and H. M. Ramos, *Pumps as Turbines*. Cham: Springer International Publishing, 2018.

[39] R. Defeld, *Prakticheskoye rukovodstvo po tsentrobezhnym nasosam*, ONTI. Moscow, Leningrad, 1937.

[40] A. Lomakin, *Tsentrobezhnyye i osevyye nasosy*. Lieningrad, USSR: Mashinostroyeniye, 1965.

[41] C. Pfleiderer, *Центробежные и пропеллерные насосы*. Moskva: ONTI GREL, 1937.

[42] A. Mikhailov and V. Maliushenko, *Лопастные насосы. Теория, расчет и конструирование*. Moscow: Maszinostroienie, 1971.

[43] A. Mashin, *Raschet i proyektirovaniye spiral'nogo otvoda*. Moscow, USSR: Moskovskiy energeticheskiy institut, 1980.

[44] Church Austin H., *Centrifugal Pumps and Blowers*. John Wiley and Sons Inc., New York, 1944.

[45] S. Łazarkiewicz and A. Troskolański, *Pompy wirowe*, 3rd ed. Warszawa: Wydawnictwo naukowo-techniczne, 1973.

[46] W. Jędral, *Pompy wirowe*. Warsaw: Ofiyna Wydawnicza Politechniki Warszawskiej, 2014.

[47] M. Aizenstein, *Tsentrobezhnyye nasosy dlya neftyanoy promyshlennosti*. Moscow, USSR: Gostoptekhizdat, 1957.

[48] V. S. Lobanoff and R. R. Ross, *Centrifugal pumps: design and application*, 2nd ed. Houston, TX: Gulf Publishing Company, 1992.

[49] Q. Gou, S. Xiao, T. Wang, and J. Yan, "Analysis and Comparison of Two Kinds of Design Approaches for Volutes of Centrifugal Pump," *Energ. 2023 Vol 16 Page 6128*, vol. 16, no. 17, p. 6128, Aug. 2023.

[50] T. (**王桃**) Wang, H. (**余河**) Yu, Y. (**方玉建**) Fang, R. (**向茹**) Xiang, N. (阚能琪) Kan, and J. (严敬) Yan, "A new design for energy-saving volutes in centrifugal pumps," *Phys. Fluids*, vol. 34, no. 11, p. 115119, Nov. 2022.

[51] H. S. Shim and K. Y. Kim, "Numerical Investigation on Hydrodynamic Characteristics of a Centrifugal Pump with a Double Volute at Off-Design Conditions," *IOP Conf. Ser. Earth Environ. Sci.*, vol. 49, p. 032007, Nov. 2016.

[52] A. Al-Obaidi, S. Pradhan, T. Asim, R. Mishra, and K. Zala, "Numerical studies of the velocity distribution within the volute of a centrifugal pump.," Sep. 2014.

[53] I. V. Krishtop, P. M. Kalinichenko, and A. G. Gusak, "Calculation and designing of volutes of rotodynamic pumps," *IOP Conf. Ser. Mater. Sci. Eng.*, vol. 233, no. 1, p. 012005, Aug. 2017.

[54] C. H. Son, H. B. Jin, M. J. Kim, and W. J. Chung, "Spiral casing of a volute centrifugal pump," *J. Mech. Sci. Technol.*, vol. 28, no. 7, pp. 2697–2706, Jul. 2014.

[55] Y. Tao, S. Yuan, J. Liu, and F. Zhang, “Influence of Cross-Sectional Flow Area of Annular Volute Casing on Transient Characteristics of Ceramic Centrifugal Pump,” *Chin. J. Mech. Eng.*, vol. 32, no. 1, p. 4, Jan. 2019.

[56] M. F. Khan, T. Gjernes, N. Guenther, and J.-P. Hickey, “Impact of Volute Throat Area and Gap Width on the Hydraulic Performance of Low-Specific-Speed Centrifugal Pump,” *Modelling*, vol. 5, no. 3, pp. 659–672, Sep. 2024.

[57] H.-S. Shim and K.-Y. Kim, “Effects of the Cross-Sectional Area of a Volute on Suction Recirculation and Cavitation in a Centrifugal Pump,” *J. Fluids Eng.*, vol. 142, no. 051204, Feb. 2020.

[58] H.-S. Shim and K.-Y. Kim, “Design Optimization of the Impeller and Volute of a Centrifugal Pump to Improve the Hydraulic Performance and Flow Stability,” *J. Fluids Eng.*, vol. 142, no. 101211, Jul. 2020.

[59] W. Stiefel, “Experiences in the Development of Radial Compressors,” *Von Karrnan Inst. Fluid Dyn. Lect. Ser. 50 Adv. Radial Compress.*, May 1972.

[60] B. D. Baloni and S. A. Channiwala, “Design and Analysis of Volute Casing: A Review,” presented at the ASME Turbo Expo 2012: Turbine Technical Conference and Exposition, 2013, pp. 657–664.

[61] J.-H. KIM, K. Oh, K. Pyun, C.-K. Kim, Y.-S. Choi, and J.-Y. Yoon, “Design optimization of a centrifugal pump impeller and volute using computational fluid dynamics,” *IOP Conf. Ser. Earth Environ. Sci.*, vol. 15, p. 2025, Nov. 2012.

[62] S. Yang, F. Kong, and B. Chen, “Research on Pump Volute Design Method Using CFD,” *Int. J. Rotating Mach.*, vol. 2011, no. 1, p. 137860, 2011.

[63] H. Mishina and I. Gyobu, “Performance Investigations of Large Capacity Centrifugal Compressors,” in *Volume 1A: General*, London, England, 1978, p. V01AT01A003.

[64] C. Abdelmadjid, S.-A. Mohamed, and B. Boussad, “CFD Analysis of the Volute Geometry Effect on the Turbulent Air Flow through the Turbocharger Compressor,” *Energy Procedia*, vol. 36, pp. 746–755, Jan. 2013.

[65] D. Pan, A. Whitfield, and M. Wilson, “Design considerations for the volutes of centrifugal fans and compressors,” *Proc. Inst. Mech. Eng. Part C*, vol. 213, no. 4, pp. 401–410, Apr. 1999.

[66] J. Zhang, D. Appiah, F. Zhang, S. Yuan, Y. Gu, and S. N. Asomani, “Experimental and numerical investigations on pressure pulsation in a pump mode operation of a pump as turbine,” *Energy Sci. Eng.*, vol. 7, no. 4, pp. 1264–1279, 2019.

[67] C. Ji, Y. Wang, and L. Yao, “Numerical Analysis and Optimization of the Volute in a Centrifugal Compressor,” in *Challenges of Power Engineering and Environment*, Berlin, Heidelberg, 2007, pp. 1352–1356.

[68] C. Ji and Y. Wang, “The design and flow simulation of the volute casing of a mixed flow pump,” in *Proceedings of 2011 International Conference on Electronic & Mechanical Engineering and Information Technology*, 2011, vol. 2, pp. 820–823.

[69] Z. Chen, V. T. T. Nguyen, and N. T. Tran, “Optimum Design of the Volute Tongue Shape of a Low Specific Speed Centrifugal Pump,” *J. Electr. Electron. Syst.*, vol. 06, no. 02, 2017.

[70] P. Lin, C. Wang, P. Song, and X. Li, “Analysis of the Energy Loss and Performance Characteristics in a Centrifugal Pump Based on Sinusoidal Tubercle Volute Tongue,” *Entropy*, vol. 25, no. 3, p. 545, Mar. 2023.

[71] X. Li, Z. Zhu, Y. Li, and X. Chen, “Experimental and numerical investigations of head-flow curve instability of a single-stage centrifugal pump with volute casing,” *Proc. Inst. Mech. Eng. Part J. Power Energy*, vol. 230, no. 7, pp. 633–647, Nov. 2016.

[72] C. Wang, Y. Zhang, H. Hou, Z. Yuan, and M. Liu, “Optimization design of an ultra-low specific-speed centrifugal pump using entropy production minimization and taguchi method,” *Int. J. Fluid Mach. Syst.*, vol. 13, no. 1, pp. 55–67, 2020.

[73] L. Zhou, J. Hang, L. Bai, Z. Krzemianowski, M. A. El-Emam, E. Yasser, and R. Agarwal, “Application of entropy production theory for energy losses and other investigation in pumps and turbines: A review,” *Appl. Energy*, vol. 318, p. 119211, Jul. 2022.

[74] M. Golbabaei Asl, R. Torabi, and S. A. Nourbakhsh, “Experimental and FEM failure analysis and optimization of a centrifugal-pump volute casing,” *Eng. Fail. Anal.*, vol. 16, no. 6, pp. 1996–2003, Sep. 2009.

[75] D. O. Baun, L. Ko¨stner, and R. D. Flack, “Effect of Relative Impeller-to-Volute Position on Hydraulic Efficiency and Static Radial Force Distribution in a Circular Volute Centrifugal Pump,” *J. Fluids Eng.*, vol. 122, no. 3, pp. 598–605, May 2000.

[76] L. Tan, D. Zhang, W. Shi, L. Zhou, and X. Cai, “Influence of volute basic circle diameter on the pressure fluctuations and flow noise of a low specific speed sewage pump,” *J. Vibroengineering*, vol. 19, no. 5, pp. 3779–3796, Aug. 2017.

[77] W. Li, W. Shi, X. Jiang, T. Jiang, and B. Chen, “Impact of the Volute Basic Circle Diameter of Sewage Pump on Pressure Pulsation,” *Przegląd Elektrotechniczny*, vol. R. 89, nr 3b, 2013.

[78] C. Wang, B. Zhang, B. Xu, H. Wang, H. Li, and S. Wu, “Investigation of internal flow characteristics in volute with varying inlet widths for low specific speed centrifugal pumps,” *J. Braz. Soc. Mech. Sci. Eng.*, vol. 46, no. 5, p. 261, Apr. 2024.

[79] M. Shah, B. Baloni, and S. Channiwala, “Optimization of Centrifugal Pump Based on Impeller-Volute Interactions,” *Adv. Technol. Innov.*, vol. 7, no. 3, pp. 216–227, Feb. 2022.

[80] M. Shadab, M. Karimipour, A. F. Najafi, R. Paydar, and S. A. Nourbakhsh, “Effect of impeller shroud trimming on the hydraulic performance of centrifugal pumps with low and medium specific speeds,” *Eng. Appl. Comput. Fluid Mech.*, vol. 16, no. 1, pp. 514–535, Dec. 2022.

[81] R. Gangipamula, P. Ranjan, and R. S. Patil, “Study on fluid dynamic characteristics of a low specific speed centrifugal pump with emphasis on trimming operations,” *Int. J. Heat Fluid Flow*, vol. 95, p. 108952, Jun. 2022.

[82] Z. Shen, W. Chu, S. Yan, X. Chen, Z. Guo, and Y. Zhong, “Study of the performance and internal flow in centrifugal pump with grooved volute casing,” *Mod. Phys. Lett. B*, vol. 34, no. 25, p. 2050268, Sep. 2020.

[83] Z. Shen, W. Han, Y. Zhong, B. Luo, R. Li, and W. Chu, “Influence of grooved volute casing parameters on pressure pulsation and erosion wear characteristics in a centrifugal pump,” *Mod. Phys. Lett. B*, vol. 36, Jan. 2022.

[84] I. Goltz, G. Kosyna, and A. Delgado, “Eliminating the head instability of an axial-flow pump using axial grooves,” *Proc. Inst. Mech. Eng. Part A*, vol. 227, no. 2, pp. 206–215, Mar. 2013.

[85] Y.-L. Zhang, J.-F. Li, T. Wang, J.-J. Xiao, X.-Q. Jia, and L. Zhang, “Pressure Distribution on the Inner Wall of the Volute Casing of a Centrifugal Pump,” *Sci. Technol. Nucl. Install.*, vol. 2022, no. 1, p. 3563459, 2022.

[86] X. (贾晓奇) Jia, Y. (厉宇鹏) Li, J. (张峻) Zhang, C. (颜朝寿) Yan, Z. (林哲) Lin, and Z. (朱祖超) Zhu, “Research on the effects of volute area ratios on centrifugal pump internal flow and noise,” *Phys. Fluids*, vol. 36, no. 7, p. 075111, Jul. 2024.

[87] Z. Han, S. Yang, J. Chen, and W. Wang, “Research on the effect of various tongue types on large volute pumps,” *J. Phys. Conf. Ser.*, vol. 2707, no. 1, p. 012031, Feb. 2024.

[88] Q. Si, J. Yuan, S. Yuan, W. Wang, L. Zhu, and G. Bois, “Numerical Investigation of Pressure Fluctuation in Centrifugal Pump Volute Based on SAS Model and Experimental Validation,” *Adv. Mech. Eng.*, vol. 6, p. 972081, 2014.

[89] R. Dong, S. Chu, and J. Katz, “Effect of Modification to Tongue and Impeller Geometry on Unsteady Flow, Pressure Fluctuations, and Noise in a Centrifugal Pump,” *J. Turbomach.*, vol. 119, no. 3, pp. 506–515, Jul. 1997.

[90] N. Zhang, B. Gao, B. Xia, and Q. Jiang, “Effect of the volute tongue cut on pressure pulsations of a low specific speed centrifugal pump,” *J. Hydrodyn.*, vol. 32, no. 4, pp. 758–770, Aug. 2020.

[91] C. Ye, K. Xia, H. Yan, S. Cao, Z. Wang, Q. Tian, B. P. M. van Esch, Y. Zheng, and C. Yang, “Study on the influence of volute structure on the performance of seawater-pumped storage hydropower plant unit,” *J. Energy Storage*, vol. 90, p. 111848, Jun. 2024.

[92] H. Wang, Z. Tan, S. Kuang, and A. Yu, “Numerical modeling and analysis of particle-fluid flow and wall erosion in centrifugal slurry pumps under different solid concentrations,” *Powder Technol.*, vol. 410, p. 117861, Sep. 2022.

[93] W. Zhang, S. Yang, D. Wu, and J. Mou, “Effect of particle mass concentration on erosion characteristics of self-priming pump,” *Proc. Inst. Mech. Eng. Part C J. Mech. Eng. Sci.*, vol. 235, no. 23, pp. 6782–6797, Dec. 2021.

[94] S. Baocheng, J. Pan, L. Wu, X. Zhang, Y. Qiu, and Y. Zhang, “A Prediction Method of Wear for Volute Casing of a Centrifugal Slurry Pump,” *Geofluids*, vol. 2020, pp. 1–12, Dec. 2020.

[95] G. Peng, X. Huang, L. Zhou, G. Zhou, and H. Zhou, “Solid-liquid two-phase flow and wear analysis in a large-scale centrifugal slurry pump,” *Eng. Fail. Anal.*, vol. 114, p. 104602, Aug. 2020.

[96] J. A. Lorett and S. Gopalakrishnan, “Interaction Between Impeller and Volute of Pumps at Off-Design Conditions,” *J. Fluids Eng.*, vol. 108, no. 1, pp. 12–18, Mar. 1986.

[97] “Study on Energy Conversion Characteristics in Volute of Pump as Turbine,” *Fluid Dyn. Mater. Process.*, vol. 17, no. 1, pp. 201–214, Jan. 2021.

[98] L. Zemanová and P. Rudolf, “Flow Inside the Sidewall Gaps of Hydraulic Machines: A Review,” *Energies*, vol. 13, no. 24, p. 6617, Jan. 2020.

[99] W. Lorenz, M. Janczak, and M. Sitniewski, “Analiza pracy pompy normowej w ruchu pompowym i turbinowym (PAT),” *Pompy Pompow.*, no. 1, 2023.

[100] H. Kang, Q. Xin, J. Du, Z. Ge, and J. Huang, “Investigation on the Effects of Volute Geometric Parameters on the Performance of Pico Francis Turbines Used in Water Pipes,” *Water*, vol. 16, no. 12, p. 1722, Jan. 2024.

[101] H. A. Arani, M. Fathi, M. Raisee, and S. A. Nourbakhsh, “A novel volute design for reducing radial force in pump and PAT,” *IOP Conf. Ser. Earth Environ. Sci.*, vol. 240, no. 4, p. 042004, Mar. 2019.

[102] S. Saremian and M. H. Shojaeefard, “Study on the impact of volute geometric modification on the performance of centrifugal pump as turbine,” *Renew. Energy*, vol. 253, p. 123632, Nov. 2025.

[103] S.-S. Yang, H.-L. Liu, F.-Y. Kong, B. Xia, and L.-W. Tan, “Effects of the Radial Gap Between Impeller Tips and Volute Tongue Influencing the Performance and Pressure Pulsations of Pump as Turbine,” *J. Fluids Eng.*, vol. 136, no. 054501, Mar. 2014.

[104] A. Morabito, E. Vagnoni, M. Di Matteo, and P. Hendrick, “Numerical investigation on the volute cutwater for pumps running in turbine mode,” *Renew. Energy*, vol. 175, pp. 807–824, Sep. 2021.

[105] H. Alemi Arani, M. Fathi, M. Raisee, and S. A. Nourbakhsh, “The effect of tongue geometry on pump performance in reverse mode: An experimental study,” *Renew. Energy*, vol. 141, pp. 717–727, Oct. 2019.

[106] T. Lin, J. Zhang, J. Li, X. Li, and Z. Zhu, “Pressure Fluctuation–Vorticity Interaction in the Volute of Centrifugal Pump as Hydraulic Turbines (PATs),” *Processes*, vol. 10, p. 2241, Nov. 2022.

[107] R. Gaji, A. Doshi, and M. Bade, “Investigating the Impact of Back Cavity Filling and Axial Clearance on the Flow Physics and Performance of a Pump as Turbine,” *J. Appl. Fluid Mech.*, vol. 17, no. 4, pp. 799–815, Jan. 2024.

[108] J. Graciano-Uribe, J. Sierra, and E. Torres, “Instabilities and influence of geometric parameters on the efficiency of a pump operated as a turbine for micro hydro power generation: A review,” *J. Sustain. Dev. Energy Water Environ. Syst.*, vol. N/A, Jul. 2020.

[109] K. Kan, M. Binama, H. Chen, Y. Zheng, D. Zhou, W. Su, and A. Muhirwa, “Pump as turbine cavitation performance for both conventional and reverse operating modes: A review,” *Renew. Sustain. Energy Rev.*, vol. 168, p. 112786, Oct. 2022.

[110] J. Pan, Y. Pan, Q. Liu, S. Yang, R. Tao, D. Zhu, and R. Xiao, “FED evaluation in a small double-suction reversible pump turbine considering sediment erosion,” *J. Energy Storage*, vol. 76, p. 109549, Jan. 2024.

[111] S. Y. Liu, S. S. Yang, P. Singh, and L. Zhou, “Analysis of double suction pumps in both pump and turbine modes using entropy factor,” *Renew. Energy*, vol. 237, p. 121555, Dec. 2024.

[112] “Katalog pomp Hydro Vacuum S.A.” .

[113] “Omega - Single-stage axially split volute casing pump | KSB.” [Online]. Available: https://www.ksb.com/en-tw/lc/products/pump/dry-installed-pump/omega/O00A. [Accessed: 08-Dec-2025].

[114] ANSYS, Inc., “ANSYS Release Notes,” ANSYS, Inc., Canonsburg, PA, Mar. 2026.

[115] A. Błaszczyk, *Pompy spełniające specjalne wymagania ruchowe*. 2011.

[116] T. Kajishima and K. Taira, *Computational Fluid Dynamics*. Cham: Springer International Publishing, 2017.

[117] V. M. Arocena and L. A. M. Danao, “Improving the Modeling of Pressure Pulsation and Cavitation Prediction in a Double-Volute Double-Suction Pump Using Mosaic Meshing Technology,” *Processes*, vol. 11, no. 3, p. 660, Mar. 2023.

References

[118] P. J. Roache, “Verification of Codes and Calculations,” *AIAA J.*, vol. 36, no. 5, pp. 696–702, May 1998.

[119] T. Adams, C. Grant, and H. Watson, “A Simple Algorithm to Relate Measured Surface Roughness to Equivalent Sand-grain Roughness,” *Int. J. Mech. Eng. Mechatron.*, 2012.

[120] “ISO 9906 Rotodynamic pumps – Hydraulic performance acceptance tests – Grades 1, 2 and 3.” International Organization for Standardization, Switzerland, 2012.

[121] S. Fontanella, O. Fecarotta, B. Molino, L. Cozzolino, and R. Della Morte, “A Performance Prediction Model for Pumps as Turbines (PATs),” *Water*, vol. 12, no. 4, p. 1175, Apr. 2020.

[122] G. L. Harris and V. R. Miller, “NISTIR 7383, Selected Procedures for Volumetric Calibrations (2019 Ed),” *NIST*, May 2019.

[123] M. T. M. Emmerich and A. H. Deutz, “A tutorial on multiobjective optimization: fundamentals and evolutionary methods,” *Nat. Comput.*, vol. 17, no. 3, pp. 585–609, Sep. 2018.

[124] А. Окара, *Економетрія: навчальний посібник*, vol. 144. Одеса: ОДАБА, 2018.

[125] L. Tan, D. Zhang, W. Shi, L. Zhou, and X. Cai, “Influence of volute basic circle diameter on the pressure fluctuations and flow noise of a low specific speed sewage pump,” *J. Vibroengineering*, vol. 19, no. 5, pp. 3779–3796, Aug. 2017.

[126] M. Volk, *Pump Characteristics and Applications*, 3rd ed. New York: Taylor & Francis, 2014.

[127] B. R. Munson, Ed., *Fundamentals of fluid mechanics*, 7. ed. Hoboken, NJ: Wiley, 2013.

Appendices

Appendix A. Classification of pumps and impellers based on specific speed

Table A.1 - Classification of pumps and impellers based on specific speed

Mikhailov [42]		**Volk [126]**		**Munson** [127]		**Lomakin [40]**			**Jędral [46]**		
n_q	Category	n_q	Category	n_q	Category	n_q	D_2/D_0	Category	n_q	D_2/D_0	Category
10 ÷ 19	Low specific speeds	0÷39	Radial flow	0÷19	Radial flow	11 ÷ 22	≈ 2.5	Low specific speeds	5 ÷ 20	3.5 ÷ 2	Radial single curvature blades impeller
22 ÷ 33	Normal specific speeds					22 ÷ 38	≈ 2	Normal specific speeds	20 ÷ 50	2 ÷ 1.5	Radial double-curvature blades impeller
41 ÷ 68	High specific speeds					38 ÷ 82	≈ 1.8 ÷ 1.4	High specific speeds	50 ÷ 80	1.5 ÷ 1.3	Helicoidal impeller
82 ÷ 137	Diagonal pumps	39÷155	Mixed flow	19÷155	Mixed flow	82 ÷ 164	≈ 1.2 ÷ 1.1	Diagonal pumps	80 ÷ 150	1.2 ÷ 1.1	Helicoidal or Diagonal impeller
192 ÷ 274	Axial pumps	>155	Axial flow	>155	Axial flow	164 ÷ 493	≈ 0.8 ÷ 0.6	Axial pumps	135 ÷ 600	1	Axial impeller

Appendix B. Detailed overview of fundamental literature of volute casing design

Table B.1 – An overview of the design parameters of the volute casing from authors who adhere to the **method of angular momentum conservation**

Characteristic	Pfleiderer [32], [41]	Lomakin [40]	Mikhailov [42]
Method	Method of conservation of angular momentum of the flow		
Angular momentum in volute	$c_u \cdot r = K$, $K = \frac{g \cdot H_t}{\omega}$, $\omega = \frac{\pi \cdot n}{30}$ where: H_t – head of impeller, ω - circumferential velocity, n – rotation speed [41, p. 182], [32, p. 141]	$v_u \cdot r = v'_{u2} \cdot r_2 = \frac{g \cdot H_t}{\omega} = \frac{\Gamma_c}{2\pi}$ where: v_u – circumferential component of the absolute velocity, Γ_c – constant of volute, H_t – head, r - distance from the rotation axis. [40, p. 118]	$\vartheta_{ui} \cdot r_i = \vartheta_{2u} \cdot r_2 = K_2 = const$ where: ϑ_i – circumferential component of the absolute velocity [42, p. 79]
Inlet width (b_3)	$b_3 = b_2 + 1 \dots 2$ [41, p. 160]	$b_3 = b_2 + 0{,}05 \cdot D_2$ [40, p. 120]	$b_3 = b_2` + (0{,}02 \dots 0{,}05) \cdot D_2$ [42, p. 82]
Inlet diameter (D_3)	-	$D_3 = (1{,}03 \dots 1{,}05) \cdot D_2$ [40, p. 118]	Usually, $D_3 = (1{,}03 \dots 1{,}05) D_2$ For $n_s \leq 100$: $D_3 = (1{,}1 \dots 1{,}15) D_2$ For $n_s > 100$: $D_3 = (1{,}15 \dots 1{,}2) D_2$ [42, p. 81]
Volute throat area	1) to determine the area at section 8, the cross section is divided into n elementary areas ΔS_i of the same height Δr (Figure B.1, Figure B.4) $b \cdot dr = dS$ 2) the fluid flow rate through each elementary area is determined, and the resulting flows are summed $Q_i = K_2 \int_{R_3}^{r_i} \frac{b}{r} dr$, $Q_8 = \sum_{i=1}^{n} \Delta Q_i$. 3) the calculation is performed until the total flow rate exceeds the pump flow rate value $Q_8 \approx 1{,}05Q$. 4) Knowing the final height of cross section r, a trapezoid cross section can be created (Figure B.4, Figure B.1). The trapezoid is limited by the selected values of b_3 and the angle ε. Using Table B.2. 5) Graph is constructed from tabular data linked to the meridional section of the volute (Figure B.5, Figure B.2). To account for friction losses, Q is increased by10-15%		$F = \frac{Q \varphi_s}{c_{u,av} \cdot 2\pi}$; $c_{u,av} = \frac{30 \cdot g}{\pi \cdot \eta_h} \cdot \frac{H}{n} \cdot \frac{1}{r_{cp}}$ where: $c_{u\,av}$ – v average velocity; φ - angle of volute casing coverage. Graphical integration: $\Delta Q = K_3 \frac{B_i + B_{i+1}}{2} \Delta r \frac{2\pi}{\varphi}$ Calculated according to Table B.2. For pumps with small, narrow impellers, the volute throat area must be reduced by 5%. [42, pp. 97–100]
Height of throat area	See Table B.2		See Table B.2
Area of intermediate cross sections	To calculate the intermediate cross sections, Q_8 is divided into equal parts, the number of which corresponds to the number of volute sections. Using the flow rate Q at each intermediate section and the previously calculated values employed to determine the volute throat area, the geometric dimensions of each cross-section can be determined in an analogous manner.		The cross-sectional area changes proportionally to the angle φ between the 8 cross sections: $F = F_{pc} \cdot \frac{\varphi}{\varphi_v}$ [42, p. 82]
Intermediate section shape and trapezoid rounding	Round and trapezoidal cross-sections are shown. The sharp corners of the trapezoidal cross section are rounded using round arcs of given radius, provided that the equality of the static moments of areas F_x and F_y is maintained $F_x \cdot r_x = F_y \cdot r_y$, where r_x and r_y are the radii of the centers of gravity of the areas F_x and F_y [41, p. 184], [40, p. 121], [42, p. 101]		
Wall opening angle (ε)	$\cos(\delta) = \frac{\cos \varepsilon - \cos^2 \alpha_3}{\sin \alpha_3}$ where: δ – wall opening angle, α_3 – the angle formed by the tangent to the circle	-	20º - 26º

Characteristic	Pfleiderer [32], [41]	Lomakin [40]	Mikhailov [42]
	and the flow velocity c, with ε being the actual angle of opening [41, p. 189]		
Cutwater angle	No specific value. Quote from [41, p. 189] "The input edge X [the edge where the cutwater begins - author's note] of the volute is not brought to the very surface of the impeller, but is located at some distance from it in order..." [Own translation]	-	n_s=60 φ=360˚ n_s=90 φ=350˚ n_s=130 φ=340˚ n_s=190 φ=330˚ n_s=280 φ=315˚ [42, p. 81]
Diffuser expansion angle	No more than 10º [41, p. 189]	8º [40, p. 121]	8-10º ; for pump with $n_s <$ 400, angle = 8-12º [42, p. 83]
Calculation example	[41, pp. 187–189, 195–196]	[40, pp. 122–123]	-

Table B.2 – Calculations to determine the area of the design cross section

	$\Delta \boldsymbol{r}$, m	$\boldsymbol{r_i}$, m	$\boldsymbol{b_i}$, m	$\frac{\boldsymbol{B_i}}{\boldsymbol{r_i}} = \frac{\boldsymbol{b_i}}{\boldsymbol{r_i}}$	$\frac{\boldsymbol{B_i + B_{i+1}}}{\boldsymbol{2}}$	$\frac{\boldsymbol{g \cdot H_t}}{\boldsymbol{\omega}} \cdot \frac{\boldsymbol{B_i + B_{i+1}}}{\boldsymbol{2}} \cdot \Delta \boldsymbol{r}$	$\Delta \boldsymbol{Q_i}$	$\sum_{\boldsymbol{i=1}}^{\boldsymbol{n}} \Delta \boldsymbol{Q_i}$
1	0,001	r_3	b_3		-	-	$\Delta Q_1 = 0$	-
2	0,001	$r_3 + \Delta$r	$b_{i+1} = b_i + 2\Delta b_{i+1} = b_i + 2 \cdot \Delta r \cdot tg(\gamma)$, see Figure B.4, Figure B.5				ΔQ_2	-
…	…	…	…	…	…	…	…	…
n	0,001	$r_3 + n\Delta$r	b_n				ΔQ_n	Q_8

Table B.3 - An overview of the design parameters of the volute casing from authors who adhere to the **method of angular momentum conservation**

<table>
<tr><th>Characteristic</th><th>Polotskiy [31]</th><th>Mashin [43]</th><th>Kolisnichenko [34]</th><th>Church [44]</th></tr>
<tr><td>Method</td><td colspan="4">Method of conservation of angular momentum of the flow</td></tr>
<tr><td>Angular momentum in volute</td><td>$\vartheta_{u3} = \frac{K_2}{r_3}$,
$where$
ϑ_{u3} - circumferential component of absolute velocity,
K_2 – moment of velocity, m²/s,
r_3 - volute inlet radius, m
[31, p. 12]</td><td colspan="2">$K_2 = V_{u_2} \cdot R_2, \quad K_2 = \frac{g \cdot H_m}{\omega}$,
V_{u_2} – circumferential component of the absolute flow velocity at the outlet of the impeller, m/s; R_2 radius of the impeller, m; $H_m = \frac{H}{\eta_e}$ – theoretical head, m; $g = 9{,}81$– acceleration due to gravity, m/s²;
$\omega = \frac{\pi \cdot n}{30}$ – angular velocity of the working wheel, s⁻¹.
For double-entry pump: $K_2 = \frac{gH_m}{\omega} + K_1$, where K_1 – speed moment at the impeller inlet $K_1 = 0{,}06\sqrt[3]{Q^2 \cdot n}$ (for double-entry pump instead of Q, the value Q/2 is substituted) [34, p. 18], [43, p. 16]</td><td>$RV_u = const$</td></tr>
<tr><td>Inlet width (b_3)</td><td>$b_3 = b_2^{`} + (0{,}04 \dots 0{,}06) \cdot D_2$<br>$b_2^{`}$ - impeller width at the outlet taking into account the thickness of shrouds</td><td>For double-entry pump [43, p. 14]:
$b_3 = m2b_2$
For pump type overhung and multistage pump:
$b_3 = mb_2$,
where m – coefficient from table below
<table>
<tr><th rowspan="2">n_s</th><th colspan="2">Type of pump</th></tr>
<tr><th>Overhung</th><th>Double-entry and multistage pump</th></tr>
<tr><td>60</td><td>2.6-2.8</td><td>1.85-1.95</td></tr>
<tr><td>80</td><td>2.3-2.5</td><td>1.7-1.8</td></tr>
<tr><td>100</td><td>2.1-2.25</td><td>1.6-1.7</td></tr>
<tr><td>120</td><td>1.9-2.05</td><td>1.45-1.55</td></tr>
<tr><td>150</td><td>1.75-1.85</td><td>1.35-1.45</td></tr>
<tr><td>180</td><td>1.62-1.7</td><td>1.28-1.38</td></tr>
<tr><td>220</td><td>1.52-1.62</td><td>1.2-1.3</td></tr>
<tr><td>260</td><td>1.5-1.57</td><td>1.15-1.25</td></tr>
</table></td><td>$b_3 \approx b_2 + 0{,}05D_2$
For double-entry pump:
$b_3 \approx 2(b_2 + 0{,}05D_2)$
[34, p. 12]</td><td>$b = b_3 + 2x \tan\frac{\theta}{2}$
where
x – distance between any radius R and the impeller outside radius R_2,
θ – Wall opening angle
[44, p. 121]</td></tr>
<tr><td>Inlet diameter (D_3)</td><td>$D_3 = (1{,}04 \dots 1{,}15)D_2$</td><td colspan="2">$D_3 = 2R_3 = 2(1{,}03 - 1{,}05)R_2$ [34, p. 12], [43, p. 13]</td><td>$D_3 = (1{,}1 \dots 1{,}2)D_2$</td></tr>
<tr><td>Volute throat area</td><td>Theoretical Volute throat area:
$A_{vol} = \frac{1}{s}\frac{F}{a}$
$F = \int_{r_3}^{r_s} B_a \, dr$
a - an arbitrary linear dimension (length) introduced for the graphical evaluation of the integral;
B_a - width of the volute cross-section at the design point</td><td>Actions for calculating:
Determine D_3, b_3
Set the inclination of the volute side walls
Determine the volute opening angle φ
Determine equivalent linear flow measure of the volute
$A = \frac{\phi}{360} \cdot \frac{\pi\eta_e nQ}{30gH}$
Calculate the area of the 8 cross sections of the volute:</td><td colspan="2">$Q_i = K_2 \int_{R_3}^{r_i} \frac{b}{r} dr \quad Q_8 = \sum_{i=1}^{n} \Delta Q_i$
$\Delta Q_i = K_2 \cdot \frac{B_i + B_{i+1}}{2} \cdot \Delta r \cdot \frac{360}{\phi_{cn}}$
See Table B.2
5.3) the calculation is carried out until the total flow rate exceeds the pump flow rate value $Q_8 \approx 1{,}05Q$.
5.4) knowing the final height of cross section r, a trapezoid cross section can be created (Figure B.1). Trapezoid is limited by the selected values of b_3 and the angle ε.</td></tr>
</table>

<table>
<tr><th>Characteristic</th><th>Polotskiy [31]</th><th>Mashin [43]</th><th>Kolisnichenko [34]</th><th>Church [44]</th></tr>
<tr><td></td><td>The graphical calculation of the integral is presented in [31, pp. 15–17]</td><td colspan="2">5.1) to determine the area 8-th of the cross section, the cross section is divided into n elementary areas ΔS_i of the same height Δr (Figure B.1, Figure B.1) $b \cdot dr = dS$
5.2) the fluid flow rate through the areas is determined, the resulting flows are summed</td><td colspan="2">5.5) a graph is constructed based on tabular data, which is connected to the meridian section of the volute (Figure B.5). Verify the accuracy of the calculated cross-sectional area [34, pp. 12–22], [43, pp. 15–18],[44, p. 121]</td></tr>
<tr><td>Height of throat area</td><td>See Table B.2</td><td colspan="2">See Table B.2</td><td>-</td></tr>
<tr><td>Area of intermediate cross sections</td><td>The cross-sectional area changes proportionally to the angle φ between the 8 cross section and the calculated $F = F_{pc} \cdot \frac{\varphi}{\varphi_v}$ [31, p. 18]</td><td>The cross-sectional area changes proportionally to the angle φ between the 8 cross section and the calculated $F = F_{pc} \cdot \frac{\varphi}{\varphi_v}$ [43, p. 17]</td><td>On graph (Figure B.1) Q_8 is divided into equal parts, the number of which corresponds to the number of sections of the volute [34, p. 21]</td><td>Table B.2</td></tr>
<tr><td>Shape of intermediate sections and trapezoid rounding method</td><td>Claims that the cross-sectional shape does not significantly influence pump performance. The cross-sectional area at the diffuser entrance has the greatest influence [31, p. 20]</td><td colspan="2">Claims that there are three shapes: trapezoidal, round, and rectangular with rounded edges. The most popular are trapezoidal. The sharp corners of the trapezoid are rounded with a radius, provided that the equality of the static moments of areas F_x and F_y is maintained $F_x \cdot r_x = F_y \cdot r_y$, where r_x and r_y are the radii of the centers of gravity of the areas F_x and F_y</td><td>The shape of the intermediate sections – Trapezoid. The sharp corners are rounded the same way to [34], [43]</td></tr>
<tr><td>Wall opening angle (ε)</td><td>-</td><td colspan="2">For $n_s = 50 - 60, \frac{a}{h} = 0{,}18 - 0{,}3; \gamma = 10 - 16^o$.
For $n_s > 80 \frac{a}{h} = 0{,}25 - 0{,}4; \gamma = 14 - 22^o$
When $n_s > 80$ it is recommended to gradually reduce the angle ε, moving from the calculated cross section to zero
where: a – the dimension characterizing the width of the volute casing walls' opening; h – the dimension characterizing the hight of the volute casing walls' opening; γ – Wall opening angle (Figure B.5) [34, p. 14], [43, p. 14]</td><td>The maximum total angle between the sides is usually about 60˚.[44, p. 119] Volutes with smaller angles give better results, however, this results in increased pump dimensions.</td></tr>
<tr><td>Cutwater angle</td><td>$n_s \leq 60$ $\varphi = 360^\circ$
$n_s = 88$ $\varphi = 348^\circ$
$n_s = 130$ $\varphi = 337{,}5^\circ$
$n_s = 190$ $\varphi = 327^\circ$
$n_s = 280$ $\varphi = 315^\circ$
[31, p. 15]</td><td colspan="2"><table><tr><td>n_s</td><td>50-70</td><td>70-90</td><td>90-110</td><td>110-130</td><td>130-150</td><td>150 - 180</td><td>180 -210</td><td>210 -240</td><td>>240</td></tr><tr><td>φ</td><td>360</td><td>350</td><td>345</td><td>340</td><td>335</td><td>330</td><td>325</td><td>320</td><td>315</td></tr></table>[34, p. 15], [43, p. 14]</td><td>Theoretical cutwater: $\varphi = \frac{132 \log 10\, R/R_2}{\tan \alpha_2'}$
Actual cutwater $\varphi = \frac{132 \log 10\, R_t/R_2}{\tan \alpha_2'}$
where α_2' – s the constant angle of the volute or the angle at which the water leaves the impeller Figure B.6 [44, p. 121]</td></tr>
<tr><td>Diffuser expansion angle</td><td>No more than 6˚- 8˚ [31, p. 18]</td><td colspan="2">The average speed at the pump outlet (V_{out}) should be in the range from 2 to 8 m/s. The outlet diameter of the diffuser: $D_{out} = \sqrt{\frac{4Q}{\pi \cdot V_{out}}}$. Optimal diffuser expansion angle 8-10º [34, p. 24], [43, p. 22]</td><td>10˚ [44, p. 118]</td></tr>
<tr><td>Calculation example</td><td>-</td><td>-</td><td>-</td><td>[44, p. 120]</td></tr>
</table>

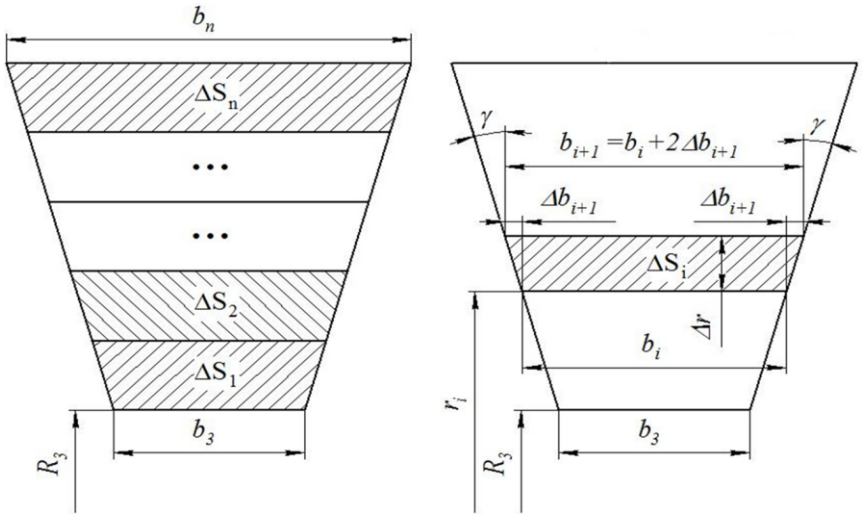

Figure B.1 – Scheme for determining the area of the calculated cross section of the volute casing and the main dimensions characterizing this cross section (Illustration from [34])

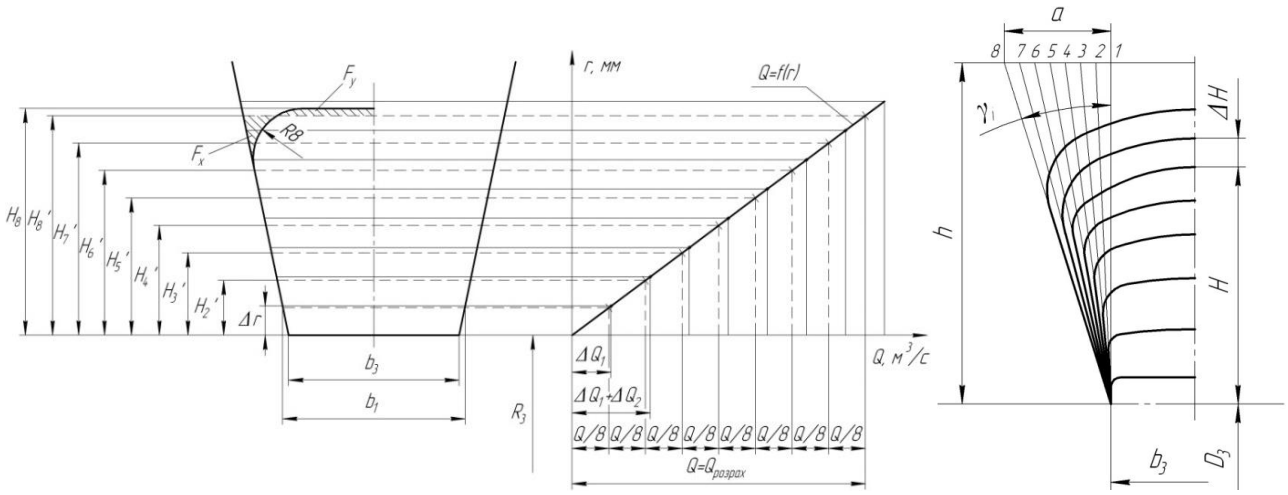

Figure B.2 – Scheme for determining the dimensions of the calculated cross section at 8 intermediate positions and the wall opening angle (Illustration from [34])

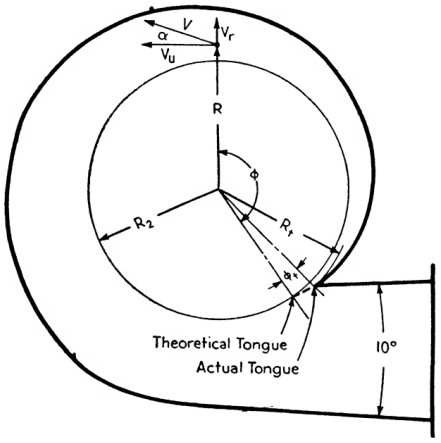

Figure B.3 – Geometric parameters for volute casing design [44]

Table B.4 - An overview of the design parameters of the volute casing from authors who adhere to the **method of angular momentum conservation**

<table>
<tr><th>Characteristic</th><th>Polotskiy [31]</th><th>Mashin [43]</th><th>Kolisnichenko [34]</th><th>Church [44]</th></tr>
<tr><td>Method</td><td colspan="4">Method of conservation of angular momentum of the flow</td></tr>
<tr><td>Angular momentum in volute</td><td>$\vartheta_{u3} = \frac{K_2}{r_3}$,
ϑ_{u3} - circumferential component of absolute velocity,
K_2 – moment of velocity, m²/s,
r_3 - volute inlet radius, m
[31, p. 12]</td><td colspan="2">V_{u_2} – circumferential component of the absolute flow velocity at the outlet of the impeller, m/s; R_2 radius of the impeller, m; $H_m = \frac{H}{\eta_г}$ – theoretical head, m; $g = 9{,}81$– acceleration due to gravity, m/s²;
$\omega = \frac{\pi \cdot n}{30}$ – angular velocity of the working wheel, s⁻¹.
For double-entry pump: $K_2 = \frac{gH_m}{\omega} + K_1$, where K_1 – speed moment at the impeller inlet $K_1 = 0{,}06\sqrt[3]{Q^2 \cdot n}$ (for double-entry pump instead of Q, the value Q/2 is substituted) [34, p. 18], [43, p. 16]</td><td></td></tr>
<tr><td>Inlet width (b_3)</td><td>$b_2^{`}$ - impeller width at the outlet taking into account the thickness of shrouds</td><td>For double-entry pump [43, p. 14]:
For pump type overhung and multistage pump:
$b_3 = mb_2$,
where m – coefficient from table below
<table>
<tr><th rowspan="2">n_s</th><th colspan="2">Type of pump</th></tr>
<tr><th>Overhung</th><th>Double-entry and multistage pump</th></tr>
<tr><td>60</td><td>2.6-2.8</td><td>1.85-1.95</td></tr>
<tr><td>80</td><td>2.3-2.5</td><td>1.7-1.8</td></tr>
<tr><td>100</td><td>2.1-2.25</td><td>1.6-1.7</td></tr>
<tr><td>120</td><td>1.9-2.05</td><td>1.45-1.55</td></tr>
<tr><td>150</td><td>1.75-1.85</td><td>1.35-1.45</td></tr>
<tr><td>180</td><td>1.62-1.7</td><td>1.28-1.38</td></tr>
<tr><td>220</td><td>1.52-1.62</td><td>1.2-1.3</td></tr>
<tr><td>260</td><td>1.5-1.57</td><td>1.15-1.25</td></tr>
</table></td><td>For double-entry pump:
[34, p. 12]</td><td>where
x – distance between any radius R and the impeller outside radius R_2,
θ – Wall opening angle
[44, p. 121]</td></tr>
<tr><td>Inlet diameter (D_3)</td><td></td><td colspan="2">$D_3 = 2R_3 = 2(1{,}03 - 1{,}05)R_2$ [34, p. 12], [43, p. 13]</td><td></td></tr>
<tr><td>Volute throat area</td><td>Theoretical Volute throat area:
a - an arbitrary linear dimension (length) introduced for the graphical evaluation of the integral;
B_a - width of the volute cross-section at the design point
The graphical calculation of the integral is presented in
[31, pp. 15–17]</td><td colspan="2">Actions for calculating:
Determine D_3, b_3
Set the inclination of the volute side walls
Determine the volute opening angle φ
Determine equivalent linear flow measure of the volute. Calculate the area of the 8 cross sections of the volute:
5.1) to determine the area 8-th of the cross section, the cross section is divided into n elementary areas ΔS_i of the same height Δr (Figure B.1)
5.2) the fluid flow rate through the areas is determined, the resulting flows are summed
See Table B.2
5.3) the calculation is carried out until the total flow rate exceeds the pump flow rate value $Q_8 \approx 1{,}05Q$.
5.4) knowing the final height of cross section r, a trapezoid cross section can be created (Figure B.1). Trapezoid is limited by the selected values of b_3 and the angle ε.
5.5) a graph is constructed based on tabular data, which is connected to the meridian section of the volute (Figure B.5).
Verify the accuracy of the calculated cross-sectional area
[34, pp. 12–22], [43, pp. 15–18],[44, p. 121]</td><td></td></tr>
<tr><td>Height of throat area</td><td>See Table B.2</td><td colspan="2">See Table B.2</td><td>-</td></tr>
</table>

<table>
<tr><td>Area of intermediate cross sections</td><td>The cross-sectional area changes proportionally to the angle φ between the 8 cross section and the calculated
$F = F_{pc} \cdot \frac{\varphi}{\varphi_v}$ [31, p. 18]</td><td colspan="2">The cross-sectional area changes proportionally to the angle φ between the 8 cross section and the calculated
$F = F_{pc} \cdot \frac{\varphi}{\varphi_v}$ [43, p. 17]</td><td>On graph (Figure B.1) Q_8 is divided into equal parts, the number of which corresponds to the number of sections of the volute [34, p. 21]</td><td>Table B.2</td></tr>
<tr><td>Shape of intermediate sections and trapezoid rounding method</td><td>Claims that the cross-sectional shape does not significantly influence pump performance. The cross-sectional area at the diffuser entrance has the greatest influence [31, p. 20]</td><td colspan="3">Claims that there are three shapes: trapezoidal, round, and rectangular with rounded edges. The most popular are trapezoidal. The sharp corners of the trapezoid are rounded with a radius, provided that the equality of the static moments of areas F_x and F_y is maintained $F_x \cdot r_x = F_y \cdot r_y$,
where r_x and r_y are the radii of the centers of gravity of the areas F_x and F_y</td><td>The shape of the intermediate sections – Trapezoid. The sharp corners are rounded the same way to [34], [43]</td></tr>
<tr><td>Wall opening angle (ε)</td><td>-</td><td colspan="3">For $n_s = 50 - 60, \frac{a}{h} = 0{,}18 - 0{,}3; \gamma = 10 - 16^o$.
For $n_s > 80 \frac{a}{h} = 0{,}25 - 0{,}4; \gamma = 14 - 22^o$
When $n_s > 80$ it is recommended to gradually reduce the angle ε, moving from the calculated cross section to zero
where: a – the dimension characterizing the width of the volute casing walls' opening; h – the dimension characterizing the hight of the volute casing walls' opening; γ – Wall opening angle (Figure B.5) [34, p. 14], [43, p. 14]</td><td>The maximum total angle between the sides is usually about 60˚.[44, p. 119] Volutes with smaller angles give better results, however, this results in increased pump dimensions.</td></tr>
<tr><td>Cutwater angle</td><td>$n_s \leq 60$ φ=360˚
n_s=88 φ=348˚
n_s=130 φ=337,5˚
n_s=190 φ=327˚
n_s=280 φ=315˚
[31, p. 15]</td><td colspan="3"><table><tr><td></td><td>50-70</td><td>70-90</td><td>90-110</td><td>110-130</td><td>130-150</td><td>150 - 180</td><td>180 -210</td><td>210 -240</td><td>>240</td></tr><tr><td>φ</td><td>360</td><td>350</td><td>345</td><td>340</td><td>335</td><td>330</td><td>325</td><td>320</td><td>315</td></tr></table>[34, p. 15], [43, p. 14]</td><td>Theoretical cutwater:
Actual cutwater
where α_2' – s the constant angle of the volute or the angle at which the water leaves the impeller Figure B.3 Figure B.3 [44, p. 121]</td></tr>
<tr><td>Diffuser expansion angle</td><td>No more than 6˚- 8˚ [31, p. 18]</td><td colspan="3">The average speed at the pump outlet (V_{out}) should be in the range from 2 to 8 m/s.
The outlet diameter of the diffuser: $D_{out} = \sqrt{\frac{4Q}{\pi \cdot V_{out}}}$. Optimal diffuser expansion angle 8-10º [34, p. 24], [43, p. 22]</td><td>10˚ [44, p. 118]</td></tr>
<tr><td>Calculation example</td><td>-</td><td colspan="2">-</td><td>-</td><td>[44, p. 120]</td></tr>
</table>

Table B.5 – An overview of the design parameters of the volute casing from various authors who adhere to the **constant velocity method**

Characteristic	**Aizenstein [47]**	**Stepanoff [33]**	**Lobanoff [48]**
Method	Constant velocity method		
K3 coeff. estimation	$c_3 = K_3\sqrt{2gH}$ where K_3 factor chosen according to Figure B.4 and depends on n_s	$c_3 = K_3\sqrt{2gH}$ where K_3 is experimental design factor (Figure B.6b)	-
Inlet width (b_3)	$b_3 = (0.5 \dots 0.7)b_2$ 0,5 for n_s>130 0,7 for $n_s \leq$130	For pumps with: - low n_s: $b_3 = 2 \cdot b_2$; - medium n_s: $b_3 = 1.75 \cdot b_2$; - n_s>210, double-entry $b_3 = 1{,}6 \cdot b_2$	***b₃*** / ***N*s.US** (US units) / ***n*s** $2.0b_2$ / <1000 / 19 $1.75b_2$ / 1000-3000 / 19-58 $1.6b_2$ / >3000 / 58 [48, p. 36]
Inlet diameter (D_3)	$D_3 = D_2 \cdot K_{start}$ K_{start} – coefficient (see Figure B.4)	According to the Figure B.6b $\rho = \frac{D_3 - D_2}{D_2}$ [33, p. 117]	***D₃*** / ***N*s.US** / ***n*s** $1.05D_2$ / 600-1000 / 12-19 $1.06D_2$ / 1000-1500 / 19-29 $1.07D_2$ / 1500-2500 / 29-48 $1.09D_2$ / 2500-4000 / 48-78 [48, p. 36]
Volute throat area	$A_\varphi = \frac{Q}{c_3}$	$A = \frac{Q}{c_3}$ $A = b_2 \cdot D_3 \cdot \pi \cdot \sin\alpha_\vartheta$ where α_ϑ – volute angle (see Figure B.6a)	$A = \frac{0.04 \cdot GPM}{K_3 . H^{-5}}$ *GPM* – flow rate, gal per meter; *H* – head, ft, K_3 – coefficient from Figure B.5. For double-entry pump this value should be divided by 2 [48, p. 33]
Hight of throat area	$E_8 = K_{op} \cdot \frac{D_2}{2} - \frac{D_3}{2}$	-	-
Area of intermediate cross sections	The cross-sectional area changes proportionally to the angle φ between the 8 cross sections and is calculated $A_\varphi = \frac{Q}{c_3} \cdot \frac{\varphi}{360}$		-
Shape of intermediate sections and trapezoid rounding method	Gives examples of round and trapezoidal cross sections.	-	For low flow rate (500-600 GPM) or low to medium specific speed ($N_{s.US}$ < 1,100, (n_s = 21)) pumps - rectangular volute design. Round volutes - below $n_{s.US}$ of 600 (n_s = 12), round volutes don't used for multi-stage pump [48, p. 58]
Wall opening angle (ε)	35^0 - 45^0	-	Schematic diagram indicating wall opening angles of 30˚ and 45˚[48, p. 60]
Cutwater angle	The angle created by the cutwater must be equal to the angle of the flow direction at the impeller outlet (α_3) $\alpha_3 = \frac{\arctan c_{r2}}{c_{u3}}$, c_{r2}– meridional component of absolute velocity, c_{u3}– radial component of absolute velocity, 2-impeller; 3 – volute. The cutwater is shortened by 12^0-15^0 from the theoretical one, which begins at the 8th cross section.	According to the Figure B.6b	-
Diffuser expansion angle	-	-	No more than 7˚- 13˚
Calculation example	[47, p. 88]	-	[48, pp. 33, 60]

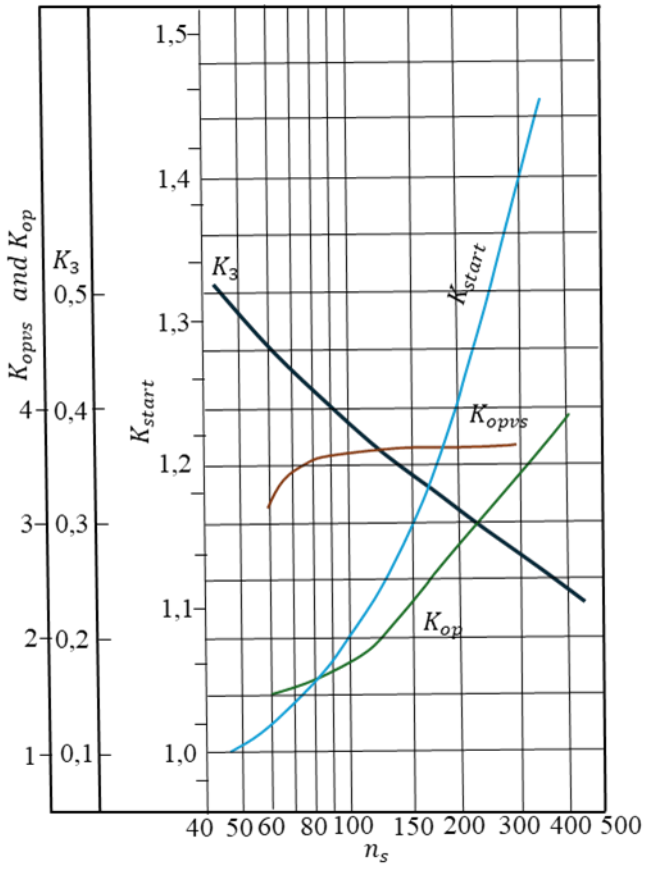

Figure B.4 – Coefficient curves for volute casing design according to [47] (created by the author based on Figure 54 from [47]), where K_{start} – coefficient for determining D_3 of the volute casing, K_{op} – volute casing opening size, K_3 – coefficient for determining the velocity in volute casing

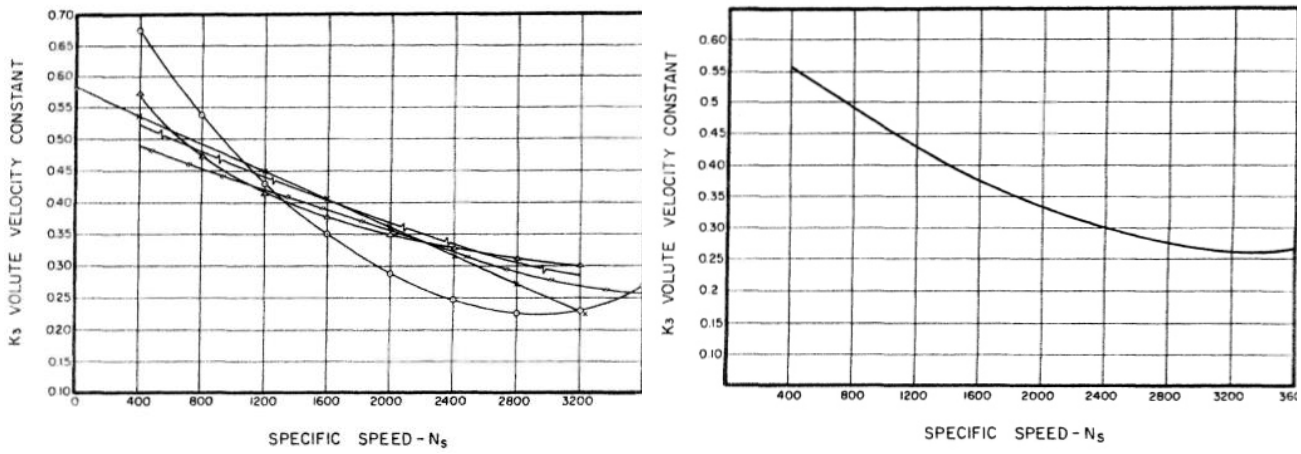

Figure B.5– Coefficient curves for volute casing design according to [48, p. 35]: a) data acquisition of different pump companies; b) Lobanoff recommendation

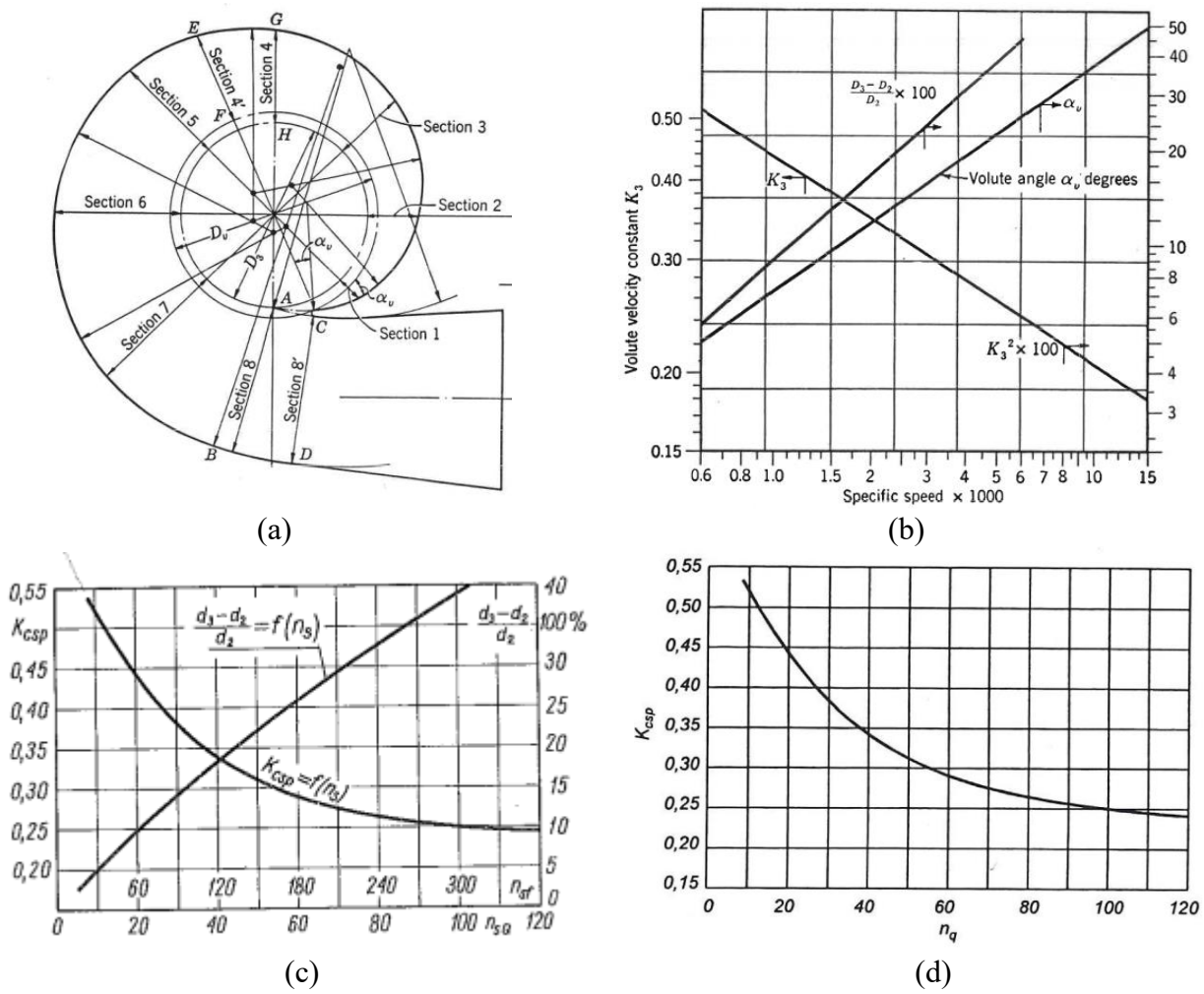

Figure B.6 – Geometric parameters for volute casing design:
a) cross section of volute casing with location of geometric parameters [33];
b) graph of constants for volute casing design (specific speed $N_{s.US}$ calculated in US customary units [33]: n in rpm, Q in gpm, H in ft);
c) graph of constants for volute casing design according to [45] based on [33];
d) graph of constants for volute casing design according to [46, p. 158]

Table B.6 – An overview of the design parameters of the volute casing from various authors who adhere to the **constant velocity method**, the **method of conservation of angular momentum** of the flow and other

Characteristic	Defeld [39]	Lazarkiewicz [45]	Jędral [46]	Gülich [35]
Method	Method of conservation of angular momentum of the flow and Constant velocity method			
Average velocity in the volute / Angular momentum in volute	Considers 4 types of volutes: (see Table 2.1) [39, p. 55]	-	-	For n_q < 25 to 35 - constant velocity; For n_q > 25 to 35 - the conservation of angular momentum [35, p. 462]. Min. losses - angular momentum conservation method.
Inlet width (b_3)	-	$b_3 = (1.4 \dots 1.8)\, b_2$ [45, p. 320]	$b_3 = [1.4 \dots 1.8(2.0)] b_2$ [46, p. 153]	At small n_q b_3 =(2.0…4.0) b_2. For hight n_q b_3=(1.05..1.2) b_2 [35, p. 458].
Inlet diameter (D_3)	-	According to the Figure B.6c $\rho = \frac{D_3 - D_2}{D_2}$ [45, p. 319]	$d_3 = (1.03 \dots 1.05) d_2$ [46, p. 153]	$\frac{d_z}{d_2} \geq 1.03 + 0.1 \frac{n_q}{n_{q\,ref}} + +0.07 \frac{\rho}{\rho_{ref}} \frac{H_{st}}{H_{ref}}$ $n_{q\,ref}$ = 40; H_{st} – head per stage; $H_{ref} = 1000\ m$; $\rho_{ref} = 1000$ kg/m^3; d_z – cutwater distances [35, p. 667]
Volute throat area	*Method of conservation of angular momentum of the flow* *Graphical method.* Divide the longitudinal section of the volute into 8 equal parts (marked "m" Figure B.7a). Each formed small volute will have a flow rate of 1/8 of the total. In section 1, the area will be equal to $Q/8v_2$ (v_s – velocity in volute). In the middle of 0-1 section area will be equal $Q/2 \cdot 8 \cdot v_2$. In section 3, the area is equal to $Q/8v_s$. The area of the second small volute, by analogy with the first in section 2, should be equal $Q/8v_2$. Such calculations are performed for all small volutes. Then they are summed up. Thus, a plane diagram is Figure B.7b. *Formulas method:* Area of inlet cross section $A_1 = \frac{Q}{v_{vol}}$	*Method of conservation of angular momentum of the flow* $dQ = dAc_u = \frac{b}{r} dr$ For the selected cross section shape, the radius r_w and increments Δr are assumed, and then the ratios *b/r* are found for them. The area $\Delta A = b(R)_m \Delta r$ is calculated as the area of the trapezoid. Then the sum $\sum \Delta A$ is created. The angle ϑ is calculated for it: $\vartheta = \frac{360\chi}{Q} \int_{r_w}^{r_z} \frac{b}{r} dr$ where $\chi = c_{u3} r_a = gH_{th}/\omega$. Based on the assumed value of r_w and Δr, the curve $\vartheta - f(r)$ is plotted. Then the area increasing according to the Pfleiderer correction	*Method of conservation of angular momentum of the flow* Volute is divided into 8 - 10 sections, which is then divided into segments with widths Δr = 3…10 mm. The rounding radius for individual cross sections should increase as *R* grows. Through the entire cross-section flows: $Q_v = K_2 \int_{r_3}^{R} \frac{b}{r} dr$ For each cross section: $\int_{r_3}^{R} \frac{b}{r} dr \approx \sum_i \frac{b_i}{r_i} \Delta r$ The next step is to create a graph $R(\vartheta)$. On its basis, a cross section of the volute is graphically constructed.	*Method of conservation of angular momentum of the flow* An elemental fluid volume $dQ = c_u \cdot b dr = c_{2u} \cdot \frac{r2}{r} \cdot b \cdot dr$ flows through an area element $dA = b \cdot dr$ located on the radius *r* within cross section *A*. The flow rate through the entire cross section is obtained by integration $Q(\varepsilon) = c_{2u} \cdot r_2 \int \frac{b}{r} dr$. From the start of the volute (point S in Figure B.9) to the cross section A, the impeller discharges the flow $Q(\varepsilon) = Q_{opt}\, \varepsilon^\circ / 360^\circ$ in the design point. The cross section A must be designed according to formula: $\int_{r_z}^{r_A} \frac{b}{r} dr = \frac{Q_{opt} \varepsilon}{360 c_{2u} r_2}$ $Q = \int c_{2u} \frac{r_2}{r} b dr\ m$[35, p. 113] Full instructions [35, p. 461]

Characteristic	Defeld [39]	Lazarkiewicz [45]	Jędral [46]	Gülich [35]
	$A_8 = \frac{Q}{2m}\left(\frac{n+1}{v_2} + \frac{m-1}{v_{vol}}\right)$ n – number of small volutes, m – number of cross sections of the volute, v_{vol} – velocity in volute, v_2 – velocity at impeller outlet. *Constant velocity method*: $A_8 = \frac{Q}{v_{vol}}$, v_{vol} – velocity in volute	$\Delta A = \frac{0.04}{8}\frac{\pi}{180} r_z \int_0^v b\, dr$ *Constant velocity method* $c_3 = K_3\sqrt{2gH}$, $A = \frac{Q}{c_3}$ [45, pp. 315-316,319]	Cross-sectional areas are adjusted using Pfleiderer's correction: $\Delta A_\vartheta = \frac{0.04}{8}\frac{\pi}{180} R \int_0^\vartheta b_{av}\, dv$ *Constant velocity method*: $A_{max} = \frac{Q}{c_{sp}}$ Velocity in volute: $c_{sp} = K_{c\,sp}\sqrt{2gH}$ where $K_{c\,sp}$ is experimental design factor (Figure B.6d)	*Constant velocity method* The velocity in the throat area then amounts to: $c_{3q} = \frac{Q_{Le}}{A_{3q}}, A_{3q} = \int_{r_z}^{r_A} b\, dr$
Hight of throat area	-	-	-	For rectangular volute: $a_3 = r_a - r_z^{`} = r_z^{`} \exp\left\{\frac{Q_{Le} \cdot \varepsilon_{sp}}{b_3 c_{2u} r_2 2_\pi} - 1\right\}$
Area of intermediate cross sections	$A_\varphi = \frac{Q}{v_{vol}} \cdot \frac{\varphi}{360}$		$A_v = \frac{A_{\max \cdot \vartheta}}{360}$ [46, p. 158]	*Method of conservation of angular momentum of the flow* The circumferential angle on which the cross section under consideration has to be arranged (Figure B.9) $\varepsilon = 360\frac{c_{2u} r_2}{Q_{Le}} \sum_{r_z}^{r_A} \frac{b}{r} \Delta r$ Q_{Le} – flow rate through diffuser *Constant velocity method* $A(\varepsilon) = \frac{Q(\varepsilon)}{c_{3q}} = \frac{Q_{Le} \cdot \varepsilon}{c_{3q} \cdot \varepsilon_{sp}} = A_{3q}\frac{\varepsilon}{\varepsilon_{sp}}$ ε - circumferential angle A_{3q} - volute throat area
Shape of intermediate sections and trapezoid rounding method	Round shape has less losses, but other shapes such as trapezoidal and rectangular also can be used	Gives examples of all cross sections	Round and trapezoidal shapes are most popular. Rectangular shapes are rarely used to simplify casting and provide additional strength. Roundings are calculated according to algebraic relationships [46, p. 166]	It is expected that flat cross section (i.e. a cross-section flattened in shape, with its width greater than its height) result in less intense secondary flow than round cross sections, thereby generating fewer losses. Rectangular and trapezoidal shapes offer the advantage to be developed on surfaces of revolution, something that facilitates design and manufacture. Volute casings with round cross sections that cannot be arranged on surfaces of revolution are employed, for

Characteristic	Defeld [39]	Lazarkiewicz [45]	Jędral [46]	Gülich [35]
				instance, when the volute is welded together from segments. In double volutes the cross sections of the inner volute and the outer channel must be matched so that the casing outer wall is given an easily producible shape, and a simple transition to the round discharge nozzle is achieved.
Wall opening angle (ε)	-	-	30º- 40º[46, p. 153]	-
Cutwater	-	-	-	Should be profiled elliptically, must be short and thick. The leading edge thickness e_3 of the cutwater can be defined by a circle; its diameter should be approximately $0.02 \times d_2$. In order to reduce noise and vibrations an oval-shaped leading edge of the cutwater may be selected. [35, p. 458] $\varepsilon > 30^{\circ}$ [35, p. 667] *Cutwater angle* $\alpha_{3B} = \alpha_3' + i_3$, incidence 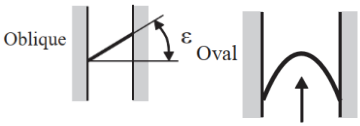 $i3 = \pm 3^{\circ}$ (Figure B.9) $\tan(\alpha_3^{`}) = \frac{c_{3m}}{c_{3u}}$, $c_{3u} = c_{2u}\frac{d_2}{d_3}$
Diffuser expansion angle and geometrical parameters	No more 7º-10º Area of diffuser outlet: $A_{diff} = \frac{10Q}{8\,v_{vol}}$ v_{vol} – velocity in volute [39, pp. 48, 46]	Selected from the figure Figure B.8 [45, p. 323] (identical to the [46, p. 160]	Selected from the Figure B.8 length of diffuser $tg\frac{\delta}{2} = \frac{d_t - d_0}{2l}$ where δ – opening angle; dt – diameter of the diffuser outlet according to the ISO 6708 so that the exit velocity is within 4…6 m/s; l – less of diffuser [46, p. 159]	Equivalent inlet radius $R_{1,eq} = \sqrt{\frac{A_1}{\pi}}$ Equivalent opening angle $\vartheta_{eq} = \frac{R_{1,eq}}{L}\left\{\sqrt{\frac{A_1}{\pi}} - 1\right\}$ 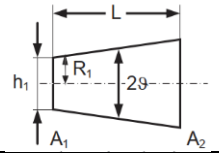
Calculation example	[39, pp. 47, 53]	[45, p. 323]	[46, p. 165]	-

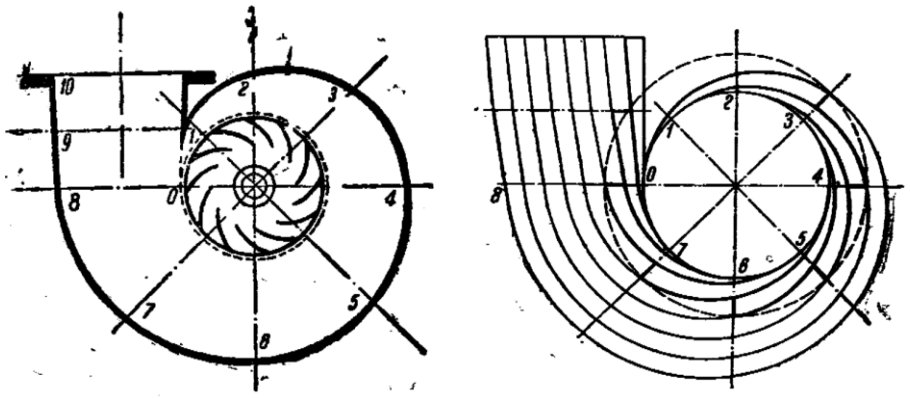

(a)

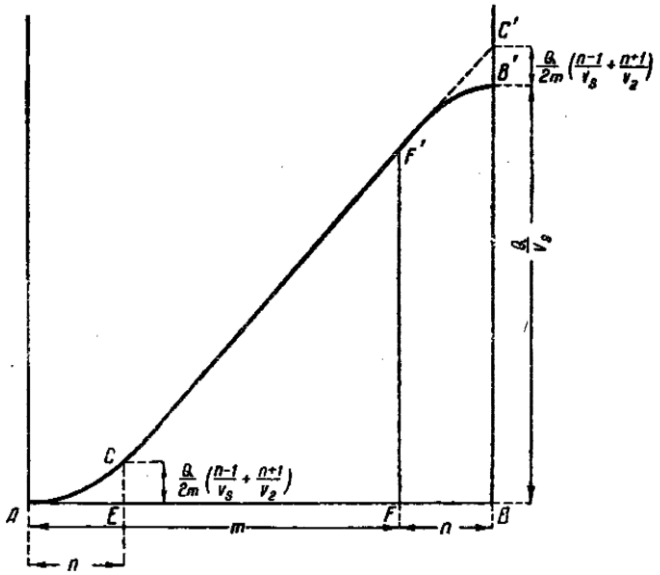

(b)

Figure B.7 – Volute casing division for calculation by of angular momentum conservation method: a) the longitudinal section of the volute, which is divided into eight equal parts, b) construction of the planar diagram of the volute based on the calculated cross-section areas [39, p. 48]

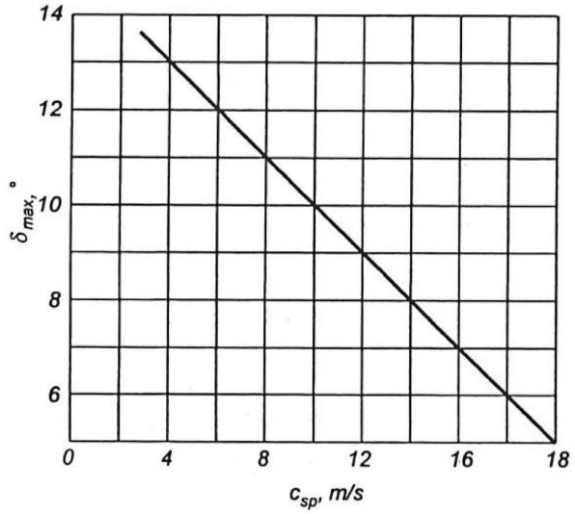

Figure B.8 – Dependence of the diffuser opening angle on velocity c_{sp} [46, p. 160]

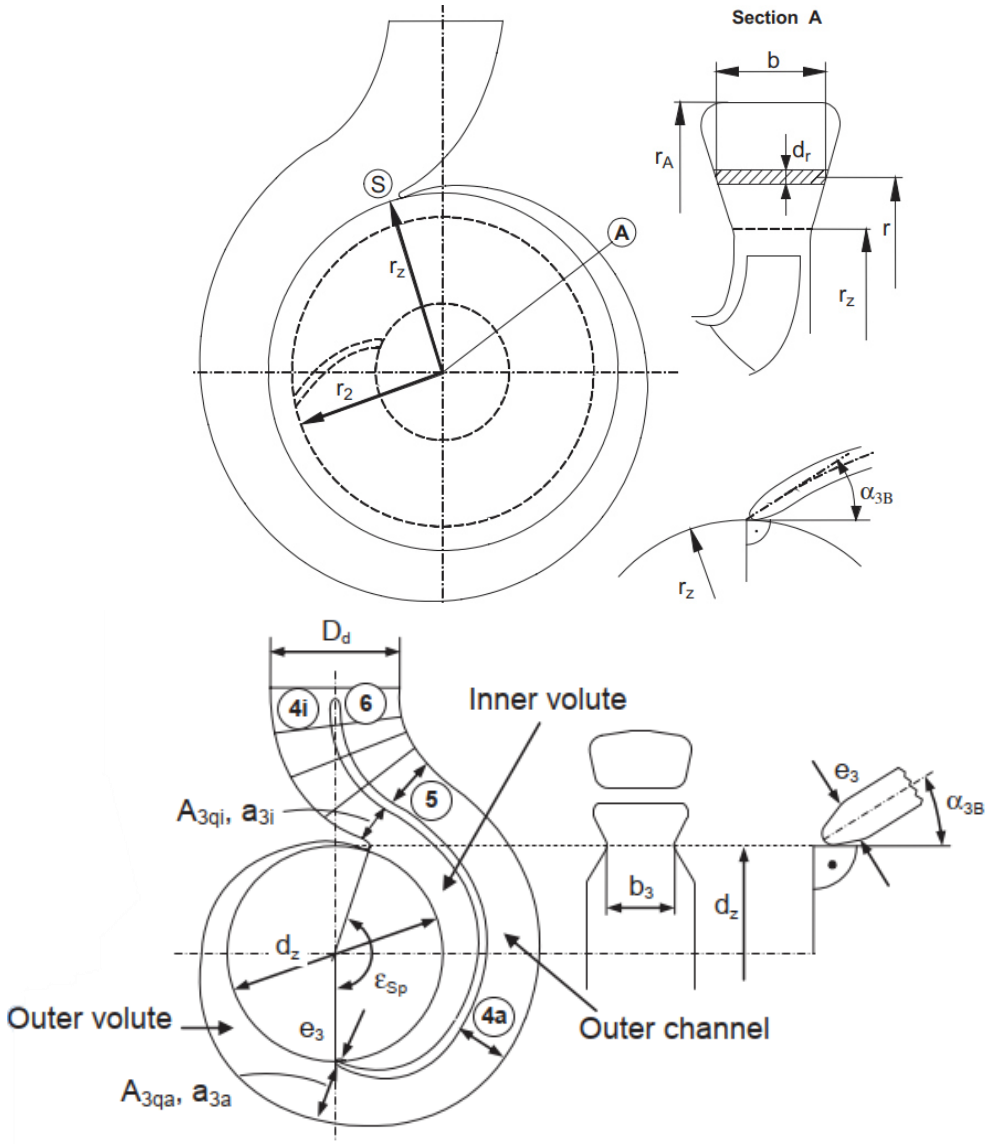

Figure B.9 – Determining the dimensions of the volute casing [35]

Appendix C. Influence of the volute opening angle of the walls on Omega pump and PAT performance. Full graphs

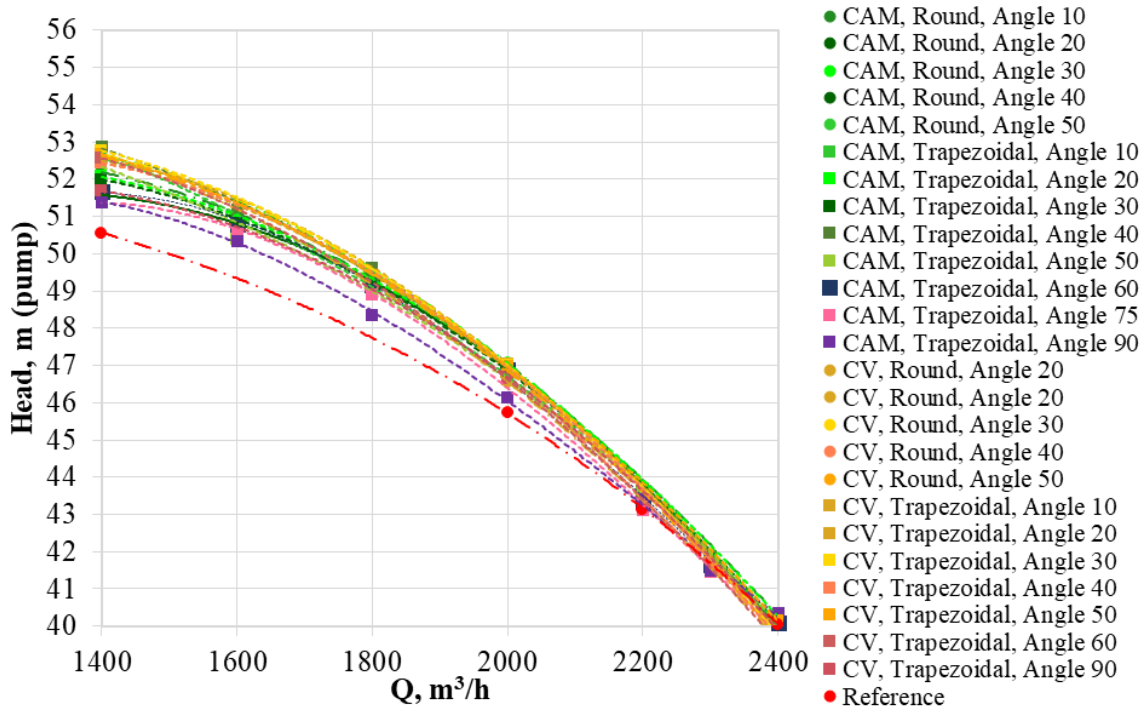

(a)

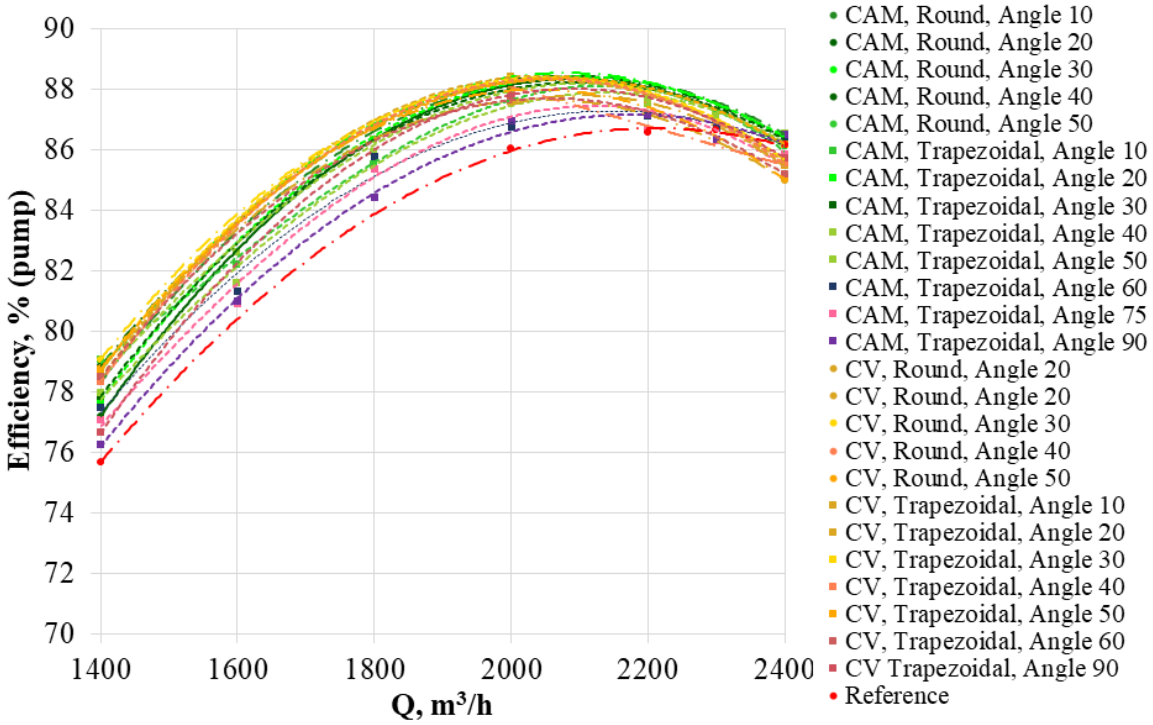

(b)

Figure C.10 – Influence of the volute opening angle of the walls on the Omega pump performance parameters in pump mode (full graph): a) head curves and b) efficiency curves

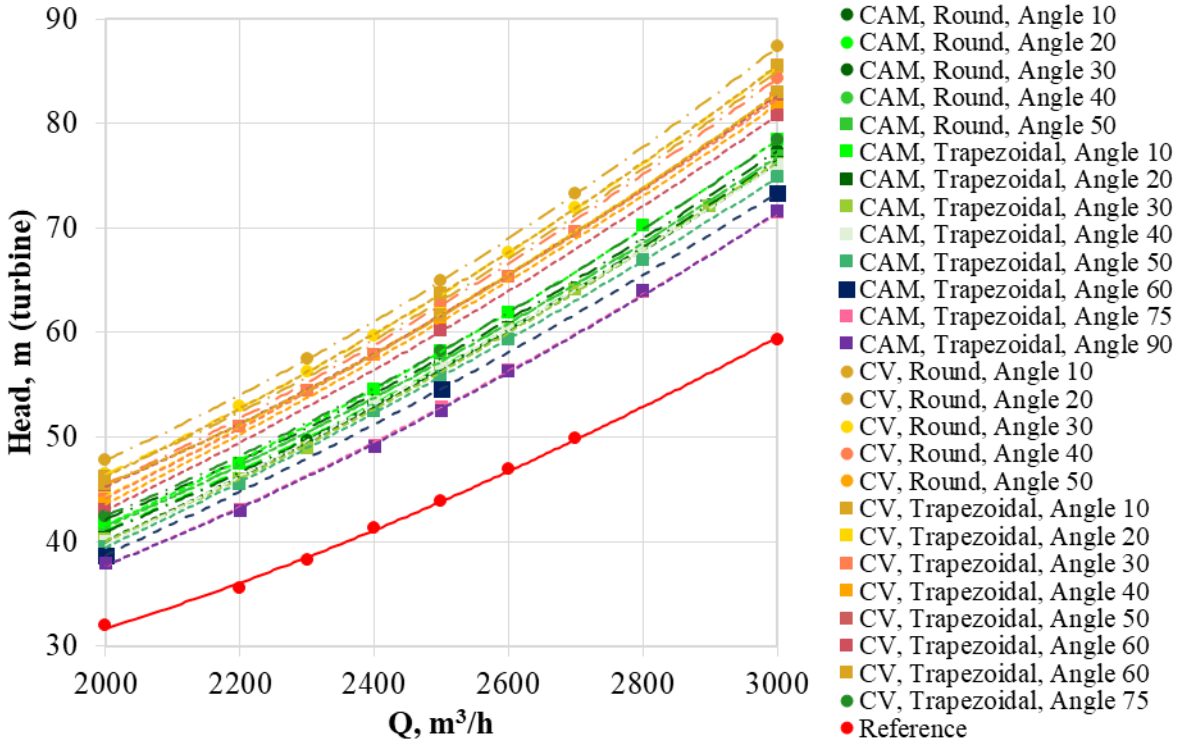

(a)

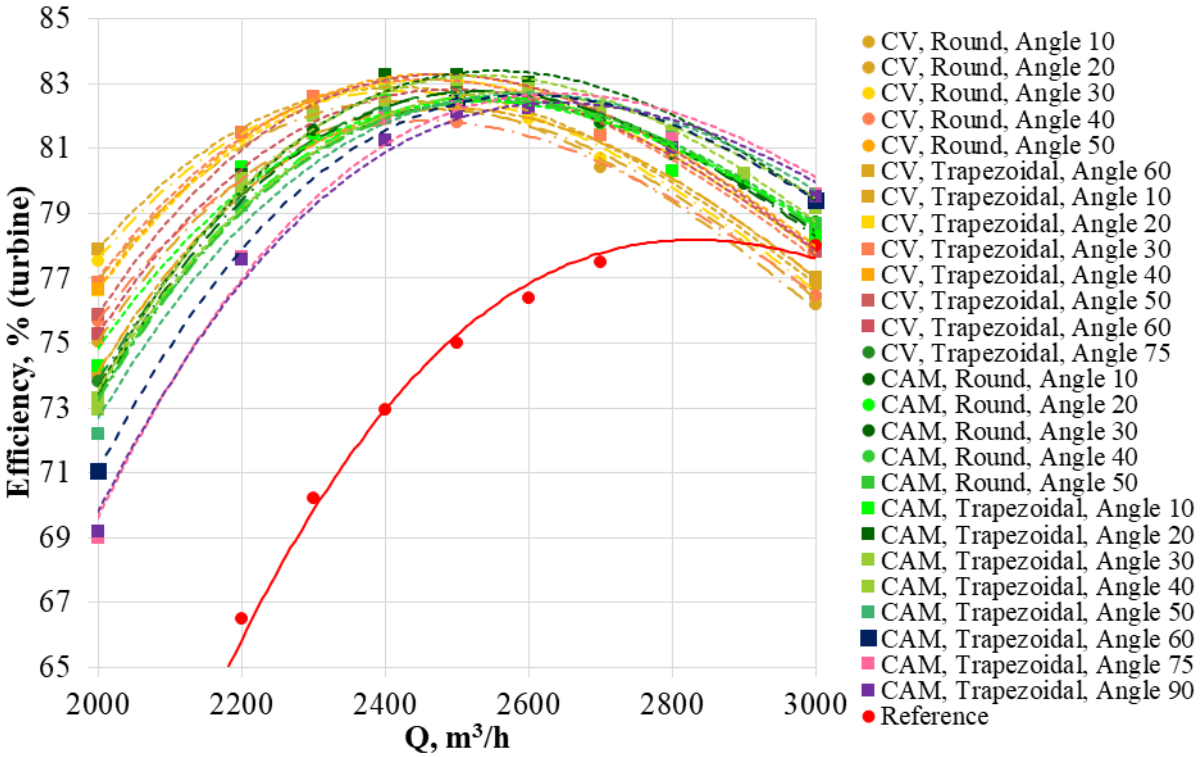

(b)

Figure C.20 – Influence of the volute opening angle of the walls on the pump characteristics in turbine mode (full graph): a) head curves and b) efficiency curves

Appendix D. Influence of method of volute casing`s design, D_3, b_3, cross-sectional shape on the Omega pump performance. Full graphs

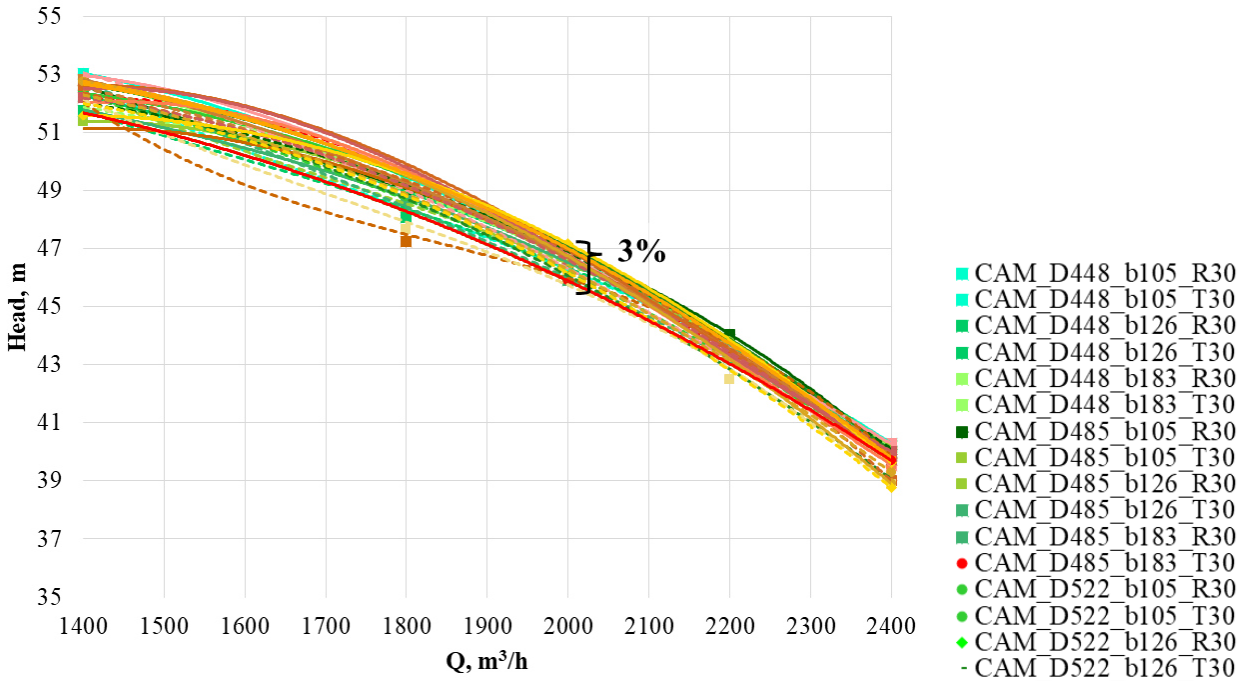

(a)

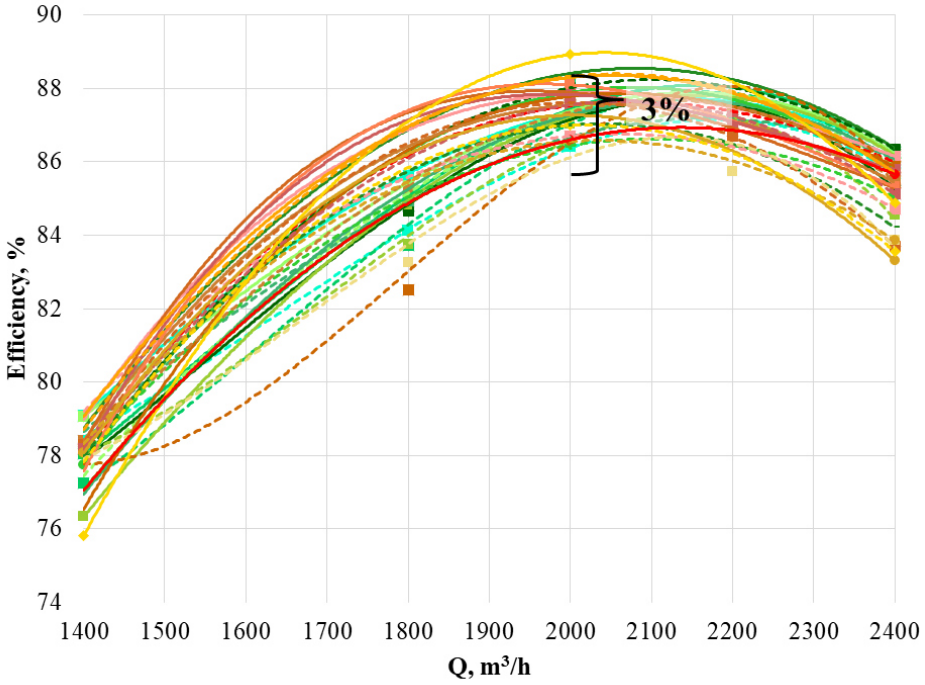

(b)

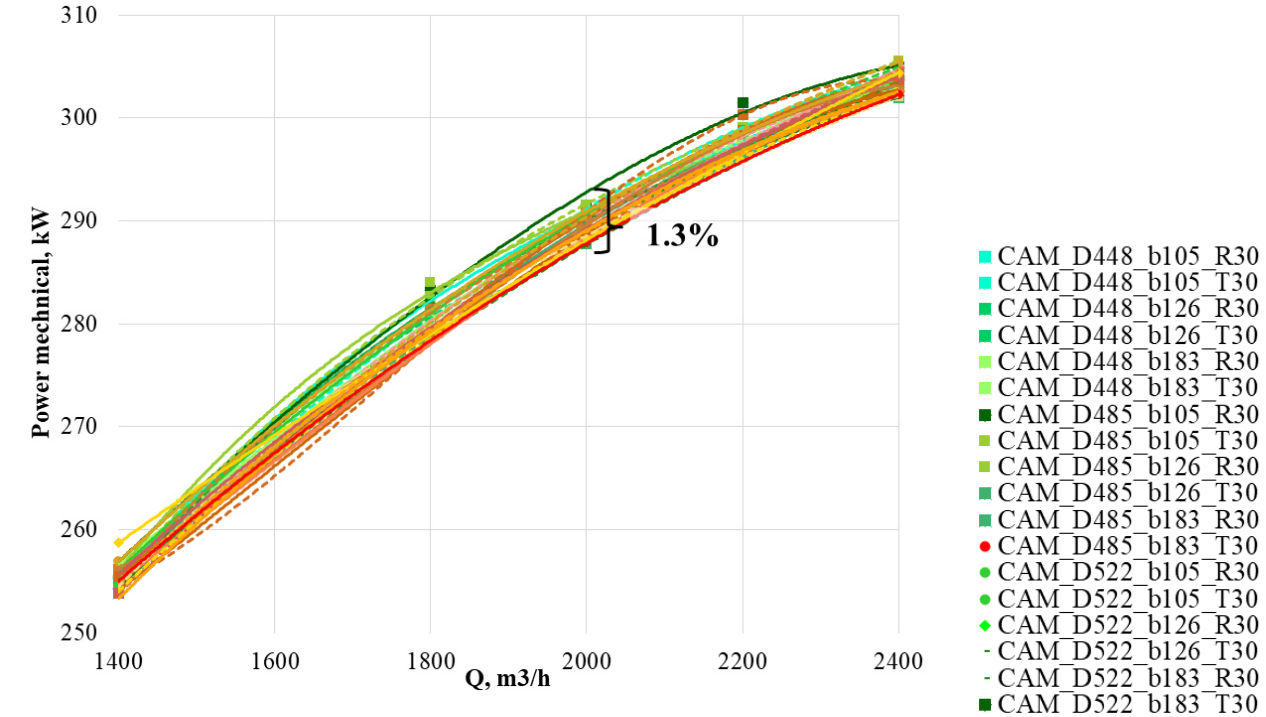

(c)

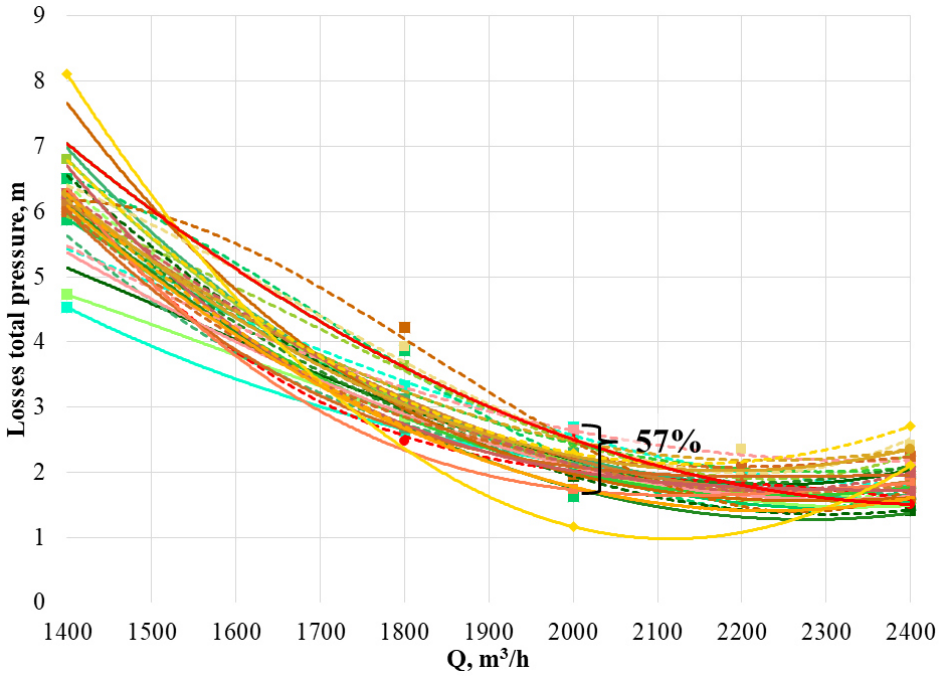

(d)

Figure D.11 - Influence of the method of volute casing`s design, D_3, b_3, cross-sectional shape on the Omega pump characteristics in pump mode (full graph): a) Head curves, b) Efficiency curves, c) Power mechanical, d) Losses total pressure

Appendix E. Influence of design method, D_3, b_3, cross-sectional shape on Omega PAT performance. Full graphs

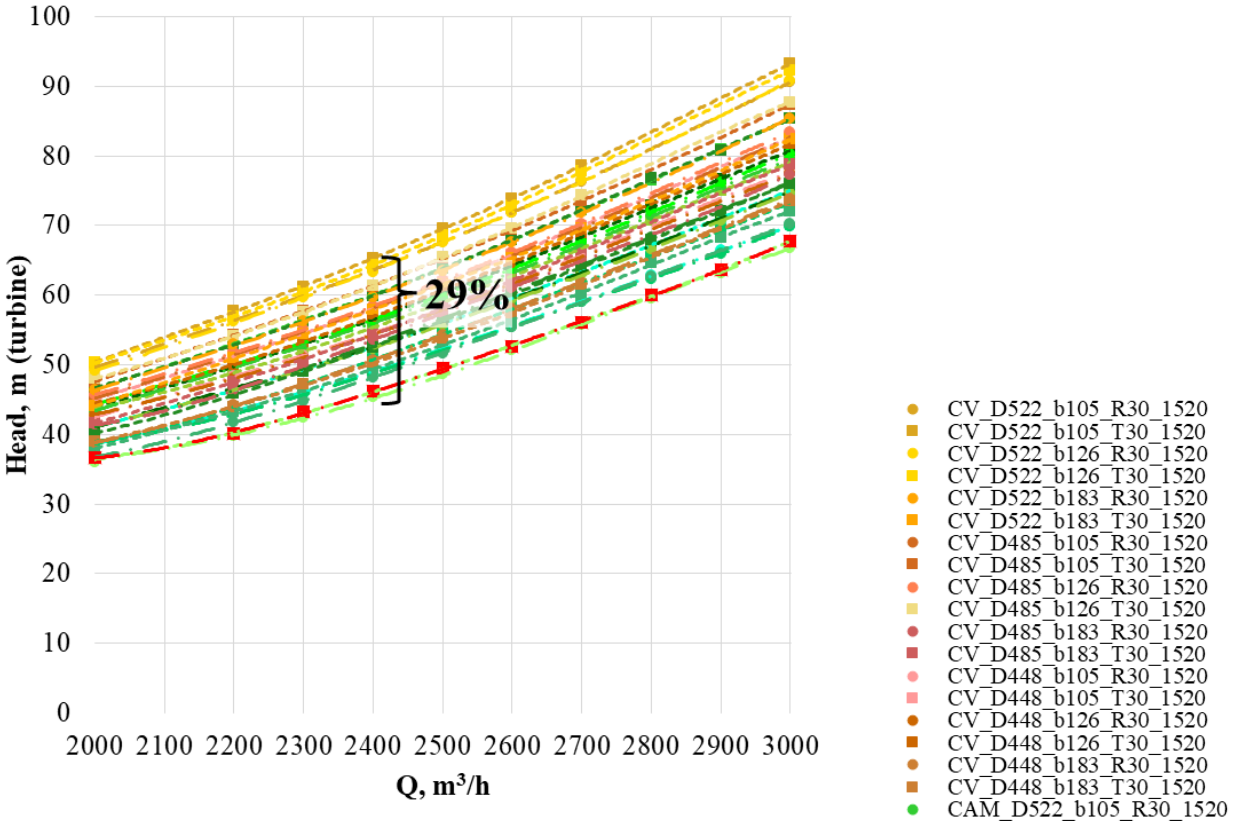

(a)

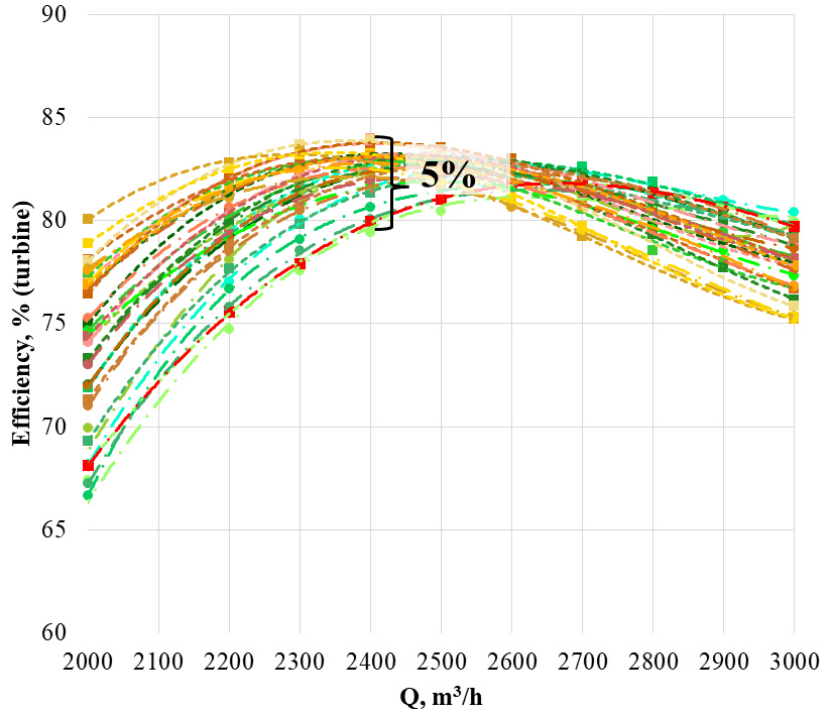

(b)

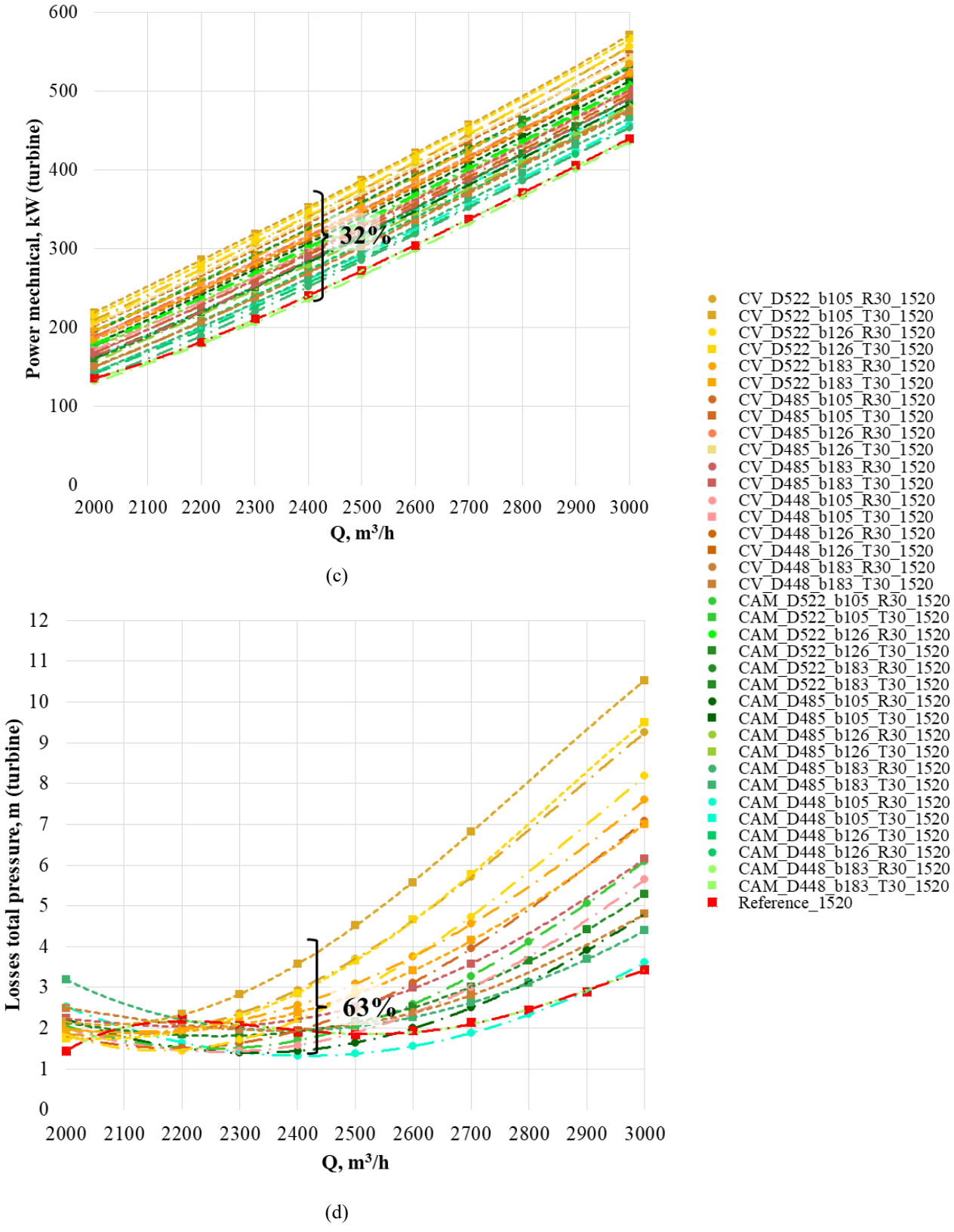

Figure E.12 - Influence of the method of volute casing`s design, D_3, b_3, cross-sectional shape on the Omega PAT characteristics in turbine mode (full graph): a) head curves and b) efficiency curves

Appendix F. Comparison of curing curves for Omega PAT at different geometric parameters

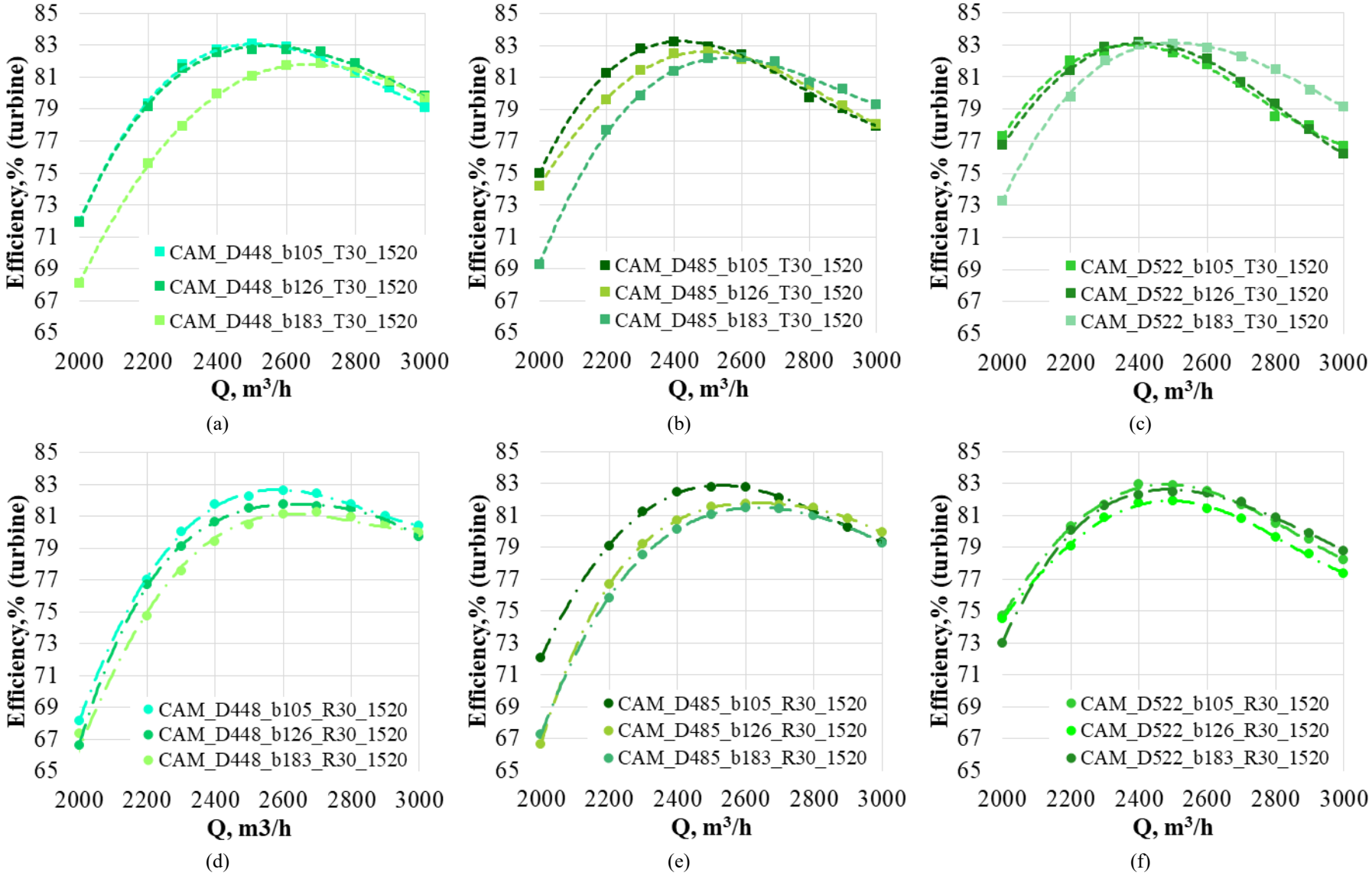

Figure F.13 – Comparison of PAT efficiency for varying b_3 at constant D_3, for round and trapezoidal volute shapes designed using the CAM method:
a) varying b_3, D_3 = 448 mm, trapezoidal; b) varying b_3, D_3 = 485 mm, trapezoidal; c) varying b_3, D_3 = 522 mm, trapezoidal; d) varying v, D_3 = 448 mm, round; e) varying b_3, D_3 = 485 mm, round; f) varying b_3, D_3 = 522 mm, round

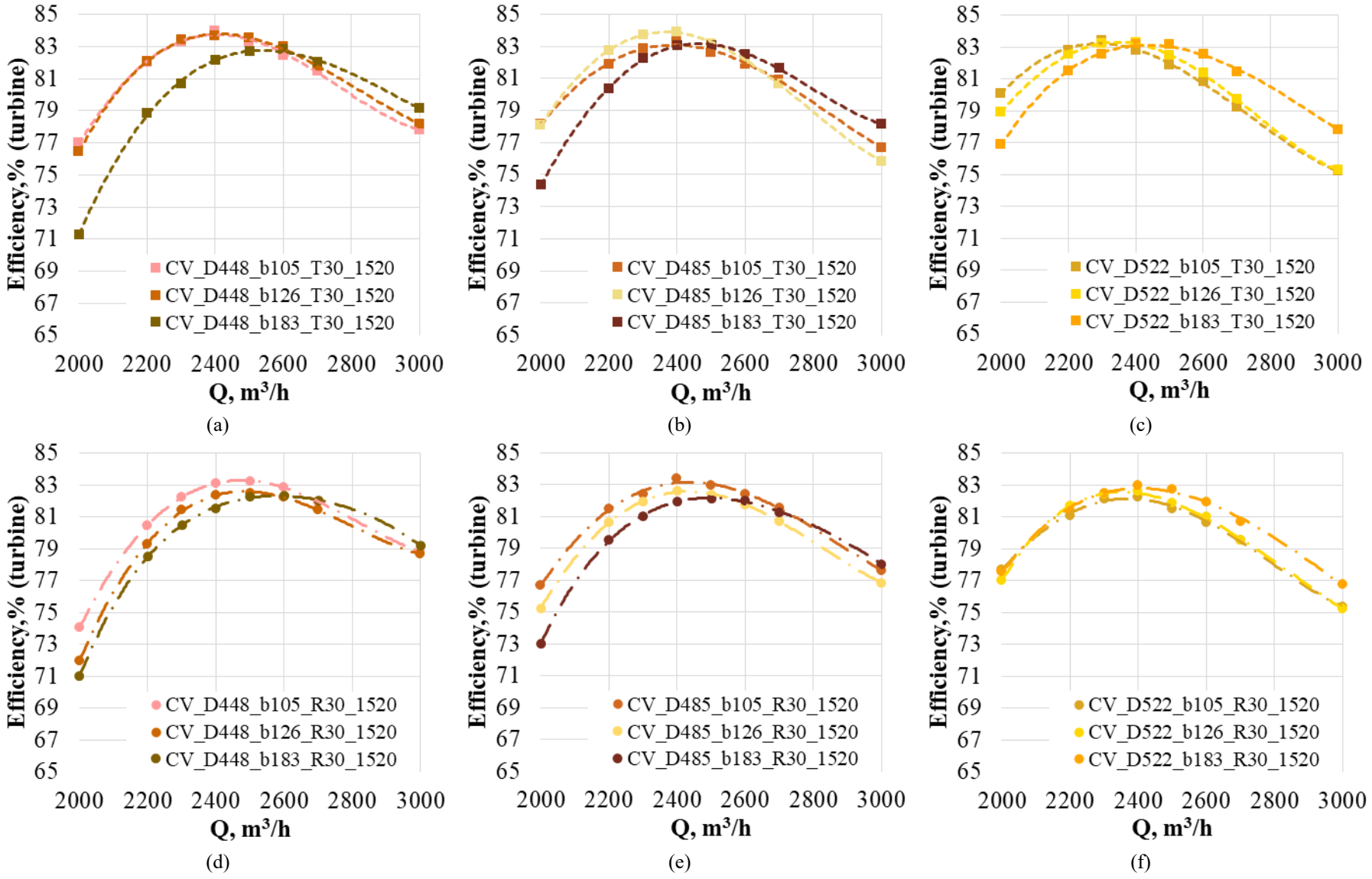

Figure F.14 – Comparison of PAT efficiency for varying b_3 at constant D_3, for round and trapezoidal volute shapes designed using the CV method: a) varying b_3, D_3 = 448 mm, trapezoidal; b) varying b_3, D_3 = 485 mm, trapezoidal; c) varying b_3, D_3 = 522 mm, trapezoidal; d) varying b_3, D_3 = 448 mm, round; e) varying b_3, D_3 = 485 mm, round; f) varying b_3, D_3 = 522 mm, round

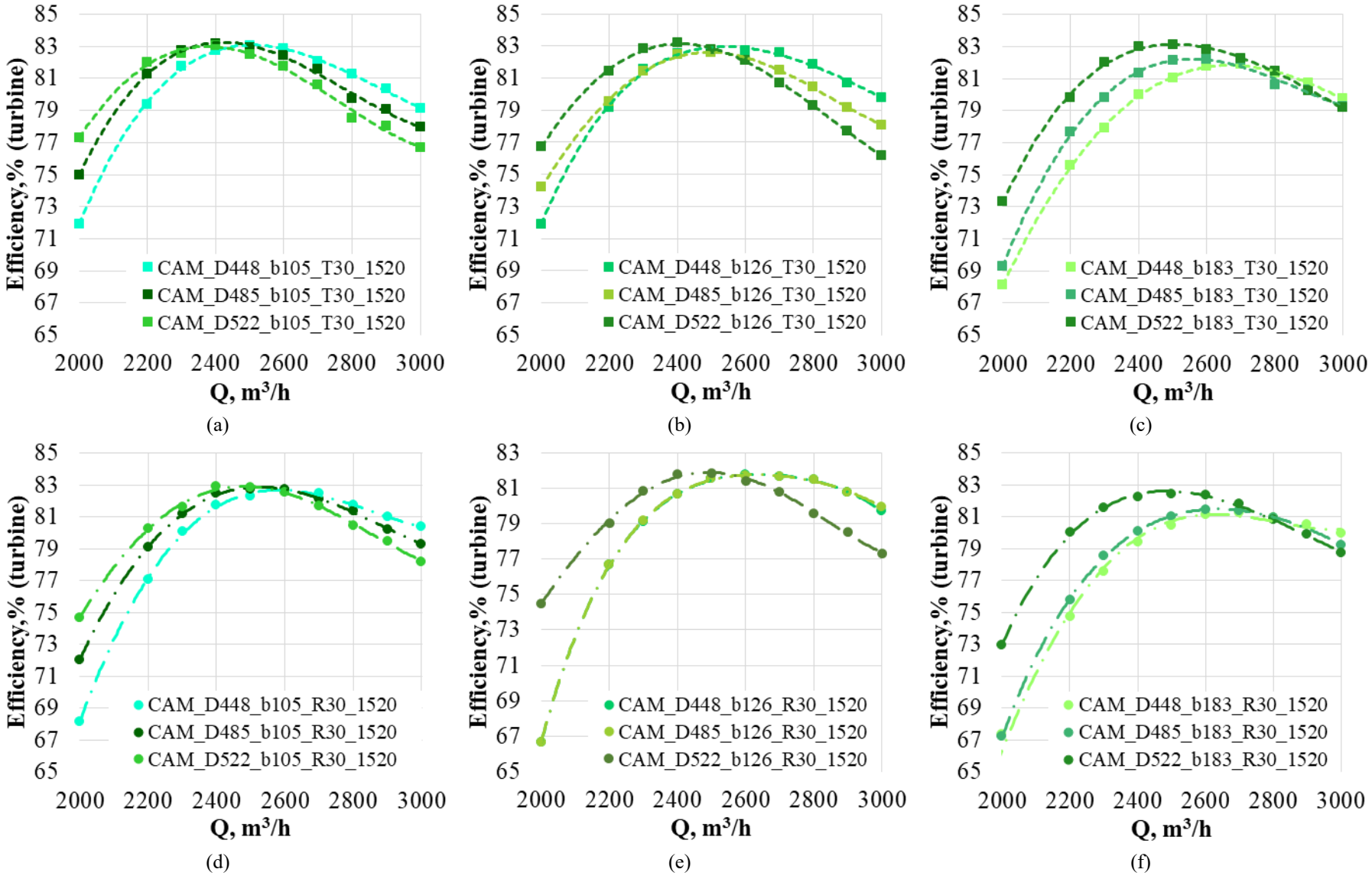

Figure F.15 – Comparison of PAT efficiency for varying D_3 at constant b_3, for round and trapezoidal volute shapes designed using the CAM method: a) varying D_3, b_3 = 105 mm, trapezoidal; b) varying D_3, b_3 = 126 mm, trapezoidal; c) varying D_3, b_3 = 183 mm, trapezoidal; d) varying D_3, b_3 = 105 mm, round; e) varying D_3, b_3 = 126 mm, round; f) varying D_3, b_3 = 183 mm, round

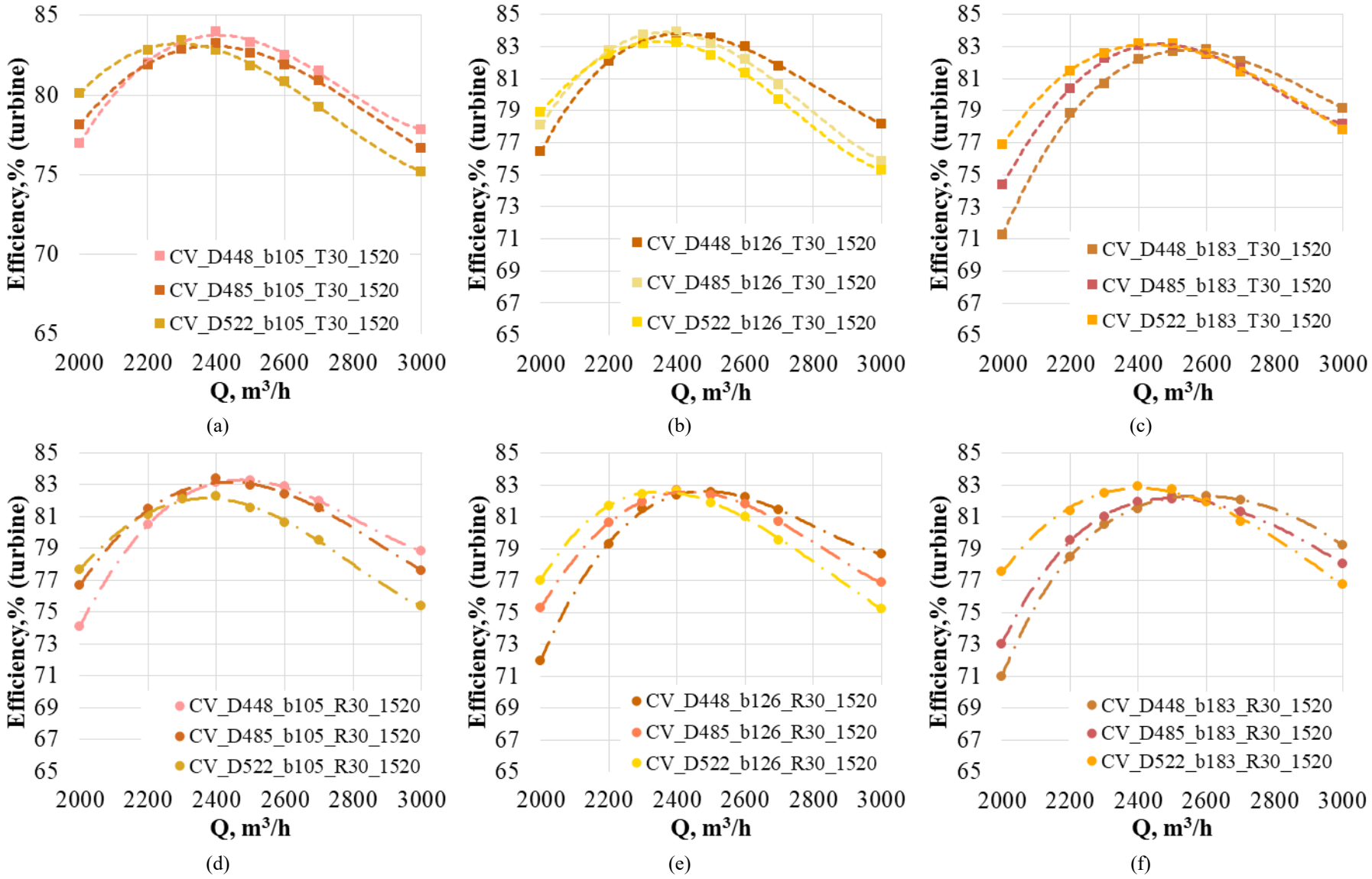

Figure F.16 – Comparison of PAT efficiency for varying D_3 at constant b_3, for round and trapezoidal volute shapes designed using the CV method: a) varying D_3, b_3 = 105 mm, trapezoidal; b) varying D_3, b_3 = 126 mm, trapezoidal; c) varying D_3, b_3 = 183 mm, trapezoidal; d) varying D_3, b_3 = 105 mm, round; e) varying D_3, b_3 = 126 mm, round; f) varying D_3, b_3 = 183 mm, round

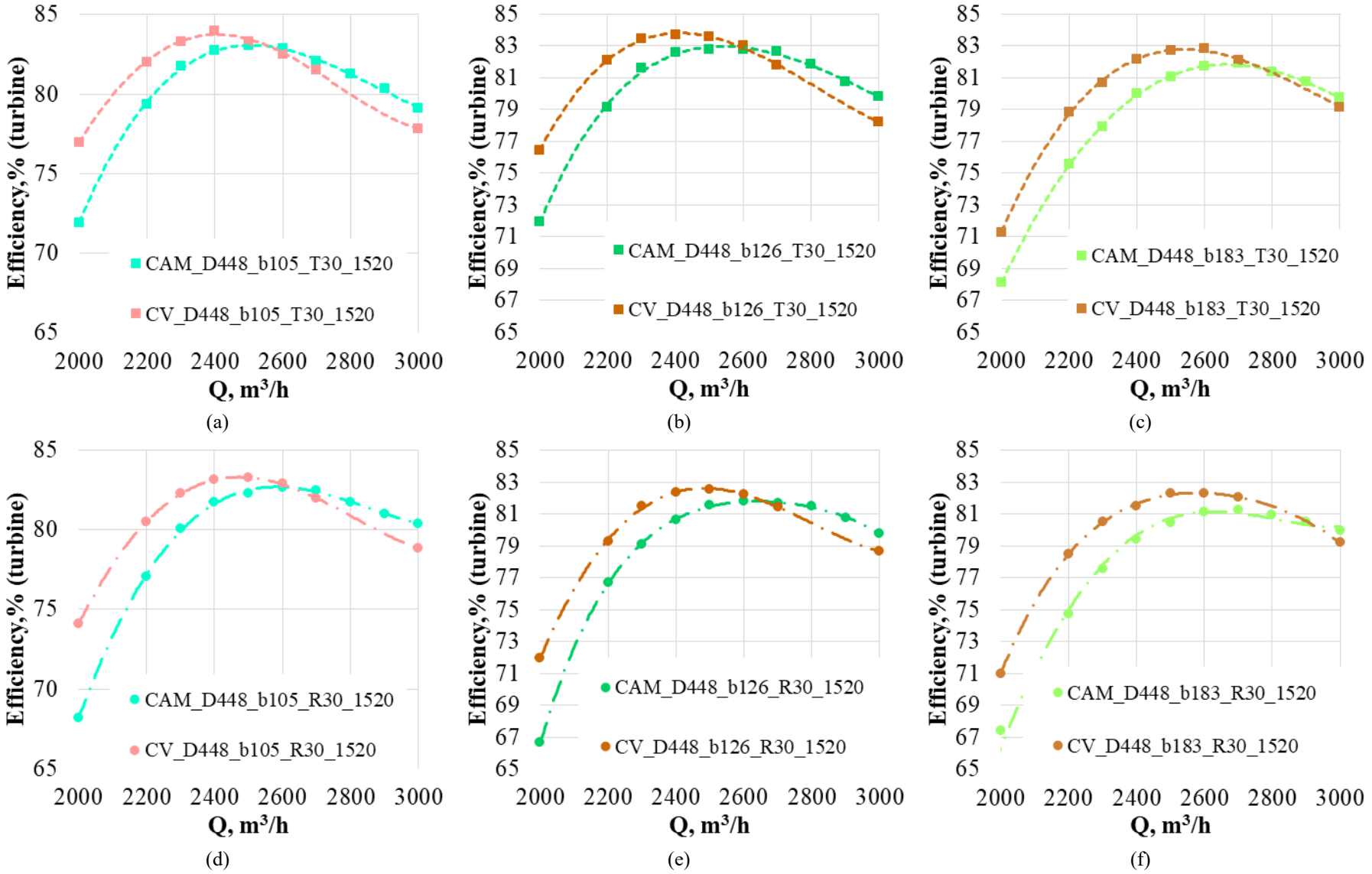

Figure F.17 – Comparison of PAT efficiency at constant b_3 and D_3, designed using the CV and CAM method: b_3 = 105 mm, D_3 = 448 mm, trapezoidal; b) b_3 = 126 mm, D_3 = 448 mm, trapezoidal; c) b_3 = 183 mm, D_3 = 448 mm, trapezoidal; d) b_3 = 105 mm, D_3 = 485 mm, round; e) b_3 = 126 mm, D_3 = 485 mm, round; f) b_3 = 183 mm, D_3 = 485 mm, round

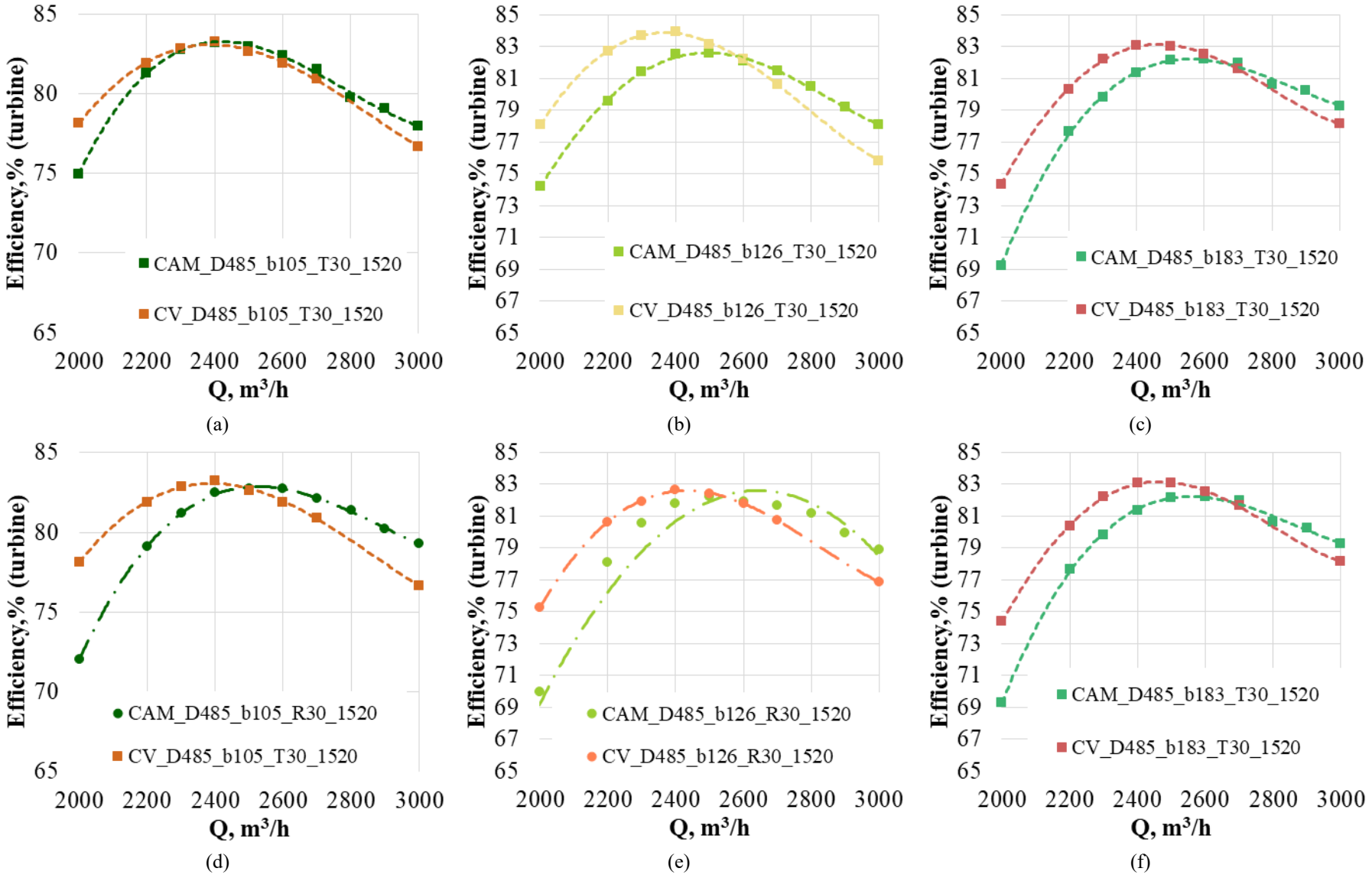

Figure F.18 – Comparison of PAT efficiency at constant b_3 and D_3, designed using the CV and CAM method: b_3 = 105 mm, D_3 = 448 mm, trapezoidal; b) b_3 = 126 mm, D_3 = 448 mm, trapezoidal; c) b_3 = 183 mm, D_3 = 448 mm, trapezoidal; d) b_3 = 105 mm, D_3 = 485 mm, round; e) b_3 = 126 mm, D_3 = 485 mm, round; f) b_3 = 183 mm, D_3 = 485 mm, round

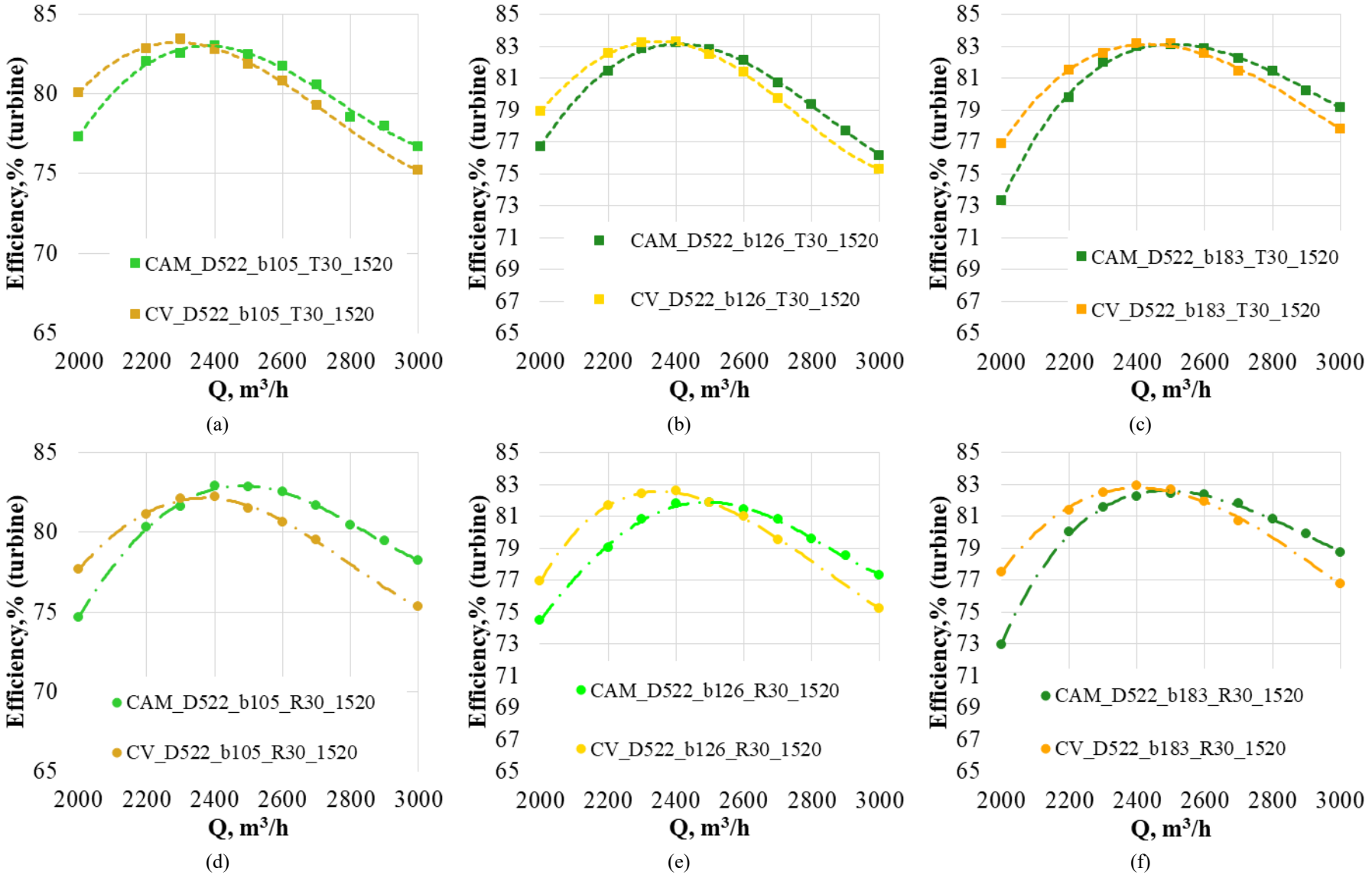

Figure F.19 – Comparison of PAT efficiency at constant b_3 and D_3, designed using the CV and CAM method: b_3 = 105 mm, D_3 = 448 mm, trapezoidal; b) b_3 = 126 mm, D_3 = 448 mm, trapezoidal; c) b_3 = 183 mm, D_3 = 448 mm, trapezoidal; d) b_3 = 105 mm, D_3 = 485 mm, round; e) b_3 = 126 mm, D_3 = 485 mm, round; f) b_3 = 183 mm, D_3 = 485 mm, round

Appendix G. Change in the velocity triangle components

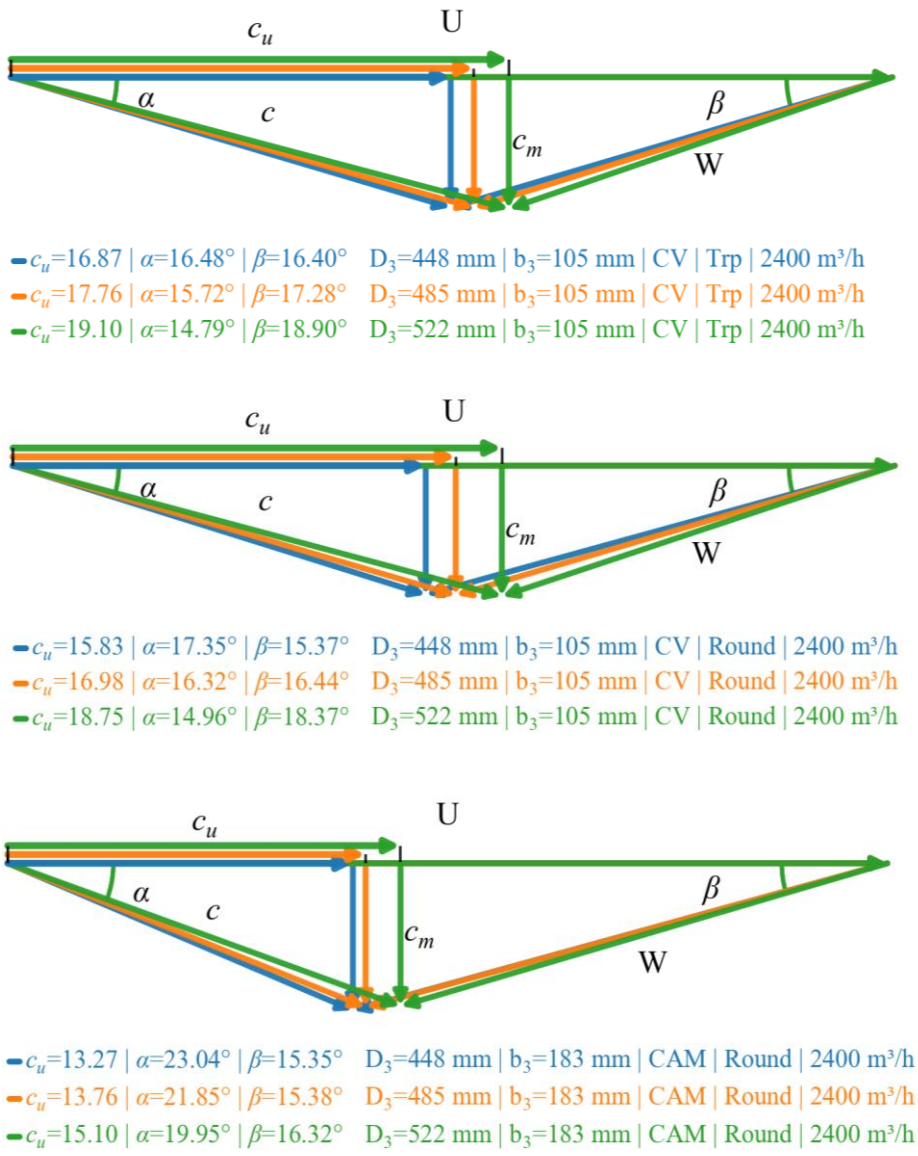

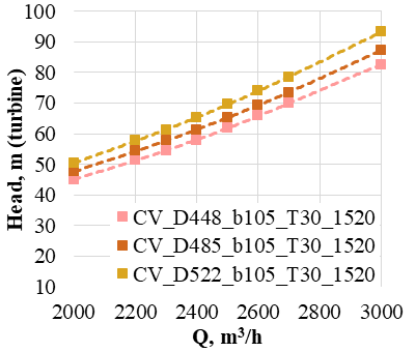

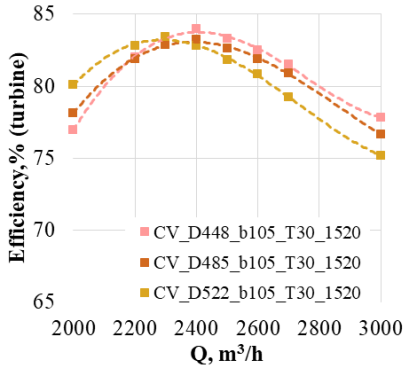

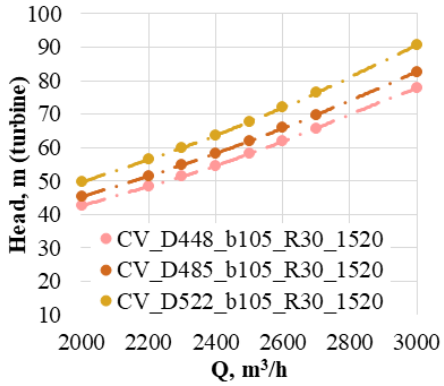

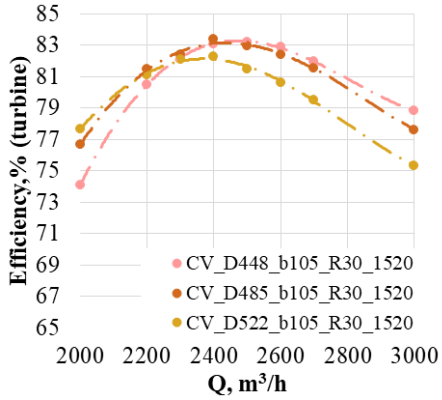

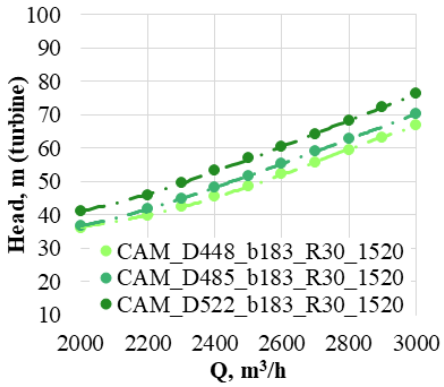

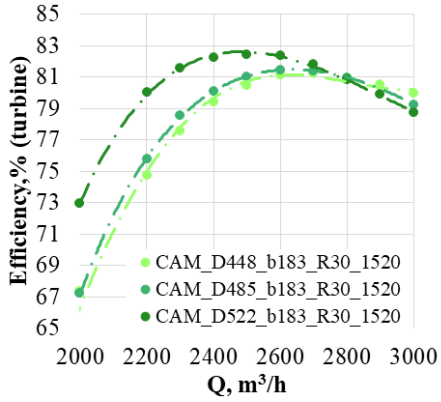

Figure G.20 - Change in the velocity triangle components at the impeller inlet (D_2) of the PAT due to changes in D_3 at 2400 m^3/h

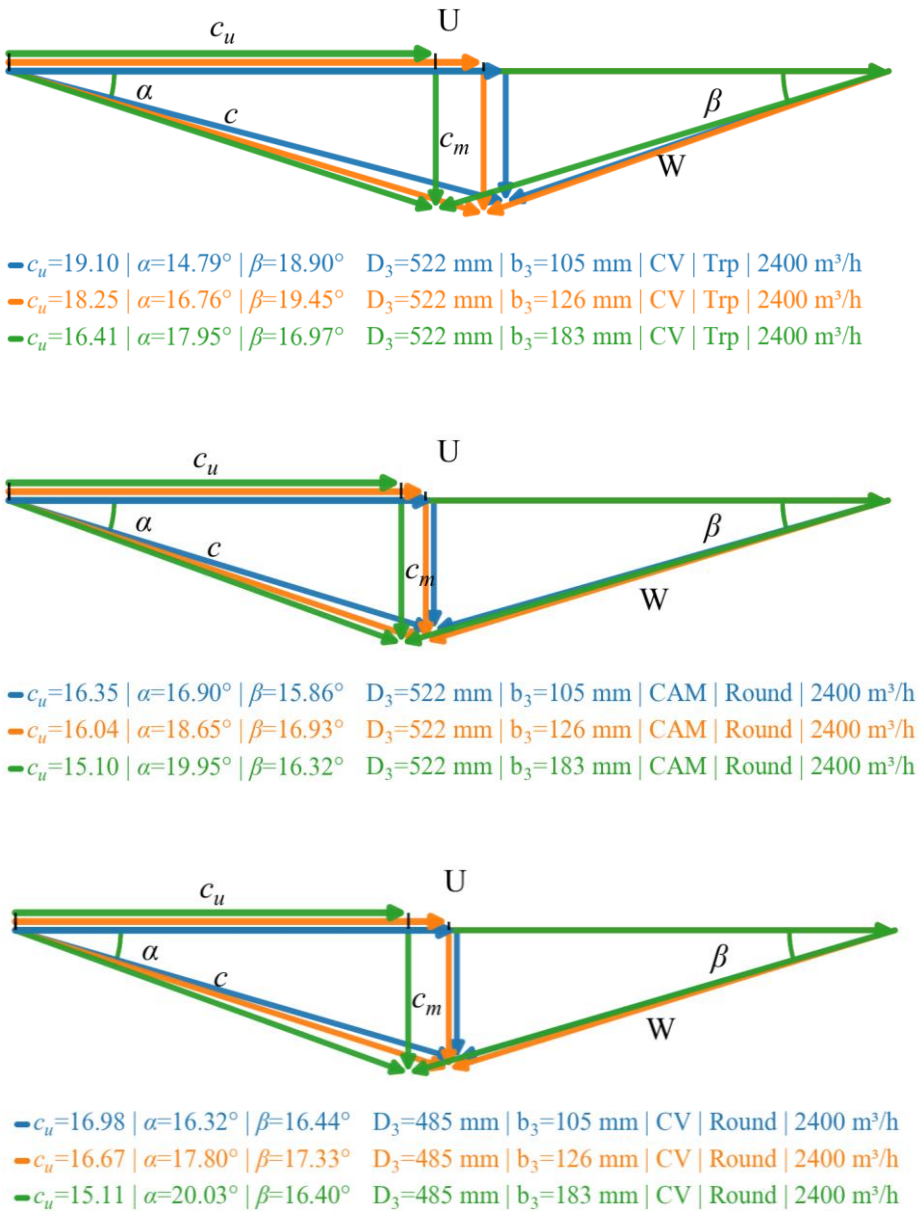

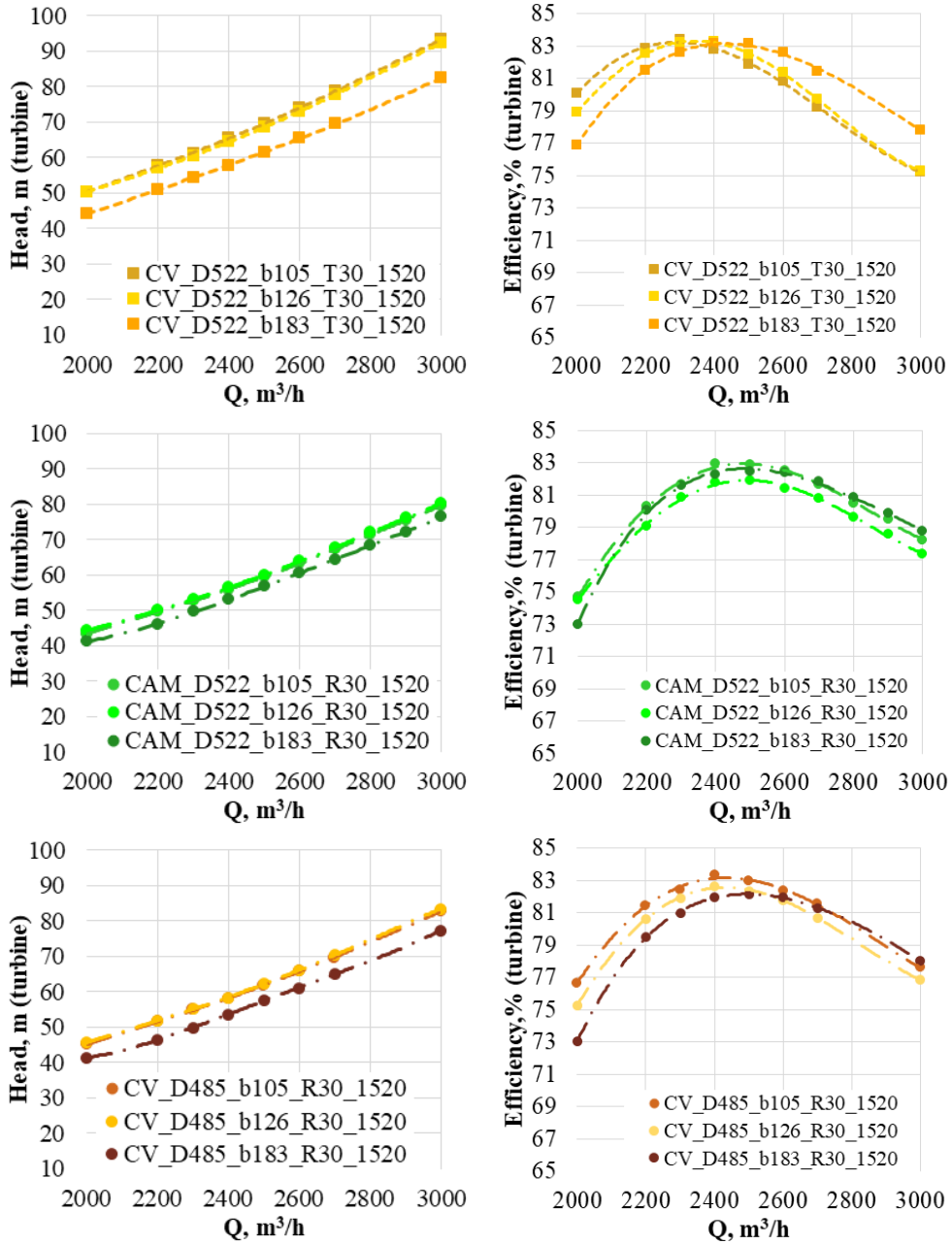

Figure G.21 - Change in the velocity triangle components at the impeller inlet (D_2) of the PAT due to changes in b_3 at 2400 m^3/h

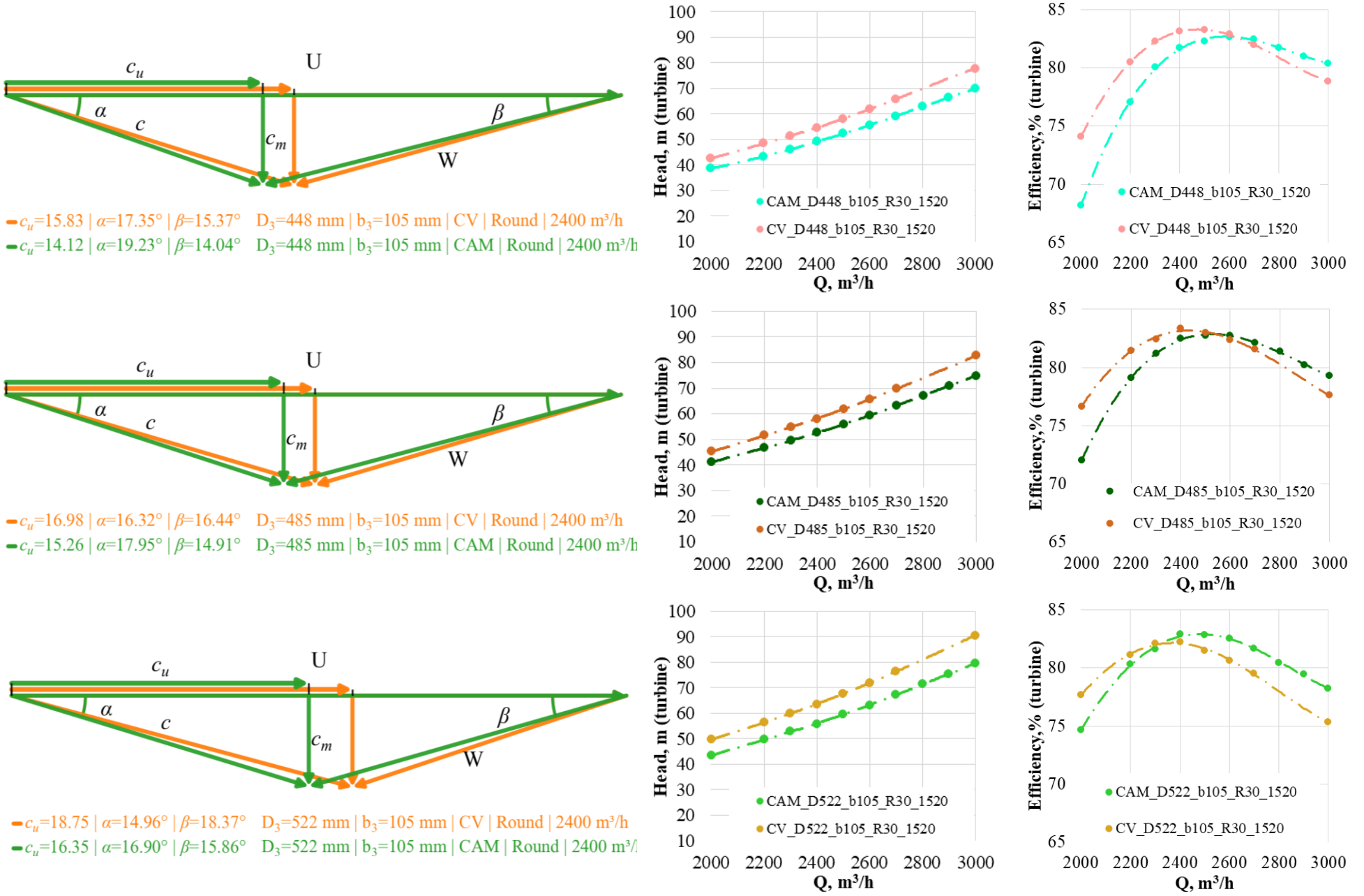

Figure G.22 - Change in the velocity triangle components at the impeller inlet (D_2) of the PAT for different volute design methods at 2400 m^3/h

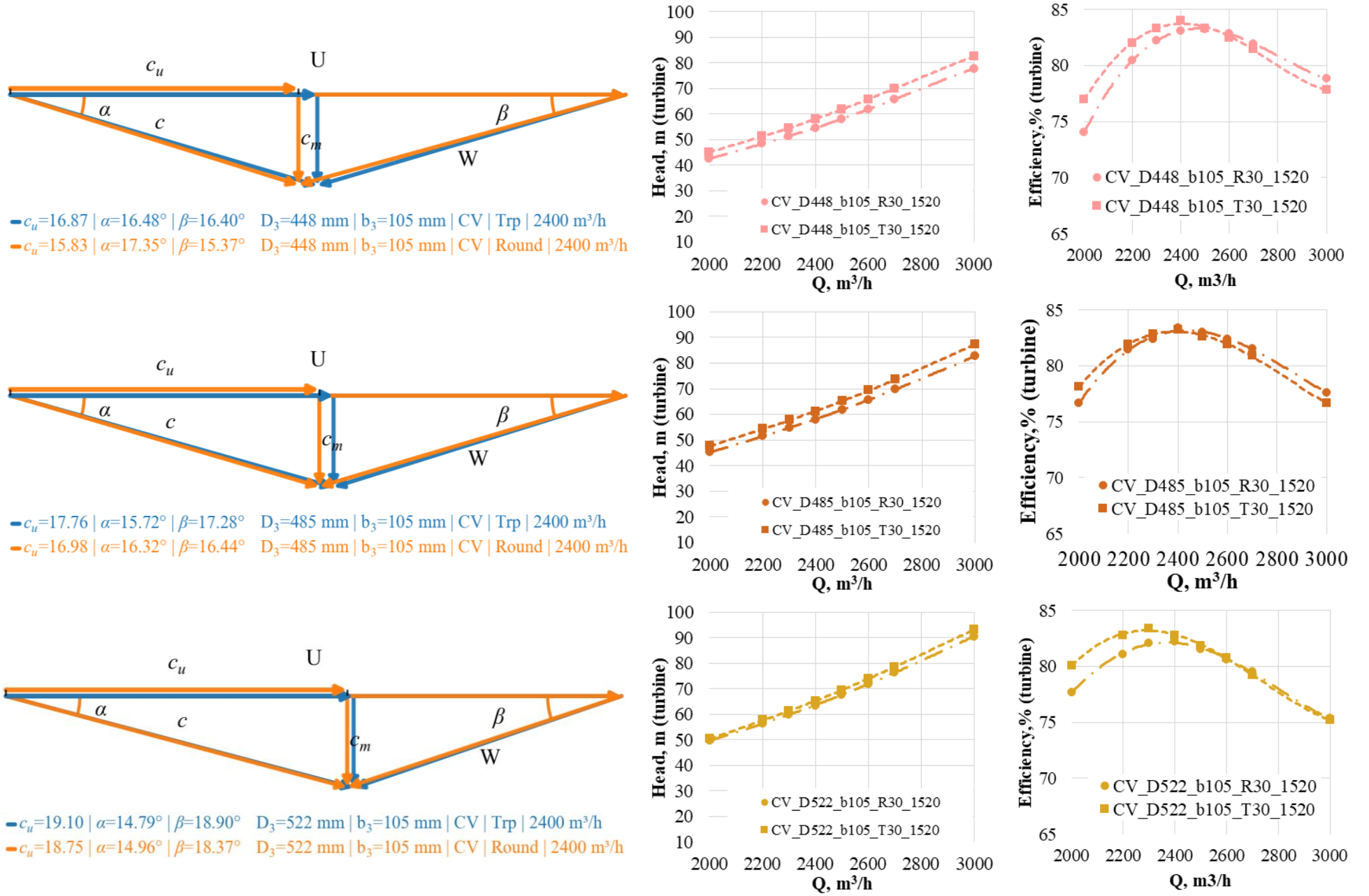

Figure G.23 - Change in the velocity triangle components at the impeller inlet (D_2) of the PAT for different volute shapes at 2400 m³/h

Appendix H. Flow distribution in the Omega PAT with volutes of different geometric parameters

Figure H.24 – Distribution of streamlines coloured by relative velocity at the impeller in the PAT under different flow rates

Appendix I. Factor effects in the regression model of Omega pump in pump mode

Table I.1 - Factor effects in the regression model at flow rate 1400 m^3/h

Head								Power mechanical							
Factor	R^2	ΔR^2 (drop-one)	Partial R^2	F	Numerator df	Denominator df	p-value	Factor	R^2	ΔR^2 (drop-one)	Partial R^2	F	Numerator df	Denominator df	p-value
b_3	0.431	0.393	0.409	10.02	2	29	4.93×10^{-4}	Shape	0.275	0.243	0.251	9.71	1	29	4.11×10^{-3}
Method	0.431	0.027	0.045	1.36	1	29	2.53×10^{-1}	b_3	0.275	0.026	0.034	0.52	2	29	6.01×10^{-1}
D_3	0.431	0.009	0.015	0.22	2	29	8.06×10^{-1}	Method	0.275	0.005	0.006	0.19	1	29	6.70×10^{-1}
Shape	0.431	0.002	0.004	0.11	1	29	7.47×10^{-1}	D_3	0.275	0.002	0.003	0.04	2	29	9.59×10^{-1}
Efficiency								**Losses total pressure**							
Factor	R^2	ΔR^2 (drop-one)	Partial R^2	F	Numerator df	Denominator df	p-value	Factor	R^2	ΔR^2 (drop-one)	Partial R^2	F	Numerator df	Denominator df	p-value
b_3	0.380	0.278	0.309	6.50	2	29	4.66×10^{-3}	b_3	0.503	0.373	0.429	10.89	2	29	2.97×10^{-4}
Shape	0.380	0.061	0.090	2.85	1	29	1.02×10^{-1}	D_3	0.503	0.078	0.136	2.29	2	29	1.20×10^{-1}
Method	0.380	0.031	0.048	1.47	1	29	2.35×10^{-1}	Method	0.503	0.036	0.068	2.13	1	29	1.56×10^{-1}
D_3	0.380	0.009	0.015	0.22	2	29	8.05×10^{-1}	Shape	0.503	0.016	0.031	0.92	1	29	3.46×10^{-1}

Table I.2 - OLS estimates of factor-level effects vs base level at flow rate 1400 m^3/h

Head								Power mechanical							
Factor	Parametr			Δ, m	p-value	95% CI, lower	95% CI, upper	Parametr			Δ, kW	p-value	95% CI, lower	95% CI, upper
Method	CAM	lower than	CV	-0.15	0.25	-0.41	0.11	CAM	higher than	CV	0.14	0.67	-0.53	0.82
D_3	448	higher than	485	0.10	0.53	-0.22	0.42	448	lower than	485	-0.10	0.80	-0.93	0.72
D_3	448	higher than	522	0.07	0.65	-0.25	0.39	448	lower than	522	-0.01	0.99	-0.84	0.82
D_3	485	lower than	522	-0.03	0.86	-0.35	0.29	485	higher than	522	0.10	0.81	-0.73	0.93
b_3	105	higher than	126	0.70	0.0001	0.38	1.02	105	higher than	126	0.231	0.57	-0.60	1.06
b_3	105	higher than	183	0.30	0.07	-0.02	0.62	105	higher than	183	0.41	0.32	-0.42	1.24
b_3	126	lower than	183	-0.40	0.016	-0.72	-0.08	126	higher than	183	0.181	0.66	-0.65	1.01
Shape	Round	lower than	Trapezoidal	-0.04	0.75	-0.30	0.22	Round	higher than	Trapezoidal	1.03	0.00	0.35	1.71
Efficiency								**Losses total pressure**						
Factor	Parametr			Δ, pp	p-value	95% CI, lower	95% CI, upper	Parametr			Δ, m	p-value	95% CI, lower	95% CI, upper
Method	CAM	lower than	CV	-0.27	0.24	-0.73	0.19	CAM	lower than	CV	-0.25	0.16	-0.59	0.10
D_3	448	higher than	485	0.18	0.52	-0.38	0.74	448	lower than	485	-0.18	0.39	-0.60	0.24
D_3	448	higher than	522	0.11	0.70	-0.45	0.67	448	lower than	522	-0.44	0.04	-0.86	-0.02
D_3	485	lower than	522	-0.07	0.79	-0.63	0.49	485	lower than	522	-0.26	0.22	-0.68	0.16
b_3	105	higher than	126	0.97	0.001	0.41	1.53	105	lower than	126	-0.926	0.00	-1.35	-0.50
b_3	105	higher than	183	0.32	0.25	-0.24	0.88	105	lower than	183	-0.69	0.00	-1.11	-0.27
b_3	126	lower than	183	-0.65	0.025	-1.21	-0.09	126	higher than	183	0.239	0.26	-0.18	0.66
Shape	Round	lower than	Trapezoidal	-0.38	0.10	-0.84	0.08	Round	higher than	Trapezoidal	0.16	0.35	-0.18	0.51

Table I.3 - Factor effects in the regression model at flow rate 2400 m^3/h

Head								Power mechanical							
Factor	R^2	ΔR^2 (drop-one)	Partial R^2	F	Numerator df	Denominator df	p-value	Factor	R^2	ΔR^2 (drop-one)	Partial R^2	F	Numerator df	Denominator df	p-value
Method	0.510	0.193	0.283	11.42	1	29	2.09×10^{-3}	b_3	0.511	0.449	0.478	13.29	2	29	8.01×10^{-5}
D_3	0.510	0.186	0.275	5.50	2	29	9.42×10^{-3}	D_3	0.511	0.041	0.077	1.21	2	29	3.11×10^{-1}
Shape	0.510	0.069	0.123	4.09	1	29	5.26×10^{-2}	Shape	0.511	0.021	0.041	1.24	1	29	2.74×10^{-1}
b_3	0.510	0.062	0.112	1.83	2	29	1.78×10^{-1}	Method	0.511	0.000	0.000	0.00	1	29	9.64×10^{-1}
Efficiency								Losses total pressure							
Factor	R^2	ΔR^2 (drop-one)	Partial R^2	F	Numerator df	Denominator df	p-value	Factor	R^2	ΔR^2 (drop-one)	Partial R^2	F	Numerator df	Denominator df	p-value
Method	0.598	0.200	0.333	14.46	1	29	6.82×10^{-4}	b_3	0.592	0.213	0.343	7.56	2	29	2.28×10^{-3}
b_3	0.598	0.165	0.291	5.95	2	29	6.84×10^{-3}	Method	0.592	0.184	0.311	13.07	1	29	1.13×10^{-3}
D_3	0.598	0.134	0.250	4.84	2	29	1.53×10^{-2}	Shape	0.592	0.126	0.236	8.96	1	29	5.59×10^{-3}
Shape	0.598	0.099	0.198	7.16	1	29	1.21×10^{-2}	D_3	0.592	0.069	0.144	2.45	2	29	1.04×10^{-1}

Table I.4 - OLS estimates of factor-level effects vs base level at flow rate 2400 m^3/h

Head								Power mechanical							
Factor	Parametr			Δ, m	p-value	95% CI, lower	95% CI, upper	Parametr			Δ, kW	p-value	95% CI, lower	95% CI, upper
Method	CAM	higher than	CV	0.35	0.002	0.14	0.56	CAM	lower than	CV	-0.01	0.96	-0.56	0.54
D_3	448	higher than	485	0.27	0.04	0.01	0.53	448	higher than	485	0.30	0.38	-0.38	0.97
D_3	448	higher than	522	0.42	0.003	0.16	0.68	448	higher than	522	0.51	0.13	-0.16	1.19
D_3	485	higher than	522	0.15	0.26	-0.12	0.41	485	higher than	522	0.22	0.52	-0.46	0.89
b_3	105	higher than	126	0.03	0.82	-0.23	0.29	105	higher than	126	1.452	0.0001	0.78	2.13
b_3	105	lower than	183	-0.20	0.14	-0.46	0.07	105	higher than	183	1.49	0.0001	0.82	2.16
b_3	126	lower than	183	-0.22	0.09	-0.48	0.04	126	higher than	183	0.037	0.91	-0.64	0.71
Shape	Round	higher than	Trapezoidal	0.21	0.05	0.00	0.42	Round	lower than	Trapezoidal	-0.30	0.27	-0.85	0.25
Efficiency								Losses total pressure							
Factor	Parametr			Δ, pp	p-value	95% CI, lower	95% CI, upper	Parametr			Δ, m	p-value	95% CI, lower	95% CI, upper
Method	CAM	higher than	CV	0.76	0.0007	0.35	1.17	CAM	lower than	CV	-0.27	0.0011	-0.43	-0.12
D_3	448	higher than	485	0.50	0.05	0.00	1.00	448	lower than	485	-0.17	0.08	-0.36	0.02
D_3	448	higher than	522	0.75	0.005	0.25	1.25	448	lower than	522	-0.19	0.05	-0.38	0.00
D_3	485	higher than	522	0.25	0.31	-0.25	0.75	485	lower than	522	-0.02	0.84	-0.21	0.17
b_3	105	lower than	126	-0.34	0.17	-0.84	0.16	105	higher than	126	0.156	0.10	-0.03	0.35
b_3	105	lower than	183	-0.84	0.002	-1.34	-0.34	105	higher than	183	0.36	0.0006	0.17	0.55
b_3	126	lower than	183	-0.50	0.05	-1.00	0.00	126	higher than	183	0.203	0.04	0.01	0.39
Shape	Round	higher than	Trapezoidal	0.54	0.012	0.13	0.94	Round	lower than	Trapezoidal	-0.23	0.006	-0.38	-0.07

Appendix J. Factor effects in the regression model of Omega pump in turbine mode

Table J.1 - Factor effects in the regression model at flow rate 2000 m^3/h on the PAT

Head								Power mechanical							
Factor	R^2	ΔR^2 (drop-one)	Partial R^2	F	Numerator df	Denominator df	p-value	Factor	R^2	ΔR^2 (drop-one)	Partial R^2	F	Numerator df	Denominator df	p-value
D_3	0.94	0.35	0.87	93.04	2	29	2.41×10^{-13}	D_3	0.94	0.36	0.863	91.14	2	29	3.12×10^{-13}
Method	0.94	0.28	0.84	149.11	1	29	5.93×10^{-13}	Method	0.94	0.31	0.845	158.70	1	29	2.76×10^{-13}
b_3	0.94	0.28	0.83	72.43	2	29	5.27×10^{-12}	b_3	0.94	0.22	0.799	57.47	2	29	8.15×10^{-11}
Shape	0.94	0.03	0.35	15.57	1	29	4.63×10^{-4}	Shape	0.94	0.05	0.486	27.45	1	29	1.30×10^{-5}
Efficiency								**Losses total pressure**							
Factor	R^2	ΔR^2 (drop-one)	Partial R^2	F	Numerator df	Denominator df	p-value	Factor	R^2	ΔR^2 (drop-one)	Partial R^2	F	Numerator df	Denominator df	p-value
Method	0.90	0.33	0.76	94.03	1	29	1.32×10^{-10}	b_3	0.22	0.09	0.105	1.71	2	29	1.99×10^{-1}
D_3	0.90	0.32	0.76	45.52	2	29	1.13×10^{-9}	D_3	0.22	0.08	0.092	1.46	2	29	2.48×10^{-1}
b_3	0.90	0.14	0.58	19.67	2	29	4.00×10^{-6}	Method	0.22	0.04	0.052	1.59	1	29	2.18×10^{-1}
Shape	0.90	0.11	0.51	30.77	1	29	5.56×10^{-6}	Shape	0.22	0.01	0.009	0.27	1	29	6.10×10^{-1}

Table J.2 - OLS estimates of factor-level effects vs base level at flow rate 2000 m^3/h

Head									Power mechanical							
Factor	Parametr			Δ, m	Δ, %	p-value	95% CI, lower	95% CI, upper	Factor	Parametr			Δ, kW	Δ, %	p-value	95% CI, lower	95% CI, upper
Method	CAM	lower than	CV	-4.26	-9.85	5.93×10^{-13}	-4.98	-3.55	Method	CAM	lower than	CV	-27.01	-15.51	2.76×10^{-13}	-31.39	-22.62
D_3	448	lower than	485	-2.43	-5.87	3.77×10^{-6}	-3.31	-1.56	D_3	448	lower than	485	-14.27	-8.84	7.57×10^{-6}	-19.64	-8.90
D_3	448	lower than	522	-5.81	-12.95	4.23×10^{-14}	-6.68	-4.93	D_3	448	lower than	522	-35.24	-19.33	5.71×10^{-14}	-40.61	-29.87
D_3	485	lower than	522	-3.38	-7.53	1.05×10^{-8}	-4.25	-2.50	D_3	485	lower than	522	-20.97	-11.50	8.31×10^{-9}	-26.34	-15.60
b_3	105	higher than	126	0.275	0.710	5.25×10^{-1}	-0.60	1.15	b_3	105	higher than	126	3.842	2.681	1.54×10^{-1}	-1.53	9.21
b_3	105	higher than	183	4.59	13.33	1.30×10^{-11}	3.71	5.46	b_3	105	higher than	183	26.07	21.54	7.75×10^{-11}	20.70	31.44
b_3	126	higher than	183	4.313	12.527	5.42×10^{-11}	3.44	5.19	b_3	126	higher than	183	22.231	18.367	2.50×10^{-9}	16.86	27.60
Shape	Round	lower than	Trapez.	-1.38	-3.41	4.63×10^{-4}	-2.09	-0.66	Shape	Round	lower than	Trapez.	-11.23	-7.09	1.30×10^{-5}	-15.62	-6.85
Efficiency									**Losses total pressure**							
Factor	Parametr			Δ, p.p	Δ, %	p-value	95% CI, lower	95% CI, upper	Factor	Parametr			Δ, m	Δ, %	p-value	95% CI, lower	95% CI, upper
Method	CAM	lower than	CV	-4.30	-5.82	1.32×10^{-10}	-5.20	-3.39	Method	CAM	higher than	CV	0.15	7.25	2.18×10^{-1}	-0.09	0.38
D_3	448	lower than	485	-2.00	-2.79	9.52×10^{-4}	-3.11	-0.89	D_3	448	lower than	485	-0.18	-7.63	2.19×10^{-1}	-0.47	0.11
D_3	448	lower than	522	-5.14	-6.88	2.27×10^{-10}	-6.25	-4.03	D_3	448	higher than	522	0.05	2.53	7.10×10^{-1}	-0.24	0.34
D_3	485	lower than	522	-3.14	-4.21	2.87×10^{-6}	-4.25	-2.03	D_3	485	higher than	522	0.23	10.99	1.13×10^{-1}	-0.06	0.52
b_3	105	higher than	126	1.20	1.76	3.51×10^{-2}	0.09	2.31	b_3	105	higher than	126	0.236	12.318	1.06×10^{-1}	-0.05	0.52
b_3	105	higher than	183	3.36	5.08	9.51×10^{-7}	2.25	4.47	b_3	105	higher than	183	0.02	0.99	8.83×10^{-1}	-0.27	0.31
b_3	126	higher than	183	2.16	3.26	4.26×10^{-4}	1.05	3.27	b_3	126	lower than	183	-0.215	-10.089	1.39×10^{-1}	-0.50	0.07
Shape	Round	lower than	Trapez.	-2.46	-3.42	5.56×10^{-6}	-3.36	-1.55	Shape	Round	lower than	Trapez.	-0.06	-2.69	6.10×10^{-1}	-0.30	0.18

Table J.3 - Factor effects in the regression model at flow rate 2700 m^3/h on the PAT

Head								Power mechanical							
Factor	R^2	ΔR^2 (drop-one)	Partial R^2	F	Numerator df	Denominator df	p-value	Factor	R^2	ΔR^2 (drop-one)	Partial R^2	F	Numerator df	Denominator df	p-value
D_3	0.95	0.39	0.89	115.60	2	29	1.52×10^{-14}	D_3	0.95	0.36	0.89	114.70	2	29	1.69×10^{-14}
Method	0.95	0.32	0.87	193.61	1	29	2.30×10^{-14}	Method	0.95	0.33	0.88	205.79	1	29	1.04×10^{-14}
b_3	0.95	0.19	0.80	58.50	2	29	6.63×10^{-11}	b_3	0.95	0.20	0.82	63.92	2	29	2.35×10^{-11}
Shape	0.95	0.05	0.50	29.26	1	29	8.13×10^{-6}	Shape	0.95	0.06	0.56	37.22	1	29	1.21×10^{-6}
Efficiency								**Losses total pressure**							
Factor	R^2	ΔR^2 (drop-one)	Partial R^2	F	Numerator df	Denominator df	p-value	Factor	R^2	ΔR^2 (drop-one)	Partial R^2	F	Numerator df	Denominator df	p-value
D_3	0.64	0.38	0.51	15.33	2	29	2.87×10^{-5}	D_3	0.90	0.38	0.80	56.81	2	29	9.31×10^{-11}
Method	0.64	0.17	0.33	13.97	1	29	8.12×10^{-4}	Method	0.90	0.32	0.77	94.69	1	29	1.22×10^{-10}
b_3	0.64	0.09	0.20	3.59	2	29	4.03×10^{-2}	b_3	0.90	0.12	0.55	17.43	2	29	1.07×10^{-5}
Shape	0.64	0.00	0.00	0.01	1	29	9.40×10^{-1}	Shape	0.90	0.09	0.47	25.67	1	29	2.11×10^{-5}

Table J.4 - OLS estimates of factor-level effects vs base level at flow rate 2700 m^3/h

Head									Power mechanical							
Factor	Parametr			Δ, m	Δ, %	p-value	95% CI, lower	95% CI, upper	Parametr			Δ, kW	Δ, %	p-value	95% CI, lower	95% CI, upper
Method	CAM	lower than	CV	-6.89	-10.33	2.29×10^{-14}	-7.90	-5.88	CAM	lower than	CV	-37.54	-9.43	1.06×10^{-14}	-42.89	-32.18
D_3	448	lower than	485	-3.92	-6.15	4.49×10^{-7}	-5.16	-2.68	448	lower than	485	-21.11	-5.53	3.22×10^{-7}	-27.67	-14.56
D_3	448	lower than	522	-9.19	-13.32	2.59×10^{-15}	-10.43	-7.95	448	lower than	522	-48.41	-11.84	2.81×10^{-15}	-54.96	-41.85
D_3	485	lower than	522	-5.27	-7.64	1.45×10^{-9}	-6.51	-4.03	485	lower than	522	-27.30	-6.68	2.20×10^{-9}	-33.85	-20.74
b_3	105	higher than	126	0.62	1.05	3.12×10^{-1}	-0.62	1.86	105	higher than	126	4.710	1.324	1.52×10^{-1}	-1.84	11.26
b_3	105	higher than	183	5.97	11.09	9.52×10^{-11}	4.73	7.21	105	higher than	183	33.47	10.23	2.44×10^{-11}	26.91	40.02
b_3	126	higher than	183	5.34	9.93	1.07×10^{-9}	4.10	6.58	126	higher than	183	28.758	8.794	7.26×10^{-10}	22.20	35.31
Shape	Round	lower than	Trapez.	-2.68	-4.29	8.13×10^{-6}	-3.69	-1.67	Round	lower than	Trapez.	-15.96	-4.24	1.21×10^{-6}	-21.32	-10.61
Efficiency									**Losses total pressure**							
Factor	Parametr			Δ, p.p	Δ, %	p-value	95% CI, lower	95% CI, upper	Parametr			Δ, m	Δ, %	p-value	95% CI, lower	95% CI, upper
Method	CAM	higher than	CV	0.68	0.84	8.12×10^{-4}	0.31	1.06	CAM	lower than	CV	-1.38	-40.00	1.22×10^{-10}	-1.67	-1.09
D_3	448	higher than	485	0.48	0.59	4.07×10^{-2}	0.02	0.94	448	lower than	485	-0.84	-28.89	3.92×10^{-5}	-1.19	-0.49
D_3	448	higher than	522	1.23	1.52	6.46×10^{-6}	0.77	1.69	448	lower than	522	-1.85	-47.18	1.57×10^{-11}	-2.20	-1.49
D_3	485	higher than	522	0.75	0.93	2.25×10^{-3}	0.29	1.21	485	lower than	522	-1.01	-25.71	2.75×10^{-6}	-1.36	-0.65
b_3	105	higher than	126	0.20	0.25	3.68×10^{-1}	-0.25	0.66	105	higher than	126	0.632	44.035	1.04×10^{-3}	0.28	0.99
b_3	105	lower than	183	-0.39	-0.47	9.51×10^{-2}	-0.85	0.07	105	higher than	183	1.01	96.23	2.44×10^{-6}	0.66	1.37
b_3	126	lower than	183	-0.59	-0.72	1.32×10^{-2}	-1.05	-0.13	126	higher than	183	0.382	36.237	3.58×10^{-2}	0.03	0.74
Shape	Round	lower than	Trapez.	-0.01	-0.02	9.40×10^{-1}	-0.39	0.36	Round	lower than	Trapez.	-0.72	-25.77	2.11×10^{-5}	-1.01	-0.43

Appendix K. Factor effects in the regression model of DHV pump in pump mode

Table K.1 - Factor effects in the regression model at flow rate 74 m3/h

Head								Power mechanical							
Factor	R^2	ΔR^2 (drop-one)	Partial R^2	F	Numerator df	Denominator df	p-value	Factor	R^2	ΔR^2 (drop-one)	Partial R^2	F	Numerator df	Denominator df	p-value
b_3	0.666	0.441	0.569	6.60	2	10	1.49×10^{-2}	b_3	0.334	0.265	0.285	1.99	2	10	1.87×10^{-1}
Method	0.666	0.104	0.237	3.11	1	10	1.08×10^{-1}	Method	0.334	0.050	0.069	0.75	1	10	4.08×10^{-1}
D_3	0.666	0.077	0.188	1.16	2	10	3.54×10^{-1}	D_3	0.334	0.018	0.026	0.13	2	10	8.77×10^{-1}
Efficiency								**Losses total pressure**							
Factor	R^2	ΔR^2 (drop-one)	Partial R^2	F	Numerator df	Denominator df	p-value	Factor	R^2	ΔR^2 (drop-one)	Partial R^2	F	Numerator df	Denominator df	p-value
b_3	0.705	0.505	0.631	8.55	2	10	6.85×10^{-3}	b_3	0.414	0.213	0.267	1.82	2	10	2.12×10^{-1}
Method	0.705	0.110	0.271	3.71	1	10	8.29×10^{-2}	Method	0.414	0.080	0.120	1.37	1	10	2.69×10^{-1}
D_3	0.705	0.051	0.147	0.86	2	10	4.51×10^{-1}	D_3	0.414	0.067	0.102	0.57	2	10	5.83×10^{-1}

Table K.2 - OLS estimates of factor-level effects vs base level at flow rate 74 m^3/h

Head								Power mechanical						
Factor	Parametr			Δ, m	p-value	95% CI, lower	95% CI, upper	Parametr			Δ, kW	p-value	95% CI, lower	95% CI, upper
Method	CAM	higher than	CV	0.31	0.11	-0.08	0.69	CAM	lower than	CV	-0.02	0.41	-0.09	0.04
D_3	281	lower than	297	-0.25	0.23	-0.70	0.19	281	lower than	297	-0.01	0.76	-0.08	0.06
D_3	281	higher than	329	0.05	0.84	-0.47	0.57	281	lower than	329	-0.02	0.63	-0.10	0.06
D_3	297	higher than	329	0.30	0.23	-0.22	0.82	297	lower than	329	-0.01	0.82	-0.09	0.07
b_3	27	lower than	40	-0.65	0.02	-1.18	-0.13	27	higher than	40	0.03	0.40	-0.05	0.12
b_3	27	lower than	52	-0.66	0.01	-1.10	-0.21	27	higher than	52	0.06	0.07	-0.01	0.13
b_3	40	lower than	52	0.00	0.99	-0.53	0.52	40	higher than	52	0.03	0.43	-0.05	0.11
Efficiency								**Losses total pressure**						
Factor	Parametr			Δ, p.p	p-value	95% CI, lower	95% CI, upper	Parametr			Δ, m	p-value	95% CI, lower	95% CI, upper
Method	CAM	higher than	CV	1.08	0.08	-0.17	2.32	CAM	higher than	CV	1.01	0.27	-0.91	2.92
D_3	281	lower than	297	-0.58	0.39	-2.02	0.85	281	higher than	297	1.00	0.34	-1.21	3.21
D_3	281	higher than	329	0.36	0.64	-1.32	2.04	281	higher than	329	0.88	0.47	-1.72	3.47
D_3	297	higher than	329	0.94	0.24	-0.74	2.63	297	lower than	329	-0.12	0.92	-2.71	2.48
b_3	27	lower than	40	-2.19	0.02	-3.87	-0.51	27	lower than	40	-2.209	0.09	-4.80	0.39
b_3	27	lower than	52	-2.52	0.00	-3.95	-1.08	27	lower than	52	-0.62	0.54	-2.84	1.59
b_3	40	lower than	52	-0.33	0.68	-2.01	1.36	40	higher than	52	1.586	0.20	-1.01	4.18

Table K.3 - Factor effects in the regression model at flow rate 105 m3/h

Head								Power mechanical							
Factor	R^2	ΔR^2 (drop-one)	Partial R^2	F	Numerator df	Denominator df	p-value	Factor	R^2	ΔR^2 (drop-one)	Partial R^2	F	Numerator df	Denominator df	p-value
b_3	0.871	0.683	0.841	26.48	2	10	1.01×10^{-4}	b_3	0.443	0.303	0.353	2.72	2	10	1.14×10^{-1}
D_3	0.871	0.087	0.404	3.39	2	10	7.52×10^{-2}	D_3	0.443	0.158	0.221	1.42	2	10	2.86×10^{-1}
Method	0.871	0.004	0.032	0.33	1	10	5.81×10^{-1}	Method	0.443	0.003	0.005	0.05	1	10	8.20×10^{-1}
Efficiency								Losses total pressure							
Factor	R^2	ΔR^2 (drop-one)	Partial R^2	F	Numerator df	Denominator df	p-value	Factor	R^2	ΔR^2 (drop-one)	Partial R^2	F	Numerator df	Denominator df	p-value
b_3	0.868	0.673	0.836	25.44	2	10	1.20×10^{-4}	b_3	0.435	0.259	0.314	2.29	2	10	1.51×10^{-1}
D_3	0.868	0.104	0.441	3.94	2	10	5.48×10^{-2}	D_3	0.435	0.074	0.116	0.65	2	10	5.41×10^{-1}
Method	0.868	0.002	0.017	0.17	1	10	6.87×10^{-1}	Method	0.435	0.032	0.054	0.57	1	10	4.66×10^{-1}

Table K.4 - OLS estimates of factor-level effects vs base level at flow rate 105 m^3/h

Head								Power mechanical							
Factor	Parametr			Δ, m	p-value	95% CI, lower	95% CI, upper	Parametr			Δ, kW	p-value	95% CI, lower	95% CI, upper	
Method	CAM	lower than	CV	-0.07	0.58	-0.36	0.21	CAM	lower than	CV	0.00	0.82	-0.04	0.03	
D_3	281	lower than	297	-0.06	0.71	-0.39	0.28	281	lower than	297	-0.01	0.49	-0.05	0.03	
D_3	281	higher than	329	0.38	0.06	-0.01	0.77	281	lower than	329	-0.04	0.12	-0.09	0.01	
D_3	297	higher than	329	0.44	0.03	0.05	0.83	297	lower than	329	-0.02	0.31	-0.07	0.03	
b_3	27	lower than	40	-0.96	0.00	-1.35	-0.57	27	higher than	40	0.01	0.71	-0.04	0.06	
b_3	27	lower than	52	-1.00	0.00	-1.33	-0.66	27	higher than	52	0.04	0.05	0.00	0.08	
b_3	40	lower than	52	-0.04	0.83	-0.43	0.35	40	higher than	52	0.03	0.16	-0.02	0.08	
Efficiency								Losses total pressure							
Factor	Parametr			Δ, p.p	p-value	95% CI, lower	95% CI, upper	Parametr			Δ, m	p-value	95% CI, lower	95% CI, upper	
Method	CAM	lower than	CV	0.69	0.16	-1.23	0.84	CAM	higher than	CV	0.54	0.24	-1.04	2.12	
D_3	281	lower than	297	0.91	0.93	-1.25	1.13	281	higher than	297	0.82	0.50	-1.01	2.65	
D_3	281	higher than	329	0.03	0.74	0.16	2.96	281	higher than	329	0.89	0.17	-1.25	3.03	
D_3	297	higher than	329	0.03	0.81	0.22	3.02	297	higher than	329	0.07	0.48	-2.07	2.21	
b_3	27	lower than	40	0.00	0.17	-4.55	-1.75	27	lower than	40	-2.054	0.01	-4.20	0.09	
b_3	27	lower than	52	0.00	0.01	-4.80	-2.41	27	lower than	52	-0.87	0.03	-2.70	0.96	
b_3	40	lower than	52	0.49	0.21	-1.85	0.95	40	higher than	52	1.181	0.57	-0.96	3.32	

Table K.5 - Factor effects in the regression model at flow rate 126 m3/h

Head								Power mechanical							
Factor	R^2	ΔR^2 (drop-one)	Partial R^2	F	Numerator df	Denominator df	p-value	Factor	R^2	ΔR^2 (drop-one)	Partial R^2	F	Numerator df	Denominator df	p-value
b_3	0.814	0.554	0.748	14.88	2	10	1.01×10^{-3}	b_3	0.691	0.443	0.589	7.17	2	10	1.17×10^{-2}
D_3	0.814	0.109	0.370	2.93	2	10	9.95×10^{-2}	D_3	0.691	0.107	0.257	1.73	2	10	2.27×10^{-1}
Method	0.814	0.087	0.319	4.68	1	10	5.59×10^{-2}	Method	0.691	0.091	0.228	2.95	1	10	1.17×10^{-1}
Efficiency								Losses total pressure							
Factor	R^2	ΔR^2 (drop-one)	Partial R^2	F	Numerator df	Denominator df	p-value	Factor	R^2	ΔR^2 (drop-one)	Partial R^2	F	Numerator df	Denominator df	p-value
b_3	0.839	0.596	0.787	18.47	2	10	4.39×10^{-4}	b_3	0.464	0.249	0.317	2.32	2	10	1.48×10^{-1}
D_3	0.839	0.115	0.416	3.56	2	10	6.81×10^{-2}	D_3	0.464	0.116	0.178	1.09	2	10	3.74×10^{-1}
Method	0.839	0.060	0.271	3.72	1	10	8.25×10^{-2}	Method	0.464	0.011	0.019	0.20	1	10	6.65×10^{-1}

Table K.6 - OLS estimates of factor-level effects vs base level at flow rate 126 m^3/h

Head								Power mechanical							
Factor	Parametr			Δ, m	p-value	95% CI, lower	95% CI, upper	Parametr			Δ, kW	p-value	95% CI, lower	95% CI, upper
Method	CAM	lower than	CV	-0.31	0.06	-0.62	0.01	CAM	lower than	CV	-0.02	0.12	-0.04	0.00
D_3	281	lower than	297	-0.11	0.50	-0.48	0.25	281	lower than	297	-0.01	0.38	-0.03	0.01
D_3	281	higher than	329	0.35	0.10	-0.08	0.77	281	lower than	329	-0.02	0.09	-0.05	0.00
D_3	297	higher than	329	0.46	0.04	0.03	0.89	297	lower than	329	-0.01	0.31	-0.04	0.01
b_3	27	lower than	40	-0.68	0.01	-1.10	-0.25	27	higher than	40	0.03	0.03	0.00	0.06
b_3	27	lower than	52	-0.86	0.00	-1.23	-0.50	27	higher than	52	0.04	0.00	0.02	0.06
b_3	40	lower than	52	-0.19	0.36	-0.61	0.24	40	higher than	52	0.01	0.51	-0.02	0.04
Efficiency								Losses total pressure							
Factor	Parametr			Δ, p.p	p-value	95% CI, lower	95% CI, upper	Parametr			Δ, m	p-value	95% CI, lower	95% CI, upper
Method	CAM	lower than	CV	-0.95	0.08	-2.04	0.15	CAM	higher than	CV	0.21	0.67	-0.83	1.24
D_3	281	lower than	297	-0.33	0.58	-1.59	0.93	281	higher than	297	0.57	0.32	-0.63	1.76
D_3	281	higher than	329	1.40	0.06	-0.08	2.88	281	higher than	329	0.87	0.20	-0.53	2.28
D_3	297	higher than	329	1.73	0.03	0.25	3.21	297	higher than	329	0.31	0.64	-1.10	1.71
b_3	27	lower than	40	-2.61	0.00	-4.09	-1.13	27	lower than	40	-1.289	0.07	-2.69	0.12
b_3	27	lower than	52	-3.32	0.00	-4.58	-2.06	27	lower than	52	-0.80	0.17	-2.00	0.40
b_3	40	lower than	52	-0.72	0.31	-2.19	0.76	40	higher than	52	0.489	0.46	-0.92	1.89

Appendix L. Factor effects in the regression model of DHV pump in turbine mode

Table L.1 - Factor effects in the regression model at flow rate 126 m3/h

Head								Power mechanical							
Factor	R^2	ΔR^2 (drop-one)	Partial R^2	F	Numerator df	Denominator df	p-value	Factor	R^2	ΔR^2 (drop-one)	Partial R^2	F	Numerator df	Denominator df	p-value
D_3	0.913	0.635	0.879	36.43	2	10	2.56×10^{-5}	D_3	0.845	0.540	0.777	17.38	2	10	5.56×10^{-4}
Method	0.913	0.269	0.755	30.88	1	10	2.42×10^{-4}	Method	0.845	0.301	0.659	19.33	1	10	1.34×10^{-3}
b_3	0.913	0.039	0.309	2.24	2	10	1.57×10^{-1}	b_3	0.845	0.032	0.169	1.02	2	10	3.96×10^{-1}
Efficiency								**Losses total pressure**							
Factor	R^2	ΔR^2 (drop-one)	Partial R^2	F	Numerator df	Denominator df	p-value	Factor	R^2	ΔR^2 (drop-one)	Partial R^2	F	Numerator df	Denominator df	p-value
b_3	0.474	0.177	0.252	1.68	2	10	2.34×10^{-1}	D_3	0.893	0.684	0.865	32.01	2	10	4.50×10^{-5}
D_3	0.474	0.170	0.244	1.61	2	10	2.47×10^{-1}	Method	0.893	0.196	0.647	18.30	1	10	1.62×10^{-3}
Method	0.474	0.127	0.194	2.41	1	10	1.52×10^{-1}	b_3	0.893	0.042	0.280	1.94	2	10	1.94×10^{-1}

Table L.2 - OLS estimates of factor-level effects vs base level at flow rate 126 m^3/h

Head								Power mechanical							
Factor	Parametr			Δ, m	p-value	95% CI, lower	95% CI, upper	Parametr			Δ, kW	p-value	95% CI, lower	95% CI, upper	
Method	CAM	higher than	CV	2.40	0.00	1.44	3.36	CAM	higher than	CV	0.72	0.00	0.36	1.09	
D_3	281	lower than	297	-2.13	0.00	-3.24	-1.02	281	lower than	297	-0.69	0.00	-1.11	-0.27	
D_3	281	lower than	329	-4.98	0.00	-6.28	-3.67	281	lower than	329	-1.28	0.00	-1.77	-0.78	
D_3	297	lower than	329	-2.85	0.00	-4.15	-1.54	297	lower than	329	-0.58	0.03	-1.08	-0.09	
b_3	27	lower than	40	-0.82	0.19	-2.12	0.49	27	lower than	40	-0.31	0.19	-0.81	0.18	
b_3	27	higher than	52	0.42	0.42	-0.69	1.53	27	lower than	52	-0.08	0.67	-0.51	0.34	
b_3	40	higher than	52	1.24	0.06	-0.07	2.54	40	higher than	52	0.23	0.32	-0.26	0.73	
Efficiency								**Losses total pressure**							
Factor	Parametr			Δ, p.p	p-value	95% CI, lower	95% CI, upper	Parametr			Δ, m	p-value	95% CI, lower	95% CI, upper	
Method	CAM	higher than	CV	1.47	0.15	-0.64	3.58	CAM	higher than	CV	1.46	0.00	0.70	2.22	
D_3	281	lower than	297	-1.97	0.10	-4.41	0.47	281	lower than	297	-1.12	0.02	-1.99	-0.24	
D_3	281	lower than	329	-0.97	0.47	-3.83	1.89	281	lower than	329	-3.69	0.00	-4.72	-2.66	
D_3	297	higher than	329	0.99	0.46	-1.87	3.85	297	lower than	329	-2.57	0.00	-3.60	-1.54	
b_3	27	lower than	40	-1.25	0.351	-4.12	1.61	27	lower than	40	-0.584	0.23	-1.61	0.45	
b_3	27	lower than	52	-2.00	0.10	-4.43	0.44	27	higher than	52	0.33	0.43	-0.55	1.20	
b_3	40	lower than	52	-0.74	0.58	-3.60	2.12	40	higher than	52	0.911	0.08	-0.12	1.94	

Table L.3 - Factor effects in the regression model at flow rate 157 m3/h

Head								Power mechanical							
Factor	R^2	ΔR^2 (drop-one)	Partial R^2	F	Numerator df	Denominator df	p-value	Factor	R^2	ΔR^2 (drop-one)	Partial R^2	F	Numerator df	Denominator df	p-value
D_3	0.910	0.602	0.870	33.35	2	10	3.77×10^{-5}	D_3	0.818	0.475	0.723	13.06	2	10	1.63×10^{-3}
Method	0.910	0.294	0.765	32.59	1	10	1.96×10^{-4}	Method	0.818	0.322	0.639	17.72	1	10	1.80×10^{-3}
b_3	0.910	0.042	0.316	2.31	2	10	1.49×10^{-1}	b_3	0.818	0.052	0.223	1.43	2	10	2.84×10^{-1}
Efficiency								Losses total pressure							
Factor	R^2	ΔR^2 (drop-one)	Partial R^2	F	Numerator df	Denominator df	p-value	Factor	R^2	ΔR^2 (drop-one)	Partial R^2	F	Numerator df	Denominator df	p-value
D_3	0.808	0.679	0.780	17.71	2	10	5.17×10^{-4}	D_3	0.896	0.641	0.860	30.82	2	10	5.30×10^{-5}
Method	0.808	0.105	0.354	5.48	1	10	4.13×10^{-2}	Method	0.896	0.173	0.625	16.65	1	10	2.21×10^{-3}
b_3	0.808	0.017	0.081	0.44	2	10	6.56×10^{-1}	b_3	0.896	0.054	0.340	2.58	2	10	1.25×10^{-1}

Table L.4 - OLS estimates of factor-level effects vs base level at flow rate 157 m^3/h

Head								Power mechanical							
Factor	Parametr			Δ, m	p-value	95% CI, lower	95% CI, upper	Parametr			Δ, kW	p-value	95% CI, lower	95% CI, upper	
Method	CAM	higher than	CV	3.80	0.00	2.32	5.28	CAM	higher than	CV	0.99	0.00	0.47	1.52	
D_3	281	lower than	297	-3.07	0.00	-4.78	-1.35	281	lower than	297	-0.85	0.01	-1.46	-0.24	
D_3	281	lower than	329	-7.34	0.00	-9.35	-5.33	281	lower than	329	-1.59	0.00	-2.31	-0.88	
D_3	297	lower than	329	-4.27	0.00	-6.28	-2.27	297	lower than	329	-0.74	0.04	-1.46	-0.03	
b_3	27	lower than	40	-1.08	0.26	-3.09	0.93	27	lower than	40	-0.24	0.47	-0.95	0.47	
b_3	27	higher than	52	0.85	0.30	-0.86	2.56	27	higher than	52	0.29	0.31	-0.32	0.89	
b_3	40	higher than	52	1.93	0.06	-0.08	3.94	40	higher than	52	0.53	0.13	-0.19	1.24	
Efficiency								Losses total pressure							
Factor	Parametr			Δ, p.p	p-value	95% CI, lower	95% CI, upper	Parametr			Δ, m	p-value	95% CI, lower	95% CI, upper	
Method	CAM	lower than	CV	-1.39	0.04	-2.71	-0.07	CAM	higher than	CV	1.96	0.00	0.89	3.03	
D_3	281	higher than	297	0.86	0.24	-0.67	2.38	281	lower than	297	-1.67	0.01	-2.91	-0.43	
D_3	281	higher than	329	4.65	0.00	2.86	6.44	281	lower than	329	-5.11	0.00	-6.56	-3.66	
D_3	297	higher than	329	3.79	0.00	2.01	5.58	297	lower than	329	-3.44	0.00	-4.89	-1.99	
b_3	27	higher than	40	0.74	0.379	-1.05	2.53	27	higher than	40	0.176	0.79	-1.28	1.63	
b_3	27	higher than	52	0.15	0.83	-1.37	1.68	27	higher than	52	1.20	0.06	-0.04	2.43	
b_3	40	lower than	52	-0.58	0.48	-2.37	1.20	40	higher than	52	1.021	0.15	-0.43	2.47	

Appendix M. Confirmation of implementation in production

ul. Droga Jeziorna 8, skr. poczt. 31, 86-303 Grudziądz
tel. +48(56) 45 07 400; fax: +48(56) 46 25 955
NIP 876-02-03-813 www.hv.pl

- Dział Obsługi Klienta
  tel. +48(56) 45 07 340, 45 07 457, 45 07 331
  tel. +48(56) 45 07 502, 45 07 476
  fax:+48(56) 45 07 338
- Dział Eksportu
  tel. +48(56) 45 07 437, 45 07 554, 45 07 547
  fax:+48(56) 45 07 346
- Serwis
  tel. +48(56) 45 07 452
  Serwis 24h 0 661 389 000

Grudziądz, 14.10.2024r

Oświadczenie

Oświadczam, że w dniach od 11 do 15 marca 2024 r. doktorantka Politechniki Wrocławskiej Anna Chernobrova odbyła staż w dziale Badawczo-Rozwojowym Hydro-Vacuum S.A. na stanowisku Referent ds. Technicznych. W trakcie tygodniowego stażu zaznajomiła się z profilem produkcji fabryki a także poznała praktyczne zastosowanie technik wytwarzania elementów maszyn, takie jak: odlewnictwo, obróbka skrawaniem, spawalnictwo oraz przetwórstwo tworzyw sztucznych. Miała również możliwość poznać technologię montażu oraz badania wyrobów.

Do głównych obowiązków Pani Anny Chernobrovej należało wykonanie projektu wraz z analizami CFD, spiralnego kanału zbiorczego dla pompy jednostopniowej zgodnej z normą PN-EN 733 o typowielkości 80-200. W związku z otrzymaniem pozytywnych wyników analiz, spirala zbiorcza wg projektu doktorantki została wdrożona do produkcji pompy NHVf.80-200 w Hydro-Vacuum S.A.

W trakcie stażu Pani Anna Chernobrova wykazała się bardzo dużym zaangażowaniem i starannością w wykonywaniu powierzonych jej obowiązków. Aktywnie kreowała nowe rozwiązania oraz wykazała się umiejętnością pracy zarówno samodzielnie jak i w grupie.

DYREKTOR
ds. Badań i Rozwoju
Marcin Janczak

Produkujemy
Pompy głębinowe, pompy zatapialne, pompy samozasysające, przepompownie i tłocznie, ścieków, zystemy do podnoszenia ciśnienia, pompy pionowe, pompy odśrodkowe, pompy próżniowe i dmuchawy, pompy przemysłowe, urządzenia zabezpieczająco-sterujące pracą pomp i układów pompowych.

Kapitał Zakładowy 2.265.631,65 zł opłacony w całości, KRS nr 0000026737 – Sąd Rejonowy w Toruniu, VII Wydział Gospodarczy KRS, Nr BDO 000018483

Hydro-Vacuum S.A. informuje, że przetwarza Pana/Pani dane osobowe zgodnie z obowiązującymi przepisami Ustawy o ochronie danych osobowych. Szczegółowe informacje można uzyskać na stronie www.hv.pl/rodo.php